The Pennsylvania State University

The Graduate School

Department of Mechanical and Nuclear Engineering

AN IMPROVED STEADY-STATE MODEL OF LOOP HEAT PIPES BASED ON

EXPERIMENTAL AND THEORETICAL ANALYSES

A Thesis in

Mechanical Engineering

by

Po-Ya Abel Chuang

Submitted in Partial Fulfillment
of the Requirements
for the Degree of

Doctor of Philosophy

December 2003

The thesis of Po-Ya Abel Chuang was reviewed and approved* by the following:

John M. Cimbala
Professor of Mechanical Engineering
Thesis Advisor
Chair of Committee

Jack S. Brenizer
Professor of Mechanical and Nuclear Engineering
Program Chair of Nuclear Engineering

Ralph L. Webb
Professor of Mechanical Engineering

Fan-Bill Cheung
Professor of Mechanical and Nuclear Engineering

Triem T. Hoang
President of TTH Research, Inc.

Richard C. Benson
Professor of Mechanical Engineering
Head of the Department of Mechanical and Nuclear Engineering

*Signatures are on file in the Graduate School

ABSTRACT

A loop heat pipe (LHP), a two-phase heat transfer device, was studied both analytically and experimentally. Thermocouples were used to measure temperatures along the loop, and neutron radiography was employed as a visualization tool to see-through the metal shell. A new gravity-assisted operating theory was formulated based on these experimental measurements and observations. Trends of steady-state operating temperature are presented and explained at adverse, zero, and positive elevations.

An improved 1-D steady-state model was developed, based on the newly formulated operating theory at various elevations. The effects of sink temperature, ambient temperature, elevation, external thermal conductance of the condenser, two-phase heat transfer and pressure drop correlations, heat leak, and insulation, on the performance of a LHP were studied in detail.

Experimental results of the measured temperatures when the LHP was operated at 2-inch adverse, zero, 1-inch, 3-inch, and 5-inch positive elevations, are presented and discussed. Temperature hysteresis and low-power start-up problems were observed and are also discussed. The measured temperatures are also compared to the results predicted by the steady-state model when the LHP was operated at 3 ½-inch adverse, zero, and 3 ½-inch positive elevations. In all cases, there is excellent agreement between the experimental data and the predicted results.

The most significant result of this study is the discovery, development, and modeling of the operating theory at gravity-assisted conditions. The operating characteristics when the LHP is operating at these conditions are unique and have never

been studied before. In this study, the gravity-assisted operating theory is explained

thoroughly and the LHP performance can be predicted analytically.

TABLE OF CONTENTS

LIST OF FIGURES

LIST OF TABLES

LIST OF SYMBOLS

A_h — Heating surface area, m^2

A_W — Cross-sectional area of the primary wick, m^2

C_P — Specific heat at constant pressure, J/kg-K

D_W^I — Inner diameter of the primary wick, m

D_W^O — Outer diameter of the primary wick, m

E — Total energy of the system, J

f — Darcy friction factor

g — Gravity, 9.81 m/s^2

h — Height between the evaporator and the condenser, m

$h_{2\phi}$ — Two-phase convective heat transfer coefficient, W/m^2-K

j_g — Vapor superficial velocity, m/s

j_L — Liquid superficial velocity, m/s

k — Thermal conductivity of working fluid, W/m-K

K — Minor loss coefficient

k_{EFF} — Effective thermal conductivity of primary wick, W/m-K

k_{WICK} — Thermal conductivity of wick material, W/m-K

L_{LVI} — Location of the liquid-vapor interface in the condenser, m

L_{WICK} — Length of primary wick, m

$L_{2\phi}$ — Length of two-phase fluid flow in the loop, m

$\dot{m}$ — Mass flow rate, kg/s

$\dot{m}_{TOTAL}$ — Total mass flow rate of the system, kg/s

Nu — Nusselt number

$\left(dP/dz\right)_{2\phi}$ — Pressure gradient for two-phase flow through tube, Pa/m

$\left(dP/dz\right)_g$ — Pressure gradient for vapor flow alone through tube, Pa/m

$\left(dP/dz\right)_L$ — Pressure gradient for liquid flow alone through tube, Pa/m

$\left(dP/dz\right)_{LO}$	Pressure gradient for entire flow as liquid through tube, Pa/m
ΔP_{BAY}	Pressure drop in the bayonet, N/m^2
ΔP_C	Pressure drop in the condenser, N/m^2
ΔP_{CAP}	Pressure gain from the surface tension across the evaporating menisci, N/m^2
$\Delta P_{CAP,\mathrm{max}}$	Maximum capillary head of a porous material, N/m^2
ΔP_{GRAV}	Pressure drop/gain from gravitational head, N/m^2
$\Delta P_{L.L.}$	Pressure drop in the liquid line, N/m^2
ΔP_{TOTAL}	Total pressure drop of the system, N/m^2
$\Delta P_{V.C.}$	Pressure drop in the vapor channel, N/m^2
$\Delta P_{V.L.}$	Pressure drop in the vapor line, N/m^2
ΔP_{WICK}	Pressure drop of liquid flow through the primary wick, N/m^2
Pr	Prandtl number
$\dot{Q}$	Rate of heat added to the system, W
$\dot{Q}_{APP}$	Total heat load applied to the evaporator, W
$\dot{Q}_{C-A}$	Heat loss/gain between the condenser and the ambient, W
$\dot{Q}_{C-S}$	Heat loss/gain between the condenser and the heat sink, W
$\dot{Q}_{EVAP}$	Amount of heat carried by the working fluid exiting the evaporator via vapor line, W
$\dot{Q}_{HL}$	Heat leak from the evaporator to the reservoir, W
$\dot{Q}_{HL,A}$	Heat leak by axial conduction through the joint between the evaporator and the reservoir, W
$\dot{Q}_{HL,R}$	Heat leak by radial conduction across the primary wick, W
$\dot{Q}_{LL-A}$	Heat exchange between the liquid line and the ambient, W
$\dot{Q}_{R-A}$	Heat exchange between the reservoir and the ambient, W
$\dot{Q}_{SC}$	Amount of subcooling brought back by the liquid in the liquid line, W
$\dot{Q}_{VL-A}$	Heat exchange between the vapor line and the ambient, W

r	Radial coordinate, m
R	Local radius of the meniscus in the primary wick, m
Re	Reynolds number
r_{EFF}	Effective radius of the meniscus in the primary wick, m
T_{AMB}	Ambient temperature, which refers to the temperature measured around the test LHP, K
$T_{EFF,SINK}$	Effective sink temperature, K
T_{EVAP}	Temperature at the outer surface of the evaporator body, K
T_F	Fluid temperature, K
T_{RES}	Reservoir temperature, K
T_{SINK}	Sink temperature, which refers to the cooling water inlet temperature, K
T_{SAT}^I	Saturation temperature at the inner surface of the primary wick, K
T_{SAT}^O	Saturation temperature at the outer surface of the primary wick, K
T_{SSOT}	Steady-state operating temperature of the LHP, K
T_W	Wall temperature, K
TC_{OUT}	Liquid temperature at the exit of the condenser, K
TL_{OUT}	Liquid temperature at the end of the liquid line before entering the reservoir, K
TVC_{OUT}	Vapor temperature at the exit of the vapor channel, K
$\Delta T_{AC.WICK}$	Temperature difference across primary wick, K
$(UA)_{HL}$	Overall heat transfer coefficient from the evaporator to the reservoir, W/K
$(UA)_{LHP}$	Overall heat transfer coefficient of a LHP, W/K
$\left(\dfrac{UA}{L}\right)_{F-A}$	Overall heat transfer coefficient from the working fluid to the ambient per unit length, W/m-K
$\left(\dfrac{UA}{L}\right)_{F-S}$	Overall heat transfer coefficient from the working fluid to the heat sink per unit length, W/m-K

$\left(\dfrac{UA}{L}\right)_{F-A}^{2\phi}$ Overall heat transfer coefficient from two-phase fluid to the ambient per unit length, W/m-K

$\left(\dfrac{UA}{L}\right)_{F-S}^{2\phi}$ Overall heat transfer coefficient from two-phase fluid to the heat sink per unit length, W/m-K

v Specific volume, m^3/kg

$\dot{W}$ Rate of work done by the system, W

x Thermodynamic vapor quality

X Martinelli parameter

z Axial coordinate, m

α Void fraction

ε Wick porosity

κ Wick permeability, m^2

λ Latent heat of vaporization, J/kg

μ Fluid viscosity, N s m^{-2}

θ Contact angle, rad

θ_a Advancing contact angle, rad

θ_r Receding contact angle

ρ Density, kg/m^3

σ Surface tension, N/m

ϕ_L Two-phase multiplier, $\left[\left(dP/dz\right)_{2\phi}/\left(dP/dz\right)_L\right]^{1/2}$

ϕ_g Two-phase multiplier, $\left[\left(dP/dz\right)_{2\phi}/\left(dP/dz\right)_g\right]^{1/2}$

ϕ_{LO} Two-phase multiplier, $\left[\left(dP/dz\right)_{2\phi}/\left(dP/dz\right)_{LO}\right]^{1/2}$

Φ Viscous dissipation, J

Subscripts

C Capillary-controlled mode

g Vapor phase

in	Inlet condition
G	Gravity-controlled mode
L	Liquid phase
out	Exit condition
1ϕ	Single-phase
2ϕ	Two-phase

Superscripts

$-$	Mean value
$\sim$	Metastable state
'	Non-equilibrium state

ACKNOWLEDGMENTS

2003 supervised by Dr. Triem T. Hoang and Tamara O'Connell. I am also grateful for the research funding received from Bechtel Bettis, Inc.

I am indebted to Dr. Budugur Lakshminarayana and Gita Talmage for their guidance and help in the early stage of my Ph.D. study. Without Dr. Lakshminarayana, I would not be here at Penn State; without Dr. Talmage, I would not be in Mechanical Engineering. Special thanks are due to Dr. Chung-Kuei Chang (Steven), my dearest friend and a tremendously positive "pivotal person" in my life. I was inspired by each of our conversations in the past four and half years.

Finally I wish to dedicate this work to my family: my parents, Sheng-Chung Chuang and Hsing-Mei Yin, my wife, Wen-Lan Hsieh (Daisy), and my brother, Po-Yu Chuang, for their unconditional love and consistent support. We are all looking forward to adding one more member, our baby, in April, 2004. Mom and Dad, we will surely pass what you have given us to our children in the near future. To my beloved wife, Daisy: your beauty conquers me, your words enlighten me, and your love completes me.

This thesis also marks the embarking for another journey. Now, I am ready to taste the sweet and bitter in the real world. Wish I can keep learning as well as sharing in every journey.

Chapter 1

INTRODUCTION

Thermal management is always a challenging and interesting topic in various applications, like permafrost stabilization, electronic equipment cooling, aerospace, etc. How to effectively remove heat from the heat source or supply heat to the heat sink has became a major obstacle for many newly developed technologies. Heat pipes have been the solution to a lot of engineering problems for the past several decades. A heat pipe is a two-phase heat transfer device used to transport heat in a highly efficient and effective manner. The effective coefficient of thermal conductivity of a heat pipe can be orders of magnitude higher than that of highly conductive solid materials, such as copper.

The heat transfer device investigated in this entire study is called a Loop Heat Pipe (LHP). It is a particular kind of heat pipe in which the evaporator and condenser components are separated, with the working fluid transported between the two components via tubing or pipes. After successfully demonstrating the heat transport capability and reliability in space applications, LHPs started gaining worldwide attention in the 1990s. LHPs are proven to be robust, self-starting and passive thermal transfer devices under regular operating conditions. Currently, LHPs have been used mainly in the spacecraft industry. With more and more ground test data, engineers who design terrestrial applications may find themselves interested in the development of LHPs.

1.1   FUNDAMENTAL OPERATING PRINCIPLES OF LOOP HEAT PIPES

A LHP consists of five key components: an evaporator, a reservoir, a condenser, a liquid line, and a vapor line. Surface tension developed in a porous material is the source of the pumping force used to circulate the fluid. A schematic diagram of a typical LHP with a detailed cross-sectional drawing of the evaporator is shown in Fig. 1.1.

When heat is applied to the evaporator body, it is conducted radially into the primary wick. Due to capillary action and surface tension, the liquid at the outer surface of the primary wick is vaporized and collected in the vapor channel. The amount of liquid vaporized depends on how much heat is applied to the evaporator. Because the vapor in the vapor channel has the highest pressure in the system, it flows through the vapor line to the condenser. In the condenser, where the heat is rejected, the vapor is condensed back to liquid and slightly subcooled. The liquid then flows through the liquid line back to the evaporator. In the evaporator/reservoir assembly, the liquid line is referred to as the bayonet, which directs the liquid all the way to the closed end of the evaporator. After the liquid exits the bayonet into the evaporator core, most of the liquid wets the primary wick and the secondary wick. The excess liquid goes back to the reservoir through the non-wick flow path. This completes the flow cycle in a LHP.

The primary wick in the evaporator is the divider between the vapor channel and the evaporator core. The primary wick is usually made of sintered metal with very fine pores (on the order of 1 μm) to increase the pumping capability of the system. Unlike the primary wick, the secondary wick resides in both the evaporator and the reservoir. It physically connects the evaporator and reservoir to prevent the primary wick from drying

out when the heat load is extremely high. The secondary wick usually has greater pore size (on the order of 100 μ m) than does the primary wick to minimize the pressure drop induced by the liquid flow in it. The detailed design and specification of primary and secondary wicks have significant influence on the performance of a LHP and are usually proprietary.
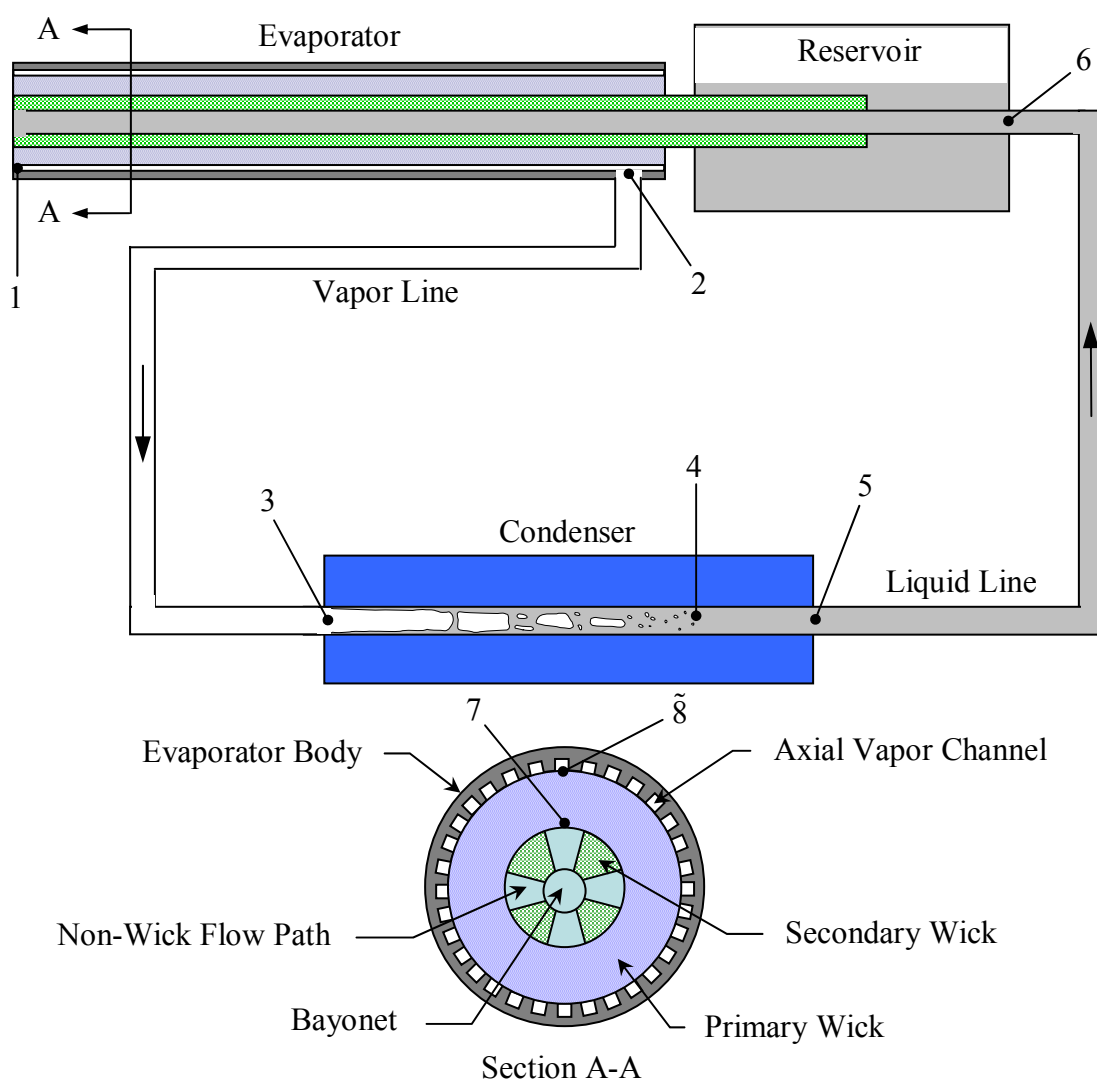
Fig. 1.1: Schematic diagram of a loop heat pipe. The numbers indicate the locations inside the LHP, and are used in Fig. 4.1 and Fig. 4.7 with corresponding thermodynamic states.

Because the evaporator and the condenser are separated by smooth and flexible transportation lines, the pressure drop for the liquid returning to the evaporator is much less than that in a traditional heat pipe. Along with the high pumping capability provided by the primary wick with very fine pore size, LHPs can be operated against gravity efficiently. This also allows the heat source and heat sink to be at different locations within a reasonable distance (on the order of meters), while the system still functions properly with minimal temperature differences. Another unique design of LHPs is that the evaporator and the reservoir are physically connected. This design not only prevents the primary wick from drying out but also allows vapor to exist in the evaporator core. Excess liquid and vapor inside the evaporator core flow back to the reservoir following the non-wick flow path. Since the reservoir contains both liquid and vapor, it remains at saturation temperature while the LHP is operating.

1.2   DESIGN OF LOOP HEAT PIPES

For different applications, each LHP has its own design requirements. The common requirements are:

1. Maximum and minimum non-operating temperature, which is the LHP temperature when it is not functioning.

2. Maximum and minimum operating temperature, which is the LHP temperature when it is operating.

3. Maximum and minimum heat to be removed from the heat source.

4. Distance between the heat source and heat sink.

5. Other criteria like the orientation flexibility of the LHP or special operating conditions may be encountered.

After determining all the design requirements, a series of choices has to be made before a LHP can be manufactured, including the working fluid, the properties and material of the primary wick, the size and design of each component, and how much working fluid needs to be charged into the system. This section introduces the general guidelines for making the choices in each design stage.

1.2.1 Working Fluids

The working fluid in the LHP determines the range of the operating temperature. Table 1.1 lists some of the commonly used working fluids, their melting and boiling points at atmospheric pressure, and the operating temperature range [Faghri, 1995]. Depending on the operating temperature, LHPs are classified into four categories: cryogenic (4-200 K), low (200-550 K), medium (550-750 K), and high (750 K and above) temperature ranges. Most LHP applications fall in the low temperature range.

Another concern about deciding the working fluid is the compatibility between the working fluid and the material of the LHP. Any chemical reaction between the working fluid and the material of the LHP creates non-condensable gas (NCG) in the system. The existence of NCG degenerates the performance of a LHP. Information concerning compatibility of metals with working fluids can be found in [Faghri, 1995].

Table 1.1: Operating temperature range of various working fluids [Faghri, 1995].

Working fluid	Melting point, K at 1 atm	Boiling point, K at 1 atm	Operating temperature range, K	Classified temperature application
Helium	1.0	4.2	2-4	Cryogenic
Hydrogen	13.8	20.4	14-31	
Neon	24.4	27.1	27-37	
Nitrogen	63.1	77.4	70-103	
Argon	83.9	87.3	84-116	
Oxygen	54.7	90.2	73-119	
Krypton	115.8	119.7	116-160	
Ammonia	195.5	239.9	213-373	Low temperature
Pentane	143.1	309.2	253-393	
Freon 113	236.5	320.8	263-373	
Acetone	180.0	329.4	273-393	
Water	273.1	373.1	303-473	
Mercury	234.2	630.1	523-923	Medium temperature
Sulphur	385.9	717.8	530-947	
Sodium	371.0	1151	873-1473	High temperature
Lithium	453.7	1615	1273-2073	
Silver	1234	2385	2073-2573	

1.2.2 Primary Wick and Secondary Wick

The primary wick to a LHP is like the heart to a human, because the capillaries in the primary wick provide the required pressure to circulate the fluid in the system. Thus, the selection of the primary wick is critical to the design of a LHP. There are three major properties of the primary wick that have to be considered, including effective pore radius, wick permeability, and thermal conductivity. The effective pore radius determines the capillary limit of the primary wick (Eq. 4.11), the wick permeability determines the pressure drop induced by the liquid flow across the primary wick (Eq. 5.66), and the thermal conductivity determines the radial heat leak of the system. All three of them

have great impact on the performance of a LHP. An ideal primary wick should have small effective pore radius (1-5 μm), high permeability (> 1.0×10^{-14} m^2), and low thermal conductivity. However, these properties are contradictory in the design of a primary wick. For example, a wick with small effective pore radius and low thermal conductivity may have a low permeability. Therefore, some compromise on properties may be required in the real design process.

The secondary wick is used to supply the liquid from the reservoir to the evaporator to prevent wick dry out. This requires much lower pumping capability than that of the primary wick. Thus, the effective pore radius is usually much higher (50-200 μm) than that of the primary wick (1-5 μm). A typical design of the secondary wick is stainless steel wire mesh.

1.2.3   Sizing of Each Component

The size of the evaporator and the primary wick depends strongly on the maximum heat load. Most evaporators are between 2-inch long with 1/4-inch O.D. and 24-inch long with 1-inch O.D. The size of the transportation line is determined relative to the size of the evaporator, and is typically between 1/16-inch and 1/4-inch. The main design criterion is that the LHP does not exceed all the heat transfer limitations discussed in Section 2.2 when operating within the operating heat load range.

The length and size of the transportation lines influence the pressure drop in the system, heat transfer between the fluid and the ambient, and the size of the reservoir, all depend on the distance required between the heat source and the heat sink. After

determining the size and length of the transportation lines, the size of the reservoir can be calculated. Sizing the reservoir is one of the most critical tasks in the design of a LHP. The rule-of-thumb is that the volume of the reservoir be at least 110 % of the combined volume of the vapor line and the condenser. Once the size of the reservoir is determined, the total volume in the LHP is also determined. A reasonable safety margin must always be considered when determining the size of each component.

1.2.4   Amount of Working Fluid Charged into the LHP

The amount of working fluid charged into the system is also critical to the performance of a LHP. There are guidelines to be followed: one sets the minimum value and the other sets the maximum value. Assuming the LHP is at the lowest non-operating temperature and the transportation lines and the condenser are filled with liquid, there has to be enough liquid left in the reservoir to prime the primary and secondary wicks. This provides the minimum amount of working fluid to be charged in the LHP. On the other hand, when the LHP is at the highest non-operating temperature, the liquid volume must be smaller than the entire volume of the LHP. Also, when the LHP is at the highest operating temperature, the liquid volume must be smaller than the sum of volumes in the liquid line, evaporator core, and reservoir. The lower of these two criteria becomes the maximum amount of working fluid to be charged in the LHP.

After the analysis, if the minimum value of working fluid is higher than the maximum value, then the physical sizes of the components have to be redesigned. This is usually achieved by enlarging the size of the reservoir.

1.2.5 Design of Evaporator/Primary Wick Assembly

The performance of a LHP also depends on the design of the evaporator and the primary wick. Fig. 1.2 illustrates four different designs of the evaporator and the primary wick. In Fig. 1.2a), axial vapor channels are extruded on the evaporator body to provide the vapor flow to the vapor line. In Fig. 1.2b) and c), circumferential grooves are threaded on the evaporator body to provide vapor flow to the main axial vapor channels. In Fig. 1.2d), circumferential grooves are threaded on the primary wick to provide vapor flow to the main axial vapor channel. These designs of the evaporator and primary wick result in differences in heating area, heat transfer coefficient across the heating area, and vapor pressure drop in the vapor channel. Therefore, the performance of the LHP changes accordingly.
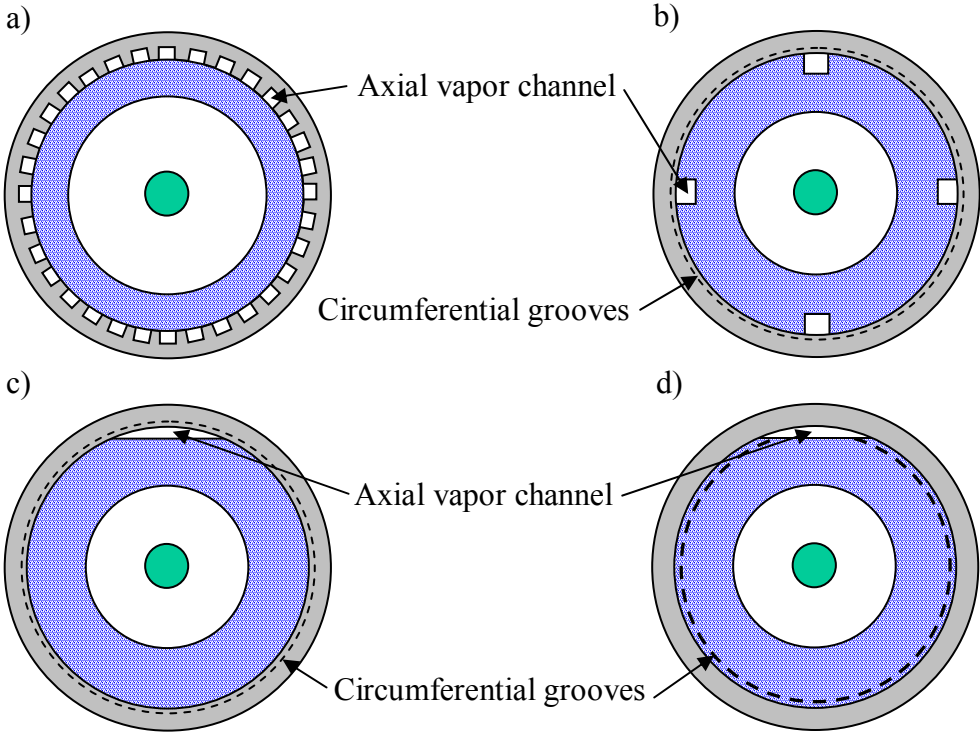
Fig. 1.2: Design of evaporator and primary wick.

1.3 **INTRODUCTION TO NEUTRON RADIOGRAPHY**

All material objects are formed from an arrangement of atoms, which can take many forms, varying from the regular pattern of a crystal lattice to the free moving single atoms within a gas plasma. No one has ever seen an atom – although the electron microscope allows us to get very close – and modern theory represents it as a tiny nucleus surrounded by a diffuse cloud of electrons, the outer boundary of which is not clearly defined and may not even be spherical. The nucleus is itself a group of closely bound neutrons and protons, the overall diameter of which is some 10,000 times smaller than the size of the atom. For simplicity, an atom can be imagined as consisting of an extremely small and dense nucleus surrounded by an enormous empty space (on the nuclear scale) in which a retinue of electrons maintains their regular orbital motions. The radiographic process requires free neutrons, and so they must be dislodged from the nucleus. This is achieved by bombarding the nucleus and causing it to change into smaller nuclei and a number of free neutrons. These liberated neutrons are electrically neutral (i.e. no charge) and so are able to pass through the electron cloud surrounding an atom without disturbing interactions.

Unlike the X-ray, which interacts with the electron cloud, the neutron interaction is not characterized by a rational dependence on the atomic number of the object. There are practically no generalizations that can be made which relate neutron characteristics to atomic mass or atomic number, and the interaction between a neutron and an atom of a particular nuclide is unique, the nature of the reaction being related only to the energy of the neutron. A comparison of neutron radiography and X-ray radiography is shown in

Fig. 1.3, where the mass attenuation coefficients of X-rays and thermal neutrons have been plotted against the atomic numbers of most of the elements [Von Der Hardt and Röttger, 1981]. X-rays show a continuous curve and so any two materials having a similar atomic number lie close to each other on the curve and consequently have similar absorption coefficients. Therefore, both materials attenuate an X-ray beam by about the same amount, and it is difficult for a detector to discriminate one from the other. The attenuation of neutrons, however, is a function of the nucleus rather than the density of electrons in a material, and it is frequently found that adjacent-number elements, for example boron and carbon, shown marked differences in neutron-attenuation coefficient and are therefore readily discriminated. Hydrogen has high neutron attenuation, and so it is possible to detect rubbers and plastics. Conversely dense materials such as lead and tungsten have low coefficients and are readily penetrated by thermal neutrons.

To produce a neutron radiograph a continuous supply of free neutrons, must be directed onto the object to be radiographed. The object modifies the neutron beam by scattering or absorbing the radiation, and the beam reaching the detector has an intensity pattern representative of the structure of the object.

Neutron imaging is an ideal flow visualization tool for LHP study if the working fluid contains hydrogen (high neutron attenuation), and the shell of the LHP is made of aluminum or stainless steel, which is nearly transparent to thermal neutrons. Liquids and vapors can also be easily distinguished since a liquid attenuates neutrons much more than a vapor of the same substance, because of the large density difference.
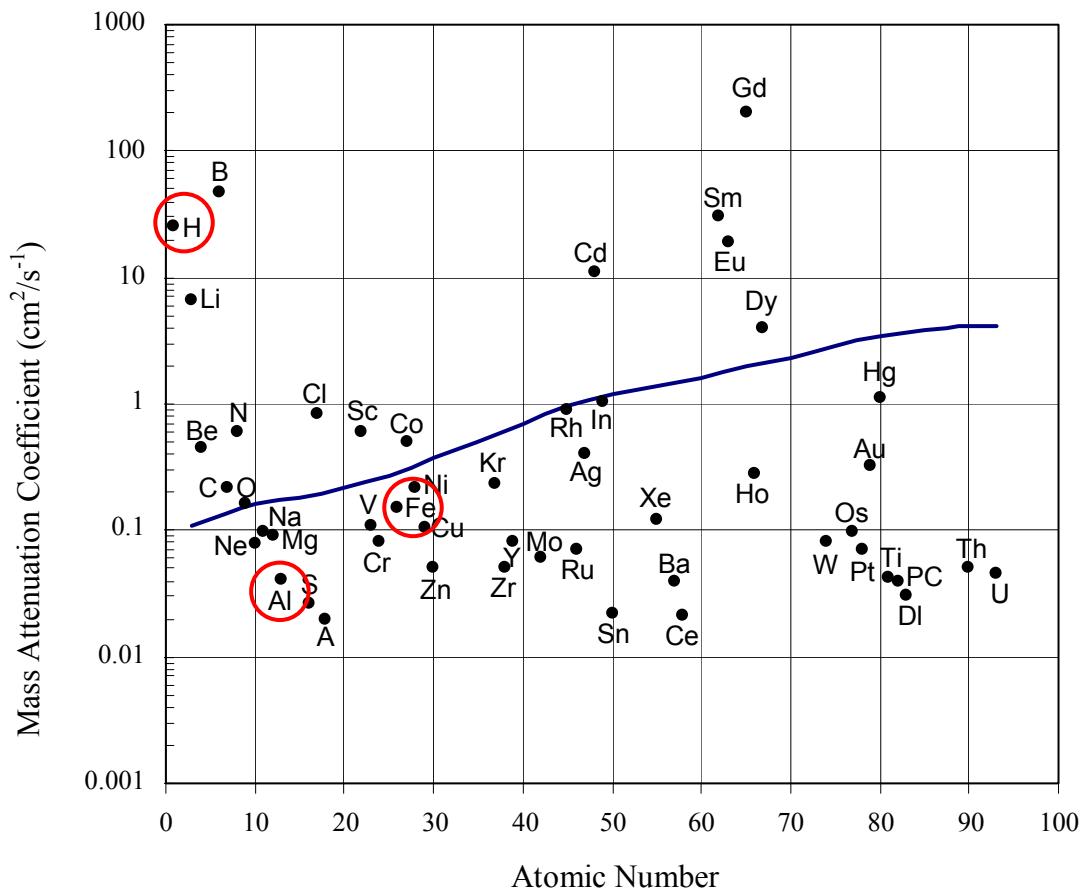
Fig. 1.3: A comparison of mass attenuation coefficients for the elements for both medium energy x-ray (about 125kV, solid line) and thermal neutrons (dots). Hydrogen (H), aluminum (Al), and iron (Fe) are highlighted.

1.4   RESEARCH OBJECTIVES

Loop heat pipes are very attractive heat transfer devices that have great potential in various applications. Although many papers regarding LHPs have been published, most of them present test results and discussions on certain specific aspects of LHP operation. Some aspects of LHP behavior are still not fully understood. Thus, a

complete detailed operating theory of LHPs has not yet been developed and needs to be studied further. The main objectives of this research were:

1. To study the characteristics of LHPs.

2. To verify the feasibility of using neutron radiography as a flow visualization tool for study of LHPs.

3. To improve the performance of a 1-D steady-state analytical model based on experimental studies and flow visualization observations.

4. To observe and explain the operating characteristics when a LHP is operated at a gravity-assisted condition, which means the condenser is located above the evaporator.

5. To develop a 1-D steady-state analytical model to predict the performance of a LHP when it is operated at a gravity-assisted condition.

Chapter 2

LITERATURE SURVEY

This chapter introduces the historical development of heat pipes, which are considered the ancestor of LHPs, and LHPs. Various operating limitations of LHPs and current issues regarding the performance characteristics are also included and discussed.

2.1   HISTORICAL DEVELOPMENT

Since a loop heat pipe is a particular kind of heat pipe, the history of heat pipes must be discussed first. The uniqueness of a heat pipe is the existence of a wick structure in the system to transport heat against gravity by an evaporation-condensation cycle. However, many heat pipe applications do not need to rely on this feature, and the Perkins Tube, which was invented decades before the heat pipe, is basically a form of thermosyphon that is still being used today. Therefore, the Perkins Tube became an essential part of the history of the heat pipe.

2.1.1   The Perkins Tube (Thermosyphon)

The predecessor of the heat pipe, the Perkins tube, was introduced by the Perkins family from the mid-nineteenth to the twentieth century through a series of patents in the United Kingdom. Most of the Perkins tubes were wickless gravity-assisted thermosyphons, in which heat transfer was achieved by evaporation. A thermosyphon

refers to a heat transfer device in which the working fluid is circulated by the density difference between a cold temperature and a hot temperature fluid or between vapor and liquid. The design of the Perkins tube, which is closest to the present heat pipe, was described in a patent by Jacob Perkins [1836]. A schematic drawing of the Perkins tube is shown in Fig. 2.1. This design was a closed tube containing a small quantity of water operating in either a single- or two-phase cycle to transfer heat from a furnace to a boiler.
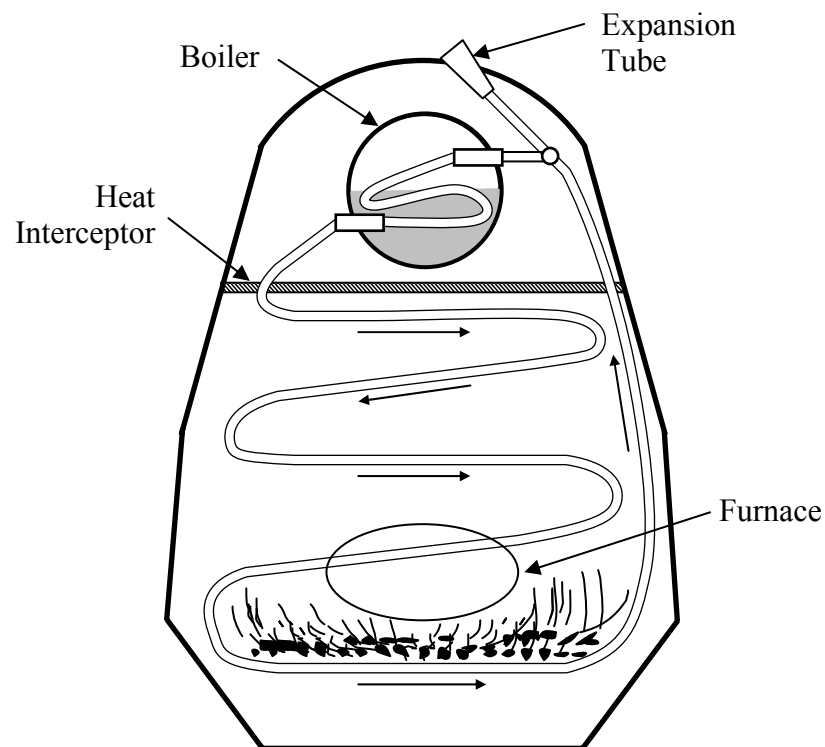
Fig. 2.1: A schematic diagram of Perkins Tube.

The water in the closed loop is boiled into steam when passing through the furnace, and flows to the boiler. In the boiler, the heat is rejected and the steam is condensed back to water. Because there is no wick structure in the system, it can operate efficiently only when the boiler is placed above the furnace.

In the development of the Perkins tube, the most interesting improvements were made by L. P. Perkins and W. E. Buck [1892]. Their work focused on the study of the fluid inventory. While water was the only specific working fluid, they tested the use of anti-freeze type fluids, and fluids having a higher boiling temperature than water at atmosphere pressure.

2.1.2 The Heat Pipe

The heat pipe was first conceived by R. S. Gaugler [1944] of the General Motors Corporation in the U.S. Patent No. 2350348. Gaugler, who was working on refrigeration problems at that time, envisioned a device that would evaporate a liquid at a point above the place where condensation would occur, without requiring any additional work to move the liquid to the higher elevation. His device consisted of a closed tube in which the liquid would absorb heat at one location causing the liquid to evaporate. The vapor would then travel down the length of the tube where it would condense and release its latent heat. It would then travel back up the tube by capillary pressure to start the process over. In order to move the liquid back up to a higher point, Gaugler suggested the use of a capillary structure consisting of a sintered iron wick. However, it was not developed beyond the patent stage, as other technology currently available at that time was applied to solve the particular thermal problem at General Motors Corporation.

In 1962, Trefethen [1962] resurrected the idea of a heat pipe in connection with the space program. The heat pipe concept received relatively little attention, until Grover et al. [1964] published the results of an independent investigation and first applied the

term heat pipe to describe a "synergistic engineering structure which is equivalent to a material having a thermal conductivity greatly exceeding that of any know metal". Grover [1966] built several prototype heat pipes, the first of which used water as a working fluid and was soon followed by a sodium heat pipe which operated at 1100 K. Since that time, heat pipes have been employed in numerous applications ranging from temperature control of the permafrost layer under the Alaska pipeline to the thermal control of optical surfaces in spacecraft. The first commercial organization to work on heat pipes was RCA [Judge, 1966]. They made heat pipes using glass, copper, nickel, stainless steel, molybdenum and TZM molybdenum as wall materials. Working fluids included water, cesium, sodium, lithium, and bismuth. Maximum operating temperatures of 1650 $^{\circ}$C had been achieved.

The early development of terrestrial applications of heat pipes proceeded at a slow pace. Since heat pipes can operate in micro-gravitational fields due to capillary action without any external force field or pump, most early efforts were directed toward space applications. However, due to the high cost of energy, especially in Japan and Europe, the industrial community began to appreciate the significance of heat pipes and thermosyphons in energy savings as well as design improvements in various applications.

A heat pipe typically consists of a sealed container lined with a wicking material. The container is evacuated and backfilled with just enough liquid to fully saturate the wick. Because heat pipes operate on a closed two-phase cycle and only pure liquid and vapor are present within the container, the working fluid remains at saturation conditions as long as the operating temperature is between the triple point and the critical state. As illustrated in Fig. 2.2, a heat pipe consists of three distinct regions: an evaporator, a

condenser, and an adiabatic region. When heat is added to the evaporator region of the container, the working fluid present in the wicking structure is heated until it vaporizes. The high temperature and corresponding high pressure in this region cause the vapor to flow to the condenser region, where the vapor condenses and gives up its latent heat of vaporization. The capillary forces existing in the wicking structure then pump the liquid back to the evaporator.
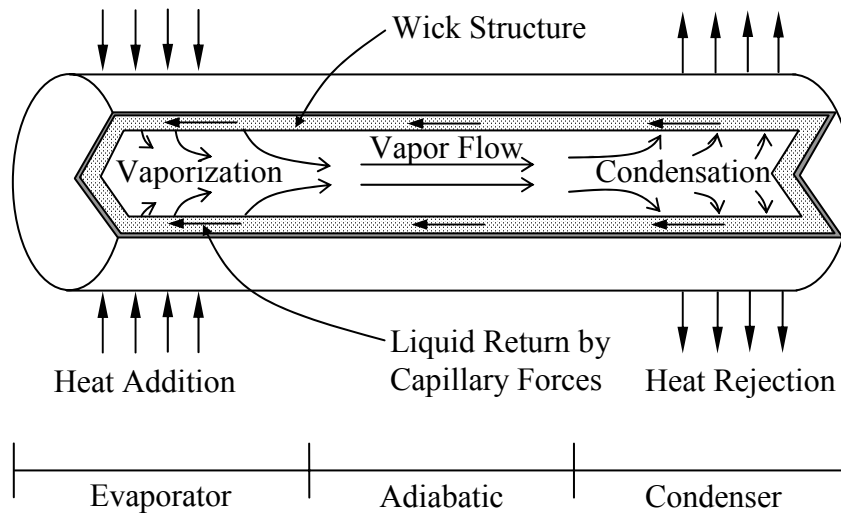
Fig. 2.2: A schematic diagram of a conventional heat pipe.

2.1.3   The Capillary Pump Loop

The capillary pumped loop (CPL) is very similar to the loop heat pipe. The CPL was invented by F. J. Stenger [1966] of NASA Lewis Research Center, but serious development did not begin until the late 1970s. In 1982, an aluminum-ammonia CPL with the capability of transporting 6.4 kW (15 W/cm^2) over 10 meters was manufactured by OAO Corporation (NASA Goddard's CPL-1). In 1985 and 1986, the first flight

experiments of CPL technology were successfully tested [Ku et al., 1986]. In the 1990s, extensive ground testing had been performed, and the potential of the CPL as a reliable and versatile thermal transport system for space applications was demonstrated. Fig. 2.3 shows a drawing of a typical capillary pumped loop.
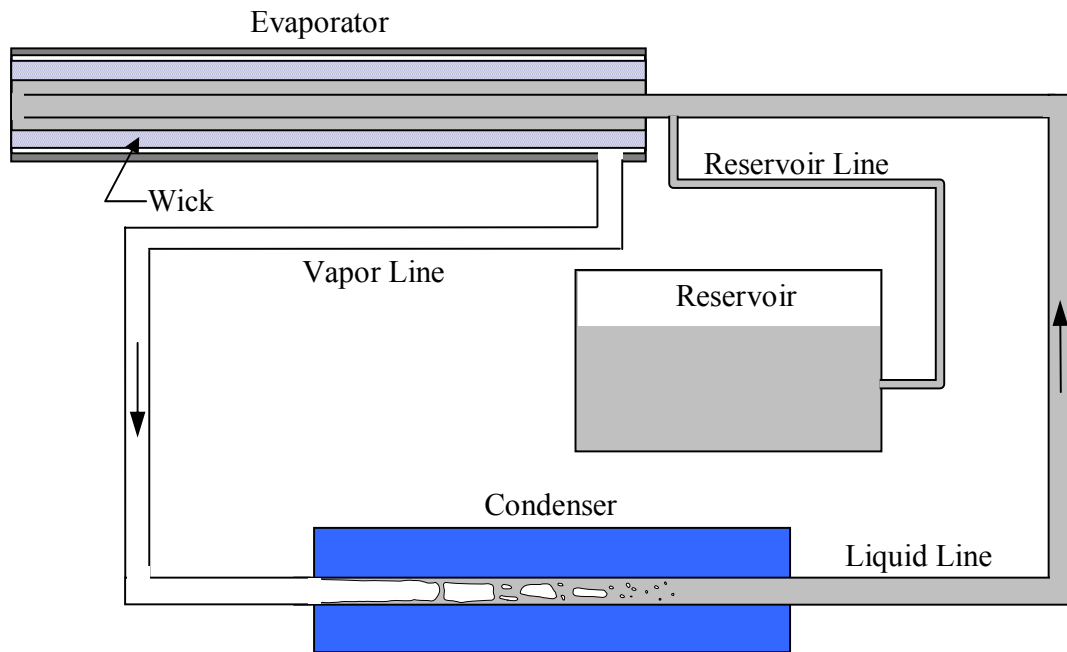
Fig. 2.3: Schematic diagram of a capillary pump loop.

The main difference between a CPL and a LHP is the location of the reservoir (a.k.a. compensation chamber). In a CPL, vapor generated in the evaporator flows to the condenser, where the vapor is condensed back to liquid, and liquid exits the condenser with a small amount of subcooling. The liquid flows back to the evaporator through the liquid line and the bayonet. In the evaporator core, a secondary wick is usually used to prevent any bubbles from blocking the liquid path to the primary wick. The liquid then flows radially to the outer surface of the primary wick to complete the cycle.

The reservoir in a CPL is physically isolated from the loop. It is connected to the liquid line by a reservoir line to store excess liquid in the system. The primary wick in the CPL is usually made of polyethylene to minimize the heat conducted through the primary wick and vaporize the liquid in the evaporator core. The pore size of a polyethylene wick is around 15 μ m. Due to these construction differences, the behavior between a CPL and a LHP differs in many ways. A major difference is the start-up characteristics. A CPL requires pre-conditioning of the loop, usually by heating the reservoir, in order to ensure that the wick is fully wetted. One advantage of CPL is that the operating temperature can be controlled precisely by the reservoir set point temperature regardless of changes in the heat load or sink temperature. CPLs and LHPs have their own advantages and disadvantages depending on the application. A detailed overview of CPLs can be found in Ku [1993].

2.1.4 The Loop Heat Pipe

Generally speaking, heat pipes are excellent heat transfer devices. Advantages of heat pipes include a very high thermal conductance, no pumping power requirements, no moving parts, and relatively low pressure drops produced by the system. But serious constraints on conventional heat pipes are the reduction of transport capabilities over long distances and when it is operated against gravity, which means the condenser is located below the evaporator. Loop heat pipes are developed to provide the solution to this problem.

Loop heat pipes (LHPs) were invented at the Urals Technical University in Russia in 1971 and patented in the USA by Maidanik et al [1985]. LHPs were used in space for thermal management purposes, especially on satellites. After successfully demonstrating the heat transport capability and reliability in space applications, LHPs started gaining worldwide attention in the late 1980s. Since then, numerous studies focusing on improving the efficiency of the system and understanding its operating characteristics have been conducted. The LHP is known for its high pumping capability and robust operation because it uses fine-pored metal wicks and the integral evaporator/reservoir design. It is the baseline design for thermal control of several spacecraft and commercial satellites.

2.2   HEAT TRANSFER LIMITATIONS OF LOOP HEAT PIPES

Similar to traditional heat pipes, LHPs are subject to a number of heat transfer limitations. Among these limitations are the viscous limit, sonic limit, capillary limit, entrainment limit, and boiling limit. Due to the different designs of LHPs, these limitations have different magnitudes and characteristics than those of traditional heat pipes.

Viscous limitation

Viscous limitation occurs when the operating temperature is extremely low and the applied heat load is small. It refers to when the viscous forces are larger than the pressure gradients caused by the applied heat load. Under this condition, there is no flow

or low flow in the system and the heat transport capability is limited. This is usually observed in cryogenic applications or in start-up from a frozen state.

Sonic limitation

Cotter [1967] proposed that compressible flow in a duct of constant cross section with mass addition and removal (i.e., vapor flow in the vapor channel) and constant mass flow in a duct of variable cross section (compressible flow in a converging-diverging nozzle) share a number of common properties. Therefore, for some LHP applications, especially those with liquid metal working fluids, the vapor velocity in the vapor channel may reach sonic values during the start-up or steady-state operation. Under this condition, the mass flow rate in the system reaches its maximum value and is referred to as choked.

Capillary limitation

With the combination of a specific primary wick and a working fluid, the pumping ability of the capillary structure to circulate the working fluid is limited. This limitation is usually called the capillary or hydrodynamic limit. If the total system pressure drops surpass the capillary limit, the wick dries out and operation of the LHP becomes unstable.

Entrainment limitation

The vapor and liquid flow in opposite directions in traditional heat pipe operation. Surface tension and shear forces interact across the liquid-vapor interface. When the vapor velocity is sufficiently high, the shear force may tear the liquid from the wick and entrain it in the vapor flow. This phenomenon inhibits the return of liquid to the evaporator. However, in LHPs, the vapor flowing to the condenser does not interact with

the liquid flowing back to the evaporator. The liquid at the outer surface of the primary wick may still be entrained by the high vapor flow in the vapor channel. However, this does not affect the supply of the liquid to the evaporator. Therefore, the entrainment limit is less important in LHP operation than in operation of traditional heat pipes.

Boiling limitation

In traditional heat pipes, the heat has to conduct all the way through the wick structure, which is saturated with liquid, and evaporate the liquid in the core area. When the applied heat load or the wall temperature becomes excessively high, boiling of the liquid in the wick structure may occur. The vapor bubbles generated inside the wick structure may block the liquid return paths and the wick can dry out.

The evaporator design of LHPs has the ability to tolerate the boiling limit better than heat pipes because the heat is conducted from the evaporator body to the primary wick, and evaporates the liquid at the outer surface in the primary wick. Boiling may still occur right below the heating surface when the heat load is excessively high. However, the generated vapor bubbles can be vented out to the vapor channel easily. Therefore, the boiling limit of LHPs is much higher than that of traditional heat pipes.

2.3   CURRENT ISSUES OF LOOP HEAT PIPES

Increased interest in various applications of LHPs has resulted in more research and development. Thus, more issues regarding the operating characteristics have been discovered and studied. Currently, there are several operating phenomena that are not yet fully understood, like temperature hysteresis, low-power start-up problem, temperature

oscillation, etc. Some of the major phenomena are introduced and discussed in the following sections.

2.3.1   Temperature Hysteresis

Early discoveries of temperature hysteresis were observed by Wolf and Bienert [1994] and Cheung et al. [1998]. Temperature hysteresis occurs when for the same operating conditions, namely sink temperature, ambient temperature and elevation, the steady-state operating temperature of a LHP depends not only on the applied heat load but also on the previous history of the heat load sequence. Kaya and Ku [1999[2]] performed a series of experiments to investigate this phenomenon at various orientations (tilt and adverse elevation). The typical trend of the steady-state operating temperature with temperature hysteresis is shown in Fig. 2.4.

Generally speaking, there are two different trends for the steady-state operating temperature to follow. The effect of the temperature hysteresis dominates the low heat load region (less than $\dot{Q}_T$ in Fig. 2.4). When heat load is higher than $\dot{Q}_T$, these two trends collapse into one and the effect of temperature hysteresis vanishes. The lower trend is not easily observed and the LHP is in an unstable operating condition. It usually happens when the starting heat load and increment of the heat load are both small. Once the heat load exceeds the transition heat load, $\dot{Q}_T$, the steady-state operating temperature should follow the upper trend from then on. Therefore, the upper trend is also referred to as the stable trend.
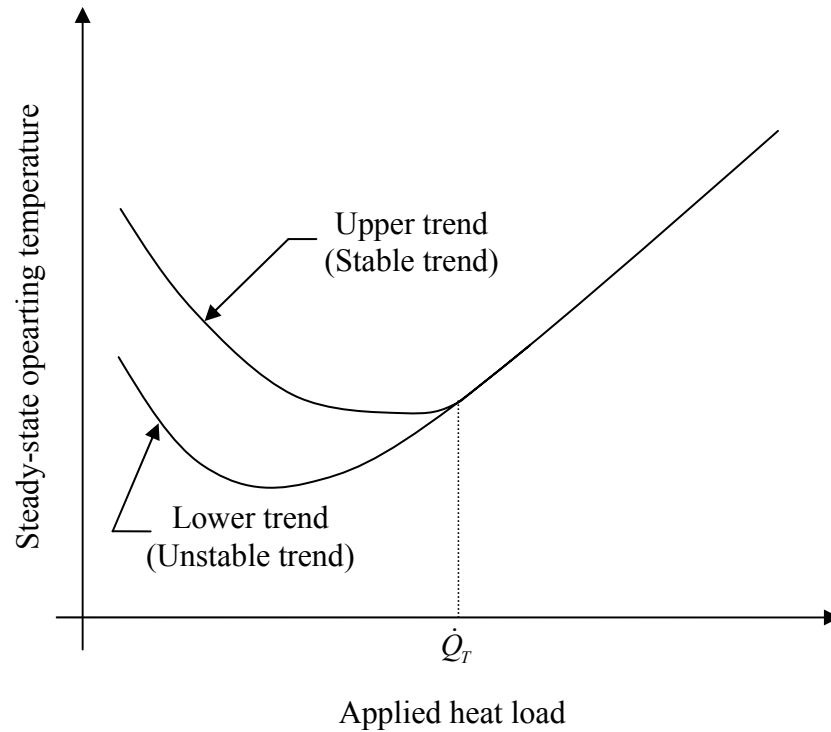
Fig. 2.4: Typical trend of steady-state operating temperature as a function of heat load when temperature hysteresis is observed.

The temperature difference between higher trend and lower trend depends on the design of the LHP and may be as large as 20 K. This may cause serious problems for thermal management of different applications. After their experimental investigations, Kaya and Ku [1999[2]] suggested that temperature hysteresis was caused by the partial dry-out of the secondary wick due to a rapid power decrease.

2.3.2   Start-Up Problems

LHPs are known to have reliable turnkey start-up ability. When heat is applied to the evaporator, the working fluid in the LHP starts circulating to remove the heat from

the evaporator to the condenser. However, a minimum heat load is required to establish the forward flow of the fluid in the system; otherwise, the LHP start-up may fail. The minimum heat load required to start a LHP depends strongly on the design and the size of the LHP.

Ku [1999] proposed four different situations of the liquid/vapor states inside the evaporator prior to start-up as plotted in Fig. 2.5. Each condition has its unique start-up characteristics, like required wall superheat or temperature overshoot. The temperature overshoot during the start-up process refers to the rise of the reservoir temperature above the initial or final steady-state operating temperature (whichever is higher). The condition where the vapor channel is filled with liquid and the evaporator core is filled with two-phase fluid (Fig. 2.5d) represents the most difficult condition for LHP start-up. Detailed explanations of different start-up situations can be found in Ku's paper.

Cheung et al. [1998] presented experimental data for the same start-up parameters: one had less than 1 $^\circ$C wall superheat and the other had more than 10 $^\circ$C wall superheat. The authors suggested that two-phase fluid existed in the vapor channel for the small superheat case, and the vapor channel was filled with liquid for the large superheat case.
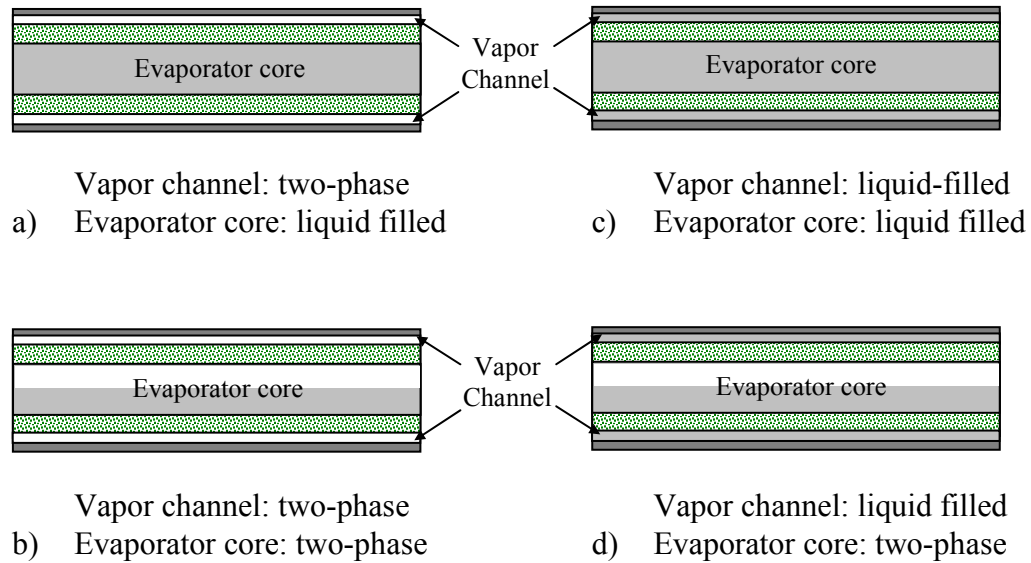
Fig. 2.5: Different start-up conditions in the evaporator [Ku, 1999].

Kaya et al. [1999[3]] performed experiments to study low power start-up characteristics with different orientations. The authors concluded that the required superheat, the maximum temperature at start-up, and the time required for start-up strongly depended on the loop orientation.

2.3.3   Temperature Oscillation

For most operating conditions, the LHP can usually reach a steady operating temperature with sufficient time. However, under certain operating conditions, the operating temperature of the LHP never reaches a stable condition but oscillates within a certain range. This phenomenon was identified by Ku et al. [2001] in a miniature LHP. It was observed that whenever the temperature oscillation occurred, the liquid-vapor

interface in the condenser moved back and forth around the condenser exit. In other words, the liquid-vapor interface oscillated between the end of the condenser and the beginning of the liquid line. The temperature oscillation is caused by thermal and hydrodynamic interactions between the evaporator, the reservoir, and the condenser. Ku et al. [2001] postulated that the oscillation of the temperature at the end of the liquid line caused the temperature of the reservoir and the void fraction inside the evaporator core to change accordingly. However, there is still no direct proof or verification of this postulation for the cause of temperature oscillation.

2.3.4 Capillary Limit in LHP Operation

When a LHP is operating in a condition that the total system pressure drop exceeds the capillary limit that the wick can provide, dry-out of the primary wick should occur. Due to the vapor penetration through the primary wick, the operating temperature of the LHP has a sudden increase when the capillary limit is exceeded. In traditional heat pipe operation, dry-out of the wick structure should cause the operation to fail. However, due to the integrated design of the evaporator and reservoir in a LHP, the LHP can still operate even through the capillary limit has been exceeded.

Ku et al. [2002] presented test data showing the performance of a LHP when the capillary limit was exceeded. Ku et al. installed a valve in the vapor line to introduce the pressure drop required to exceed the capillary limit. With the valve, the LHP could reach a high pressure drop with a low or moderate heat load. The test data showed that the operating temperature of the LHP oscillated in a high frequency manner when the

capillary limit was exceeded. With further increase of the heat load, the operating temperature reached a higher oscillating temperature but could still function. In addition, the LHP could recover from the dry-out of the primary wick by lowering the heat load without the need to remove the heat load or to start over again. The ability to recover from dry-out clearly shows that LHPs have a great advantage for high heat load application than traditional heat pipes or capillary pumped loops (CPLs).

2.3.5 Effects of Non-Condensable Gas in a LHP

Non-condensable gas (NCG) always exists in a LHP system because of several reasons, including the air left from the working fluid charging process, impurity of the working fluid, and chemical reactions between the fluid and the LHP materials. In the history of the development of heat pipes, ammonia has been shown to be compatible with aluminum, stainless steel, and nickel. The amount of NCG generated in the system is affected by factors including the amount of working fluid, surface area of the materials of construction, the manufacturing process, and the operating conditions.

The effects of NCG on the performance of a LHP depend strongly on the locations where the NCG accumulates. Possible destinations include the condenser and the reservoir. NCG may also circulate with the working fluid, or be absorbed by the primary wick. Theoretically, NCG in the reservoir increases the amount of heat leak. Thus, the steady-state operating temperature increases with an increasing amount of NCG in the LHP. Nikitkin and Bienert [1998] conducted an experimental study of effects of NCG on the LHP operation in an ammonia LHP by injecting hydrogen and nitrogen into

the loop through the vapor line. The amount of hydrogen gas injected into the system ranged from 33 % to 1100 % of the predicted NCG in the system at end-of-life (NOL). Test results indicated that the effects were almost negligible for small amounts of NCG injected (less than 600 % of the predicted NCG at NOL). When there were large quantities of NCG in the system (more than 600 % of the predicted NCG at NOL), the required start-up period and the operating temperature both increased. But no LHP failure was experienced during any of these tests. Therefore, Nikitkin and Bienert [1998] concluded that the LHP is relatively insensitive to the presence of NCG.

Chapter 3

EXPERIMENTAL SETUP

The LHP tested in this study was designed by TTH Research, Inc. and Swales Aerospace and manufactured by Swales Aerospace. The LHP is a closed high pressure tubing system with ammonia inside the tube as the working fluid. There are no pressure or flow rate measuring devices in the system. Only temperature can be measured by thermocouples on the surface of the tubing system. A data acquisition system designed and tested by Bechtel Bettis, Inc. was used to record the temperature measured throughout the experiment at a sampling rate of one data point per second. The LHP along with the data acquisition system were shipped to Penn State in September, 2000.

After receiving the test rig, a Variac and a watt meter were added to control and monitor the power applied to the evaporator. The room temperature in the Beam Laboratory at the Radiation Science and Engineering Center oscillates at a magnitude of 5 ^{o}F every few hours. To control the ambient temperature around the test LHP, an environmental chamber with an air conditioner and a control system was built.

From the observations made with neutron radioscopy, it was found that the location of the liquid-vapor interface in the condenser moves as the applied heat load changes. The performance of the LHP is very sensitive to the elevation difference between the evaporator and the liquid-vapor interface. Due to the design of the condenser, it is impossible to keep the elevation constant as heat load is varied when the condenser is placed vertically. To ensure that the elevation remains constant while the

applied heat load is changing, the condenser has to be laid horizontally throughout the experiment. Therefore, the condenser is placed onto a supporting wood plate with a jack mechanism attached underneath the wood plate.

3.1   LOOP DESIGN AND LAYOUT

The test LHP was composed of a strip heater, a cylindrical evaporator, a cylindrical reservoir, two transportation lines, and a condenser. A drawing of the test LHP with the locations of the thermocouples is shown in Fig. 3.1.

The primary wick was made of sintered nickel powder and the working fluid in the system was ammonia. The detailed specifications of the test loop are listed in Table 3.1. The system was monitored by 18 chomel/alumel (type K) thermocouples. There were four thermocouples on the outside of the reservoir: TC2 (top), TC3 (side), TC15 (side), and TC4 (bottom). Because the reservoir was always under two-phase conditions, the experimental steady-state operating temperature (SSOT) was obtained by taking the average of the temperatures measured on both sides and the top of the reservoir. The liquid near the bottom of the reservoir was usually subcooled and its temperature was thus lower than the saturation temperature; therefore, TC4 was not used in the calculation of SSOT.
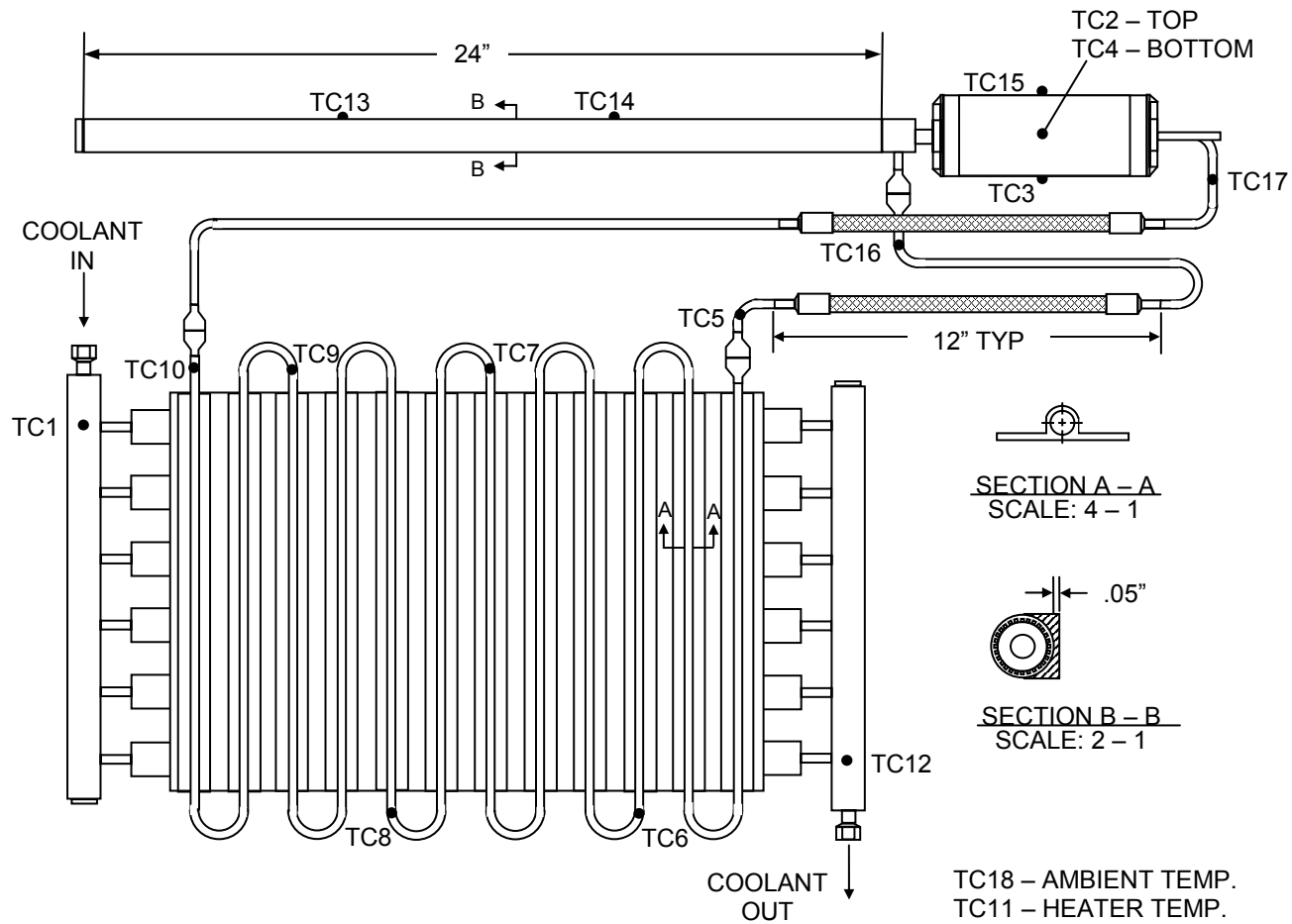
Fig. 3.1: A drawing of the test LHP with the locations of the monitoring thermocouples. (Modified from manufacturer's original drawing)

The condenser used in this LHP design is a direct condensation heat exchanger (DCHX). It is basically an aluminum plate with extruded tubes on both sides. As seen in Fig. 3.1, a single smooth-wall aluminum extruded tube was bent into twelve parallel paths attached to one side of the plate to provide a flow passage for the ammonia in the LHP. On the coolant side, the cooling water enters an inlet plenum from which the water is distributed to six evenly spaced cooling water extruded tubes. The active length of the condenser tube is defined as the length having direct contact with the condenser plate. From the flow directions of ammonia and cooling water, this condenser can be classified as a cross counter-flow heat exchanger.

Table 3.1: Specification of the test LHP.

Working fluid	Ammonia	
Designed maximum heat load	1000 W	
Designed range of operating temperature	10~50 ^{o}C	
Evaporator	Axially grooved aluminum extrusion	
Active length	24 in	0.61 m
Cylinder outer diameter	0.95 in	2.41E-2 m
No. of grooves	43	
Hydraulic diameter of each groove	0.04 in	0.10E-2 m
Primary wick	Sintered Powder Nickel	
Outer diameter	0.75 in	1.91E-2 m
Inner diameter	0.375 in	0.95E-2 m
Pore radius	1.6 μm	
Porosity	60 %	
Permeability	0.20E-13 m^2	
Reservoir	Stainless Steel	
Cylinder outer diameter	2.73 in	6.93E-2 m
Cylinder inner diameter	2.69 in	6.83E-2 m
Cylinder length	6.23 in	0.16 m
Vapor line	Stainless Steel	
Outer diameter	0.250 in	0.64E-2 m
Inner diameter	0.210 in	0.53E-2 m
Length (including 12-inch flex line)	29.2 in	0.74 m
Liquid line	Aluminum/Stainless Steel	
Outer diameter	0.250 in	0.64E-2 m
Inner diameter	0.210 in	0.53E-2 m
Length (including 12-inch flex line)	38.3 in	0.97 m
Condenser ammonia-side	Aluminum	
Outer diameter	0.250 in	0.64E-2 m
Inner diameter	0.180 in	0.46E-2 m
Active length	144 in	3.66 m
Total length	183 in	4.65 m
Condenser coolant-side	Water	
Plate length	18 in	0.46 m
Plate width	12 in	0.31 m
Plate thickness	0.25 in	0.64E-2 m
No. of parallel lines	6	
Bayonet	Aluminum	
Outer diameter	0.1875 in	0.48E-2 m
Inner diameter	0.1315 in	0.33E-2 m
Length	46.2 in	1.17 m

3.2   EXPERIMENTAL SETUP

A strip heater with maximum power output of 1000 W was attached to the saddle at the bottom of the evaporator to supply the required heat load. A Variac was used to control the power output to the strip heater and a watt meter was connected to measure the amount of heat load applied to the evaporator. The measured temperatures were displayed on the computer in real time and were also recorded every second for later analysis. A picture showing the interface of the data acquisition system is shown in Fig. 3.2.
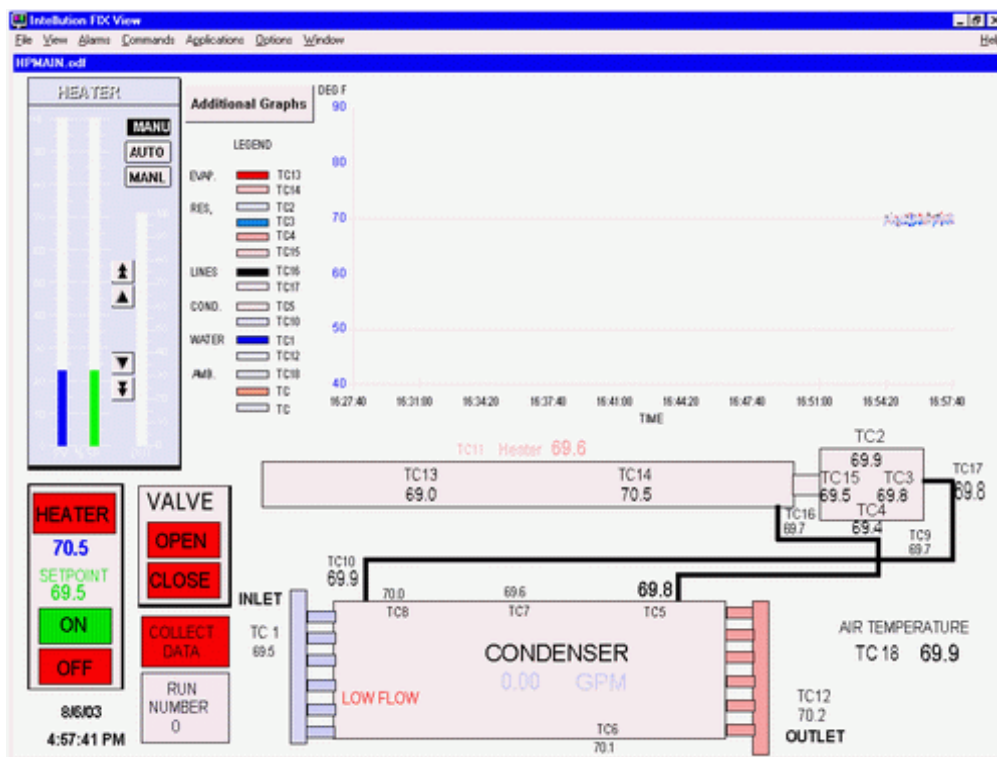
Fig. 3.2: The interface of the data acquisition system. (Designed by Bechtel Bettis, Inc.)

A recirculating chiller designed to provide a continuous supply of cooling water at a constant temperature and volume flow rate was used. The unit consists of an air-cooled refrigeration system, a sealable reservoir, recirculating pump, and a temperature controller. The temperature of the chiller ranged from 5 ^{o}C to 35 ^{o}C with temperature stability of ± 0.5 ^{o}C. The chiller reservoir can store up to 5.6 gallons of water. The maximum operating volume flow rate is 3 GPM. The design operating volume flow rate of the test LHP is 1 GPM.

For safety reasons, a control system was used to terminate heater power if evaporator temperature exceeded 65 ^{o}C, the condenser water supply dropped to less than 0.5 GPM, or the cooling water temperature rise across the condenser exceeded 5 ^{o}C. These controls ensured that the unit did not exceed design conditions.

A single set of steady-state experiments took more than 24 hours to complete and the results were very sensitive to the ambient temperature. Thus, an environmental chamber with an air conditioner and a control system was built to control the ambient temperature around the test LHP. A picture of the environmental chamber is shown in Fig. 3.3. The shell of the environmental chamber was made of ¾ inch thick plywood as an inner box of size $4 \times 3 \times 2$ feet^3 (length$\times$width$\times$height) covered by an outer box made of 1 inch thick styrofoam. The air-conditioning unit, with a temperature controller, was placed on top of the chamber. This environmental chamber does not have the ability to heat the air inside the chamber. Therefore, the chamber temperature must be set lower than the room temperature. The air conditioner has the capability to cool the chamber a maximum of 5 ^{o}C lower than the ambient room temperature with an accuracy of ± 0.5 ^{o}C. The experimental room temperature varied from 19 ^{o}C to 22 ^{o}C when the experiments

were performed. Thus, the environmental chamber was set to 18.5 $^{\circ}$C in most of the experiments.
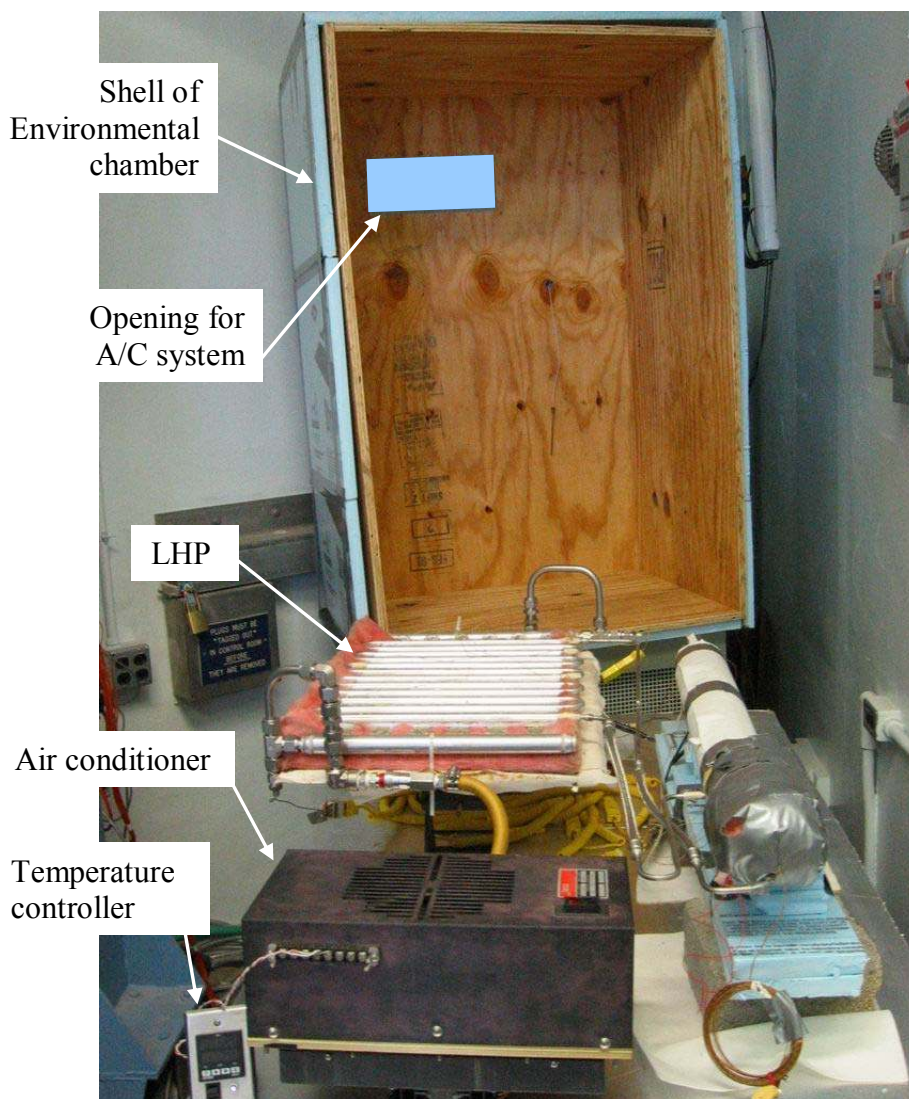
Fig. 3.3: A picture of the environmental chamber lifted open above the LHP.

The neutron beam facility at the Radiation Science and Engineering Center, the Pennsylvania State University, was utilized in this study. This facility is an ASTM E 544 Category 1 facility with a tangential collimator powered by the 1 MW TRIGA Breazeale Nuclear Reactor. A schematic diagram of the facility is shown in Fig. 3.4. The neutron

beam has an ASTM E 803 L/D ratio of 115, is 9.0 inches (0.23m) in diameter, and has a neutron-to-gamma ratio of 3.1×10^6 (n/cm^2)/mR. The neutron imaging laboratory is a $2.4\text{m} \times 3.8\text{m}$ well-shielded working area. A 9-inch Thompson tube is available for radioscopy, along with image processing and storage equipment.
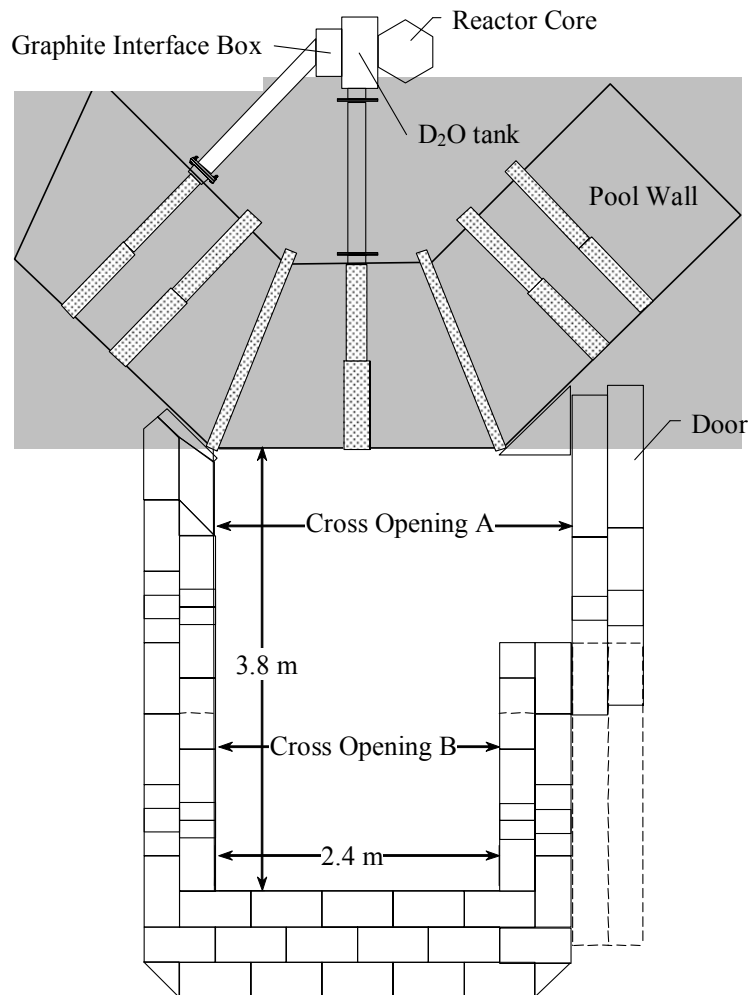
Fig. 3.4: Schematic diagram of the neutron beam lab at the Radiation Science and Engineering Center. (Top view)

A schematic diagram of the setup in the Neutron Beam Laboratory (experimental room) and control room is shown in Fig. 3.5. During neuron radiography tests, the test loop was placed in the radiation active experimental room, while the chiller, Variac, data

acquisition system, computer, monitor, and video recorder were placed in the control room. For safety, the experimental room has thick concrete walls to shield operational personnel and equipment from neutrons.
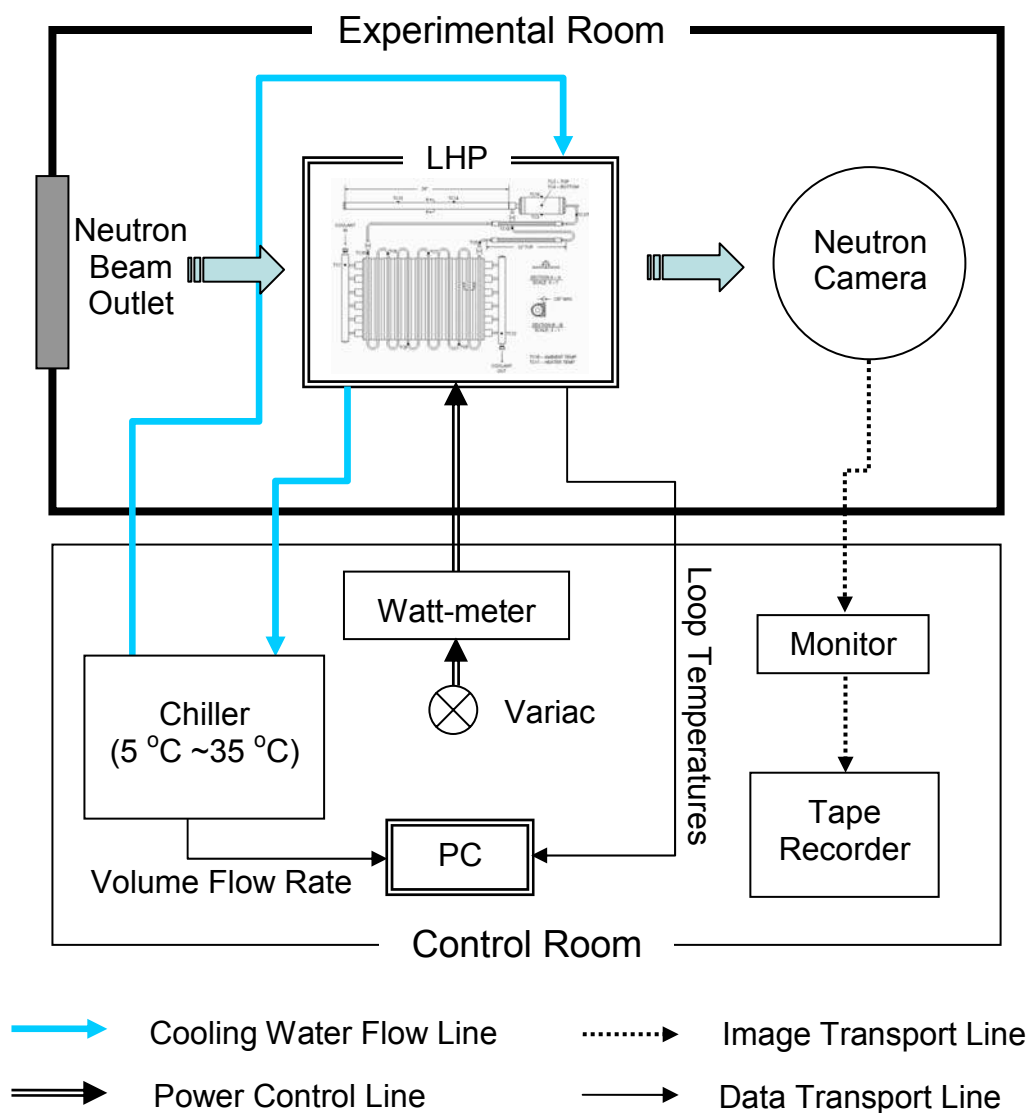
Fig. 3.5: A schematic diagram of the experimental setup in the control room and experimental room of the Neutron Beam Laboratory. (Not to scale)

A picture of the test LHP placed horizontally on a table is shown in Fig. 3.6. In this picture, the reservoir, evaporator, strip heater, and vapor line are insulated. The condenser is lower than the evaporator/reservoir assembly in Fig. 3.6; this configuration is referred to as adverse elevation.
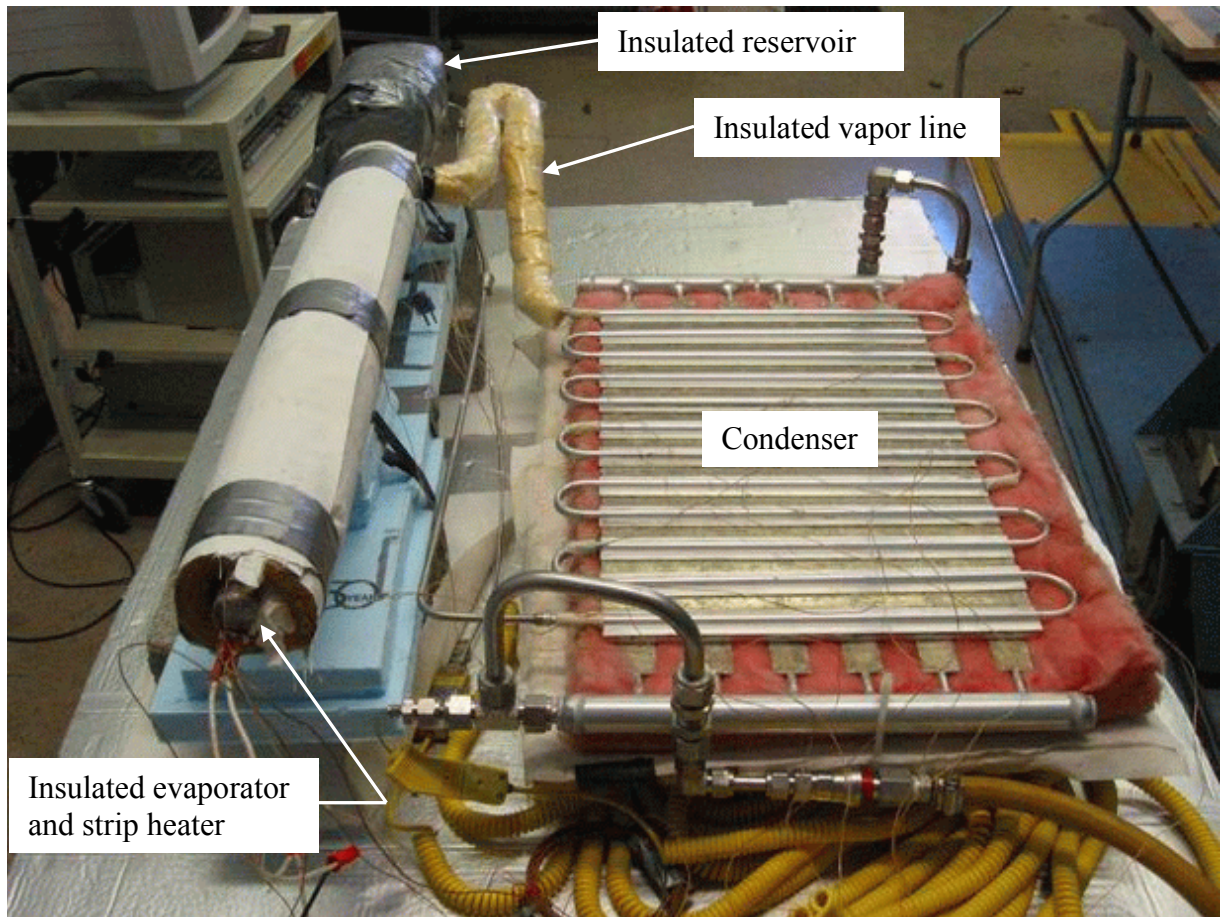
Fig. 3.6: A picture of the test LHP placed horizontally on a table.

A layer of fiberglass insulation was placed underneath the condenser to eliminate heat transfer from the ambient. A rectangular wood plate was utilized to support the condenser and the fiber glass. A jack mechanism was attached to the wood support plate

to provide a way to adjust the elevation of the condenser during the experiments.   A picture of the jack system is shown in Fig. 3.7.
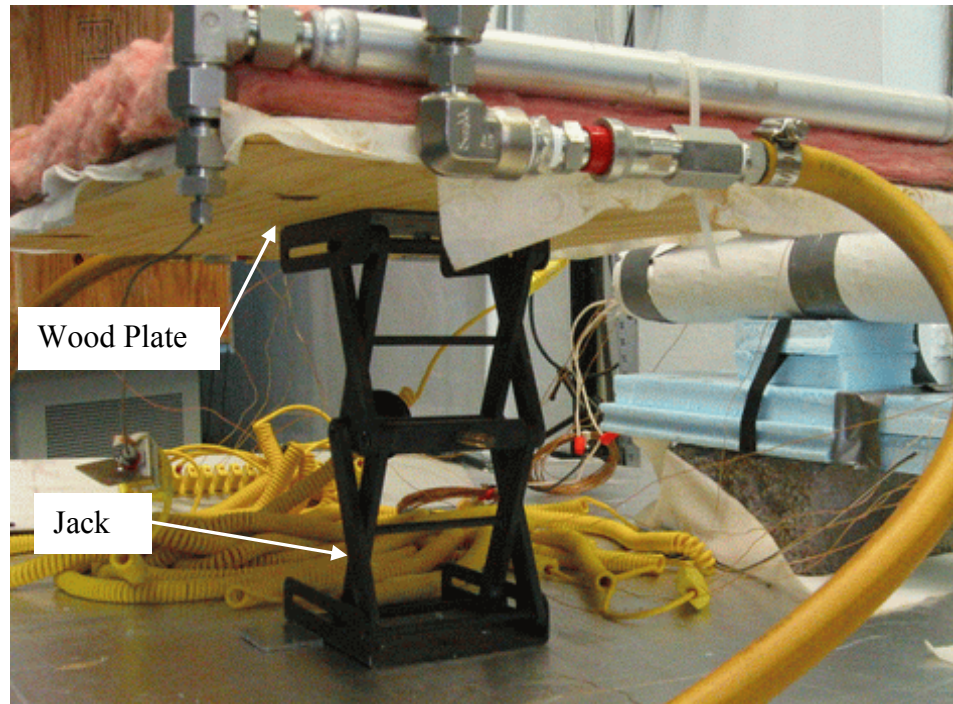
Fig. 3.7: A picture of the jack system underneath the condenser.

3.3   EXPERIMENTAL PROCEDURE

To obtain reliable experimental data, a standard procedure was implemented and always followed, as listed below.

1. Precondition the test LHP by letting it sit idle for at least two nights.

2. Adjust the elevation and insulation of the LHP.

3. Connect cooling water hoses and strip heater power cord.

4. Place the cover of the environmental chamber onto the test LHP.

5. Turn on the computer and start collecting experimental data.

6. Turn on the chiller and set a chiller temperature (T_{SINK}).

7. Adjust the cooling water volume flow rate to be 1.10 ± 0.01 GPM.

8. Turn on the air-conditioner of the environmental chamber and set an ambient temperature (T_{AMB}).

9. Wait until all the temperatures, including cooling water temperature, loop temperature, and ambient temperature, become steady. This usually takes about 30 minutes.

10. Adjust the Variac to a desired heat load and turn on the heater power.

11. Record the amount of heat load input into the evaporator from the watt-meter.

12. Wait until all the temperatures reach steady-state values (defined as no more than a 0.5 ^{o}C change over 25 minutes).

13. Adjust the Variac to another desired heat load and repeat steps 11 and 12 for all heat loads.

14. Turn off heater power, chiller, and air-conditioner of the environmental chamber.

15. Stop collecting data and export required data for post-processing.

16. Turn off the computer.

Chapter 4

STEADY-STATE OPERATING THEORY

When a LHP is operating at steady-state conditions, the temperature distribution along the loop does not change with time. In other words, the LHP has reached a thermal equilibrium condition within each component and with the surroundings. A steady-state condition should always be achieved if sufficient time is available with fixed heat load, ambient temperature, sink temperature, and physical setup of the LHP. This chapter contains a thorough discussion about the steady-state operating theory of the LHP when it is operated at different elevations in a gravitational field. Positive, zero, and adverse elevation refer to the condenser being located above, the same level as, and below the evaporator, respectively.

With more and more terrestrial applications, the performance of LHPs with the presence of gravitational force has become increasingly important. Most of the existing literature regarding studies of LHPs focuses on the behavior of a LHP operating at adverse elevation or at zero elevation. It is generally assumed that the behavior of a LHP operating at positive elevation is similar to that at adverse or zero elevation. After conducting a series of tests of an ammonia LHP operating at different elevations, it was verified that they do have similar behavior when the evaporator heat load is relatively high. However, the tests also reveal that a LHP operating at positive elevation and one operating at adverse elevation behave differently when the evaporator heat load is relatively low. In the following sections, the well formulated steady-state operating

theory at adverse and zero elevations is explained first. Then the newly formulated gravity-assisted steady-state operating theory, which applies to a LHP operated at positive elevation, is presented and discussed.

4.1 ZERO AND ADVERSE ELEVATION

When a LHP is operated at adverse elevation, the operating characteristics are very similar to those at zero elevation. The only difference is that the system needs more capillary pressure gain to balance the pressure loss due to liquid head imposed by the adverse elevation.

4.1.1 Thermodynamic Analysis using Pressure-Temperature Diagram

A thermodynamic analysis using a pressure-temperature diagram helps to explain and understand the steady-state operation of the LHP. The thermodynamic states corresponding to the different locations of the LHP when it is operated at adverse or zero elevation are shown in Fig. 4.1. The physical LHP location corresponding to each thermodynamic state is shown in Fig. 1.1. In this theoretical analysis, it is assumed that both transportation lines are perfectly insulated, so there is no heat exchange with the ambient. In real applications, the liquid line is usually not insulated; thus, the fluid in it can exchange heat with the ambient by convection. At a steady-state condition, the operating LHP must satisfy mass, momentum, and energy conservation laws. Because it is a closed loop, the mass flow rate must remain constant along the loop, the pressure

gain must equal the pressure loss, and the energy must be balanced within each component as well as in the whole system. Whenever steady-state is indicated, these conditions are presumed to be fully achieved.
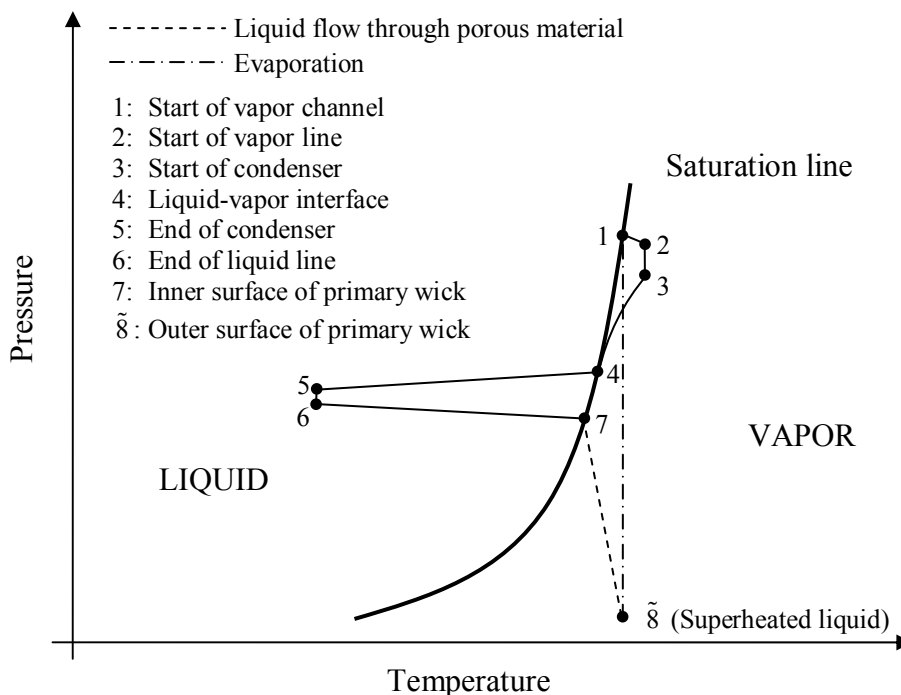
Fig. 4.1: Pressure vs. temperature diagram illustrating steady-state operating conditions when a LHP is operating at zero elevation or adverse elevation. (Not to scale)

When the LHP is operating, the flow in the LHP is driven by surface tension developed in the capillary of the primary wick. Menisci form at the outer surface of the primary wick as depicted in Fig. 4.2. In Fig. 4.2, thermodynamic states 1, vapor-phase, and $\tilde{8}$, superheated liquid-phase, are shown across the meniscus. Also, the local radius, R, corresponding to the pressure difference across the meniscus and the contact angle, θ, between the liquid (ammonia) and solid (nickel wick) are illustrated.
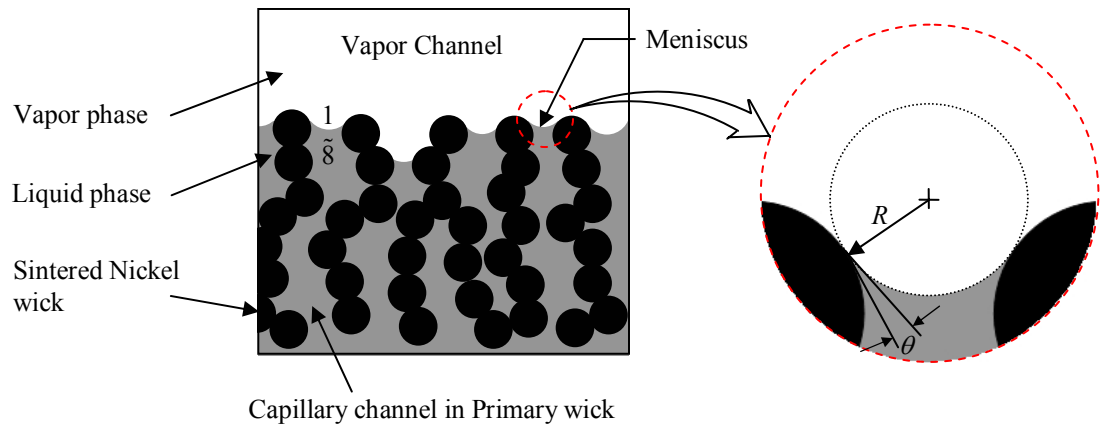
Fig. 4.2: Magnified view at the outer surface of the primary wick. (R: local radius of the meniscus in the primary wick and θ: contact angle)

At the vapor-side of the meniscus, point 1, the vapor is at saturated temperature corresponding to the highest pressure of the system. As the vapor travels down to the exit of the vapor channel, point 2, temperature is increased due to convection heat transfer from the walls, and pressure is decreased due to viscous losses. Therefore, the vapor at the exit of the vapor channel is at a superheated condition. As the vapor travels down the vapor line, the temperature remains the same while the pressure keeps on decreasing due to frictional loss. At the end of the vapor line, point 3, the vapor is even more superheated relative to the local saturation pressure. In the condenser, heat is rejected to the heat sink and the vapor is condensed back to liquid. Instead of giving up its superheat first and then condensing the saturated vapor, the sensible heat is rejected to the heat sink while the vapor is condensed back to liquid until the fluid reaches a saturated liquid condition, [Webb, 1998], point 4. This location is referred as the liquid-vapor interface in the condenser. Depending on how much heat is applied to the evaporator, the location of this liquid-vapor interface can vary from the beginning of the

condenser to almost at the end of the condenser. Downstream of the liquid-vapor interface, the liquid starts rejecting sensible heat to the heat sink and becomes more and more subcooled. At the end of the condenser, point 5, the liquid is subcooled. In the condenser, the pressure drops as the fluid travels down the tube. In single-phase flow, the pressure drops solely because of friction loss: in two-phase flow conditions, since the LHP is laid horizontally, the pressure drop comes from friction loss and acceleration loss. In the liquid line, temperature remains the same and pressure decreases gradually along the line (point 5 to point 6). If the LHP is operating at adverse elevation, the pressure drop due to liquid head loss may dominate the system pressure drop. At the end of the liquid line and the entrance of the bayonet, point 6, the liquid is still subcooled but at a lower pressure than at point 5. After the liquid line goes into the reservoir, it is referred to as the bayonet in the evaporator/reservoir assembly. In the bayonet, the liquid starts gaining heat from both the reservoir and the evaporator until it exits at the end of the bayonet and mixes with the liquid in the evaporator core. Because liquid has much higher density (and therefore much lower velocity) than vapor, the pressure drop in the liquid line and in the bayonet is very small compared to the pressure drop in the vapor line and in the condenser. Since the evaporator core is thermally and hydraulically connected to the reservoir, the temperature and pressure at the inner surface of the primary wick, point 7, should lie along the saturation line. This represents the most common operating condition, in which the evaporator core consists of both liquid and vapor. However, this may not be the case for all operating conditions, especially when the evaporator core is filled with all liquid.

Capillary action draws the liquid at the inner surface of the primary wick to the outer surface of the primary wick. As the liquid travels through the fine capillary, it is heated by the solid part of the wick and also loses pressure by going through the porous material. Thus, the liquid has the lowest pressure in the system at the liquid-side of the meniscus, point $\tilde{8}$, right before evaporation takes place. The liquid at point $\tilde{8}$ is superheated above its equilibrium saturation temperature and exists in a nonequilibrium condition referred to as a metastable state (see Appendix A for details) [Carey, 1992]. The liquid is then vaporized across the meniscus and gains pressure, required as the pumping force to drive the whole system (point $\tilde{8}$ to point 1 in Fig. 4.1). This completes the cycle of the fluid flow.

4.1.2 Trend of Steady-State Operating Temperature at Zero or Adverse Elevation

The typical trend of steady-state operating temperature (SSOT) as a function of heat load is U-shaped when the sink temperature is lower than ambient temperature as shown in Fig. 4.3. The SSOT first decreases as the heat load increases until it reaches a minimum where the heat load equals $\dot{Q}_M$ in Fig. 4.3. The SSOT then increases almost linearly as the heat load increases. The heat load $\dot{Q}_M$ corresponding to the lowest SSOT is determined by the ambient temperature, sink temperature, physical setup of the LHP, the operating conditions, and most importantly the design of the condenser. With the self-adjusting capability of the overall heat transfer coefficient, the LHP can operate at

two different modes: variable-conductance mode and fixed-conductance mode. The

differences between these two modes can be explained by the basic heat transfer equation:

$$\dot{Q}_{APP} = (UA)_{LHP}(T_{SSAT} - T_{SINK}) \qquad (4.1)$$

where $(UA)_{LHP}$ is the overall heat transfer coefficient of the LHP, T_{SSOT} is the steady-state
operating temperature, and T_{SINK} is the sink temperature.
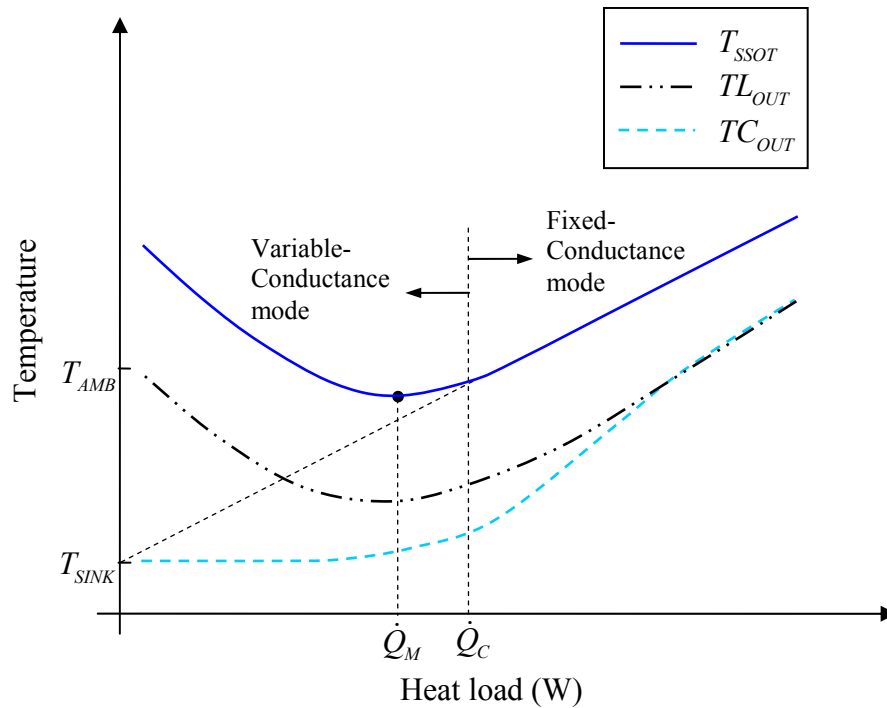
Fig. 4.3: Typical trend of steady-state operating temperature (SSOT) as a function of
heat load when the sink temperature is lower than ambient temperature and the LHP is
operated at zero elevation or adverse elevation. Also shown are the trends of
temperature exiting the liquid line and the condenser.

In the variable-conductance mode, the overall heat transfer coefficient of the LHP,

$(UA)_{LHP}$, has not reached its maximum value, which means that the condenser is not fully

utilized. Thus, part of the condenser is used to cool the liquid phase of the working fluid

rather than to condense vapor. In Fig. 4.3, the variable-conductance mode occurs when

the heat load is lower than $\dot{Q}_C$. When the heat load is equal to or greater than $\dot{Q}_C$, the LHP operates in the fixed-conductance mode and the condenser is fully utilized. The liquid-vapor interface is consistently located near the end of the condenser and the overall heat transfer coefficient of the LHP, $(UA)_{LHP}$, has reached its maximum value. Under this condition, since the overall heat transfer coefficient of the LHP and sink temperature are fixed, the steady-state operating temperature of the LHP increases linearly as the heat load increases.

To further explain this U-shaped relation, the parameters that determine the steady-state operating temperature of the LHP have to be studied. At a steady-state condition, the reservoir temperature is determined by energy interactions with the evaporator, liquid return line, and ambient air. The energy balance equation of the reservoir can be written as:

$$\dot{Q}_{HL} = \dot{Q}_{R-A} + \dot{Q}_{SC} \qquad (4.2)$$

where $\dot{Q}_{HL}$ is the heat leak from the evaporator to the reservoir, $\dot{Q}_{R-A}$ is the heat exchange between the reservoir and the ambient, and $\dot{Q}_{SC}$ is the amount of subcooling brought back by the liquid in the liquid line.

The energy that comes from the evaporator to the reservoir through the evaporator core is referred to as "heat leak". This heat leak may come from axial conduction through the evaporator body and secondary wick, convection of the liquid in the evaporator core, and heat carried by vapor evaporated at the inner surface of the primary wick and then transported back to the reservoir through the non-wick path. In general

operating conditions, the amount of heat leak is proportional to the heat load, and depends strongly on the flow conditions inside the evaporator core.

At a steady-state condition, the heat leak from the evaporator must be balanced with the heat loss to the ambient and the amount of subcooling that is brought back by the liquid in the liquid line. Since the heat exchange between the reservoir and the ambient is by natural convection, it is relatively small compared to the amount of subcooling brought back from the liquid line. The latter can be written as:

$$\dot{Q}_{SC} = \dot{m}C_P \left(T_{SSOT} - TL_{OUT}\right) \tag{4.3}$$

where TL_{OUT} is the temperature at the end of the liquid line. Theoretically, the mass flow rate of the system can be calculated by:

$$\dot{m} = \frac{\left(\dot{Q}_{APP} - \dot{Q}_{HL}\right)}{\lambda} \tag{4.4}$$

where $\dot{Q}_{APP}$ is the total heat load applied to the evaporator and λ is the latent heat of vaporization.

From Eqs. 4.2 through 4.4, it is obvious that the steady-state operating temperature depends strongly on the liquid temperature at the end of the liquid line. In the liquid line, the heat exchange between the liquid and the ambient can be written as:

$$\dot{Q}_{LL-A} = \dot{m}C_P \left(TC_{OUT} - TL_{OUT}\right) \tag{4.5}$$

where TC_{OUT} is the temperature at the exit of the condenser. The liquid temperature at the end of the liquid line depends on the liquid temperature exiting the condenser and the mass flow rate.

When the LHP is operating in the variable-conductance mode and the heat load is small – just enough to start the loop, the mass flow rate of the loop is small and the vapor is quickly condensed back to liquid in the condenser. Thus, the liquid temperature exiting the condenser is close to the sink temperature. In the liquid line, due to the low mass flow rate, heat is exchanged with the ambient by natural convection and the liquid temperature at the end of the liquid line is close to ambient temperature. As the heat load increases, the mass flow rate increases almost linearly. Since the liquid temperature exiting the condenser is still close to the sink temperature, the liquid temperature at the end of the liquid line, TL_{OUT}, decreases as the mass flow rate increases. This trend continues until the heat load is equal to $\dot{Q}_M$ and the liquid return temperature has reached its minimum. As the heat load is further increased, the liquid temperature exiting the condenser starts to rise above the sink temperature and the liquid-vapor interface in the condenser moves closer to the end of the condenser. The liquid temperature at the end of the liquid line increases as the liquid temperature exiting the condenser increases. This trend continues until the heat load reaches the transition point, $\dot{Q}_C$, where the operating condition of the LHP transfers from variable-conductance mode to fixed-conductance mode. In the fixed-conductance mode, the LHP behaves like a solid metal with fixed conductance. The liquid exiting the condenser is slightly subcooled in order to bring back the required amount of subcooling to balance the heat leak.

Because the amount of heat leak and mass flow rate both depend on the heat load, the temperature difference between the liquid temperature at the end of the liquid line and the SSOT in Eq. 4.3 remains nearly constant. Therefore, the SSOT follows the same

trend as the liquid temperature at the end of the liquid line, TL_{OUT}. Thus, the steady-state operating temperature first decreases and then increases as the heat load is increased. The above discussion explains the typical U-shaped trend of SSOT as a function of heat load.

4.1.3 Effects of Sink Temperature, Ambient Temperature, and Adverse Elevation on the Trend of SSOT

Based on the analyses of the previous section, the effect of sink temperature and ambient temperature on LHP steady-state operating temperature can be easily predicted [Kaya and Ku, 1999[1]]. Fig. 4.4 shows the trends of steady-state operating temperature at three different sink temperatures. If sink temperature is higher than ambient temperature, like $T_{SINK,1}$ in Fig. 4.4, the steady-state operating temperature increases almost linearly with the increase of applied heat load. In other words, the LHP always operates at fixed-conductance mode like a solid metal. If sink temperature is lower than ambient temperature, like $T_{SINK,2}$ or $T_{SINK,3}$ in Fig. 4.4, the typical U-shaped trend line of steady-state operating temperature is followed. The slopes of all three cases are the same when the heat load is high and the LHP is operated at fixed-conductance mode, because the overall heat transfer coefficient, $(UA)_{LHP}$ in Eq. 4.1, is constant for a specific LHP.
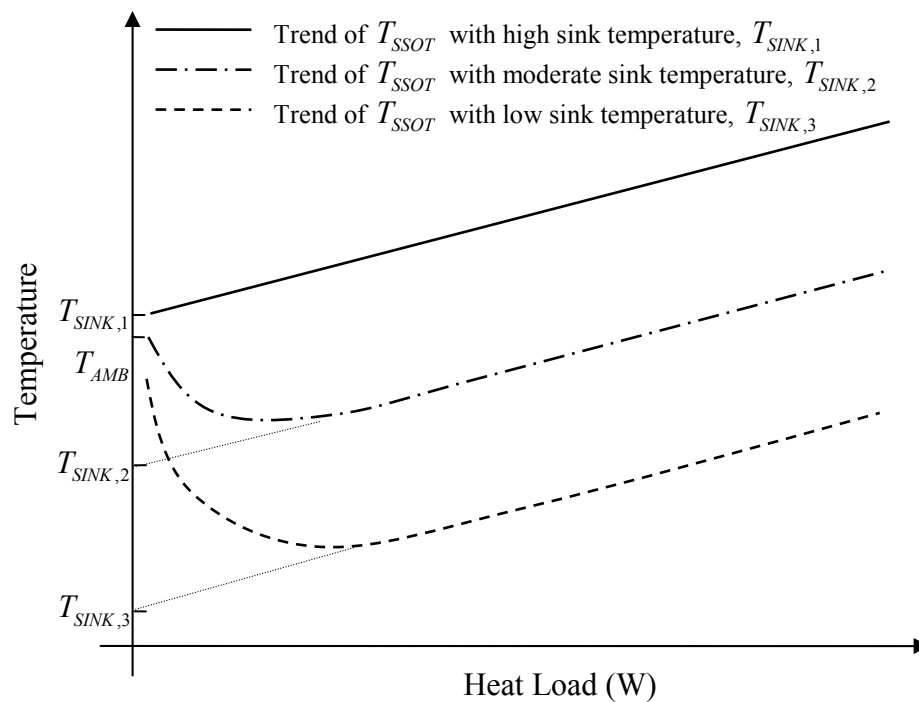
Fig. 4.4: Effect of sink temperature on steady-state operating temperature. (Ambient temperature is held constant at T_{AMB}.)

Fig. 4.5 shows the trends of steady-state operating temperature at three different ambient temperatures. When the ambient temperature is equal or less than the sink temperature, like $T_{AMB,3}$ in Fig. 4.5, the trend of the steady-state operating temperature is a straight line. Again, when the ambient temperature is higher than sink temperature, like $T_{AMB,1}$ or $T_{AMB,2}$ in Fig. 4.5, the steady-state operating temperature follows the U-shaped trend. The effect of the ambient temperature dominates the low heat load region, because the lower the mass flow rate in the system, the more the fluid temperature changes in the liquid line.
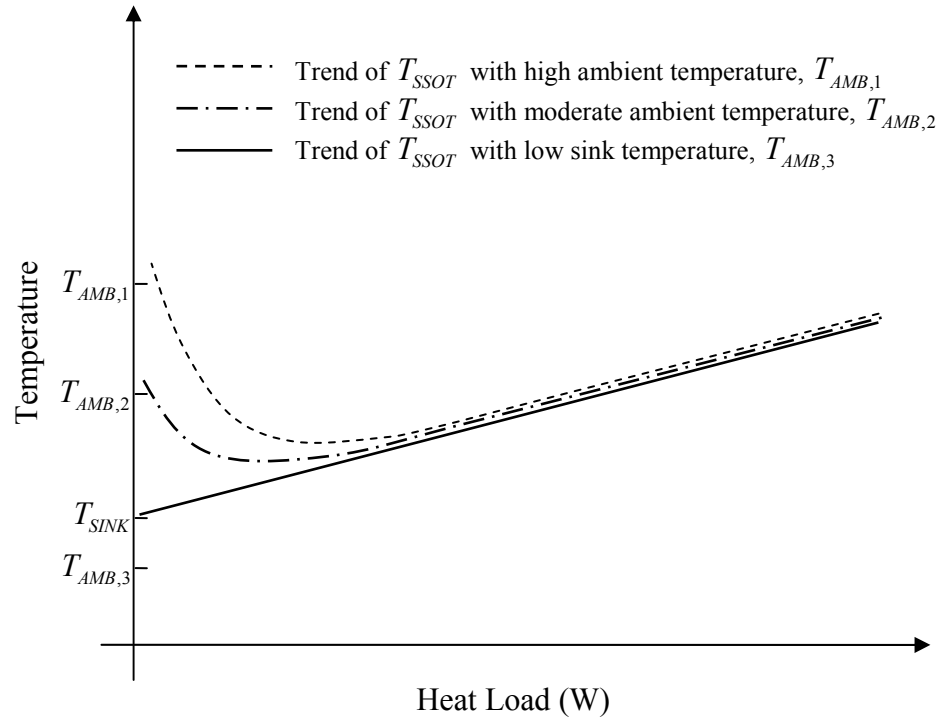
Fig. 4.5: Effect of ambient temperature on steady-state operating temperature. (Sink temperature is held constant at T_{SINK}.)

To explain the effect of adverse elevation on steady-state operating temperature, heat leak from the evaporator to the reservoir must be discussed in detail. This heat leak can be written as:

$$\dot{Q}_{HL} = (UA)_{HL} \left(T_{EVAP} - T_{SSOT} \right) \tag{4.6}$$

where $(UA)_{HL}$ is the overall heat transfer coefficient from the evaporator to the reservoir and T_{EVAP} is the evaporator temperature. The overall heat transfer coefficient from the evaporator to the reservoir, $(UA)_{HL}$, is composed of various heat flow paths. This coefficient is one of the most important parameters in determining the performance of a LHP. Heat may be conducted axially through the metal from the evaporator to the

reservoir or radially from the outer surface to the inner surface of the primary wick and into the reservoir. It is assumed that both the inner and outer surface of the primary wick are at saturated conditions, and the temperature difference can be obtained from the Clausius-Clapeyron equation [Moran and Shapiro, 1993]:

$$\left(\frac{dP}{dT}\right)_{SAT} = \frac{\lambda}{T\left(v_g - v_L\right)} \tag{4.7}$$

where v_L and v_g are the liquid and vapor specific volumes, respectively.

The saturated pressure difference between the evaporator and the reservoir comes from the fluid frictional pressure drop and liquid head. At a fixed heat load, the fluid frictional pressure drop of the system caused by fluid flow remains the same and the pressure drop due to liquid head increases as the adverse elevation increases. Therefore, the pressure difference between the evaporator and the reservoir increases as the adverse elevation increases. This in turn increases the heat leak due to a greater temperature difference in Eq. 4.6. From the energy balance of the reservoir shown in Eq. 4.2, it becomes clear that more adverse elevation leads to higher steady-state operating temperature. The theoretical analysis of the effect of adverse elevation on steady-state operating temperature is shown in Fig. 4.6. This effect has greater impact on steady-state operating temperature at low heat load than at high heat load because the pressure drop due to liquid head dominates the pressure drop of the system when the heat load is low. When the heat load is high, most of the pressure drop of the system comes from the fluid frictional pressure drop. Therefore, the effect of adverse elevation on steady-state operating temperature becomes almost negligible at high heat loads.
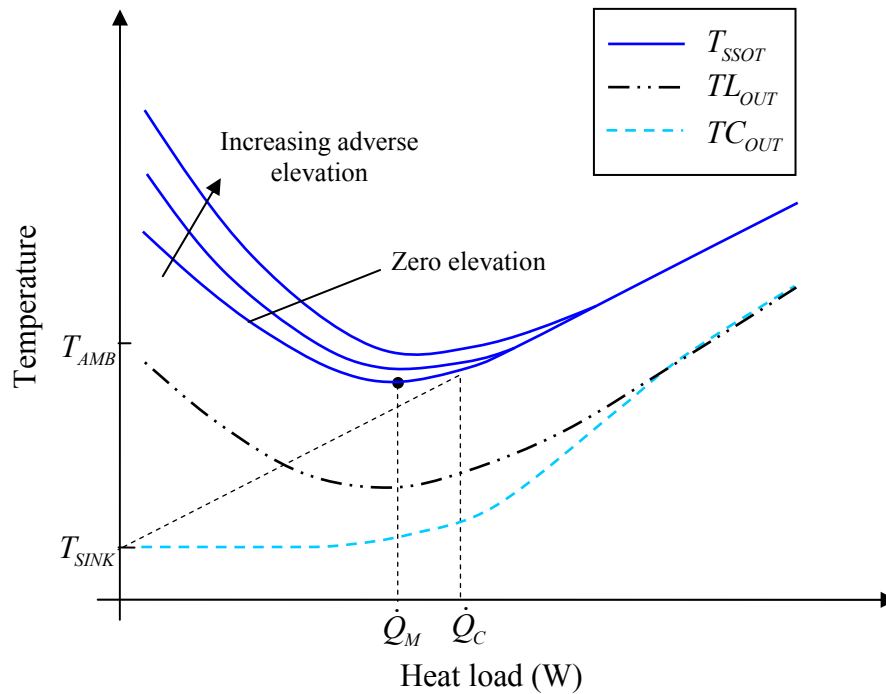
Fig. 4.6: Effect of adverse elevation on steady-state operating temperature (SSOT) when the sink temperature is lower than ambient temperature. Also shown are the trends of temperature at the end of the liquid line and the condenser.

4.2 POSITIVE ELEVATION (GRAVITY-ASSISTED OPERATING THEORY)

A LHP operates at positive elevation when the condenser is located above the evaporator/reservoir assembly. It is generally assumed that the operating characteristics at positive elevation are similar to those at zero and adverse elevation. This might be the case if the LHP is equipped with a large diameter vapor line. However, in most LHP applications, the transportation lines are small tubes. Because of the surface tension and contact angles of the working fluid, a liquid slug can be supported in a smooth vertical tube effortlessly. Fig. 4.7 shows a liquid slug in a vertical tube in gravitational field.
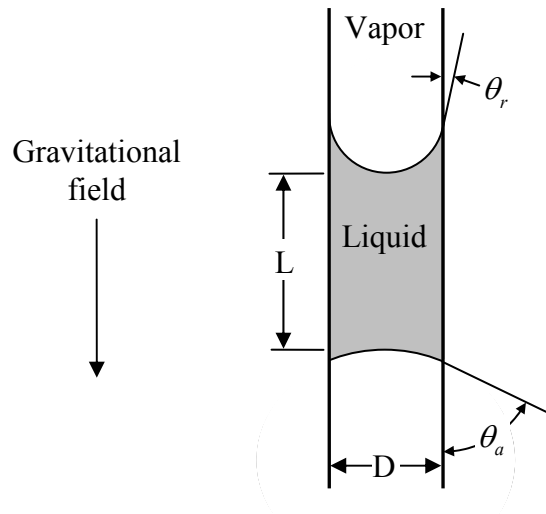
Fig. 4.7: A liquid slug in a small vertical tube to resist downward motion. (θ_a: advancing contact angle and θ_r: receding contact angle)

By assuming the pressure at the top of the liquid slug is the same as that at the bottom, the length of a liquid slug that can be supported in a vertical tube can be obtained from balancing the force in the vertical direction and can be written as:

$$\rho_L gL = \frac{4\sigma}{D}\left[\cos(\theta_r) - \cos(\theta_a)\right] \tag{4.8}$$

where θ_r is the advancing contact angle, θ_a is the receding contact angle, σ is the surface tension, and D is the diameter of the tube. If a liquid slug can be supported in a vertical tube, it can also travel with the vapor in the vapor line. From the observations of the test loop using neutron radioscopy, liquid slugs can be observed in the vapor line when the LHP is operated at positive elevation with small heat load (see Fig. 7.5). This phenomenon makes the operating characteristics at positive elevation different from that

at zero and adverse elevation. Therefore, a new operating theory has to be formulated to explain the operating characteristics when a LHP is operated at positive elevation.

The operating theory developed at positive elevation is also referred to as gravity-assisted operating theory. This is a brand new theory formulated from the experimental study and flow visualization of the test LHP. When a LHP is operated at positive elevation, vapor travels in the vapor line against gravity, while liquid traveling in the liquid line is assisted by gravity. Because of the density difference between the liquid-phase and the vapor-phase of the working fluid, the net pressure gain from the liquid head can be written as: (provided that the vapor line is 100% vapor and liquid line is 100% liquid)

$$\Delta P_{GRAV.} = \left(\rho_L - \rho_g\right)gh \qquad (4.9)$$

where ρ_L and ρ_g are the liquid and vapor density, respectively, and h is the elevation difference between the condenser and the evaporator.

4.2.1 Thermodynamic Analysis using Pressure-Temperature Diagram at Positive Elevation

A pressure-temperature diagram illustrating the general operating conditions at positive elevation is shown in Fig. 4.8. The physical LHP location corresponding to each thermodynamic state is shown in Fig. 1.1. Most of the operating characteristics are similar to those explained previously at adverse and zero elevations. The only difference is that when the LHP is operating at positive elevation, there is a significant pressure gain from the liquid head in the liquid line. Therefore, the pressure at the end of the liquid line,

point 6, is higher than the pressure at the beginning of the liquid line, point 5. The amount of pressure gained depends on the elevation difference, h, between the condenser and the evaporator, and can be calculated by Eq. 4.9. This important feature makes the operating theory unique and more difficult to predict when the LHP is operating at positive elevation. The amount of pressure gained from gravitational head also determines if the LHP is operating in the gravity-controlled mode or capillary-controlled mode. The differences between the two modes are discussed in detail later in this chapter.
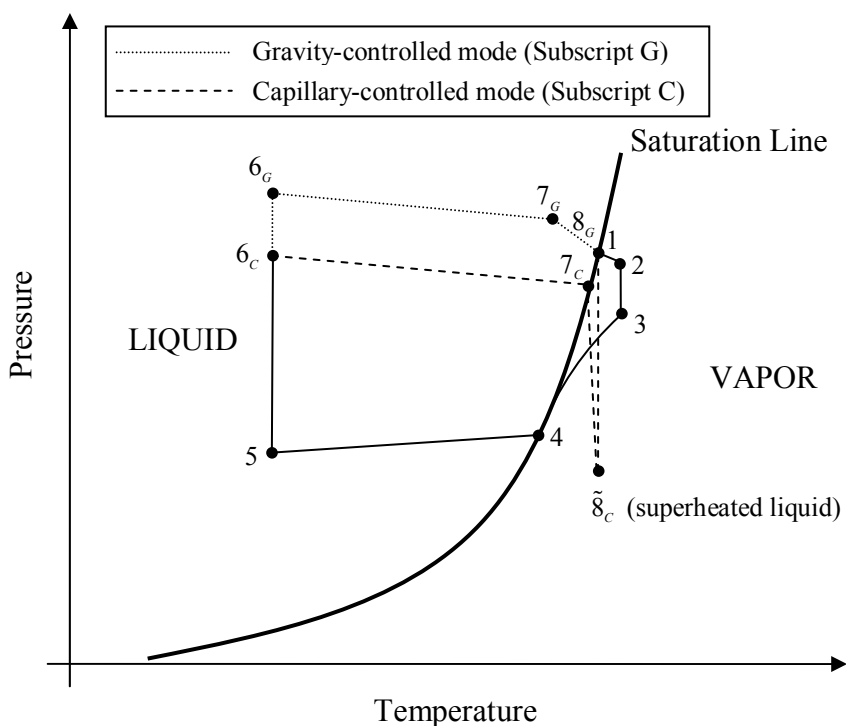
Fig. 4.8: Pressure vs. temperature diagram illustrating steady-state operating conditions when a LHP is operating at positive elevation. (Not to scale)

4.2.2 Analysis of the Pressure Balance Equation at Positive Elevation

Before discussing the trend of steady-state operating temperature in detail, it is necessary to look at the pressure balance equation of the LHP system. The total pressure drop of the system is the sum of the pressure loss in each component and can be written as:

$$\Delta P_{TOTAL} = \Delta P_{V.C.} + \Delta P_{V.L.} + \Delta P_C + \Delta P_{L.L.} + \Delta P_{BAY.} + \Delta P_{WICK} + \Delta P_{GRAV.} \qquad (4.10)$$

When at steady-state operation, the pressure gain from surface tension across the evaporating menisci equals the total system pressure drop as listed in Eq. 4.10, if the total system pressure drop is within the capillary limit of the primary wick. The capillary limit depends on the wick design and size and can be expressed by the Young-Laplace equation as:

$$\Delta P_{CAP,MAX} = \frac{2\sigma \cos\theta}{r_{EFF.}} \qquad (4.11)$$

where σ is the surface tension, θ is the contact angle between the liquid and solid, and r_{EFF} is the effective pore radius of the primary wick.

In order to achieve a steady-state condition, the pressure gain of the system must balance the pressure loss. When the LHP is operating at positive elevation, the system actually gains pressure from the liquid head. It is then appropriate to write the pressure balance equation of the system as:

$$\Delta P_{CAP} + \Delta P_{GRAV} = \Delta P_{V.C.} + \Delta P_{V.L.} + \Delta P_C + \Delta P_{L.L.} + \Delta P_{BAY} + \Delta P_{WICK} \qquad (4.12)$$

Depending upon the source of the pressure driving the system, the LHP can operate in two different modes: capillary-controlled mode and gravity-controlled mode.

When the LHP is operating in the capillary-controlled mode, the total pressure drop of the system is higher than the net pressure gain from the liquid head. Therefore, the system adjusts the local radius in the primary wick, as depicted in Fig. 4.2, to supply the pressure required to balance the total pressure drop of the system. In the capillary-controlled mode, the pressure gain from the liquid head remains at its maximum value and can be calculated from Eq. 4.9.

The LHP operates in the gravity-controlled mode when the total system pressure drop is less than the maximum pressure gain from the liquid head. In other words, the pressure gain from the liquid head itself is enough to drive the flow in the system. When the LHP is operating in the gravity-controlled mode, the capillaries in the primary wick are all filled with liquid and there is no meniscus in the primary wick (ΔP_{CAP} in Eq. 4.12 is zero).

The total pressure drop of the system can be divided into three different sources: single-phase (including vapor and liquid), two-phase, and liquid flow in capillary media. For fully developed single-phase pipe flow, the frictional pressure drop can be calculated from the Darcy-Weisbach equation:

$$\Delta P_{1\phi} = f \frac{L}{D} \frac{\rho V^2}{2} \tag{4.13}$$

The dimensionless parameter f is called the Darcy friction factor and is a function of Reynolds number and tube roughness. Two-phase pressure drop is composed of three components: frictional, accelerational, and gravitational. The accelerational two-phase

pressure drop is correlated by single-phase pressure drop and two-phase multiplier. Each component depends strongly on the quality and void fraction of the fluid and is rather difficult to calculate accurately. Generally speaking, the two-phase pressure drop increases along with the increase of the mass flow rate in the system. This chapter focuses on qualitative understanding of the operating characteristics. Chapter 5 has a more detailed discussion about the two-phase pressure drop calculation. In the analysis of the liquid flow in the wick structure, the flow is assumed to be steady, two-dimensional, incompressible, laminar flow with negligible body forces, with flow in the radial direction. Under these conditions, the pressure drop of the liquid flow across the wick can be calculated by Darcy's law for liquid flow in a porous medium:

$$\Delta P_{WICK} = \int \left(-\frac{\mu \dot{m}}{\rho A_W \kappa} \right) dr \tag{4.14}$$

where A_W is the wick cross-sectional area, κ is the permeability of the wick structure and r is the radial direction. Because the LHP is equipped with a very fine pore size metal wick, the pressure loss of the liquid traveling across the wick usually dominates the total pressure loss in the system. In summary, these three types of pressure drop are all directly related to the mass flow rate of the system.

4.2.3   Trend of Steady-State Operating Temperature at Positive Elevation

The trend of SSOT as a function of heat load when the LHP is operated at positive elevation is depicted in Fig. 4.9. It is similar to that at zero elevation or adverse elevation when the heat load is higher than $\dot{Q}_2$ (see Fig. 4.9). More specifically, the trend follows

the U-shaped trend as explained previously because the LHP is operating in the capillary-controlled mode. In contrast, the LHP operates in the gravity-controlled mode when the heat load is less than or equal to $\dot{Q}_2$. Since there is no pressure gain from surface tension across the menisci when the LHP is operating in the gravity-controlled mode, the local radius of the meniscus in the primary wick, as depicted in Fig. 4.2, approaches infinity. In other words, the liquid-vapor interface becomes a flat surface in the vapor channel. The transition heat load, $\dot{Q}_2$, depends on how high the condenser is above the evaporator, provided all other conditions remain the same. When the heat load is lower than $\dot{Q}_2$, i.e. the LHP is operating in the gravity-controlled mode, the pressure balance of the system is governed by:

$$\Delta P_{GRAV.} = \Delta P_{V.C.} + \Delta P_{V.L.} + \Delta P_C + \Delta P_{L.L.} + \Delta P_{BAY.} + \Delta P_{WICK} \tag{4.15}$$

This transition heat load also separates the fluid flow condition in the vapor channel from pure vapor (higher than $\dot{Q}_2$) to two-phase mixture (lower than $\dot{Q}_2$). With the appearance of liquid in the vapor channel, the operating characteristics become more complicated and the actual mass flow rate of the system becomes:

$$\dot{m}_{TOTAL} = \dot{m}_L + \dot{m}_g = \dot{m}_L + \frac{\left(\dot{Q}_{APP} - \dot{Q}_{HL}\right)}{\lambda} \tag{4.16}$$

where $\dot{m}_L$ is the mass flow rate of the liquid pushed into the vapor channel and $\dot{m}_g$ is the mass flow rate of the vapor evaporated in the vapor channel. When the LHP is operating in the gravity-controlled mode, the total mass flow rate of the system is self-adjusting to match the pressure balance equation, Eq. 4.15.
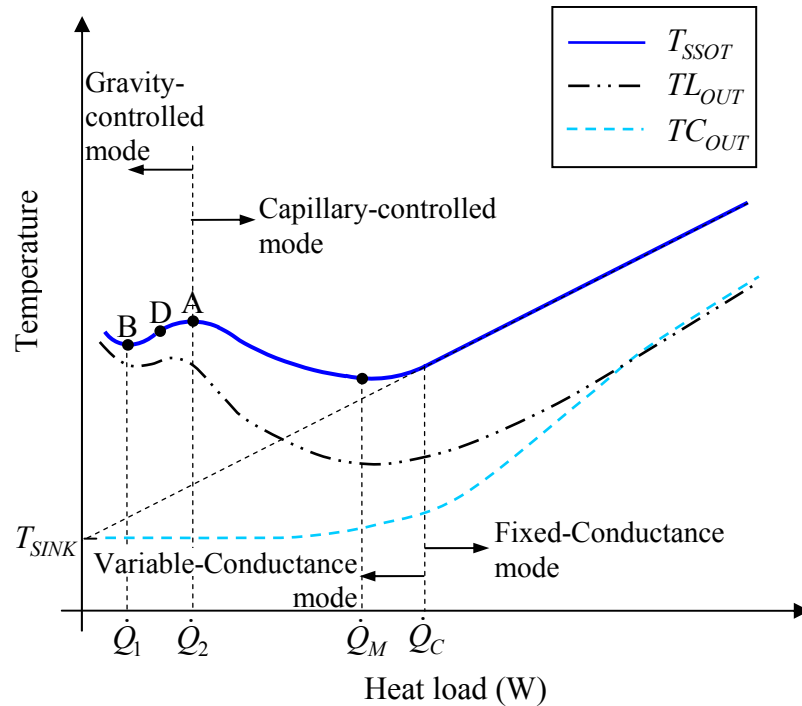
Fig. 4.9: The trend of steady-state operating temperature as a function of heat load when the sink temperature is lower than ambient temperature and the LHP is operated at positive elevation. Also shown are the trends of temperature at the end of the liquid line and the condenser.

To help explain the operating phenomena and the trend of SSOT in Fig. 4.9 when the heat load is less than $\dot{Q}_2$, the chart shown in Fig. 4.10 was generated. This chart features the vapor quality in the vapor line as a function of pressure gain from positive elevation or pressure drop of the system. It is a chart used to qualitatively explain how the LHP works when it is operating in the gravity-controlled mode. To be able to read the chart, it is essential to understand how the lines in the chart were formulated.

Gravitational Pressure Head Line:

When two-phase flow exists in the vapor line, instead of applying Eq. 4.9, the gravitational head of the system should be calculated by:

$$\Delta P_{GRAV.} = \left(\rho_L - \bar{\rho}\right)gh \tag{4.17}$$

where $\bar{\rho}$ is the average density of the fluid flow in the vapor line, which depends on the vapor quality, x, of the flow. If the two-phase flow in the vapor is assumed to be homogeneous flow, the average density can be calculated as:

$$\bar{\rho} = \frac{1}{\dfrac{(1-x)}{\rho_L} + \dfrac{x}{\rho_g}} \tag{4.18}$$

Therefore, the gravitational head becomes a function of vapor quality in the vapor line as:

$$\Delta P_{GRAV.} = \left(\frac{\rho_L - \rho_g}{(1-x)\rho_g + x\rho_L}\right)x\rho_L gh \tag{4.19}$$

Constant Heat Load Lines:

In Fig. 4.10, the constant heat load lines are obtained by assuming that the total frictional pressure drop of the system is proportional to the total mass flow rate. The vapor mass flow rate at a fixed heat load is a constant and is equal to the heat load divided by the heat of vaporization. Therefore, the total mass flow rate can be expressed as a function of vapor quality:

$$\dot{m}_{TOTAL} = \frac{\dot{m}_g}{x} = \frac{\left(\dot{Q}_{APP} - \dot{Q}_{HL}\right)}{x \cdot \lambda} \tag{4.20}$$

For each constant heat load line, the minimum total mass flow rate occurs when the vapor quality in the vapor line is equal to 1. When the vapor quality in the vapor line approaches 0, all liquid in the vapor line, the mass flow rate in the system approaches infinity. Therefore, as the vapor quality in the vapor line decreases from 1.0 to 0.0, the

total frictional system pressure drop increases from a minimum to infinity as depicted in Fig. 4.10.
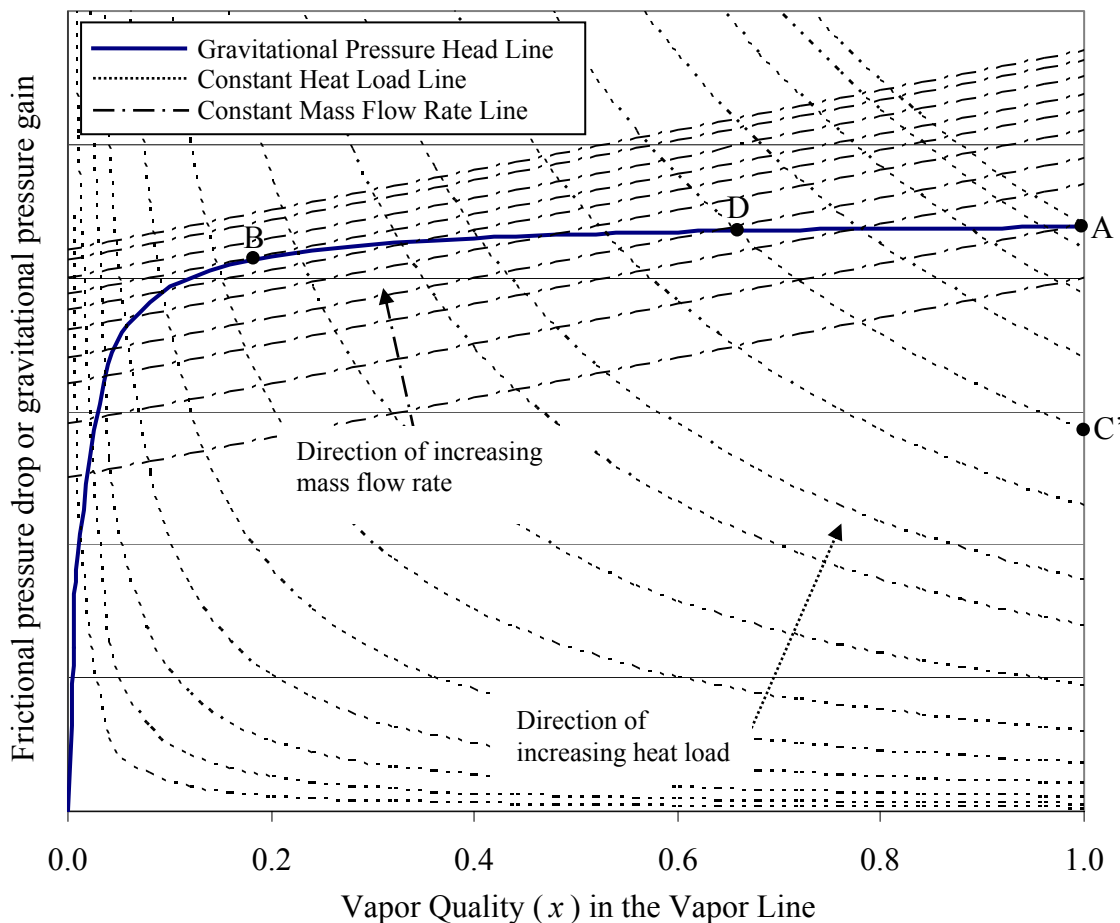
Fig. 4.10: A pressure-vapor quality chart illustrating operating conditions when the LHP is operating in the gravity-controlled mode. (For qualitative study only)

Constant Mass Flow Rate Lines:

The constant mass flow rate lines are used to show that for the same total mass flow rate, a lower heat load corresponds to a lower total pressure drop of the system. This is because to maintain a constant mass flow rate, the operating condition with lower heat load has to push more liquid into the vapor line, therefore yielding a lower vapor

quality. The total frictional pressure drop consists of vapor-phase, two-phase, and liquid-phase pressure drops, and the pressure drop due to liquid flow in capillary media. Because the LHP is operating in the gravity-controlled mode, there is no vapor-phase pressure drop in the system. The liquid-phase pressure drop is usually negligible. The two-phase pressure drop of the system is proportional to the length of the two-phase flow, which in turn is proportional to the heat load, provided that the LHP operates in the variable-conductance mode. The pressure drop of liquid flow in capillary media is proportional to the total mass flow rate. Therefore, with the same mass flow rate in the system (i.e. the same pressure drop due to liquid flow in the capillary media), the lower the heat load, the smaller the two-phase pressure drop, and thus, the smaller the total frictional pressure drop of the system.

To satisfy the kinetic energy conservation law at a steady-state condition, the pressure gain from gravitational pressure head must equal the total frictional pressure drop of the system. In Fig. 4.10, each constant heat load line has only one intersection with the gravitational pressure head line. This intersection represents a steady-state condition corresponding to this specific heat load. For a heat load lower than point A, when the vapor quality is equal to 1.0, the system yields minimum frictional pressure drop and maximum gravitational head. The system is operating at a transient condition because the pressure gain is higher than the pressure loss. To increase the total frictional pressure drop in the system, higher mass flow rate is required. To increase total mass flow rate at a fixed heat load, the system has to introduce more liquid into the vapor line. On the other hand, this also decreases the gravitational pressure head. In order to achieve

a steady-state condition, the mass flow rate adjusts itself to meet the pressure balance in the system.

Example Cases:

   Several states on Fig. 4.10 are marked to help explain how the LHP operates in the gravity-controlled mode. At nonequilibrium point C', the total pressure drop of the system is much less than the pressure gained from the gravitational head. The system increases the mass flow rate by pushing liquid into the vapor channel and then into the vapor line. By increasing mass flow rate, vapor quality decreases, total frictional pressure drop increases, and pressure gain from the liquid head decreases. This trend continues until point D, where the pressure drop and pressure gain of the system are balanced and a steady-state operating condition is achieved. Comparing steady-state condition D with other steady-state conditions A and B, the mass flow rate of the system at point D is higher than that at point A and lower than that at point B.

   The gravitational pressure head line in Fig. 4.10 corresponds to different steady-state operating conditions with specific heat loads. Point A corresponds to the steady-state condition when the heat load is equal to $\dot{Q}_2$, shown in Fig. 4.9, where the frictional pressure drop of the system is equal to the maximum gravitational gain. When the heat load is decreased from $\dot{Q}_2$, the steady-state condition follows the gravitational head line towards lower vapor quality. While the heat load is gradually decreased from $\dot{Q}_2$, the total mass flow rate corresponding to different steady-state conditions continues increasing until point B, beyond which the total mass flow rate decreases. At steady-state conditions, the maximum total mass flow rate of the system occurs at point B, where the

constant mass flow rate line has only one intersection with the gravitational pressure head line. This also explains the trend of SSOT at positive elevation when the heat load is lower than $\dot{Q}_2$. From Eq. 4.5, for the same ambient temperature and temperature at the exit of the condenser, the higher the mass flow rate, the lower the temperature at the end of the liquid line, provided that the temperature at the exit of the condenser is lower than the ambient temperature. Furthermore, less heat load leads to less heat leak in the system. In summary, with the decrease of heat load below $\dot{Q}_2$, heat leak decreases, the mass flow rate first increases then decreases, and the liquid temperature at the end of the liquid line first decreases, then increases. From the energy balance equation of the reservoir, Eq. 4.2, and the equation of subcooling, Eq. 4.3, it is clear that the steady-state operating temperature first decreases then increases when the heat load decreases below $\dot{Q}_2$. This fully explains the trend of SSOT as a function of heat load when the LHP is operating at positive elevation.

4.2.4 Effects of Positive Elevation on the Trend of SSOT

Based on the above analysis, Fig. 4.11 shows the theoretical effect of positive elevation on the steady-state operating temperature. The trends of the steady-state operating temperature are plotted qualitatively. Just as with adverse elevation, positive elevation plays an important role when the heat load is low. The trend of the steady-state operating temperature at zero elevation is also plotted to compare with those at positive elevations. The heat load corresponding to the transitional point between the capillary-

controlled mode and the gravity-controlled mode increases as the positive elevation increases. When the heat load is higher than the transitional point, i.e. the LHP is operating in the capillary-controlled mode, the trend is almost identical to that at zero elevation. When the LHP operates in the gravity-controlled mode, the steady-state operating temperature follows the characteristics illustrated in Fig. 4.10. Experimental data and flow visualization observations supporting the gravity-assisted operating theory are presented in Chapter 7.
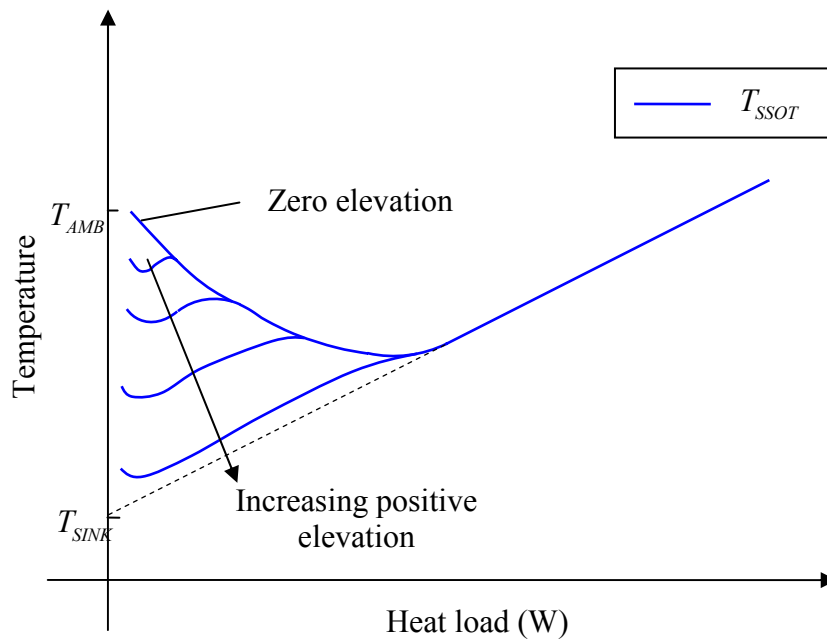
Fig. 4.11: Effect of positive elevation on steady-state operating temperature (SSOT) when the sink temperature is lower than ambient temperature.

Chapter 5

1-D STEADY-STATE ANALYTICAL MODEL

At the beginning of this study (September, 2000), a 1-D steady-state code (hereafter called the TTH code) was obtained from TTH Research, Inc. It was written based on the mathematical modeling of LHPs formulated by Hoang and Kaya [1999]. The TTH code can predict the steady-state performance of a LHP when it is operated at zero or adverse elevations, but not at positive elevation. The overall logic of the TTH code is duplicated in the steady-state analytical model presented in this section, and was used as the foundation of the new code. The new code is based on the steady-state operating theory presented in Chapter 4, and was written by the author. Comparing the new steady-state code with the TTH code, major modifications, improvements, and newly added features are listed below:

1. Selections to study the performance of a LHP with or without insulation of the reservoir or the vapor line are included in the present code.

2. All of the working fluid properties utilized in the present code are functions of fluid temperature and are curve fitted from National Institute of Standards and Technology (NIST) data. (See Section 5.5.1 and Appendix B for details.)

3. Four two-phase heat transfer correlations are included in the present code to provide comparisons of two-phase heat transfer calculations. (See Section 5.5.3 for details.)

4. Five two-phase pressure drop correlations are included in the present code to provide comparisons of two-phase pressure drop calculations. (See Section 5.5.4 for details.)

5. A new heat leak model composed of axial heat leak and radial heat leak terms is included in the present code. (See Section 5.5.7 for details.)

6. An empirical correlation is included in the present code to determine the wall superheat across the heating surface as a function of applied heat load. (See Section 5.5.8 for details.)

7. The convective heat transfer in the vapor channel between the walls and the fluid is included in the present code. (See Section 5.5.8 for details.)

8. All the minor losses from bends in the transportation lines are calculated and included in the pressure drop calculations in the present code. (See Section 5.5.9 for details.)

9. To provide the flexibility required in the liquid line and vapor line, 12-inch long corrugated metal hoses are used in the test loop. The roughness of the corrugated metal hose is included in the pressure drop calculation in the vapor line and the liquid line in the present code. (See Section 5.5.9 for details.)

10. Most importantly, the capability to predict the performance of a LHP when it is operated at positive elevation has been added to the present code. (See sections 4.2 and 5.5.10 for details.)

The steady-state model presented in this section is formulated based on large-scale control-volume analysis. In other words, the LHP system is analyzed in a finite region, making a balance of flow in versus flow out, and determining gross flow effects such as the total energy exchange.

5.1 CONSERVATION LAWS

In this model, the conservation laws were analyzed based on each component (evaporator, condenser, reservoir, etc.) and the whole LHP. Since a LHP is a closed loop, the mass of the working fluid in the system is fixed. Therefore, the conservation of mass in the whole LHP is automatically fulfilled. For each component, the conservation of mass with a number of one-dimensional inlets and outlets can be written as:

$$\int_{CV} \frac{\partial \rho}{\partial t} d\mathcal{V} + \sum_i (\rho_i A_i V_i)_{out} - \sum_i (\rho_i A_i V_i)_{in} = 0 \qquad (5.1)$$

where $\mathcal{V}$ is the total volume confined in the control volume and "cv" stands for control volume. For steady-state analysis, the conservation of mass can be further simplified and written as:

$$\sum_i (\dot{m}_i)_{out} = \sum_i (\dot{m}_i)_{in} \qquad (5.2)$$

which states that in steady flow the mass entering the control volume must be equal to the mass leaving the control volume. This becomes the steady-flow mass conservation relation.

For the momentum equation, there is no net force exerted by the surroundings on the LHP system, except to support the rig. Detailed analysis of each component is similar to that of fully developed pipe flow, where the forces due to pressure, shear, and gravity must be balanced. This is combined with the energy equation to calculate the pressure drop along the LHP.

The energy balance equations of the whole LHP and each component play the most important role in this steady-state model, because predicting the temperature is the

goal of this model. After all, a LHP is a two-phase heat transfer device. The first law of

thermodynamics says that the change of stored energy equals the sum of work done and

heat addition to a system. In rate form,

$$\frac{dE}{dt} = \dot{Q} - \dot{W}$$

(5.3)

where $\dot{Q}$ is the rate of heat added to the system, $\dot{W}$ is the rate of work done by the

system, and E is the total energy of the system. In steady-state heat transfer analysis

without additional work done on the LHP, the heat added in must be equal to the heat

coming out. This is true for the whole LHP and each component when steady-state is

achieved. For detailed energy analysis, the Reynolds transport theorem [White, 1999][1] is

applied to Eq. 5.3, and the energy equation can be written as:

$$\frac{d}{dt}\left(\int_{CV} e\rho d\mathcal{V} \right) + \int_{CS} e\rho \left(\vec{V} \cdot \bar{n} \right) dA = \dot{Q} - \dot{W}$$

(5.4)

where $\bar{n}$ is defined as the unit vector normal to surface area element dA and e is the

system energy per unit mass. The system energy includes internal energy, kinetic energy

and potential energy, and can be written as:

$$e = u + \frac{1}{2}V^2 + gz$$

(5.5)

There are three mechanisms that cause heat to be exchanged between the surroundings

and the system: conduction, convection, and radiation. The work done on the system can

also be divided into three parts:

$$\dot{W} = \dot{W}_{shaft} + \dot{W}_{pressure} + \dot{W}_{visous\ stresses} = \dot{W}_S + \dot{W}_P + \dot{W}_V$$

(5.6)

The shaft work refers to the work done by a machine, like a pump or turbine, etc., and is identically zero for a LHP heat transfer analysis. The total rate of pressure work $\dot{W}_P$ occurs at the surface of the control volume only and can be expressed as the integral over the control surface:

$$\dot{W}_P = \int_{CS} p\left(\vec{V}\cdot\vec{n}\right)dA \tag{5.7}$$

The shear work due to viscous stress occurring at the control surface can be written as:

$$\dot{W}_V = -\int_{CS} \vec{\tau}\cdot\vec{V}dA \tag{5.8}$$

where $\vec{\tau}$ is the stress vector on the elemental surface dA. For some particular types of control surfaces, the shear work may vanish or be negligible. In our LHP analysis, the control surfaces are stationary solid walls. From the viscous no-slip condition, the shear work is identically zero along these walls. Therefore, the final form for the energy equation for a fixed control volume becomes:

$$\dot{Q} = \frac{\partial}{\partial t}\left[\int_{CV}\left(u + \frac{1}{2}V^2 + gz\right)\rho d\mathcal{V}\right] + \int_{CS}\left(h + \frac{1}{2}V^2 + gz\right)\rho\left(\vec{V}\cdot\vec{n}\right)dA \tag{5.9}$$

where the enthalpy $h = u + p/\rho$. Assuming 1-D steady flow with one inlet and one outlet, Eq. 5.9 can be reduced to its most popular form as:

$$\dot{Q} = \dot{m}_{out}\left(h + \frac{1}{2}V^2 + gz\right)_{out} - \dot{m}_{in}\left(h + \frac{1}{2}V^2 + gz\right)_{in} \tag{5.10}$$

The enthalpy is composed of internal energy, u, and useful pressure head, p/ρ. In LHP analysis, it is typical to separate the heat transfer analysis from the pressure drop analysis. In the analytical model, the applied heat is used solely to increase the internal energy, and

the pressure loss in the system is due to frictional loss. It is assumed that there is no energy exchanged between internal energy and kinetic energy in the system. In other words, viscous dissipation, Φ, is neglected. Viscous dissipation represents an increase in internal energy due to friction. It causes deformation of the fluid elements and transforms kinetic energy into internal energy. In pipe flow, Φ can be calculated from the mass flow rate and the pressure drop along the loop. From a sample calculation of the LHP analysis, the viscous dissipation rate along the whole loop is less than 1.0 W for a heat load of 1000 W (see Appendix C for detail). Therefore, it is valid to neglect the effect of viscous dissipation.

5.2   ASSUMPTIONS

Because of the complexity of the related two-phase heat transfer phenomena, the present model focuses on steady-state energy balance equations. In order to modify the sophisticated LHP operating system, some simplifying assumptions must be made, as listed below:

1. Heat is uniformly applied to the evaporator without any loss to the ambient.

2. The circulating chiller is supplying cooling water to the condenser at constant volume flow rate and temperature, $T_{SINK,in}$. The temperature of the cooling water exiting the condenser, $T_{SINK,out}$, depends on the heat rejected to the heat sink.

3. The walls of the tubing system are very thin and can be neglected during the calculation of the overall heat transfer coefficient for the heat transfer between fluid and ambient and between fluid and heat sink.

4. The transporting lines, except the flexible metal hose portion, are assumed to be smooth walled for the pressure drop calculation.

5. The reservoir and the evaporator core contain both liquid and vapor. In other words, they are both at saturated conditions at all times.

6. The primary wick is usually long and thin, therefore, the mass and heat transfer through the primary wick occur only in the radial direction.

7. Heat exchange between the LHP and the ambient is assumed to be due to natural convection only.

8. Because the amount of superheat is substantially small, it is assumed that the superheated vapor coming into the condenser loses its sensible heat first, and then the saturated vapor starts to condense.

9. Axial heat conduction from the evaporator to the reservoir in the secondary wick is neglected.

10. The increase of internal energy due to viscous dissipation is negligible.

11. The change of the saturation temperature caused by the pressure drop is negligible, except for the heat leak calculation.

12. The temperature change in the evaporator body and in the primary wick is assumed to be only in the radial direction. In other words, there is no temperature change in the axial or circumferential direction.

13. The steady-state operating temperature is between 270 K and 380 K for the best curve-fit ammonia properties.

Based on the assumptions made above, an analytical 1-D steady-state model was established. The detail modeling logics and calculation procedures are discussed in the following section.

5.3   ENERGY FLOW ANALYSIS

In normal LHP steady-state operation, heat is conducted from the evaporator body to the primary wick. Because both the inner surface and the outer surface of the primary wick are at saturation conditions, evaporation can take place at both locations. Thus, vapor can be generated both at the vapor channel and evaporator core. There are two cycles of the working fluid circulation. The obvious circulation is that vapor generated in the vapor channel travels through the vapor line to the condenser to reject heat to a sink, and then the subcooled liquid returns from the condenser to the evaporator via the liquid line. This circulation of the working fluid is referred to as the outer loop, which carries the majority of the applied heat load. Another circulation path is that vapor generated in the evaporator core travels to the reservoir along the non-wick flow path, where it is condensed back to liquid. In the mean time, the same amount of liquid is supplied from the reservoir to the primary wick by the secondary wick to complete the cycle. This working fluid circulation is referred to as the inner loop, which carries only a small portion of the heat load. These two loops are strongly correlated; any change in one of the loops affects the other. In order to model a LHP system properly, the two loops must be studied simultaneously and in detail to obtain accurate steady-state solutions.

A schematic diagram showing an energy balance of the loop heat pipe at steady-state operation is illustrated in Fig. 5.1. For steady-state operation, the heat going into the LHP must equal the heat coming out from the LHP. Therefore, from the energy flow chart, the energy balance equation of the LHP can be written as:

$$\dot{Q}_{APP} + \dot{Q}_{LL-A} = \dot{Q}_{VL-A} + \dot{Q}_{C-A} + \dot{Q}_{C-S} + \dot{Q}_{R-A} \tag{5.11}$$
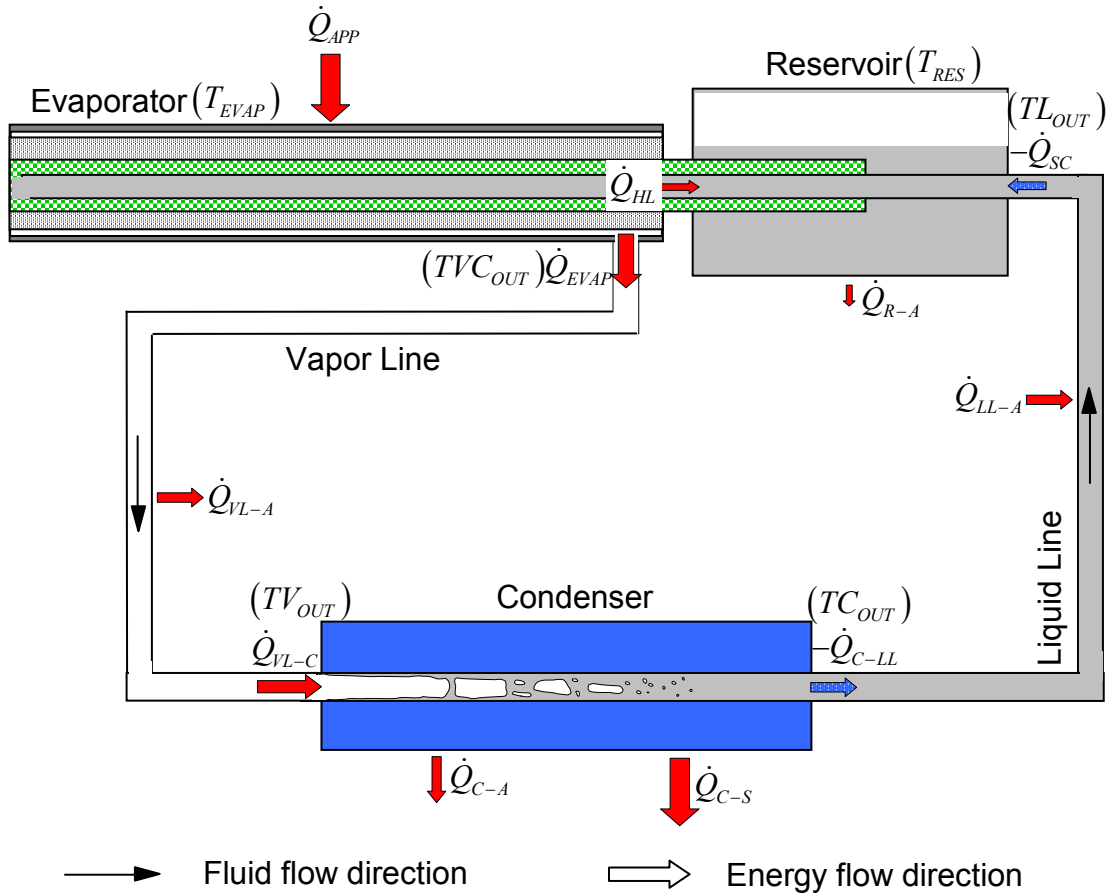
Fig. 5.1: Schematic diagram of LHP energy flow at steady-state condition. (Not to scale) Also denoted are the temperatures at various locations.

Let us examine the energy balance in each component during steady-state operation. During typical LHP operation, heat is applied uniformly to the evaporator, $\dot{Q}_{APP}$. The majority of the overall applied heat load, $\dot{Q}_{EVAP}$, vaporizes liquid on the outer surface of the primary wick and superheats the vapor in the vapor channel:

$$\dot{Q}_{EVAP} = \dot{m}\left[\lambda + C_{P,g}\left(TVC_{OUT} - T_{SAT}^{O}\right)\right] \tag{5.12}$$

where $\dot{m}$ is the rate of mass evaporated, λ is the heat of vaporization, TVC_{OUT} refers to the temperature at the exit of the vapor channel, and T_{SAT}^{O} denotes the saturation temperature at the outer surface of the primary wick. Since the latent heat is much greater than the sensible heat in Eq. 5.12, the mass flow rate is calculated by $\dot{m} = \dot{Q}_{EVAP} / \lambda$. The generated vapor travels along the axial vapor channel, and exits the evaporator to the vapor line. The remainder of the overall applied heat load, $\dot{Q}_{HL}$, leaks to the reservoir. This portion of the overall heat load is called heat leak. The steady-state energy balance equation in the evaporator can be written as:

$$\dot{Q}_{APP} = \dot{Q}_{EVAP} + \dot{Q}_{HL} \qquad (5.13)$$

In the vapor line, the fluid carrying the amount of heat $\dot{Q}_{EVAP}$ flows in from the evaporator and goes into the condenser with the amount of heat $\dot{Q}_{VL-C}$. Assuming that the ambient temperature is lower than the fluid temperature in the vapor line, and heat, $\dot{Q}_{VL-A}$, is transferred to the ambient by natural convection, the steady-state energy balance equation in the vapor line can be written as:

$$\dot{Q}_{EVAP} = \dot{Q}_{VL-A} + \dot{Q}_{VL-C} \qquad (5.14)$$

In the condenser, most of the heat is rejected to the heat sink, $\dot{Q}_{C-S}$, while some is rejected to the ambient, $\dot{Q}_{C-A}$. For LHP steady-state operation, it is typical that the fluid coming out from the condenser is subcooled, $-\dot{Q}_{C-LL}$. It is defined that the rate of heat transfer, $\dot{Q}$, is positive, therefore the subcooling liquid leaving the condenser, $-\dot{Q}_{C-LL}$,

and entering the reservoir, $-\dot{Q}_{SC}$, are both denoted with a negative sign. The steady-state

energy balance equation in the condenser can be written as:

$$\dot{Q}_{VL-C} = \dot{Q}_{C-S} + \dot{Q}_{C-A} + \left(-\dot{Q}_{C-LL}\right) \tag{5.15}$$

The energy flow in the liquid line is similar to that in the vapor line. The only difference

is that the liquid temperature in the liquid line is lower than the ambient. Therefore, heat

is transferred from the ambient to the liquid line. The steady-state energy balance

equation in the liquid line can be written as:

$$-\dot{Q}_{C-LL} + \dot{Q}_{LL-A} = -\dot{Q}_{SC} \tag{5.16}$$

In the reservoir, heat leak from the evaporator, $\dot{Q}_{HL}$, must balance the subcooling brought

back by the liquid from the liquid line, $-\dot{Q}_{SC}$, and the heat loss from the reservoir to the

ambient, $\dot{Q}_{R-A}$. The steady-state energy balance equation in the reservoir can be written

as:

$$\dot{Q}_{HL} + \left(-\dot{Q}_{SC}\right) = \dot{Q}_{R-A} \tag{5.17}$$

where the heat leak term is discussed later in Section 5.5.7. The heat exchange between

the reservoir and the ambient is through natural convection. The amount of subcooling

brought back by the liquid in the liquid line can be calculated by:

$$\dot{Q}_{SC} = \dot{m} C_{P,L} \left(T_{RES} - TL_{OUT}\right) \tag{5.18}$$

The sum of the energy balance equations in each component, Eq. 5.13 through Eq. 5.17,

must be equal to that of Eq. 5.11 in the whole LHP.

The energy balance equations in the evaporator, transport lines, and condenser are satisfied automatically during the operation of the LHP. However in LHP operation, the energy balance in Eq. 5.17 of the reservoir is achieved only at steady-state conditions. In the process to reach a steady-state condition, the LHP self-adjusts the saturation temperature in the reservoir. When a steady-state condition is achieved, this saturation temperature is also referred to as the steady-state operating temperature. This condition serves as the major iteration criterion for the steady-state calculation.

5.4   USER INPUT AND OUTPUT PARAMETERS:

For the model to function properly, a list of parameters has to be correctly supplied to the model. These user input parameters include the detailed dimensions of each component, heat load, wick porosity, wick permeability, wick effective pore radius, cooling water volume flow rate, sink temperature, ambient temperature, amount of elevation, external thermal conductance of the condenser, and selections of two-phase heat transfer and pressure drop models. By varying the parameters in the input sheet, the user can also study the effects of insulation of the vapor line and reservoir. Among these input parameters, the external thermal conductance of the condenser is the most ambiguous one. It is the heat transfer coefficient from the inner wall of the condenser tube to the heat sink, and it does not include the convective film coefficient due to the fluid flow inside the condenser tube. Typical values for the external thermal conductance per unit length of the condenser vary from 4 to 18 W/m-K, depending on the flow

arrangement and the thermal contact resistance between the condenser tube and the condenser plate [Kaya and Ku, 1999[1]]. It is usually determined empirically.

The purpose of the steady-state model is to predict the steady-state operating temperature as a function of heat load. To determine the steady-state operating temperature, detailed pressure drop and heat transfer calculations are performed. Therefore, the pressure and temperature distributions along the LHP, the location of the liquid-vapor interface, the amount of heat leak, and the amount of liquid subcooling brought back from the liquid line are all included as output parameters. The code can also be easily modified to output any steady-state parameters that needs to be studied.

5.5   MODELING CALCULATIONS AND PROCEDURES

As discussed previously, the calculation procedure can be divided into two main parts: one is the pressure drop calculation and the other is the heat transfer calculation. All detailed calculation procedures are discussed and a simplified flow chart of the steady-state code is shown later in this section.

5.5.1   Fluid Properties

To eliminate the errors caused by using incorrect properties, all of the fluid properties utilized in the code are curve fitted from National Institute of Standards and Technology (NIST) data. These properties include saturation pressure, latent heat, liquid density, vapor density, liquid viscosity, vapor viscosity, liquid thermal conductivity,

vapor conductivity, liquid specific heat, vapor specific heat, and surface tension. They are expressed as functions of saturation temperature in the form of 5th–order polynomial equations (see Appendix B for detail):

$$Y = \sum_{n=0}^{5} A_n T_{SAT}^n \tag{5.19}$$

where Y represents a fluid property and A_n are the corresponding polynomial coefficients.

5.5.2   Single-Phase Pressure Drop and Heat Transfer Calculations

The single-phase frictional pressure drop calculation can be derived from the energy equation and written as:

$$\Delta p = f\left(\frac{L}{D_h}\right)\left(\frac{\rho V^2}{2}\right) \tag{5.20}$$

This is known as the Darcy-Weisbach equation, which is valid for duct flows of any cross section and for laminar and turbulent flow [White, 1999][2]. The dimensionless parameter, f, is called the Darcy friction factor. For laminar flow, $f = 64\,\text{Re}^{-1}$; for turbulent flow, the solution proposed by H. Blasius, $f = 0.316\,\text{Re}^{-1/4}$ for 4000<Re<10^5, is used.

By assuming thin wall effects, the single-phase overall heat transfer coefficient for pipe flow can be obtained from inner and outer thermal resistances and expressed as:

$$\left(\frac{UA}{L}\right)_{F-A \text{ or } F-S} = \frac{1}{\dfrac{1}{Nu \cdot k\pi} + \left[\dfrac{1}{(h_o A_o / L)}\right]_{A \text{ or } S}} \tag{5.21}$$

where Nu is the Nusselt number, "$F - A$" represents heat exchange between the fluid and the ambient, and "$F - S$" represents heat exchange between the fluid and the heat sink. In a circular tube for laminar, fully developed flow, the Nusselt number can be shown to be [Incropera and DeWitt, 1996][1]:

$$Nu = \begin{cases} 4.36 & \text{for uniform surface heat flux} \\ 3.66 & \text{for constant wall temperature} \end{cases} \tag{5.22}$$

In the steady-state code, the Nusselt number for constant wall temperature is used for laminar flow. The Nusselt number for fully developed turbulent flow is determined by empirical correlations. The Dittus-Boelter equation is used for the calculation [Incropera and DeWitt, 1996][2]:

$$Nu = 0.023\,\mathrm{Re}^{4/5}\,\mathrm{Pr}^n \tag{5.23}$$

Where Pr is the Prandtl number and $n = 0.4$ for heating (wall temperature is higher than fluid temperature) and 0.3 for cooling.

For heat exchange with the ambient, the heat transfer coefficient from the outer wall to the ambient is assumed to be that of natural convection. The outer heat transfer coefficient, $h_{o,A}$, of a horizontal cylinder can be written as [Holman, 1990]:

$$h_{o,A} = 1.32 \left(\frac{T_W - T_{AMB}}{D_o} \right)^{1/4} \tag{5.24}$$

where T_W is the outer wall temperature. For heat exchange with the heat sink, the outer heat transfer coefficient, $h_{o,S}$, is obtained experimentally. As discussed in Section 5.4,

the external thermal conductance per unit length of the condenser, $\left(\dfrac{h_o A_o}{L}\right)_S$, is an input

parameter.

From the energy conservation equation, the temperature change of single-phase

fluid flow along the pipe can then be expressed as:

$$-\dot{m}C_P dT_F = \left[\left(\frac{UA}{L}\right)_{F-A}(T_F - T_{AMB}) + \left(\frac{UA}{L}\right)_{F-S}(T_F - T_{SINK})\right]dz \qquad (5.25)$$

Note that while in the transportation lines, the coefficient $\left(\dfrac{UA}{L}\right)_{F-S}$ is zero because there

is no heat rejected to the heat sink. To solve for the fluid temperature along the loop, a

parameter called effective sink temperature, $T_{EFF,SINK} = \dfrac{\left(\dfrac{UA}{L}\right)_{F-A}T_{AMB} + \left(\dfrac{UA}{L}\right)_{F-S}T_{SINK}}{\left(\dfrac{UA}{L}\right)_{F-A} + \left(\dfrac{UA}{L}\right)_{F-S}}$, is

introduced. Then the temperature at loop distance, L, can be expressed as a function of

inlet temperature, T_{IN}:

$$T = T_{EFF,SINK} + (T_{IN} - T_{EFF,SINK})\exp\left(-\frac{\left[(UA/L)_{F-A} + (UA/L)_{F-S}\right]}{\dot{m}C_P}L\right) \qquad (5.26)$$

5.5.3   Two-phase heat transfer models

The purpose of the two-phase heat transfer calculation is two-fold: to determine

the vapor quality along the tube, and to locate the liquid-vapor interface in the loop. In

the two-phase portion, the energy balance equation becomes:

$$-\dot{Q}_{EVAP} dx = \left[\left(\frac{UA}{L} \right)_{F-A} (T_{SAT} - T_{AMB}) + \left(\frac{UA}{L} \right)_{F-S} (T_{SAT} - T_{SINK}) \right] dz \qquad (5.27)$$

where x is the vapor quality, and the overall heat transfer coefficient between the fluid

and heat sink and ambient is similar to that in single-phase heat transfer, Eq. 5.21, and

can be written as:

$$\left(\frac{UA}{L} \right)_{F-A \text{ or } F-S} = \frac{1}{\dfrac{1}{h_{2\phi} \pi D_i} + \left[\dfrac{1}{(h_o A_o / L)} \right]_{A \text{ or } S}} \qquad (5.28)$$

where $h_{2\phi}$ is the tube-side two-phase heat transfer coefficient, which is a function of

vapor quality. The outer heat transfer coefficient, $\left(\dfrac{L}{h_O A_O} \right)_{A \text{ or } S}$, in Eq. 5.28 is the same as

that for single-phase. Since $\dot{Q}_{EVAP}$, T_{SINK}, T_{SAT}, and T_{AMB} are constants, Eq. 5.27 can then

be written as:

$$dz = \frac{\dot{Q}_{EVAP}}{T_{SAT} - T_{SINK}} f(h_{2\phi}, x) dx \qquad (5.29)$$

where $f(h_{2\phi}, x) = -\left[(UA/L)_{F-S} + \dfrac{T_{SAT} - T_{AMB}}{T_{SAT} - T_{SINK}} (UA/L)_{F-A} \right]^{-1}$. Integrating Eq. 5.29, the

two-phase length with corresponding inlet and exit vapor qualities can be obtained:

$$L_{2\phi} = \frac{\dot{Q}_{EVAP}}{T_{SAT} - T_{SINK}} \int_{x_{IN}}^{x_{OUT}} f(h_{2\phi}, x) dx \qquad (5.30)$$

To solve Eq. 5.30 explicitly, the tube-side two-phase heat transfer coefficient

must be calculated first. There are several correlations available for the convective

condensation two-phase heat transfer coefficient. Four correlations are included in the

steady-state code: Ananiev et al., Traviss et al., Shah, and two-phase multiplier. All four correlations are based on vapor quality and fluid properties. The correlation proposed by Ananiev et al. [1961] is:

$$h_{2\phi} = h_i \sqrt{\frac{\rho_L}{\rho_m}} \tag{5.31}$$

where

$$\frac{1}{\rho_m} = \left(\frac{1}{\rho_L}\right)(1-x) + \left(\frac{1}{\rho_g}\right)x \tag{5.32}$$

and h_i is the single-phase heat transfer coefficient for the entire flow as liquid. Traviss et al. [1973] proposed the following relation for annular-flow convective condensation:

$$h_{2\phi} = \left(\frac{k_L}{D}\right)\frac{0.15\,\mathrm{Pr}_L\,\mathrm{Re}_L^{0.9}}{F_T}\left[\frac{1}{X_{tt}} + \frac{2.85}{X_{tt}^{0.476}}\right], \qquad \mathrm{Re}_L = \frac{G(1-x)D}{\mu_L} \tag{5.33}$$

where

$$X_{tt} = \left(\frac{1-x}{x}\right)^{0.9}\left(\frac{\rho_g}{\rho_L}\right)^{0.5}\left(\frac{\mu_L}{\mu_g}\right)^{0.1} \tag{5.34}$$

and

$$F_T = \begin{cases} 5\,\mathrm{Pr}_L + 5\ln(1+5\,\mathrm{Pr}_L) + 2.5\ln(0.0031\,\mathrm{Re}_L^{0.812}) & \text{for } \mathrm{Re}_L > 1125 \\ 5\,\mathrm{Pr}_L + 5\ln\left[1 + \mathrm{Pr}_L(0.0964\,\mathrm{Re}_L^{0.585}-1)\right] & \text{for } 50 < \mathrm{Re}_L < 1125 \\ 0.707\,\mathrm{Pr}_L\,\mathrm{Re}_L^{0.5} & \text{for } \mathrm{Re}_L < 50 \end{cases} \tag{5.35}$$

The third two-phase heat transfer correlation in the code is that of Shah [1979]. It is based on a purely empirical approach as a best fit to available convective condensation heat transfer data for round tubes:

$$h_{2\phi} = h_{lo}\left[(1-x)^{0.8} + \frac{3.8x^{0.76}(1-x)^{0.04}}{(P/P_{cr})^{0.38}}\right] \quad (5.36)$$

where

$$h_{lo} = 0.023\left(\frac{k_L}{D}\right)\left(\frac{GD}{\mu_L}\right)^{0.8} \text{Pr}_L^{0.4} \quad (5.37)$$

and P and P_{cr} are the absolute local and critical pressures, respectively. For the working

fluid in the LHP, ammonia, the critical pressure is equal to 11,290 kPa.

The last correlation assumes that the relation between single-phase and two-phase

heat transfer coefficient is similar to that of single-phase and two-phase pressure drop.

Thus, a general correlation of two-phase heat transfer can be written as:

$$h_{2\phi} = \phi_L h_L \quad (5.38)$$

The two-phase multiplier is defined as:

$$\phi_L = \left[\frac{(dP/dz)_{2\phi}}{(dP/dz)_L}\right]^{1/2} \quad (5.39)$$

where $(dP/dz)_{2\phi}$ is the two-phase pressure drop and $(dP/dz)_L$ is the single-phase

pressure drop for liquid flow alone, which can be calculated from Eq. 5.40.

After applying a correlation to obtain the two-phase heat transfer coefficient, the

finite integral in Eq. 5.30 needs to be solved to obtain the two-phase length associated

with the inlet and exit vapor qualities. A numerical method called "Gaussian

Quadrature" with Legendre polynomials of degree 10 is applied to solve the finite

integral. A detailed description of Gaussian quadrature and a table of Legendre

polynomials can be found in Appendix D.1.

5.5.4 Two-phase pressure drop models

Two-phase pressure drop consists of gravitational pressure drop, frictional pressure drop, and accelerational pressure drop. Since the condenser is placed horizontally, the gravitational pressure drop in the condenser is identically zero. Frictional two-phase pressure drop can be calculated from the two-phase multiplier, ϕ_L, and the single-phase pressure drop, $(dP/dz)_L$, in Eq. 5.39.

The single-phase pressure drop for liquid flow alone in the tube can be written as:

$$\left(\frac{dP}{dz}\right)_L = -\frac{f_L}{D}\frac{(1-x)^2}{2\rho_L}\left(\frac{\dot{m}}{A}\right)^2 \tag{5.40}$$

where the liquid-phase friction factor, f_L, can be calculated from Reynolds number as discussed previously for single-phase pressure drop. The Reynolds number of the liquid-phase can be calculated as:

$$\mathrm{Re}_L = \frac{4\dot{m}(1-x)}{\pi\mu_L D} \tag{5.41}$$

After substituting Eq. 5.40 into Eq. 5.39 and applying the chain rule, the two-phase pressure drop becomes a function of vapor quality:

$$\left(\frac{dP}{dx}\right)_{2\phi} = -\phi_L^2\frac{f_L}{D}\frac{(1-x)^2}{2\rho_L}\left(\frac{\dot{m}}{A}\right)^2\left(\frac{dz}{dx}\right) \tag{5.42}$$

where (dz/dx) is derived from the two-phase heat transfer calculation in Eq. 5.29. Integrating Eq. 5.42 from inlet vapor quality, x_{IN}, to exit vapor quality, x_{OUT}, the frictional two-phase pressure drop can be written as:

$$\Delta P_{2\phi,f} = \int_{x_{IN}}^{x_{OUT}} \left[-\phi_L^2 \frac{f_L}{D} \frac{(1-x)^2}{2\rho_L} \left(\frac{\dot{m}}{A}\right)^2 \left(\frac{dz}{dx}\right) \right] dx \qquad (5.43)$$

To solve Eq. 5.43, several correlations are included in the code to calculate the two-phase multiplier. Among the correlations included in the code, Constant Smooth [Crowley et al., 1992], Wallis [1969], and Chen [1989] are correlations established based on annular flow. In annular flow, the two-phase pressure drop in the liquid- and vapor-phase can be written as:

$$\left(\frac{dP}{dz}\right)_{2\phi}^L = -\frac{1}{D} f_L \frac{1}{2\rho_L} \frac{(1-x)^2}{(1-\alpha)^2} \left(\frac{\dot{m}}{A}\right)^2 \qquad (5.44)$$

$$\left(\frac{dP}{dz}\right)_{2\phi}^g = -\frac{1}{D} \left(\frac{1}{\alpha^{1/2}}\right) f_i \frac{1}{2\rho_g} \frac{x^2}{\alpha^2} \left(\frac{\dot{m}}{A}\right)^2 \qquad (5.45)$$

where α is the void fraction and f_i is the interfacial frictional factor. Comparing Eq. 5.44 with Eq. 5.42, the two-phase multiplier can be written as:

$$\phi_L = \frac{1}{1-\alpha} \qquad (5.46)$$

Therefore, the two-phase multiplier can be obtained from the void fraction. The local pressure gradient of the vapor-phase, $(dP/dz)_{2\phi}^g$, and that of the liquid-phase, $(dP/dz)_{2\phi}^L$, are required to be the same, and a relation between void fraction and vapor quality can be established:

$$\frac{f_i}{f_L} = \alpha^{1/2} \left(\frac{\alpha}{1-\alpha}\right)^2 \left(\frac{1-x}{x}\right)^2 \frac{\rho_g}{\rho_L} \qquad (5.47)$$

The interfacial shear ratio f_i/f_g is typically correlated as a function of void fraction, α, and can be expressed as:

$$\frac{f_i}{f_g} = A\alpha^B + C(1-\alpha)^D \tag{5.48}$$

where constants A, B, C, and D are listed in Table 5.1 for different correlation methods.

Table 5.1: Constants of correlations for interfacial shear ratio.

Correlation	A	B	C	D
Wallis	1	0	75	1
Chen	1	0	6.8	0.39
Constant Smooth	1	0	0	0

Therefore, the relation between void fraction and vapor quality can be expressed as:

$$\frac{f_g}{f_L}\left[A\alpha^B + C(1-\alpha)^D\right] = \alpha^{1/2}\left(\frac{\alpha}{1-\alpha}\right)^2\left(\frac{1-x}{x}\right)^2\frac{\rho_g}{\rho_L} \tag{5.49}$$

where the single-phase friction factor can be calculated from Reynolds number:

$$f = \begin{cases} 64/\mathrm{Re} & \text{for laminar flow} \\ 0.316/\mathrm{Re}^{1/4} & \text{for turbulent flow} \end{cases} \tag{5.50}$$

and the Reynolds number of the vapor-phase and the liquid-phase can be calculated as:

$$\mathrm{Re}_g = \frac{4\dot{m}x}{\pi\mu_g D} \; ; \; \mathrm{Re}_L = \frac{4\dot{m}(1-x)}{\pi\mu_L D} \tag{5.51}$$

From Eq. 5.49, the relation between void fraction and quality can be obtained implicitly. A numerical method called the secant method is employed to solve for void fraction as a function of quality, $\alpha = \mathrm{func}(x)$. A detailed description of the secant method is discussed in Appendix D.2.

There are two other correlations available in the steady-state code: Lockhart-Martinelli and Friedel. Lockhart and Martinelli [1949] proposed a generalized

correlation for the two-phase multiplier from a series of two-phase flows in horizontal tubes:

$$\phi_L = \left(1 + \frac{C}{X} + \frac{1}{X^2}\right)^{1/2}$$

(5.52)

where the Martinelli parameter, X, is defined as:

$$X \equiv \left[\frac{(dP/dz)_L}{(dP/dz)_g}\right]^{0.5} = \left(\frac{f_L}{f_g}\right)^{0.5} \left(\frac{\rho_g}{\rho_L}\right)^{0.5} \left(\frac{1-x}{x}\right)$$

(5.53)

The recommended value of the constant C in Eq. 5.52 depends on the flow regimes associated with the flow of the vapor and the liquid alone in the pipe. Table 5.2 indicates the constant for four different possible combinations.

Table 5.2: C value in two-phase multiplier proposed by Lockhart and Martinelli.

liquid	Gas	Subscript	C
Turbulent	Turbulent	tt	20
Viscous	Turbulent	vt	12
Turbulent	Viscous	tv	10
Viscous	Viscous	vv	5

The last correlation available in the steady-state code is proposed by Friedel [1979]. Friedel developed a correlation for the two-phase multiplier, ϕ_{lo}, based on 25,000 data points:

$$\phi_{lo}^2 = C_{F1} + \frac{3.24 C_{F2}}{Fr^{0.045} We^{0.035}}$$

(5.54)

where

$$C_{F1} = (1-x)^2 + x^2 \left(\frac{\rho_L}{\rho_g}\right)\left(\frac{f_{go}}{f_{lo}}\right) \tag{5.55}$$

$$C_{F2} = x^{0.78}(1-x)^{0.24}\left(\frac{\rho_L}{\rho_g}\right)^{0.91}\left(\frac{\mu_g}{\mu_L}\right)^{0.19}\left(1-\frac{\mu_g}{\mu_L}\right)^{0.7} \tag{5.56}$$

$$Fr = \frac{G^2}{g d_h \rho_{tp}^2} \tag{5.57}$$

$$We = \frac{G^2 d_h}{\rho_{tp}\sigma} \tag{5.58}$$

$$\rho_{tp} = \left(\frac{x}{\rho_g} + \frac{1-x}{\rho_L}\right)^{-1} \tag{5.59}$$

Note that σ in Eq. 5.58 represents surface tension. From the definition, the relation between the two two-phase multipliers can be written as:

$$\phi_L^2 = \phi_{lo}^2 \frac{(f_{lo}/f_L)}{(1-x)^2} \tag{5.60}$$

Once the two-phase multiplier is obtained from the correlations, the finite integration in Eq. 5.42 can be solved using a numerical method called Gauss-Legendre integration (See Appendix D.1).

The accelerational pressure drop in two-phase flow can be calculated from vapor quality and void fraction:

$$-\left(\frac{dP}{dz}\right)_{2\phi,a} = \frac{d}{dz}\left[\frac{G^2 x^2}{\rho_g \alpha} + \frac{G^2(1-x)^2}{\rho_L(1-\alpha)}\right] \tag{5.61}$$

Integrating Eq. 5.61 from the inlet to the exit of a pipe yields the accelerational two-phase pressure drop:

$$-\Delta P_{2\phi,a} = \left[\frac{G^2 x^2}{\rho_g \alpha} + \frac{G^2(1-x)^2}{\rho_L(1-\alpha)}\right]_{Exit} - \left[\frac{G^2 x^2}{\rho_g \alpha} + \frac{G^2(1-x)^2}{\rho_L(1-\alpha)}\right]_{Inlet} \tag{5.62}$$

There are various correlations for void fraction as a function of vapor quality. Lockhart and Martinelli [1949] correlated the void fraction as a function of the Martinelli parameter, X:

$$\alpha = \left[1 + 0.28 X^{0.71}\right]^{-1} \tag{5.63}$$

where X is defined in Eq. 5.53. Other correlations available in the steady-state code can be shown to be of the general form:

$$\alpha = \left[1 + B_B \left(\frac{1-x}{x}\right)^{n1} \left(\frac{\rho_g}{\rho_L}\right)^{n2} \left(\frac{\mu_L}{\mu_g}\right)^{n3}\right]^{-1} \tag{5.64}$$

where the values of the unspecified constants corresponding to different correlations are listed in Table 5.3.

Table 5.3: Constants for different void fraction correlations.

Correlation	B_B	$n1$	$n2$	$n3$
Zivi model [1964]	1	1	0.67	0
Wallis model [1969]	1	0.72	0.40	0.08
Thom correlation [1964]	1	1	0.89	0.18
Baroczy correlation [1965]	1	0.74	0.65	0.13

To summarize the two-phase heat transfer and pressure drop calculation, a flow chart showing a sample iteration is drawn in Fig. 5.2. This flow chart shows how to calculate the exit vapor quality and two-phase pressure drop for a given tube length and inlet vapor quality, assuming that all the input parameters listed in Section 5.4 are known parameters. The flow chart shows the condition where both inlet and exit flows are two-phase flow. In other words, inlet and exit vapor qualities are between 0 and 1. Other conditions may also be solved from similar iteration in the steady-state code.

```
┌─────────────────────────────────────────────────────────────┐
│   Known: Tube length, L and inlet vapor quality, x_IN        │
└─────────────────────────────────────────────────────────────┘
                              │
                              ▼
          ┌─────────────────────────────────────┐
          │   Guess exit quality, x_OUT         │
          └─────────────────────────────────────┘
                              │
                              ▼
          ┌─────────────────────────────────────┐
          │  Choose a correlation for two-phase │
          │  heat transfer coefficient, h_2φ    │
          └─────────────────────────────────────┘
                              │
                              ▼
          ┌─────────────────────────────────────┐
          │ Solve Eq. 5.30 and obtain two-phase │
          │ flow length, L_2φ, corresponding to │
          │ the guessed exit quality, x_OUT     │
          └─────────────────────────────────────┘
                              │
                              ▼
   No       ┌─────────────────────────────┐
 ◄─────────│   Check if L_2φ = L          │
          └─────────────────────────────┘
                              │ Yes
                              ▼
          ┌─────────────────────────────────────┐
          │ Choose a correlation for two-phase  │
          │ multiplier, φ_L                     │
          └─────────────────────────────────────┘
                              │
                              ▼
          ┌─────────────────────────────────────┐
          │ Solve Eq. 5.43 and obtain frictional│
          │ two-phase pressure drop, ΔP_2φ,f    │
          └─────────────────────────────────────┘
                              │
                              ▼
          ┌─────────────────────────────────────┐
          │ Choose a correlation for void       │
          │ fraction, α                         │
          └─────────────────────────────────────┘
                              │
                              ▼
          ┌─────────────────────────────────────┐
          │ Solve Eq. 5.62 and get accelerational│
          │ two-phase pressure drop, ΔP_2φ,a    │
          └─────────────────────────────────────┘
                              │
                              ▼
          ┌─────────────────────────────────────┐
          │ Obtain exit quality, x_OUT, and     │
          │ two-phase pressure drop,            │
          │ ΔP_2φ = ΔP_2φ,f + ΔP_2φ,a           │
          └─────────────────────────────────────┘
```

Fig. 5.2: Iteration procedure for two-phase heat transfer and pressure drop calculations.

5.5.5 Liquid Flow in Capillary Media

In the analysis of the liquid flow in the wick structure, it is generally assumed that the liquid flow is steady, two-dimensional, incompressible, laminar flow with negligible gravity forces. The fluid and the wick structure are assumed to be in local equilibrium, and the wick is assumed to be isotropic and homogeneous. In the LHP application, the primary wick is usually long and thin; therefore, the liquid flow in the wick can be simplified as one-dimensional radial flow. Also, the liquid velocity and its gradient in the radial direction are very small. After simplifying the steady-state conservation equations for mass, momentum, and energy in the wick region, the pressure gradient in the radial direction can be written as [Faghri, 1995]:

$$\frac{dp}{dr} = -\frac{\mu_L \dot{m}}{\rho_L A_W \kappa}$$

(5.65)

where $A_W = 2\pi r L$ is the wick inner surface area, and κ is the permeability of the wick structure. The equation is also known as Darcy's law for liquid flow in a porous medium. Integrating Eq. 5.65 from the inner surface, $r = D_W^I / 2$, to the outer surface, $r = D_W^O / 2$, the pressure drop across the primary wick can be expressed as:

$$\Delta p_W = \frac{\mu_L \dot{m}}{\rho_L \kappa 2\pi} \times \ln\left(\frac{D_W^O}{D_W^I}\right)$$

(5.66)

5.5.6 Effective Thermal Conductivity of Wick Structures

The effective thermal conductivity of the wick saturated with the working fluid is required for calculating the heat leak. It is dependent on both the solid wick material and

the working fluid. Parallel (Fig. 5.3a) and series (Fig. 5.3b) models are most commonly used for calculating effective thermal conductivity. They are both based on a volumetric average of individual conductivity.

a) Parallel　　　　　　　　b) Series

Working
Fluid

Solid Wick
Material

Heat Flow
Direction

Heat Flow
Direction
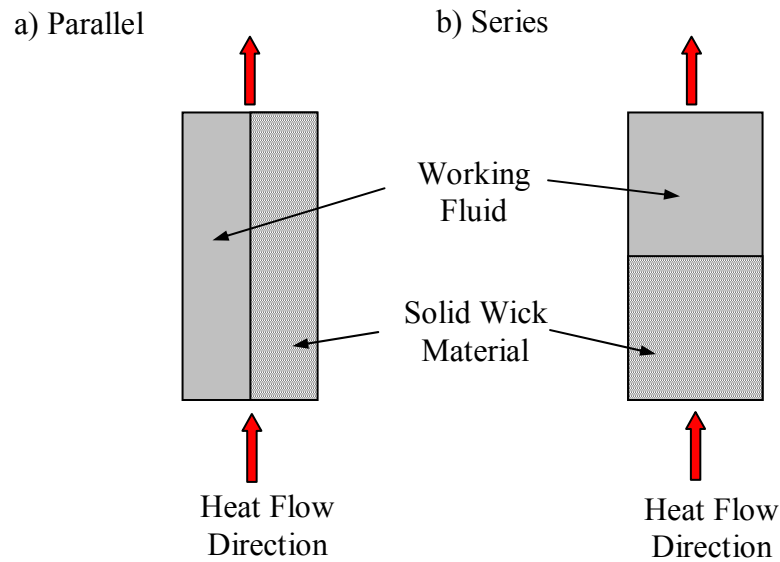
Fig. 5.3: Schematic for determining the effective thermal conductively: a) Parallel Path; b) Series path.

The effective thermal conductivity with the two phases in parallel based on volumetric average can be written as:

$$k_{EFF} = (1-\varepsilon)k_{WICK} + \varepsilon k_L \qquad (5.67)$$

where k_L is the thermal conductivity of the working fluid, k_{WICK} is the thermal conductivity of the wick material, and ε is the wick porosity. For the series case, the effective thermal conductivity can be written as:

$$k_{EFF} = \frac{k_{WICK}k_L}{\varepsilon k_{WICK} + (1-\varepsilon)k_L} \qquad (5.68)$$

Due to the requirement of very fine pore size, the primary wick in the LHP is usually sintered metal powder wick. The exact geometry of the sintered wick is impossible to predict because of the random dispersion of the particles and deformation during the sintering process. Another correlation of effective conductivity proposed by Maxwell [1891] for heterogeneous material can be expressed as:

$$k_{EFF} = k_{WICK} \left[\frac{2 + k_L / k_{WICK} - 2\varepsilon \left(1 - k_L / k_{WICK}\right)}{2 + k_L / k_{WICK} + \varepsilon \left(1 - k_L / k_{WICK}\right)} \right] \tag{5.69}$$

This correlation was verified by Gorring and Churchill [1961], and agreed with the experimental data reasonably well. Therefore, it is used in the model.

5.5.7 Heat Leak Model

There are two different heat flow paths for heat leak from the evaporator to the reservoir. One, called radial heat leak, is by radial conduction across the primary wick, into the evaporator core, and then on to the reservoir. The other, called axial heat leak, is by axial conduction through the joint between the evaporator and the reservoir:

$$\dot{Q}_{HL} = \dot{Q}_{HL,A} + \dot{Q}_{HL,R} \tag{5.70}$$

A schematic diagram of the connector between the evaporator and reservoir is drawn in Fig. 5.4. The heat can be conducted either through the solid material or into the fluid. Therefore, the axial heat leak term can be expressed as:

$$\dot{Q}_{HL,A} = kA_C \frac{\left(T_{EVAP} - T_{RES}\right)}{L} + \left(Nuk_L \pi L\right) \left(\frac{T_{EVAP} - T_{RES}}{2}\right) \tag{5.71}$$

where tube cross area $A_C = \left(\pi(D_o^2 - D_i^2)\right)/4$ and k is the thermal conductivity of the material connecting the evaporator and reservoir. Note that the average wall temperature, $\dfrac{T_{EVAP} + T_{RES}}{2}$, is used to calculate the heat conducted into the fluid.
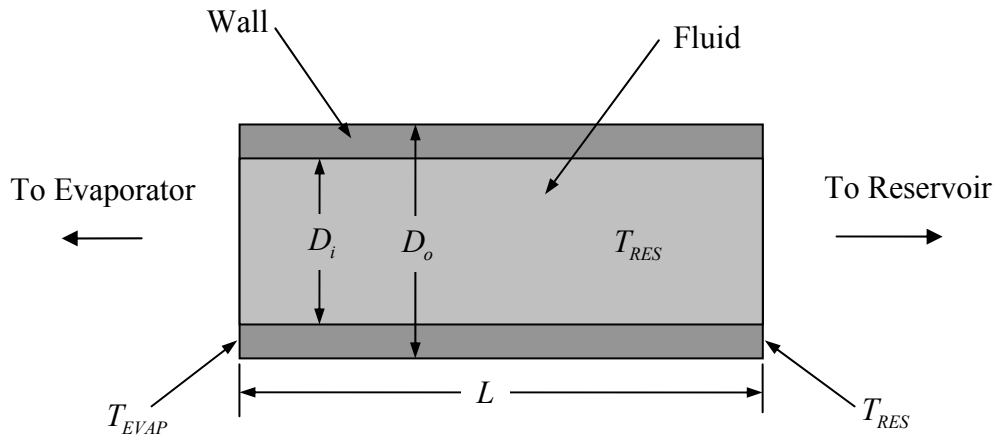
Fig. 5.4: A Schematic diagram of the connector between the evaporator and the reservoir.

Radial heat leak refers to the heat conducted radially from the outer surface to the inner surface of the primary wick. This can be derived from the combination of heat and mass transfer in the primary wick. A diagram illustrating the heat and mass flow in the primary wick is shown in Fig. 5.5 . The energy balance equation from mass transfer and heat conduction in the primary wick control volume can be written as:

$$
\dot{m}C_P \left\{ \left[T - \left(\frac{dT}{dr}\right)\frac{dr}{2} \right] - \left[T + \left(\frac{dT}{dr}\right)\frac{dr}{2} \right] \right\} -
$$

$$
2\pi k_{EFF} L_{WICK} \left\{ \left(r - \frac{dr}{2} \right) \left[\frac{dT}{dr} - \left(\frac{d^2T}{dr^2}\right)\frac{dr}{2} \right] - \left(r + \frac{dr}{2} \right) \left[\frac{dT}{dr} + \left(\frac{d^2T}{dr^2}\right)\frac{dr}{2} \right] \right\} = 0 \tag{5.72}
$$
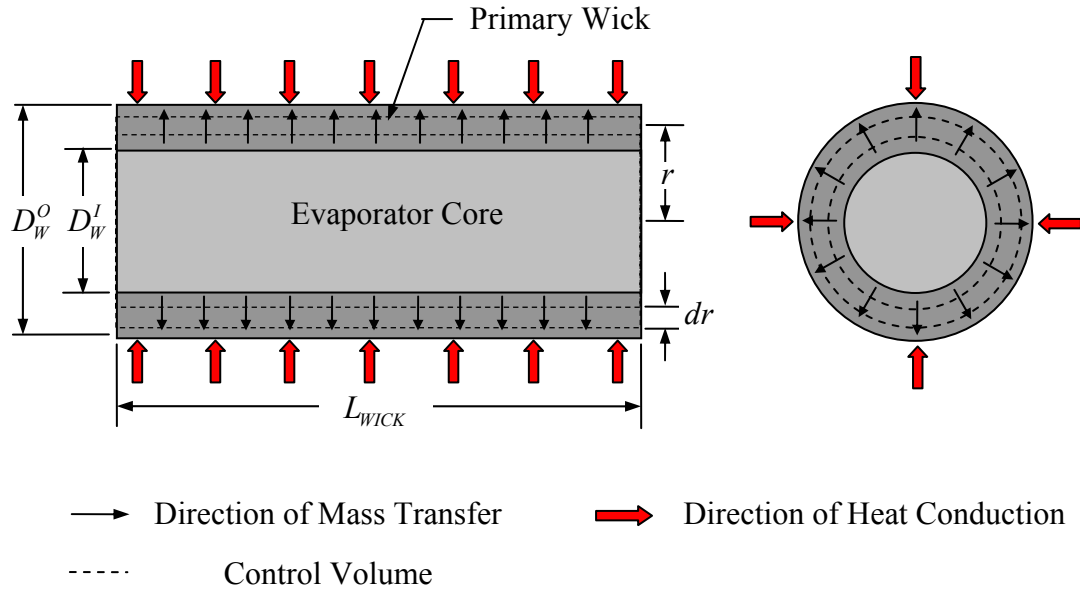
Fig. 5.5: Schematic of the heat and mass transfer in the primary wick.

After rearrangement and by neglecting the higher-order terms, a simplified equation can be obtained:

$$\frac{d}{dr}\left(r\frac{dT}{dr}\right) - \frac{\dot{m}C_P}{2\pi k_{EFF}L_{WICK}}\frac{dT}{dr} = 0 \qquad (5.73)$$

It is assumed that the evaporator core is always at a saturated condition and the outer surface of the primary wick is where the evaporation occurs. Therefore, the temperature boundary conditions can be written as:

$$\begin{cases} T = T_{SAT}^{I} & \text{at } r = D_W^I/2 \\ T = T_{SAT}^{O} & \text{at } r = D_W^O/2 \end{cases} \qquad (5.74)$$

By applying the boundary conditions on Eq. 5.73, the temperature distribution in the primary wick is given by:

$$T(r) = \left[T_{SAT}^I + \frac{T_{SAT}^O - T_{SAT}^I \left(D_W^O / D_W^I \right)^\varsigma}{\left(D_W^O / D_W^I \right)^\varsigma - 1} \right] \left(\frac{2r}{D_W^I} \right)^\varsigma - \frac{T_{SAT}^O - T_{SAT}^I \left(D_W^O / D_W^I \right)^\varsigma}{\left(D_W^O / D_W^I \right)^\varsigma - 1} \qquad (5.75)$$

where $\varsigma = \dfrac{\dot{m} C_P}{2\pi k_{EFF} L_{WICK}}$. The radial heat leak due to conduction across the primary wick

can be calculated as:

$$\dot{Q}_{HL,R} = k_{EFF} \left(\pi D_W^I L_{WICK} \right) \left(\frac{\partial T}{\partial r} \right)_{r = D_W^I / 2} \qquad (5.76)$$

Substituting Eq. 5.75 into Eq. 5.76, the heat leak can be expressed as:

$$\dot{Q}_{HL,R} = \frac{2\pi k_{EFF} L_{WICK} \varsigma}{\left(D_W^O / D_W^I \right)^\varsigma - 1} \Delta T_{AC.WICK} \qquad (5.77)$$

where the temperature across the wick $\Delta T_{AC.WICK} = \left(T_{SAT}^O - T_{SAT}^I \right)$. When the mass flow

rate in the primary wick is very small, the coefficient ς approaches zero. After

calculation, the radial heat leak in Eq. 5.77 becomes pure condition and the equation can

be written as:

$$\dot{Q}_{HL,R} = \frac{2\pi k_{EFF} L_{WICK}}{\ln \left(D_W^O / D_W^I \right)} \Delta T_{AC.WICK} \qquad (5.78)$$

For a LHP with small mass flow rate, pure conduction in the primary wick is usually

assumed to calculate the radial heat leak. The effect of fluid flow in the primary wick on

radial heat leak is studied in Appendix E. Because both the outer and inner surfaces of

the primary wick are at saturated conditions, the temperature difference across the

primary wick can be obtained from the pressure difference across the wick:

$$\Delta T_{AC.WICK} = \left(\frac{dT}{dP} \right)_{SAT} \left(\Delta P_{TOTAL} - \Delta P_{WICK} \right) \qquad (5.79)$$

where $(dT/dP)_{SAT}$ is calculated by the Clausius-Clapeyron equation in Eq. 4.7.

Combining axial and radial heat leak, the total heat leak can be written as:

$$\dot{Q}_{HL} = kA_C \frac{(T_{EVAP} - T_{RES})}{L} + (Nuk_L \pi L)\left(\frac{T_{EVAP} - T_{RES}}{2}\right) + \frac{2\pi k_{EFF} L_{WICK}}{\ln\left(D_W^O / D_W^I\right)} \Delta T_{AC.WICK} \quad (5.80)$$

This heat leak equation is valid when $\Delta T_{AC.WICK}$ is positive, i.e. the pressure at the outer surface is higher than that at the inner surface. When the LHP is operating in the capillary-controlled mode, this is always the case.

When the LHP is operating in the gravity-controlled mode, the pressure at the inner surface of the primary wick is higher than that at the outer surface. The temperature at the evaporator core might be higher than that in the vapor channel. With the existence of liquid in the vapor channel, the detailed analysis of the temperature distribution in the primary wick becomes much more complex. To simplify the calculation, it is assumed that the radial heat leak equals zero. Therefore, the heat leak model for the gravity-controlled mode can be calculated by:

$$\dot{Q}_{HL} = kA_C \frac{(T_{EVAP} - T_{RES})}{L} + (Nuk_L \pi L)\left(\frac{T_{EVAP} - T_{RES}}{2}\right) \quad (5.81)$$

5.5.8 Heat Transfer from Evaporator Body to Primary Wick

This section discusses how heat is transferred from the evaporator body to the primary wick. A relation between the overall heat load and the amount of wall superheat across the heating surface is given as:

$$\frac{\dot{Q}}{A_h} = h\left(T_W - T_{SAT}\right) \qquad\qquad (5.82)$$

where $\dot{Q}$ is the applied heat load, A_h is the heating surface area, and $\left(T_W - T_{SAT}\right)$ denotes the amount of wall superheat. A magnified view of the heating surface between the evaporator body and the primary wick is shown in Fig. 5.6.
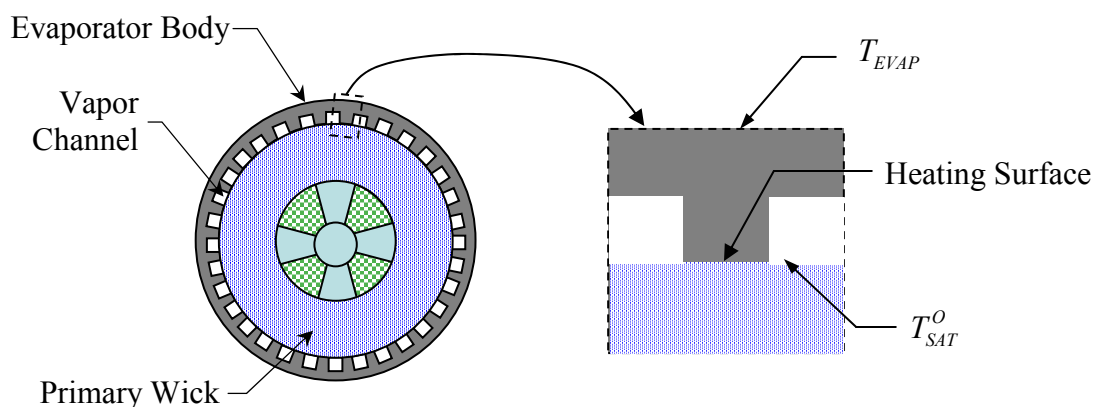
Fig. 5.6: A magnified drawing of the heating surface.

Liao and Zhao [1999] observed heat transfer phenomena from see-through experiments and presented relations between imposed heat flux and heat transfer coefficient. A qualitative diagram showing the heat transfer coefficient as a function of heat flux is drawn in Fig. 5.7. This diagram also shows the heat transfer phenomena underneath the heating surface corresponding to different levels of heat flux. A detailed explanation of the experimental observation can be found in reference [Liao and Zhao, 1999].

Heat transfer from the heater to the working fluid is a combination of conduction, convection, boiling, and evaporation. Since the wick provides additional nucleation sites,

the wall superheat required for incipient boiling is lower than that from a smooth surface. The heat transfer in the wick is much more complicated then the boiling heat transfer for plain surfaces. Therefore, most of the related studies are based on experimental data.
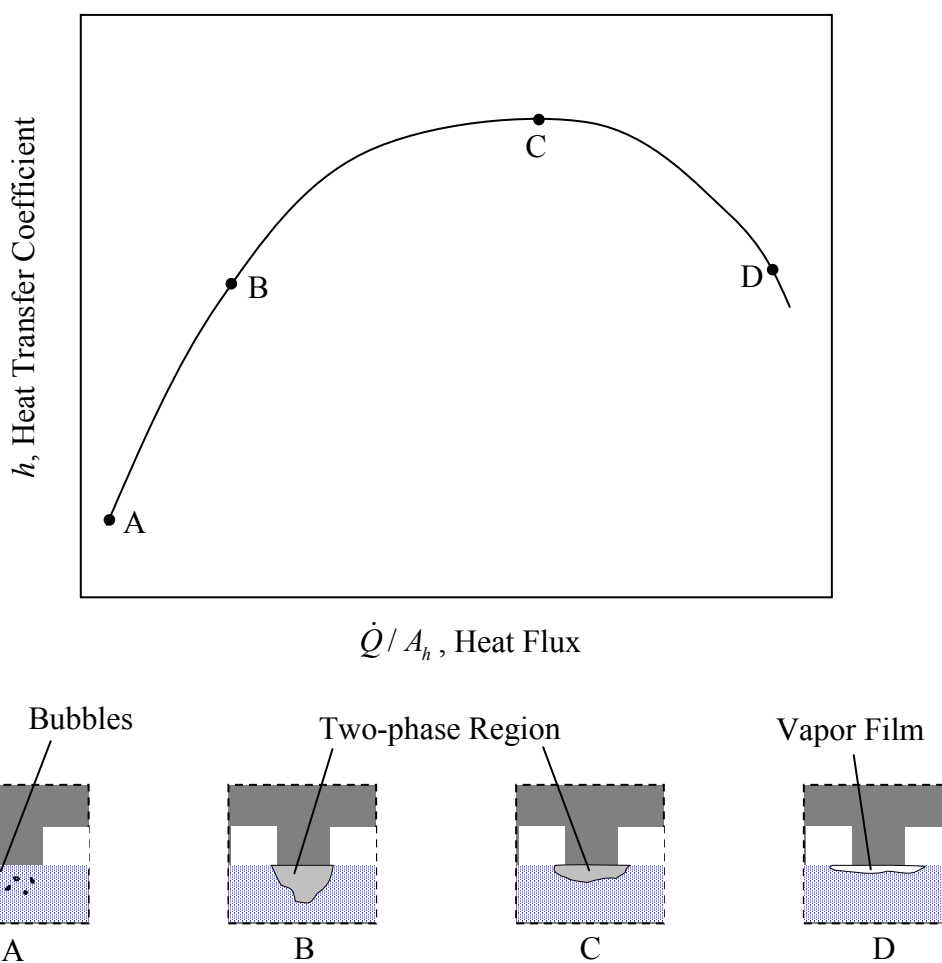
Fig. 5.7: Heat transfer coefficient vs. applied heat flux, and drawings of observations corresponding to different values of heat flux. (Adapted from Liao and Zhao, 1999)

From the current experimental measurements, it is impossible to directly measure the wall temperature and liquid saturation temperature at the heating surface. It is assumed that the temperature change in the evaporator body (thin aluminum wall) is negligible. Therefore, the temperature measured at the outer surface of the evaporator is

assumed to be equal to the wall temperature at the heating surface. Since the system is operating at a high pressure condition (around 10 atm), the change of the saturation temperature along the LHP due to pressure drop is negligible (less than 0.1 K) when the heat load is equal to 1000 W. Thus, the saturation temperature in the whole system can be assumed constant. The temperature measured at the outer surface of the reservoir (always at a saturated condition) is close to the saturation temperature at the heating surface. Using these assumptions, the amount of wall superheat, $(T_{EVAP} - T_{RES})$, can be calculated from the experimental data. The heat transfer from the evaporator body to the working fluid can then be written as:

$$\frac{\dot{Q}_{APP}}{A_h} = h(T_{EVAP} - T_{RES}) \qquad (5.83)$$

Fig. 5.8 shows the experimental results of the heat transfer coefficient as a function of heat flux when the LHP is operated at zero elevation. The heat transfer coefficient increases with the increase of applied heat flux. Compared to Fig. 5.7, it is clear that for the range of applied heat load, the heat transfer coefficient has not yet achieved its maximum value. Due to the constraint of the maximum heat load, the condition where a vapor film resides underneath the heating surface cannot be achieved with the present experimental setup.
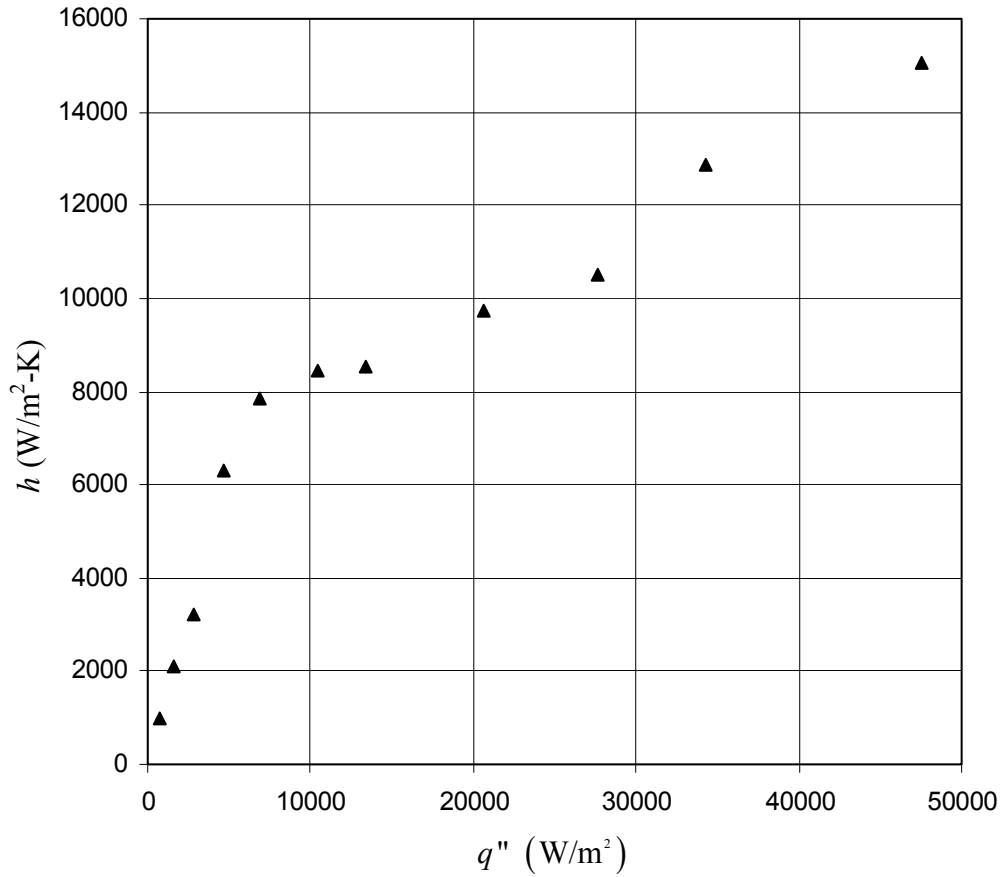
Fig. 5.8: Experimental data of heat transfer coefficient as a function of heat flux.

Another chart showing the relation between the wall superheat and heat flux is presented in Fig. 5.9. This chart is commonly used for nucleate boiling heat transfer studies. There are five data sets at different elevations shown in Fig. 5.9, including 4-inch and 2-inch adverse elevation, zero elevation, and 1-inch and 3-inch positive elevation. A 4th-order polynomial trend line is made to fit the experimental data:

$$q'' = \sum_{n=0}^{4} C_n \left(T_{EVAP} - T_{RES} \right)^n \tag{5.84}$$

where C_0 = -43650.42 W/m^2, C_1 = 102311.69 W/m^2-K, C_2 = -73757.95 W/m^2-K^2, C_3 = 23698.18 W/m^2-K^3, C_4 = -2513.69 W/m^2-K^4. This equation is used in the steady-state

code to calculate the amount of wall superheat with corresponding heat flux. In Fig. 5.9, the experimental data agree with the trend line within 10% when the heat flux is higher than 2×10^4 W/m^2. When the heat flux is lower than 2×10^4 W/m^2, greater differences in superheat can be found between various elevations, and the experimental data agree with the trend line within 30%. In this study, the effect of elevation on heating surface heat transfer coefficient was neglected in the steady-state code because of the small amount of scatter in the data (less than 1 $^{\circ}$C). If the range of elevation of the LHP were larger, the effect of elevation would have to be accounted for in the code.
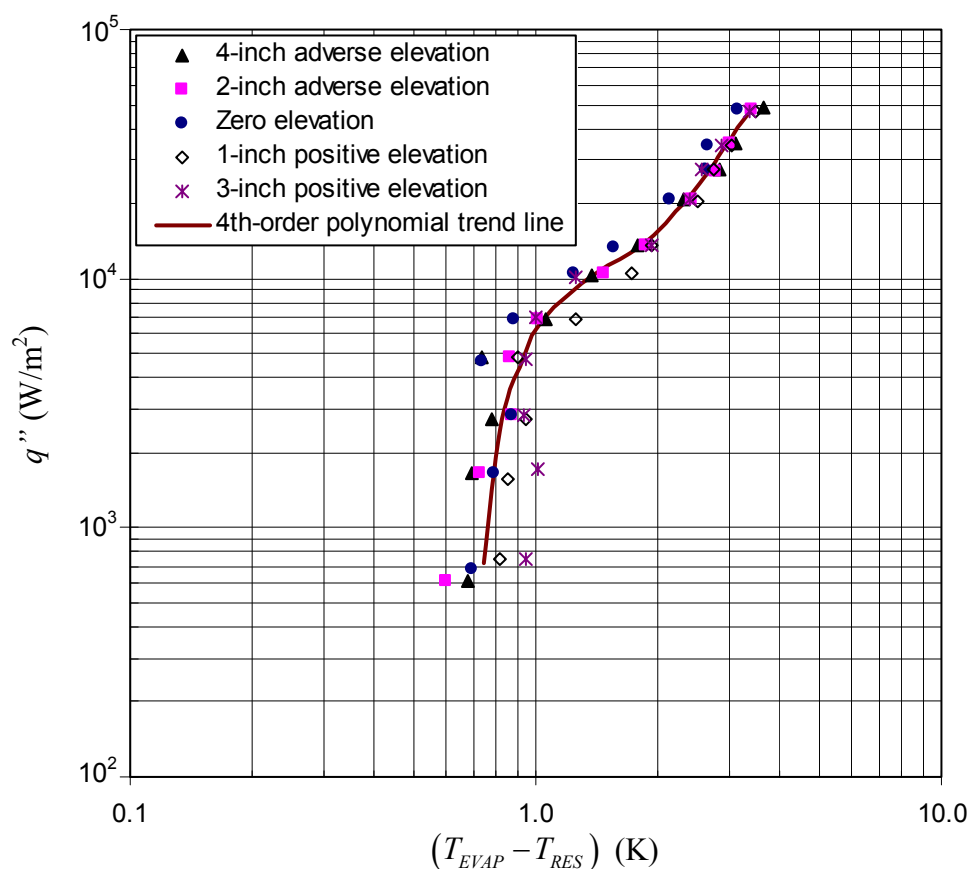
Fig. 5.9: Amount of wall superheat vs. heat flux from experimental data.

There are two reasons to calculate the amount of wall superheat, i.e., the temperature difference between the evaporator body and the reservoir: one is to obtain the axial heat leak in Eq. 5.71 and the other is to calculate the superheated exit vapor temperature in the vapor channel, TVC_{OUT}. The exit vapor temperature in the vapor channel can be calculated from:

$$TVC_{OUT} = T_{EVAP} - \left(T_{EVAP} - T_{SAT}^{O} \right) \exp \left[-\frac{\left(hA/L \right)}{\dot{m}C_{P,g}} \Delta L \right]$$

(5.85)

where A refers to the evaporator body wall area in the vapor channel.

5.5.9 Minor Losses and Tube Roughness

There are various minor losses in LHP system including sudden expansion or contraction, bends, fittings, valves, etc. To accurately predict all the minor losses is extremely difficult because the detailed configuration of the LHP is usually considered proprietary by the manufacturer. Besides, the complexity of the fluid flow condition makes it even more unpredictable. In the steady-state model, only minor loss due to bends is considered. Since there are usually many bends in the transportation lines and in the condenser, the corresponding pressure drop is substantial, especially in the vapor line and in the condenser. The pressure drop induced by minor loss is calculated by loss coefficient, K, and can be expressed as:

$$\Delta p = K \left(\frac{\rho V^2}{2} \right) = K \left(\frac{\dot{m}^2}{\rho A^2} \right)$$

(5.86)

For two-phase flow conditions, the average density defined in Eq. 4.18 is applied into Eq. 5.86.

Smooth walls are assumed in most of the flow paths in a LHP. Some LHPs (such as the one used here) are equipped with flexible hose in both the vapor line and liquid line to permit elevation changes. The flexible hose is usually made of corrugated tubes and the roughness of the tube is significant. Therefore, the effect of rough walls is considered in the steady-state model when a corrugated tube exists in a LHP. A formula given by Haaland [1983] is used to calculate the friction factor in turbulent flow with rough walls:

$$\frac{1}{f^{1/2}} \approx -1.8 \log \left[\frac{6.9}{\mathrm{Re}_d} + \left(\frac{\delta/d}{3.7} \right)^{1.11} \right] \tag{5.87}$$

where δ is the roughness height and (δ/d) is the roughness ratio.

5.5.10 Positive Elevation

When a LHP is operated at a positive elevation, it can operate in capillary-controlled mode or gravity-controlled mode. When a LHP is operating in capillary-controlled mode, the vapor channel is filled with 100% vapor, and the total mass flow rate can be calculated as:

$$\dot{m}_{TOTAL} = \dot{m}_g = \frac{\dot{Q}_{EVAP}}{\lambda} \tag{5.88}$$

When a LHP is operating in the gravity-controlled mode, the fluid flow in the vapor channel becomes two phase. The mass flow rate is then calculated as:

$$\dot{m}_{TOTAL} = \dot{m}_g + \dot{m}_L = \frac{\dot{Q}_1}{\lambda} + \dot{m}_L \qquad (5.89)$$

where $\dot{m}_L$ denotes the liquid mass flow rate forced into the vapor channel. Therefore, when the LHP is operating in the gravity-controlled mode, the steady-state code has to create an additional iteration loop for the total mass flow rate in the system. In the gravity-controlled mode, the pressure gain from the liquid head must balance with the system pressure drop when a steady-state condition is achieved. Therefore, the total system pressure drop must equal zero:

$$\Delta P_{TOTAL} = \Delta P_{V.C.} + \Delta P_{V.L.} + \Delta P_C + \Delta P_{L.L.} + \Delta P_{BAY.} + \Delta P_{WICK} + \Delta P_{GRAV.} = 0 \qquad (5.90)$$

5.6   SIMPLIFIED FLOW CHART OF THE STEADY-STATE CODE

Fig. 5.10 shows a simplified flow chart of the steady-state code. First, all the input parameters have to be read in from the input data sheet. A steady-state operating temperature (SSOT) is guessed by the code to initiate the calculations. From the guessed SSOT and ambient temperature, the heat exchange between the reservoir and the ambient, $\dot{Q}_{R-A}$, is calculated from natural convection heat transfer. The evaporator body temperature is obtained using the correlation in Eq. 5.84 obtained from the experimental data. The axial heat leak is calculated from the evaporator body temperature and SSOT by Eq. 5.71.

In the initial calculation, the LHP is assumed to be operating in the capillary-controlled mode. Therefore, the total mass flow rate equals the vapor mass flow rate in the vapor channel and is obtained from Eq. 5.88. The temperature and pressure

distribution along the loop is obtained by a series of heat transfer and pressure drop calculations. The subcooling brought back by the liquid in the liquid line is calculated from Eq. 5.18, and the radial heat leak is calculated from Eq. 5.77. The steady-state operating temperature has to be iterated until the energy balance equation in the reservoir, $\dot{Q}_{HL} = \dot{Q}_{SC} + \dot{Q}_{R-A}$, is satisfied. If the LHP is operated at adverse or zero elevation, it is always operating in the capillary-controlled mode. The steady-state condition has been achieved and the SSOT is obtained when the iteration converges.

If the LHP is operated at positive elevation, it can be operating in gravity-controlled mode or capillary-controlled mode. If the pressure drop induced by the vapor mass flow rate, $\dot{m}_g$, is less than the pressure gain from the liquid head, then the system is operating in the gravity-controlled mode. When the LHP is operating in the gravity-controlled mode, an additional iteration procedure for total mass flow rate needs to be performed. The system is considered to have achieved a steady-state condition when both the energy balance equation in the reservoir and the pressure balance of the LHP meet the closure criteria. At the end of the program, all output parameters are written to several output sheets for data analysis. A more detailed flow chart of the steady-state code is included in Appendix F.

Read in input parameters

Guess steady-state operating temperature, T_{SSOT}

Calculate evaporator body temperature, T_{EVAP}, from Eq. 5.84

Calculate mass flow rate, $\dot{m}_g$, from Eq. 5.88

Calculate $\dot{Q}_{HL,A}$ from Eq. 5.71

Calculate temperature distribution along the loop

Calculate pressure drop along the loop

Calculate $\dot{Q}_{R-A}$ by natural convection

Calculate $\dot{Q}_{SC}$ from Eq. 5.18

Calculate $\dot{Q}_{HL,R}$ from Eq. 5.77

Guess a liquid mass flow rate, $\dot{m}_L$. The total mass flow rate becomes $\dot{m}_{TOTAL} = \dot{m}_L + \dot{m}_g$

Check energy balance equation in the reservoir, $\dot{Q}_{HL} = \dot{Q}_{SC} + \dot{Q}_{R-A}$

No

No

Yes

Check if total pressure drop, $\Delta P_{TOTAL} = 0$

Gravity-controlled mode

Capillary-controlled mode

Yes

Achieve steady-state condition

Write out output parameters

Fig. 5.10: Simplified flow chart of the steady-state code.

Chapter 6

PARAMETRIC STUDY OF LOOP HEAT PIPE PERFORMANCE

6.1   STUDY OF LHP PERFORMANCE USING THE STEADY-STATE MODEL

The performance of LHPs is studied using the steady-state model developed in this study. The predicted results help not only to understand the performance of LHPs at various conditions, but also to provide details of how LHPs operate. The steady-state model is the easiest and most important tool to study LHPs. As discussed in Chapter 4, LHPs perform differently when operated at zero and adverse elevations than when operated at a positive elevation. A baseline configuration is established first, and then the performances based on the baseline configuration at zero elevation and 2-inch positive elevation are studied. All results shown in this chapter were predicted from the steady-state model.

6.1.1   Baseline Configuration

The details of the baseline configuration are selected based on the experimental test conditions and are listed as follows:

1. The detailed specifications of the LHP are the same as the test loop and are listed in Table 3.1.

2. The external thermal conductance of the condenser, $\left(h_o A_o / L\right)_S$ in Eq. 5.21, is assumed to be 10 $W/(m \cdot K)$.

3. The condenser cooling water is running at a volume flow rate of 1.0 gallon-per-minute (GPM).

4. The evaporator and the vapor line are insulated to prevent any heat exchange with the ambient.

5. The condenser, liquid line, and the reservoir are not insulated.

6. The cooling water inlet temperature, T_{SINK}, is set at 5°C and the ambient temperature, T_{AMB}, is assumed to be 19 °C.

7. Constant smooth and two-phase multiplier correlations are used for two-phase pressure drop and heat transfer calculations, respectively. The void fraction calculated by the constant smooth correlation is also used to obtain the accelerational two-phase pressure drop.

8. Vapor superheat is considered in the vapor channel heat transfer calculation.

9. Both radial and axial heat leaks are considered in the heat leak calculation.

6.1.2 Zero and Adverse Elevation

The baseline configuration is applied to the input parameters in the steady-state model. The predicted results when a LHP is operated at zero elevation were studied in detail. There are 11 different heat load conditions calculated, and the predicted results obtained from the steady-state model are listed in Table 6.1. The parameters listed in Table 6.1 include the total heat load applied to the evaporator, $\dot{Q}_{APP}$, the steady-state operating temperature of the LHP, T_{SSOT}, the fluid temperature exiting the liquid line, TL_{OUT}, the fluid temperature exiting the condenser, TC_{OUT}, the amount of total heat leak,

$\dot{Q}_{HL}$, composed of radial heat leak, $\dot{Q}_{HL,R}$, and axial heat leak, $\dot{Q}_{HL,A}$, the heat leak as a percentage of total heat load, the vapor-phase pressure drop, ΔP_{VAPOR}, the liquid-phase pressure drop, ΔP_{LIQUID}, the frictional two-phase pressure drop, $\Delta P_{2\phi,f}$, the accelerational two-phase pressure drop, $\Delta P_{2\phi,a}$, the total two-phase pressure drop, $\Delta P_{2\phi}$, the pressure drop of liquid flow through the primary wick, ΔP_{WICK}, the total system pressure drop, ΔP_{TOTAL}, and the location of the liquid-vapor interface in the condenser, L_{LVI}. The total system pressure drop, ΔP_{TOTAL}, is defined as:

$$\Delta P_{TOTAL} = \Delta P_{VAPOR} + \Delta P_{LIQUID} + \Delta P_{2\phi,f} + \Delta P_{2\phi,a} + \Delta P_{WICK} + \Delta P_{GRAV} \qquad (6.1)$$

Charts were plotted based on the experimental data in Table 6.1 to analyze the performance of the LHP. These charts include trends of loop temperatures, loop pressure drops, location of the liquid-vapor interface in the condenser, amount of heat leak, and change of vapor quality in the condenser.

Table 6.1: Predicted results by 1-D steady-state model for baseline study at zero elevation.

Parameters \ Step	1	2	3	4	5	6	7	8	9	10	11
$\dot{Q}_{APP}$ (W)	10.14	25.21	40.29	70.48	100.71	202.51	304.30	405.78	507.04	759.48	981.42
$\dot{m}$ (kg/sec)	8.42E-6	2.10E-5	3.34E-5	5.81E-5	8.27E-5	1.65E-4	2.49E-4	3.35E-4	4.24E-4	6.54E-4	8.70E-4
T_{SSOT} (^{o}C)	19.84	18.59	17.30	15.44	14.21	13.02	15.39	18.47	21.64	29.49	36.62
TL_{OUT} (^{o}C)	18.65	16.09	14.01	11.55	10.20	8.32	11.21	14.79	18.33	27.20	34.95
TC_{OUT} (^{o}C)	5.62	5.62	5.62	5.62	5.62	5.77	10.14	14.43	18.30	27.60	35.63
$\dot{Q}_{HL}$ (W)	0.14	0.21	0.29	0.48	0.71	2.51	4.30	5.78	7.04	9.48	11.42
$\dot{Q}_{HL,A}$ (W)	0.11	0.12	0.13	0.15	0.17	0.25	0.32	0.38	0.41	0.48	0.52
$\dot{Q}_{HL,R}$ (W)	0.03	0.09	0.16	0.33	0.54	2.26	3.98	5.40	6.63	9.00	10.90
$\dot{Q}_{HL} / \dot{Q}_{APP}$ (%)	1.41	0.83	0.71	0.67	0.71	1.24	1.41	1.42	1.39	1.25	1.16
ΔP_{VAPOR} (Pa)	3.8	9.8	16.3	30.6	45.0	133.9	222.2	312.7	405.0	639.0	998.9
ΔP_{LIQUID} (Pa)	1.1	2.7	4.1	6.4	8.0	7.3	7.8	9.7	11.7	16.5	20.5
$\Delta P_{2\phi,f}$ (Pa)	0.1	0.8	2.2	8.7	21.9	161.0	340.7	523.0	713.9	1217.3	1646.9
$\Delta P_{2\phi,a}$ (Pa)	0.0	-0.3	-0.7	-2.2	-4.5	-18.7	-39.3	-64.5	-93.1	-174.3	-249.9
$\Delta P_{2\phi}$ (Pa)	0.1	0.5	1.6	6.5	17.4	142.3	301.4	458.5	620.8	1043.0	1397.0
ΔP_{WICK} (Pa)	17.3	43.4	69.9	123.3	177.2	356.3	528.7	695.5	858.2	1251.5	1585.0
ΔP_{GRAV} (Pa)	0.0	0.0	0.0	0.0	0.0	0.0	0.0	0.0	0.0	0.0	0.0
ΔP_{TOTAL} (Pa)	22.3	56.5	91.9	166.9	247.5	639.9	1060.1	1476.4	1895.7	2950.0	4001.4
L_{LVI} (m)	0.10	0.28	0.52	1.10	1.71	3.90	4.42	4.49	4.53	4.58	4.61

Fig. 6.1 shows the steady-state operating temperature and fluid temperatures exiting the liquid line and the condenser as functions of heat load. The trend of the steady-state operating temperature agrees very well with the U-shaped trend explained in Section 4.1.2. The minimum steady-state operating temperature occurs when the heat load is around 200 W. The transition heat load between the variable-conductance and fixed-conductance modes is a little higher than 200 W (~230 W). The fluid temperature exiting the liquid line has the same trend as the steady-state operating temperature. When the LHP is operating in the variable-conductance mode, the fluid temperature exiting the condenser is close to the sink temperature. The fluid temperature exiting the condenser increases with heat load when the LHP is operating in the fixed-conductance mode. Since the ambient temperature equals 19 $^{\rm o}$C, the fluid in the liquid line gains heat from the ambient if the temperature exiting the condenser is lower than 19 $^{\rm o}$C ($\dot{Q}_{APP} \leq 520 {\rm W}$). The fluid temperature change in the liquid line depends strongly on the mass flow rate. When the heat load is low and the mass flow rate in the LHP is small, the fluid temperature difference between the inlet and the exit of the liquid line is significant. In contrast, when the heat load is high, the fluid temperature difference between the inlet and the exit of the liquid line is barely noticeable.

Fig. 6.2 is a chart showing the ratio of component pressure drops over total pressure drop as functions of heat load. This chart classifies pressure drops according to the fluid flow conditions. The total pressure drop is divided into five different components: vapor-phase, liquid-phase, frictional and accelerational two-phase pressure drops, and the pressure drop for the liquid flow through the primary wick.
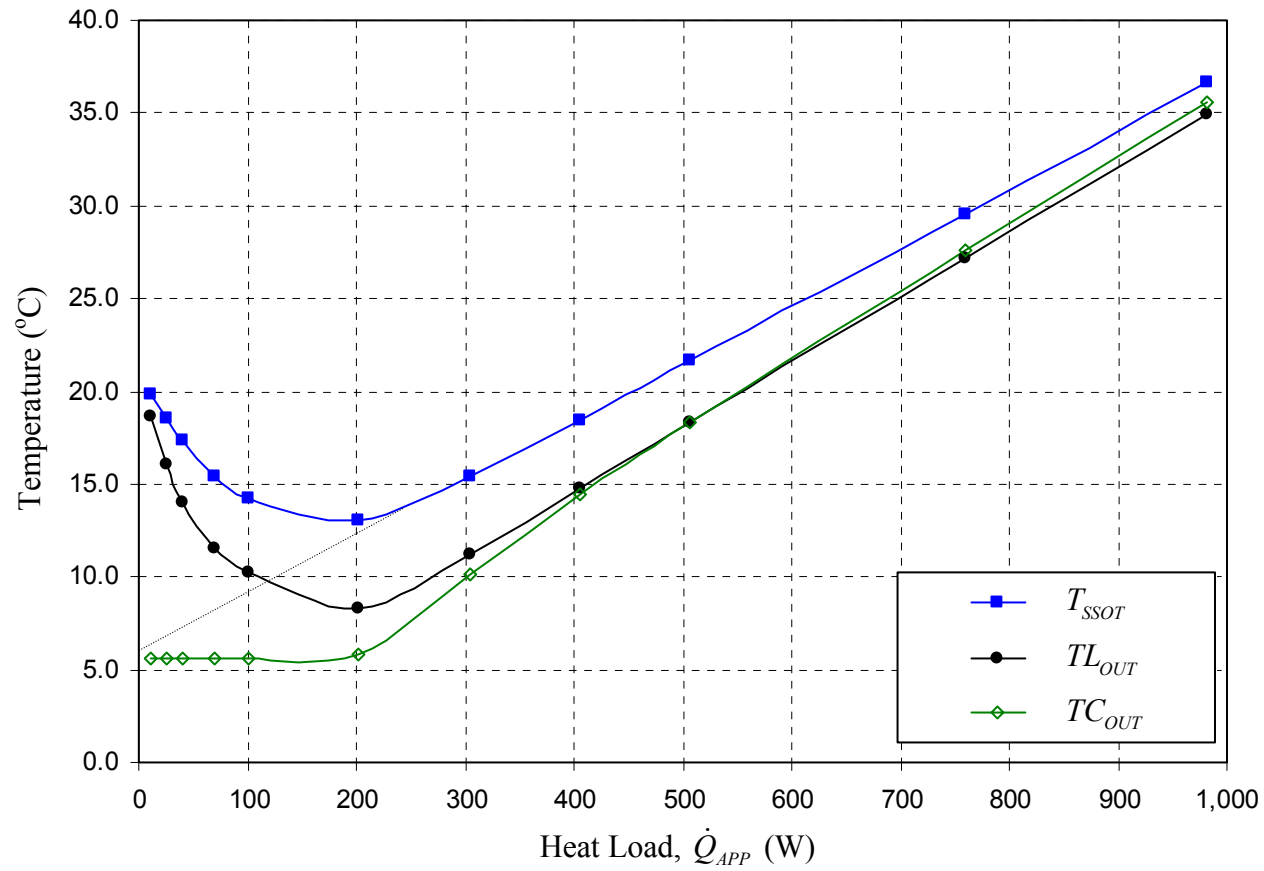
Fig. 6.1: Predicted trends of steady-state operating temperature and fluid temperatures exiting the liquid line and the condenser for the baseline configuration. ($T_{SINK} = 5\ ^{\circ}C$, $T_{AMB} = 19\ ^{\circ}C$, and zero elevation)

In Fig. 6.2 and Fig. 6.3, the frictional two-phase pressure drop is calculated by the constant smooth correlation defined in Section 5.5.4. Other two-phase pressure drop correlations predict different results. Among the available two-phase pressure drop correlations, the constant smooth correlation usually predicts the smallest two-phase pressure drop.

The accelerational two-phase pressure drop is negative because the fluid decelerates when condensing and the pressure increases. The accelerational two-phase pressure drop is typically small compared to the frictional two-phase pressure drop.

Fig. 6.3 shows the magnitudes of the component pressure drops as functions of heat load. The pressure drop of the liquid flow across the primary wick increases almost linearly with increasing heat load. The frictional pressure drop has two different trends: one when the flow is laminar, and the other when it is turbulent. The two different trends can be easily observed in Fig. 6.3. For example, the liquid-phase is always under laminar flow conditions, the two-phase flow becomes turbulent when the heat load is between 100 and 200 W, and the vapor-phase turns turbulent when the heat load is between 750 and 980 W. For this baseline configuration at zero elevation, vapor flowing in the vapor channel becomes turbulent at a much higher heat load than vapor flowing in the vapor line or the condenser because the hydraulic diameter of the vapor channel is much smaller then that of the vapor line or the condenser.

The analysis of the system pressure drop is very helpful for understanding the fundamental operating characteristics of LHPs. The amount of the system pressure drop has direct impact on radial heat leak and the amount of heat leak determines the steady-state operating temperature of the loop.
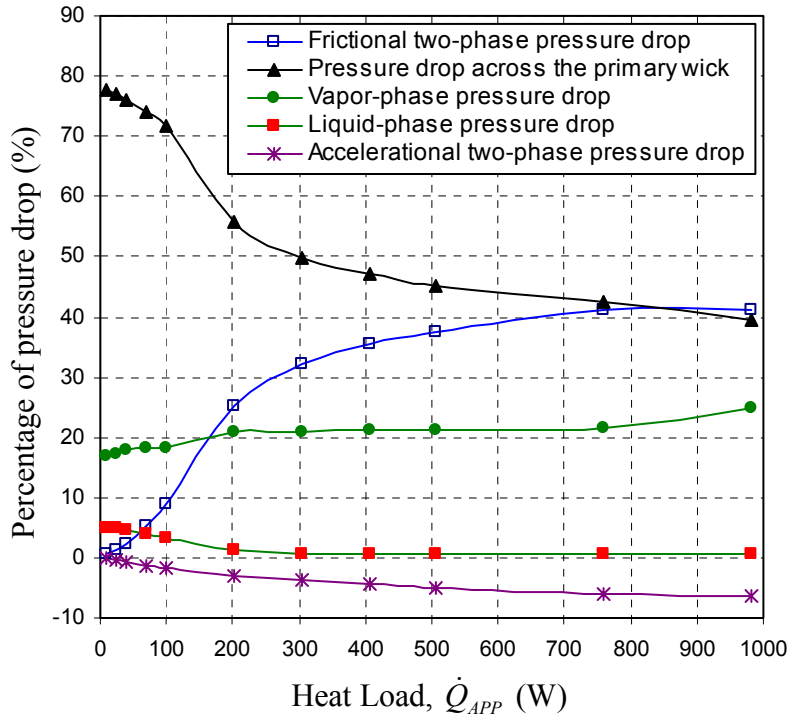
Fig. 6.2: Ratios of component pressure drops to total pressure drop as functions of heat load. ($T_{SINK} = 5\ ^{\circ}\text{C}$, $T_{AMB} = 19\ ^{\circ}\text{C}$, zero elevation, and constant smooth correlation)
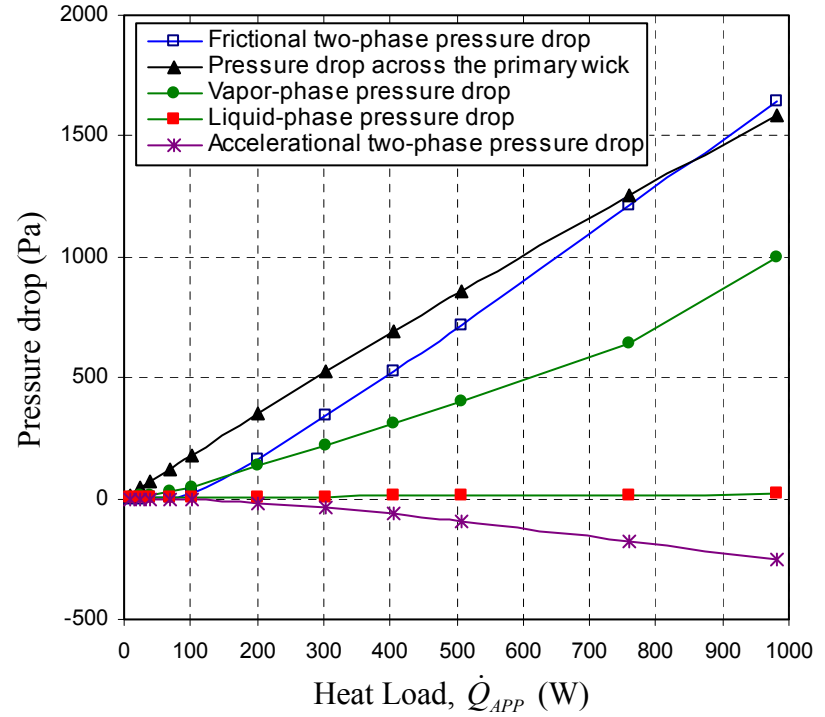
Fig. 6.3: Component pressure drops as functions of heat load. ($T_{SINK} = 5\ ^{\circ}\text{C}$, $T_{AMB} = 19\ ^{\circ}\text{C}$, zero elevation, and constant smooth correlation)

The total pressure drop in the loop is dominated by the pressure drop induced by liquid flow through the primary wick, especially when the heat load is lower than 200 W. This is typical when the primary wick is composed of very fine porous material and the permeability is extremely small. The liquid-phase pressure drop is almost negligible because the liquid velocity is much smaller than that of the vapor-phase.

Fig. 6.4 is a plot of the location of the liquid-vapor interface in the condenser and the mass flow rate as functions of heat load.
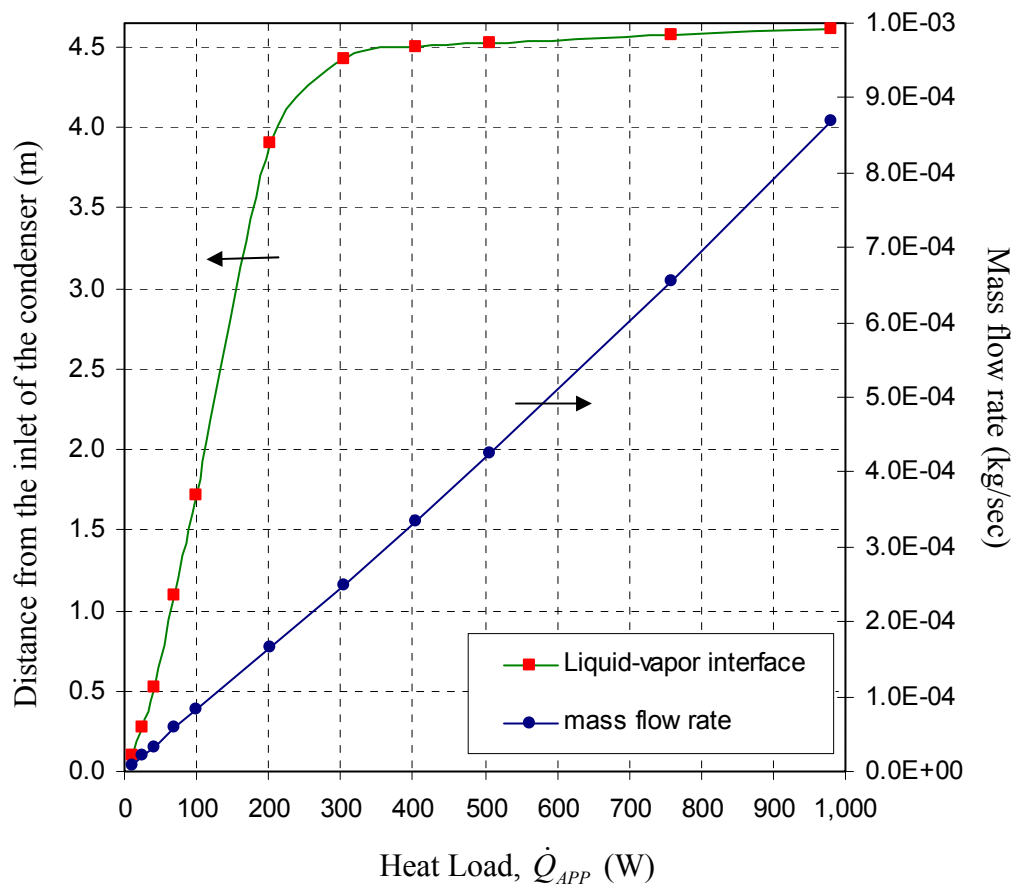
Fig. 6.4: The location of the liquid-vapor interface in the condenser and the mass flow rate as functions of heat load. ($T_{SINK} = 5 \; ^{\circ}C$, $T_{AMB} = 19 \; ^{\circ}C$, and zero elevation)

The mass flow rate increases almost linearly with increasing applied heat load. The total length of the condenser tube is 4.65 m (183 inches). When the heat load is lower than 200 W, the location of the liquid-vapor interface moves rapidly toward the end of the condenser with increasing heat load. Under these conditions, the LHP is operating in the variable-conductance mode, and the condenser is not fully utilized. When the heat load is greater than 300 W, the interface resides almost at the end of the condenser and moves toward the exit of the condenser slowly with increasing heat load. Now the LHP is operating in the fixed-conductance mode and the whole condenser is used to condense the vapor and to provide the required subcooling to the liquid. The transition heat load between the variable-conductance and fixed-conductance modes can be easily observed in Fig. 6.4, and is between 200 and 300 W. This analysis agrees with the observation from the trend of the steady-state operating temperature in Fig. 6.1.

Fig. 6.5 shows the amount of total heat leak, and the ratios of axial heat leak and radial heat leak to total heat leak as functions of heat load. Generally, radial heat leak dominates axial heat leak, especially when the heat load is high. However, when the heat load is extremely small (< 50 W), the total heat leak is dominated by axial heat leak. Total heat leak, axial heat leak, and radial heat leak are normalized by total heat load, and plotted in Fig. 6.6. The trend of the normalized total heat leak first follows that of the normalized axial heat leak when heat load is small (< 50 W), and then follows that of the normalized radial heat leak when the heat load is high (> 100 W). Axial heat leak, Eq. 5.71, follows the trend of the temperature difference between the evaporator body and the reservoir as a function of heat load (see Fig. 5.9). The radial heat leak, Eq. 5.78, is determined by the temperature across the primary wick, which is calculated by the

pressure difference across the wick times $(dT/dP)_{SAT}$. The pressure difference across the wick increases almost linearly with heat load. The temperature difference divided by pressure difference along the saturation line, $(dT/dP)_{SAT}$, is a property of the working fluid. For ammonia, $(dT/dP)_{SAT}$ decreases with increasing heat load (see Fig. B.2 for detail).
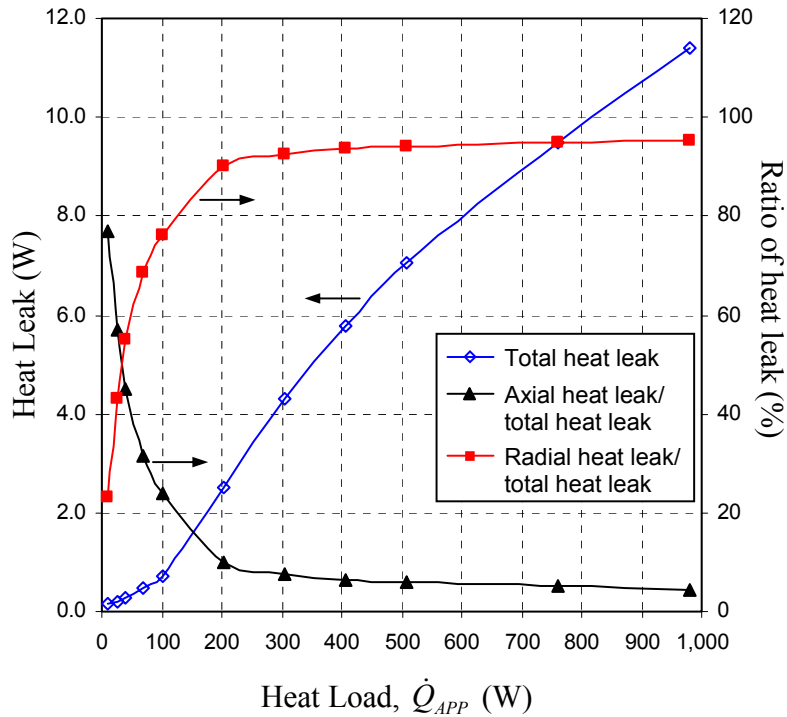
Fig. 6.5: Total heat leak and the ratios of axial heat leak and radial heat leak as functions of heat load. ($T_{SINK} = 5$ ^{o}C, $T_{AMB} = 19$ ^{o}C, and zero elevation)
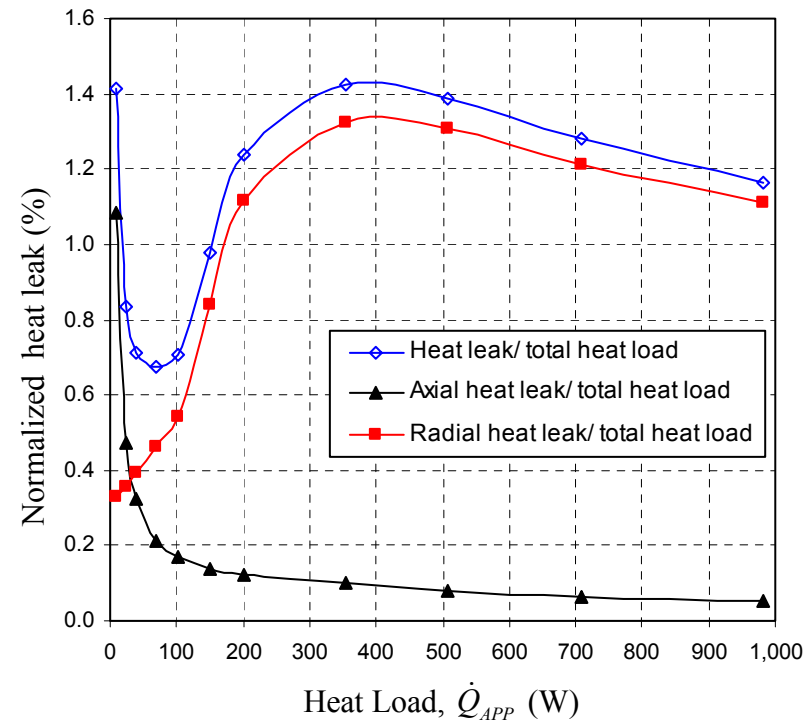
Fig. 6.6: Normalized total heat leak, axial heat leak, and radial heat leak as functions of heat load. ($T_{SINK} = 5$ ^{o}C, $T_{AMB} = 19$ ^{o}C, and zero elevation)

Besides studying various trends of LHP operating characteristics as functions of heat load, the steady-state model can also be used to study the changes of temperature, pressure, and vapor quality along the loop at a specific heat load. Fig. 6.7 shows the change of temperature and vapor quality of fluid flow when a LHP is operating at the baseline configuration and zero elevation with a heat load of 100.7 W. The x-axis in Fig. 6.7 represents the distance that the fluid travels down the loop from the high pressure side in the vapor channel. After the fluid leaves the vapor channel (V.C.), the fluid flows through the vapor line (V.L.), condenser, liquid line (L.L.), bayonet, evaporator core (E.C.), and the primary wick to return to the starting point and completes a cycle. Since the primary wick is so thin (9.5×10^{-3} m) compared to the whole length of the loop (8.8 m), it is not included on the chart. However, the conditions at the outer surface and inner surface of the primary wick can be referred to as the saturated conditions in the vapor channel and in the reservoir, respectively. To study the change of the vapor quality in detail, the condenser is divided into 12 sections. Temperature, pressure, and vapor quality are studied at the inlet and exit of each section.
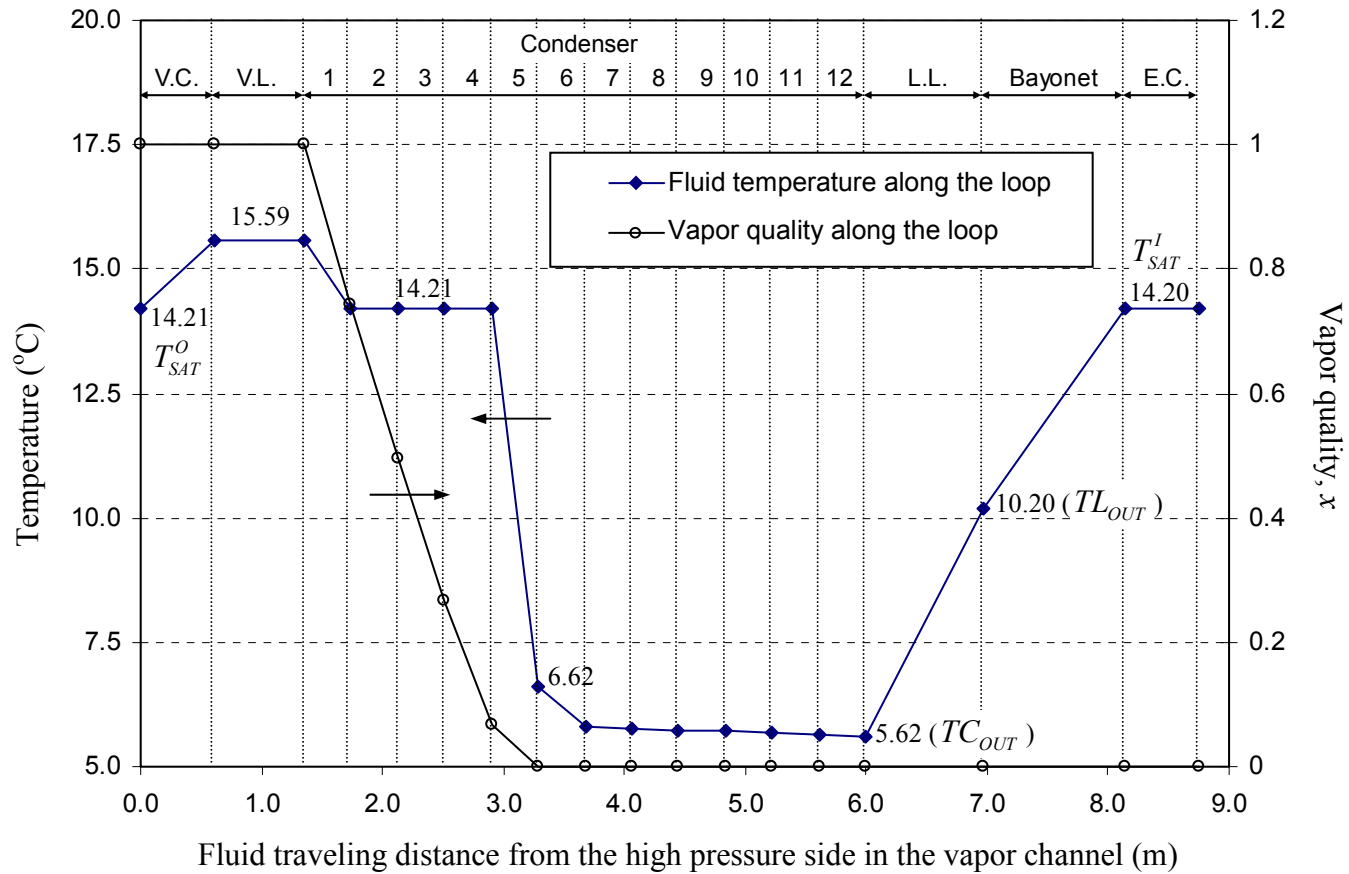
Fig. 6.7: Temperature and vapor quality of the fluid flow along the loop starting from the high pressure side in the vapor channel. ($T_{SINK} = 5 \; ^{\circ}C$, $T_{AMB} = 19 \; ^{\circ}C$, zero elevation, and $\dot{Q}_{APP} = 100.71$ W)

For the predicted results presented in Fig. 6.7, the saturation temperature in the vapor channel is equal to 14.21 $^{\circ}$C. This temperature is denoted as T_{SAT}^{O}, which means the saturation temperature at the outer surface of the primary wick. As the saturated vapor flows through the vapor channel, it is superheated by the walls and reaches a superheated temperature 15.59 $^{\circ}$C when exiting the vapor channel. It is assumed that the vapor line is perfectly insulated. Thus, no temperature change occurs in the vapor line and the vapor remains superheated.

In the first section of the condenser, the superheated vapor quickly loses its superheat and returns to its saturation temperature, 14.21 $^{\circ}$C. From the plots of vapor quality and fluid temperature in Fig. 6.7, it is seen that the saturated vapor is fully condensed back to liquid in condenser section 5. The saturated liquid is then further subcooled and the liquid temperature exiting condenser section 5 is equal to 6.62 $^{\circ}$C. After condenser section 5, the condenser is used for subcooling rather than condensing. The subcooled liquid enters the liquid line at temperature 5.62 $^{\circ}$C. In the liquid line, the liquid gains heat from the ambient by natural convection and enters the bayonet inside the reservoir at a higher subcooled liquid temperature of 10.20 $^{\circ}$C. In the bayonet, the liquid keeps gaining heat from the fluid in the reservoir and the evaporator core, and exits the bayonet into the evaporator core at a temperature of 14.21 $^{\circ}$C.

In the evaporator core and reservoir, the fluid is at another saturated condition corresponding to the local pressure. The saturation temperature in the reservoir is then equal to 14.20 $^{\circ}$C. This is denoted as T_{SAT}^{I}, which means the saturation temperature at the inner surface of the primary wick. Since the pressure difference between the vapor

channel and the reservoir is less than 100 Pa for this case, the difference between the saturation temperatures at the outer and inner surface of the primary wick is less than 0.01 $^{\circ}$C. The fluid in the evaporator core flows though the primary wick and is vaporized at the outer surface to complete the cycle.

To summarize the operating characteristics of the condition predicted in Fig. 6.7, the following observations can be drawn:

1. The steady-state operating temperature is 14.21 $^{\circ}$C.

2. The temperature of the superheated vapor exiting the vapor channel is 15.59 $^{\circ}$C, which is 1.38 $^{\circ}$C superheated.

3. The location of the liquid-vapor interface is in condenser section 5, which is near the middle of the condenser.

4. The difference between the subcooled liquid temperature at the end of liquid line and the saturation temperature is 4.0 $^{\circ}$C. This is an important index for the amount of subcooling brought back to the reservoir, $\dot{Q}_{SC}$.

5. The LHP is operating in the variable-conductance mode because the condenser is not fully utilized for condensing.

6. The LHP is operating in the capillary-controlled mode because the fluid exiting the vapor channel is 100% vapor (vapor quality=1.0).

6.1.3   Positive Elevation

The baseline configuration is applied to the input parameters in the steady-state model with 2 inches positive elevation. There are 11 different heat load conditions calculated, and the predicted results obtained from the steady-state model are listed in

Table 6.2. The parameters listed in Table 6.2 include the total heat load applied to the evaporator, $\dot{Q}_{APP}$, the mass flow rate in the system, $\dot{m}$, the vapor quality exiting the vapor channel, $x_{VC,OUT}$, the steady-state operating temperature of the LHP, T_{SSOT}, the fluid temperature exiting the liquid line, TL_{OUT}, the fluid temperature exiting the condenser, TC_{OUT}, the amount of total heat leak, $\dot{Q}_{HL}$, composed of radial heat leak, $\dot{Q}_{HL,R}$, and axial heat leak, $\dot{Q}_{HL,A}$, the heat leak as a percentage of total heat load, the vapor-phase pressure drop, ΔP_{VAPOR}, the liquid-phase pressure drop, ΔP_{LIQUID}, the frictional two-phase pressure drop, $\Delta P_{2\phi,f}$, the accelerational two-phase pressure drop, $\Delta P_{2\phi,a}$, the total two-phase pressure drop, $\Delta P_{2\phi}$, the pressure drop of liquid flow through the primary wick, ΔP_{WICK}, the total system pressure drop, ΔP_{TOTAL}, and the location of liquid-vapor interface in the condenser, L_{LVI}. The total system pressure drop, ΔP_{TOTAL}, is defined in Eq. 6.1. If the LHP is operating in the gravity-controlled mode (like case 1 through 5 in Table 6.2), the total pressure drop is zero.

As in the previous section, various charts are plotted based on the predicted results in Table 6.2 to analyze the performance of the LHP, including trends of loop temperatures, loop pressure drops, location of the liquid-vapor interface in the condenser, heat leaks, and change of vapor quality in the condenser.

Table 6.2: Predicted results by 1-D steady-state model for baseline study at 2-inch positive elevation.

Parameters \ Step	1	2	3	4	5	6	7	8	9	10	11
$\dot{Q}_{APP}$ (W)	10.11	25.12	40.13	70.15	100.17	150.21	200.28	352.95	505.19	707.51	980.18
$\dot{m}$ (kg/sec)	1.01E-4	1.06E-4	1.08E-4	1.07E-4	1.04E-4	1.23E-4	1.64E-4	2.92E-4	4.24E-4	6.07E-4	8.70E-4
T_{SSOT} (°C)	0.08	0.19	0.31	0.54	0.79	1.0	1.0	1.0	1.0	1.0	1.0
TL_{OUT} (°C)	12.42	12.22	12.19	12.25	12.39	11.77	12.05	16.71	21.50	27.81	36.54
TC_{OUT} (°C)	9.53	9.36	9.33	9.35	9.45	8.95	9.94	14.31	19.09	25.86	35.16
$\dot{Q}_{HL}$ (W)	5.62	5.62	5.62	5.62	5.62	5.63	7.87	13.84	19.09	26.20	35.84
$\dot{Q}_{HL,A}$ (W)	0.11	0.12	0.13	0.15	0.17	0.21	0.28	2.95	5.19	7.51	10.18
$\dot{Q}_{HL,R}$ (W)	0.11	0.12	0.13	0.15	0.17	0.21	0.25	0.35	0.41	0.47	0.52
$\dot{Q}_{HL}/\dot{Q}_{APP}$ (%)	0.00	0.00	0.00	0.00	0.00	0.00	0.03	2.60	4.78	7.05	9.66
ΔP_{VAPOR} (Pa)	1.10	0.48	0.33	0.21	0.17	0.14	0.14	0.84	1.03	1.06	1.04
ΔP_{LIQUID} (Pa)	0.0	0.0	0.0	0.0	0.0	94.4	138.3	268.7	406.6	593.9	1000.7
$\Delta P_{2\phi,f}$ (Pa)	13.9	14.3	14.0	12.4	9.9	6.6	5.1	8.2	11.3	15.2	20.2
$\Delta P_{2\phi,a}$ (Pa)	50.7	54.7	57.3	65.5	79.9	100.6	208.8	452.9	722.1	1139.6	1653.1
$\Delta P_{2\phi}$ (Pa)	0.0	-0.3	-0.7	-2.2	-4.5	-18.7	-39.3	-64.5	-93.1	-174.3	-249.9
ΔP_{WICK} (Pa)	50.6	54.4	56.6	63.3	75.4	81.9	169.6	388.4	628.9	965.2	1403.2
ΔP_{GRAV} (Pa)	219.5	231.7	234.2	232.5	225.4	268.8	358.0	613.2	858.6	1174.6	1585.4
ΔP_{TOTAL} (Pa)	-284.0	-300.5	-304.8	-308.2	-310.7	-310.7	-309.6	-305.6	-301.5	-295.6	-287.0
L_{LVI} (m)	0.0	0.0	0.0	0.0	0.0	141.1	361.4	972.9	1604.0	2453.3	3722.5
$\dot{Q}_{APP}$ (W)	0.02	0.13	0.31	0.90	1.75	3.52	4.45	4.54	4.56	4.59	4.62

Fig. 6.8 shows the steady-state operating temperature and the fluid temperatures exiting the liquid line and the condenser as functions of heat load. The trend of the steady-state operating temperature agrees very well with the trend proposed at positive elevation in Section 4.2.3. The transition heat load between the variable-conductance and fixed-conductance modes is around 200 W. The transition heat load between the gravity-controlled and capillary-controlled modes is between 100 and 150 W. The trend of the fluid temperature exiting the liquid line is similar to that of the steady-state operating temperature. The trend of the fluid temperature exiting the condenser is the same as that in adverse or zero elevation, and is explained in the previous section. Since the ambient temperature equals 19 ^{o}C, the fluid in the liquid line gains heat from the ambient if the temperature exiting the condenser is lower than 19 ^{o}C ($\dot{Q}_{APP} \leq 520$ W). The change in fluid temperature in the liquid line depends strongly on the mass flow rate. When the heat load is low (≤ 100 W), the LHP is operating in the gravity-controlled mode and the mass flow rate of the system does not change much. Therefore the temperature difference between the inlet and the exit of the liquid line is almost constant.

Fig. 6.9 is a chart showing the ratio of component pressure drops over total pressure drop as functions of heat load. The total pressure drop is divided into six components: vapor-phase, liquid-phase, frictional and accelerational two-phase pressure drops, the pressure drop for the liquid flow through the primary wick, and the gravitational head.
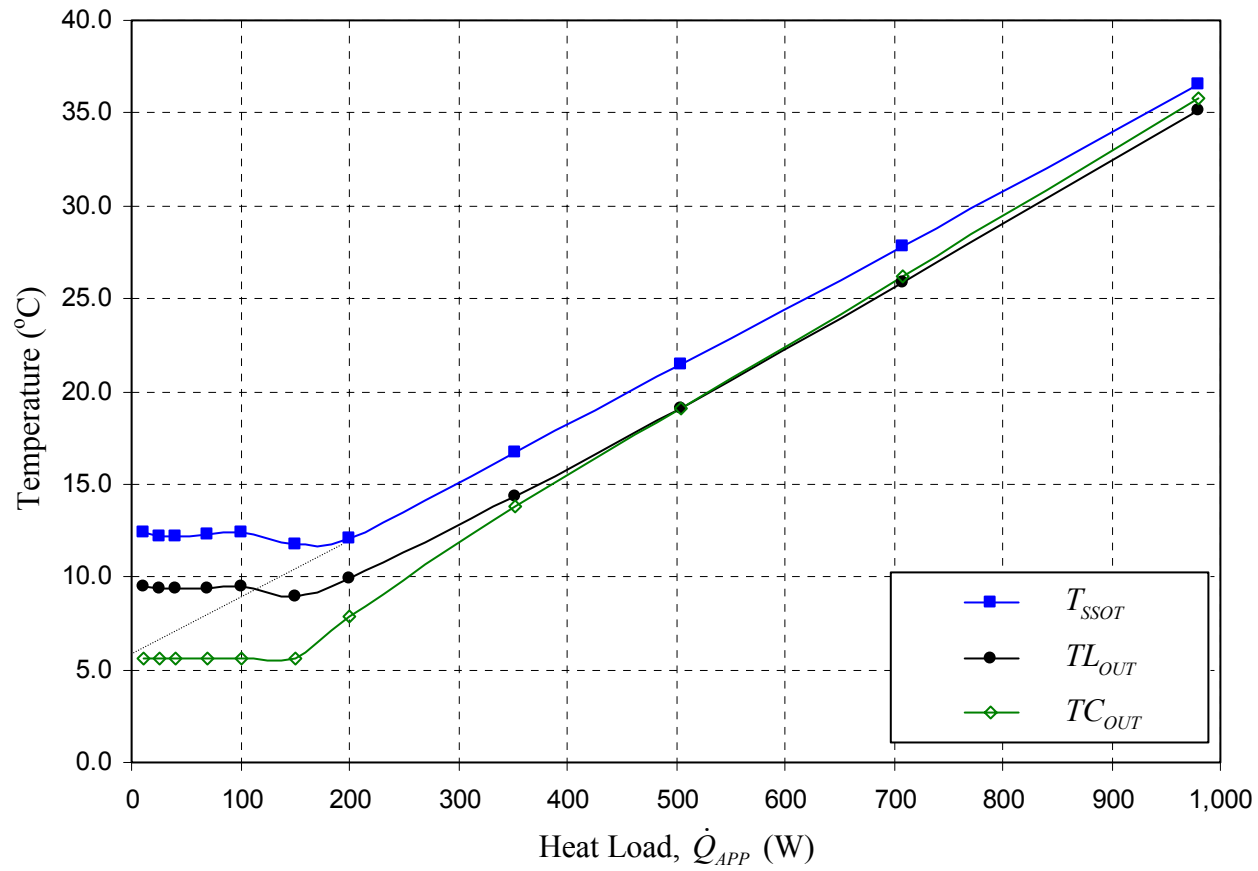
Fig. 6.8: Predicted trends of steady-state operating temperature and fluid temperatures exiting the liquid line and the condenser for the baseline configuration. ($T_{SINK} = 5$ ^{o}C, $T_{AMB} = 19$ ^{o}C, and 2-inch positive elevation)
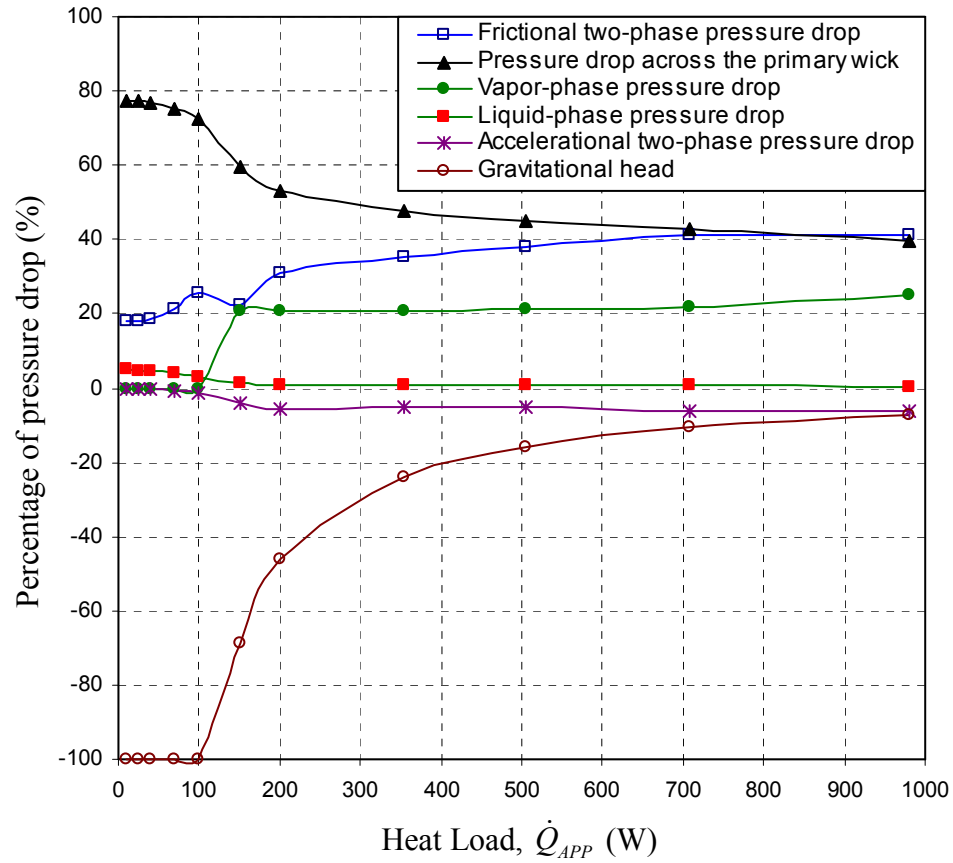
Fig. 6.9: Comparisons of pressure drop components as functions of heat load. ($T_{SINK} = 5$ ^{o}C , $T_{AMB} = 19$ ^{o}C , 2-inch positive elevation, and constant smooth correlation)

Because the LHP is operated at positive elevation, the system gains pressure due to the gravitational head. The pressure ratios in Fig. 6.9 are then defined by the individual pressure drop divided by the total pressure drop minus the gravitational head. For example, the frictional two-phase pressure drop ratio is calculated as:

$$\text{Ratio of two-phase pressure drop} \equiv \frac{\Delta P_{2\phi,f}}{\left(\Delta P_{TOTAL} - \Delta P_{GRAV}\right)} \tag{6.2}$$

When the LHP is operating in the gravity-controlled mode ($\dot{Q}_{APP} \leq 100$ W in Fig. 6.9), two observations can be made from Fig. 6.9: the gravitational head provides all the required pressure drop in the system, and the vapor-phase pressure drop is equal to zero, because there is no pure vapor flow anywhere in the system. When the LHP is operating in the capillary-controlled mode ($\dot{Q}_{APP} \geq 150$ W in Fig. 6.9), evaporation across the menisci at the outer surface of the primary wick takes place and provides the additional pressure gain required in the system. The overall behavior is then similar to that in zero and adverse elevation, as explained in the previous section.

Fig. 6.10 shows the magnitudes of component pressure drops as functions of heat load. Two different trends can be observed in the chart, one is when the LHP is operating in the gravity-controlled mode ($\dot{Q}_{APP} \leq 100$ W in Fig. 6.10) and the other is when the LHP is operating in the capillary-controlled mode ($\dot{Q}_{APP} \geq 150$ W in Fig. 6.10). When the LHP is operating in the gravity-controlled mode, the mass flow rate does not change much as the heat load changes (see Fig. 6.11). Therefore, the magnitudes of the component pressure drops are nearly constant. When the LHP is operating in the capillary-controlled mode, the mass flow rate increases almost linearly as the heat load increases (see Fig. 6.11). Thus, the component pressure drops have similar trends as that of the mass flow rate in the capillary-controlled mode. As in the zero elevation case, the pressure drop induced by liquid flow through the primary wick dominates the total pressure drop when the heat load is low.
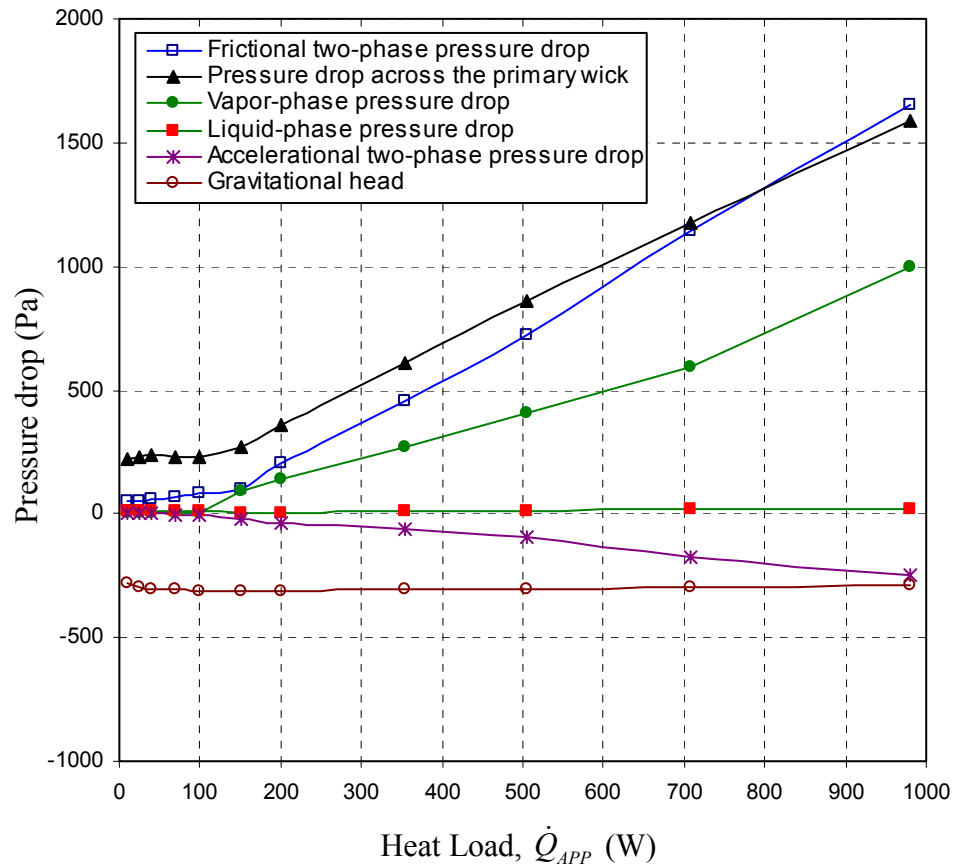
Fig. 6.10: Component pressure drops as functions of heat load. ($T_{SINK} = 5$ °C , $T_{AMB} = 19$ °C , 2-inch positive elevation, and constant smooth correlation)

The location of the liquid-vapor interface in the condenser and the mass flow rate are plotted as functions of heat load in Fig. 6.11. The mass flow rate increases almost linearly with increasing applied heat load when the LHP is operating in the capillary-controlled mode ($\dot{Q}_{APP} \geq 150$ W). When the LHP is operating in the gravity-controlled mode ($\dot{Q}_{APP} \leq 100$ W), the mass flow rate remains at around 1.0×10^{-4} kg/sec. The total length of the condenser tube is 4.65 m (183 inches). From the location of the liquid-vapor interface, the transition heat load between the variable-conductance and fixed-

conductance modes can be easily identified to be around 200 W. This analysis agrees with observations from the trend shown in Fig. 6.8 for the steady-state operating temperature.
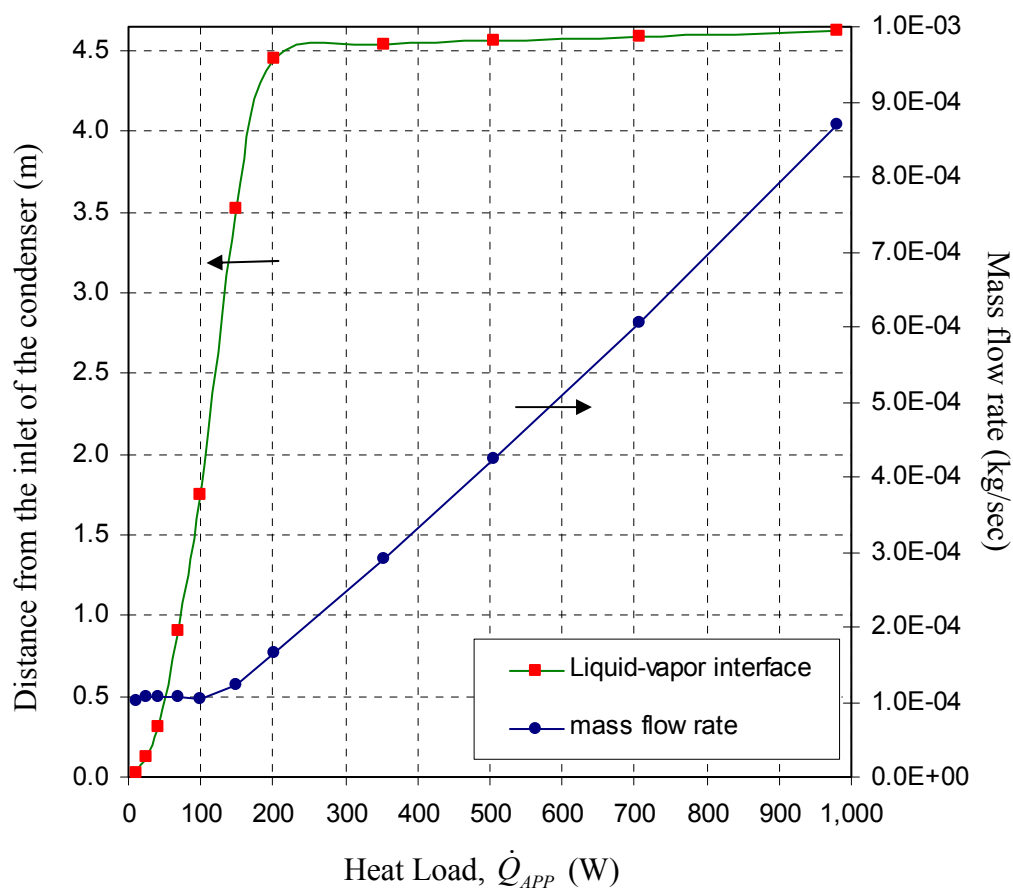
Fig. 6.11: The location of the liquid-vapor interface in the condenser. ($T_{SINK} = 5$ °C, $T_{AMB} = 19$ °C, and 2-inch positive elevation)

When the LHP is operated at positive elevation, the vapor channel can be either full of vapor (capillary-controlled mode), or a two-phase fluid (gravity-controlled mode). A plot of the vapor quality exiting the vapor channel is shown in Fig. 6.12. From this chart, by assuming the vapor quality has an linear relation with heat load when the LHP

is operating in the gravity-controlled mode, the transition heat load between the gravity-controlled and capillary-controlled modes is estimated to be 127 W.
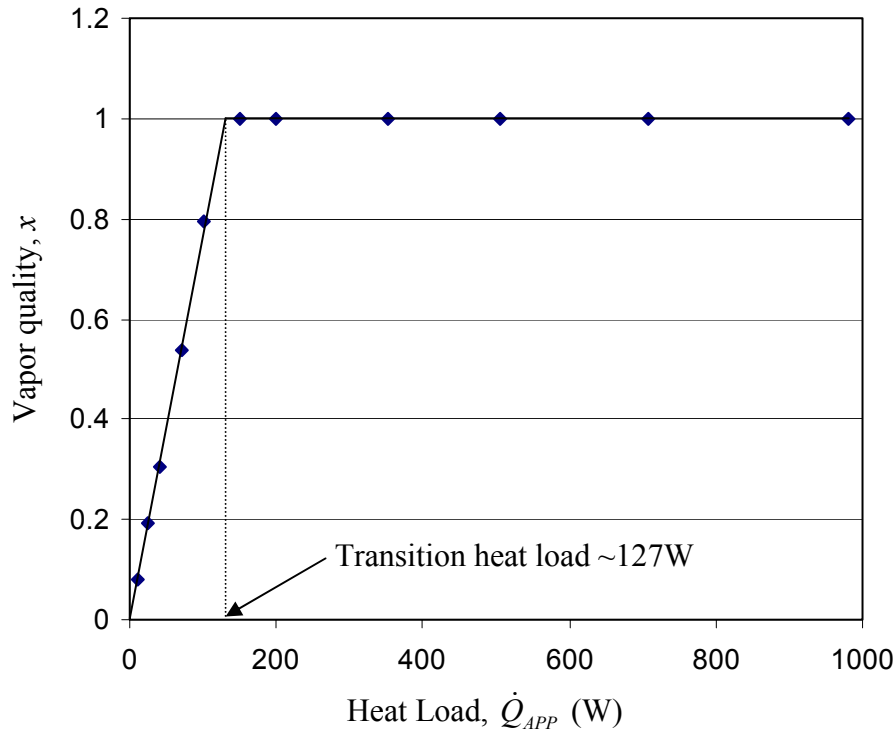
Fig. 6.12: Vapor quality exiting the vapor channel as a function of heat load. ($T_{SINK} = 5$ °C, $T_{AMB} = 19$ °C, and 2-inch positive elevation)

Fig. 6.13 shows the amount of total heat leak, and ratios of axial heat leak and radial heat leak to total heat leak as functions of heat load. From the heat leak model presented in Section 5.5.7, the radial heat leak term vanishes when the local pressure in the evaporator core is higher than that in the vapor channel. When a LHP is operating in the gravity-controlled mode, this is always the case. When the heat load is just a little higher than the transition heat load (e.g. 150 W in Fig. 6.13), the condition might still be true because of the existence of the primary wick. Thus, when the heat load is lower than 150 W, the heat leak is composed only of axial heat leak. Generally, radial heat leak

dominates axial heat leak when the LHP is operating in the capillary-controlled mode, especially at high heat load.

Total, axial, and radial heat leaks, normalized by heat load, are plotted in Fig. 6.14 as functions of heat load. The trend of normalized total heat leak first follows that of axial heat leak when the heat load is small (< 150 W) and then follows that of radial heat leak when the heat load is high (> 200 W). The trends of axial heat leak and radial heat leak are the same as those in zero elevation as explained in the previous section.
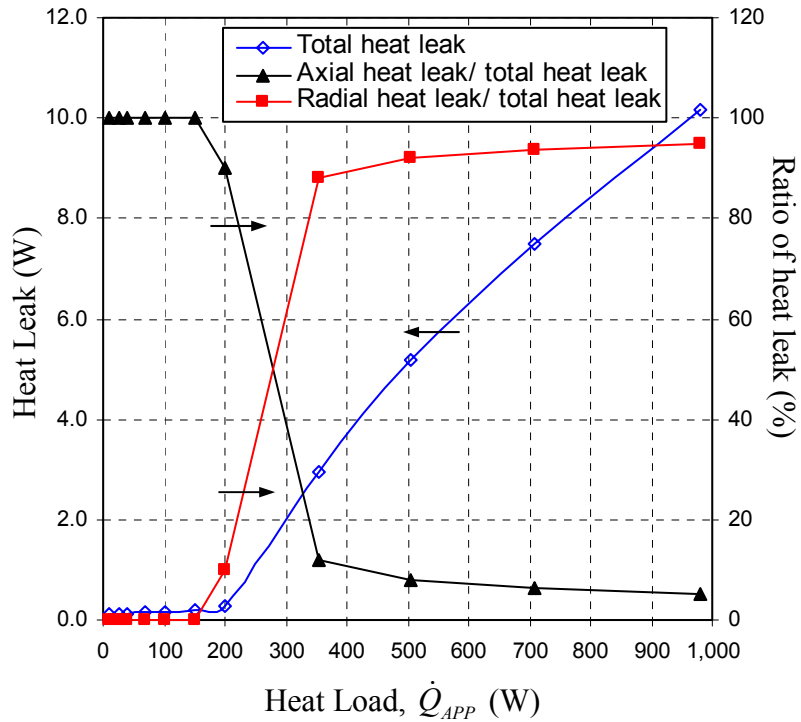
Fig. 6.13: Total heat leak and the ratios of axial heat leak and radial heat leak to total heat leak as functions of heat load. ($T_{SINK} = 5\ ^{\circ}C$, $T_{AMB} = 19\ ^{\circ}C$, and 2-inch positive elevation)
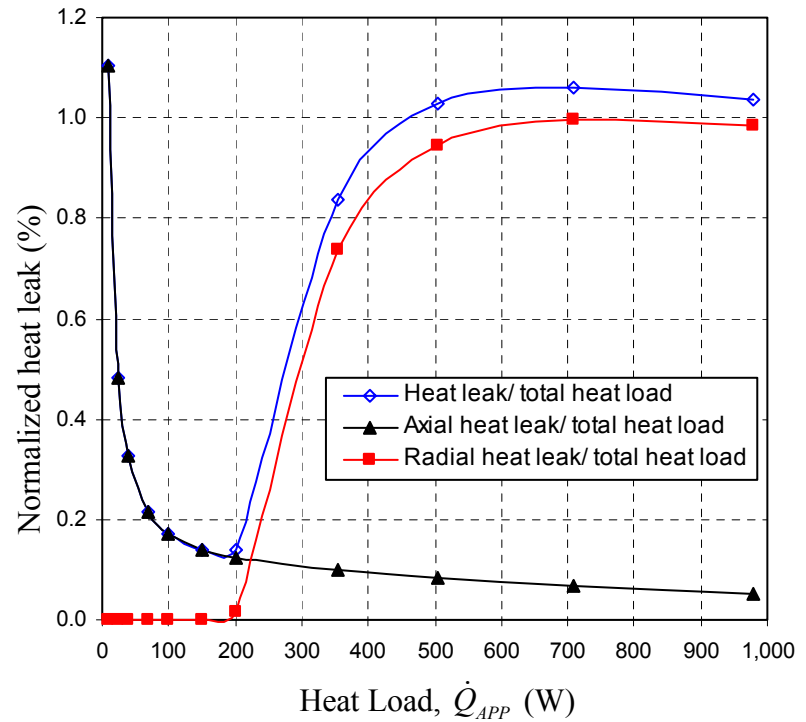
Fig. 6.14: Normalized total heat leak, axial heat leak, and radial heat leak as functions of heat load. ($T_{SINK} = 5\ ^{\circ}C$, $T_{AMB} = 19\ ^{\circ}C$, and 2-inch positive elevation)

Fig. 6.15 shows the change of temperature and vapor quality of fluid flow when the LHP is operating at the baseline configuration and 2-inch positive elevation with a heat load of 100.7 W. The x-axis in Fig. 6.15 represents the distance that the fluid travels down the loop from the high pressure side in the vapor channel. For the predicted results presented in Fig. 6.15, the saturation temperature in the vapor channel is equal to 12.39 ^{o}C. This temperature is denoted as T_{SAT}^{O}, which means the saturation temperature at the outer surface of the primary wick. The vapor quality exiting the vapor channel is equal to 0.79, which also confirms that the LHP is operating in the gravity-controlled mode. The vapor line is perfectly insulated; thus, neither temperature nor vapor quality change in the vapor line provided that the change in the saturated temperature due to pressure drop is negligible.

In the condenser, the saturated vapor begins to be condensed back to liquid. The condensation process continues in the first 4 sections. In section 5, the saturated vapor is fully condensed back to liquid and the saturated liquid starts to be subcooled. The liquid temperature exiting condenser section 5 is 7.26 ^{o}C. After condenser section 5, the condenser is used for subcooling rather than condensing. The subcooled liquid enters the liquid line at a temperature of 5.62 ^{o}C. In the liquid line, the liquid gains heat from the ambient by natural convection and enters the bayonet inside the reservoir at a higher subcooled liquid temperature of 9.45 ^{o}C. In the bayonet, the liquid keeps gaining heat from the fluid in the reservoir and the evaporator core and exits the bayonet into the evaporator core at a temperature of 12.40 ^{o}C.
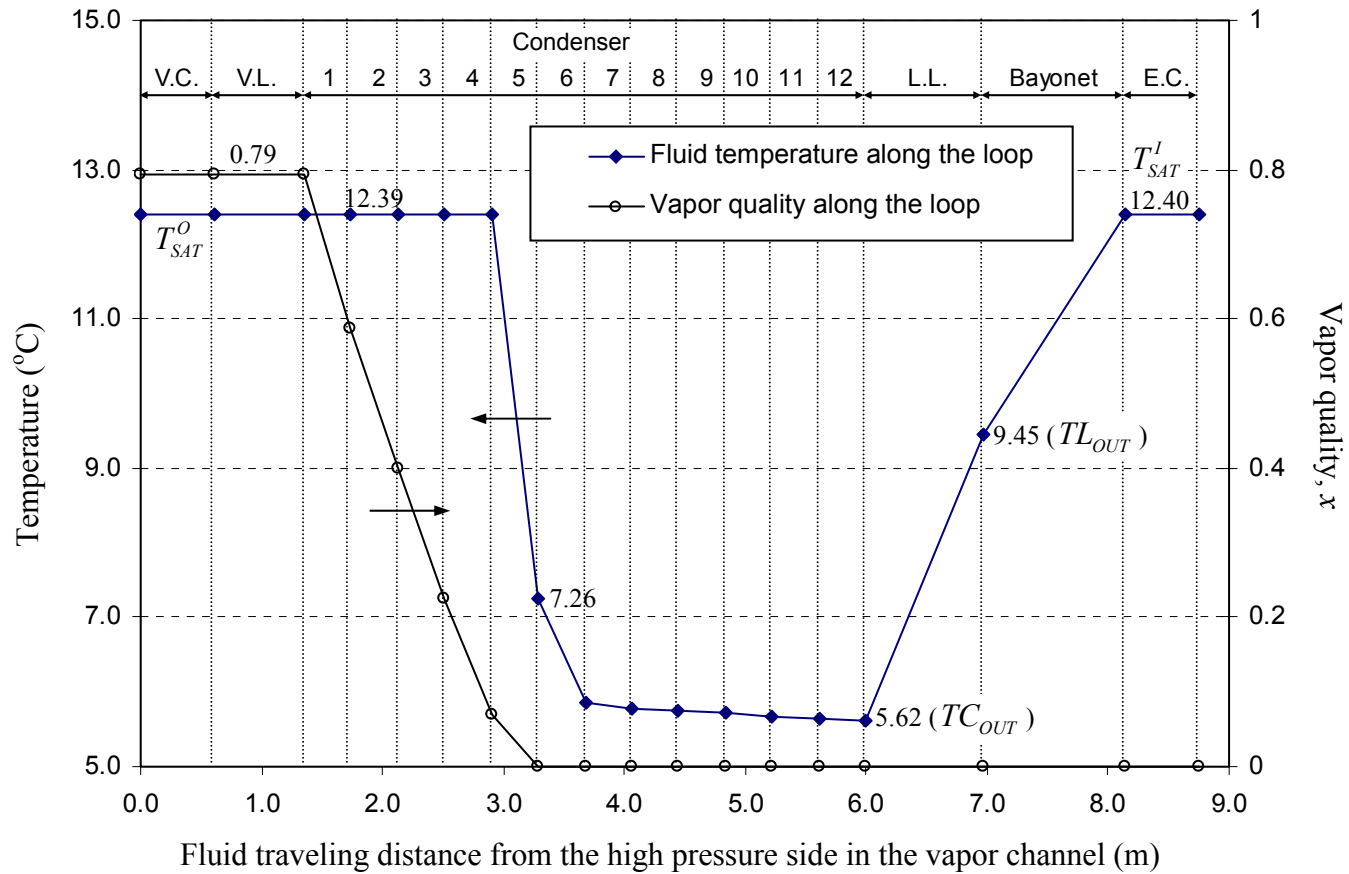
Fig. 6.15: Temperature and vapor quality of the fluid flow along the loop starting from the high pressure side in the vapor channel. ($T_{SINK} = 5$ °C, $T_{AMB} = 19$ °C, 2-inch positive elevation, and $\dot{Q}_{APP} = 100.17$ W)

Because the LHP is operating in the gravity-controlled mode, the local pressure inside the evaporator core is higher than that in the vapor channel. Therefore, the saturation temperature in the reservoir is slightly higher than that in the vapor channel and is equal to 12.40 $^{\mathrm{o}}$C. It is denoted as T_{SAT}^{I}, which means the saturation temperature at the inner surface of the primary wick.

To summarize the operating characteristics of the condition predicted in Fig. 6.15, the following observations can be drawn from the figure:

1. The steady-state operating temperature is equal to 12.39 $^{\mathrm{o}}$C.

2. The location of the liquid-vapor interface is in condenser section 5.

3. The difference between the subcooled liquid temperature at the end of liquid line and the reservoir temperature is 2.95 $^{\mathrm{o}}$C. This is an important index for the amount of subcooling brought back to the reservoir, $\dot{Q}_{SC}$.

4. The LHP is operating in the variable-conductance mode because the condenser is not fully utilized for condensing.

5. The LHP is operating in the gravity-controlled mode because the vapor channel is composed of a two-phase fluid ($x_{VC,OUT} = 0.79$).

6.2   PARAMETRIC STUDY OF LOOP HEAT PIPES

The performance of LHPs is influenced by many parameters, including the material and size of each component in the LHP, the design of the condenser, and the operating conditions. This section studies the effects of major parameters using the steady-state model, which is formulated based on the model presented in Chapter 5.

6.2.1   Effect of Sink Temperature

In this section, the effect of sink temperature on the performance of a LHP is studied at zero elevation and positive elevation. The effect of sink temperature on the performance of a LHP when it is operated at adverse elevation is similar to that at zero elevation.

Zero Elevation:

The baseline configuration is studied at three sink temperatures: 20 $^{\circ}$C, 5 $^{\circ}$C, and -10 $^{\circ}$C, when the LHP is operated at zero elevation. The trends of the steady-state operating temperature at three different sink temperatures are shown in Fig. 6.16. When the sink temperature is lower than the ambient temperature (e.g. $T_{SINK} = 5$ $^{\circ}$C or -10 $^{\circ}$C), the typical U-shaped trend line is followed. The transition head load between the variable-conductance and fixed-conductance modes is around 200 W when the sink temperature is 5 $^{\circ}$C and is around 400 W when the sink temperature is -10 $^{\circ}$C. The transition heat load increases as the sink temperature decreases because a condenser with a lower sink temperature has greater cooling capacity than one with a higher sink temperature. When the sink temperature is equal to or higher than the ambient temperature, the LHP is always operating in the fixed-conductance mode. The liquid line becomes another condenser, and the location of the liquid-vapor interface may reside at the end of the condenser or in the liquid line.
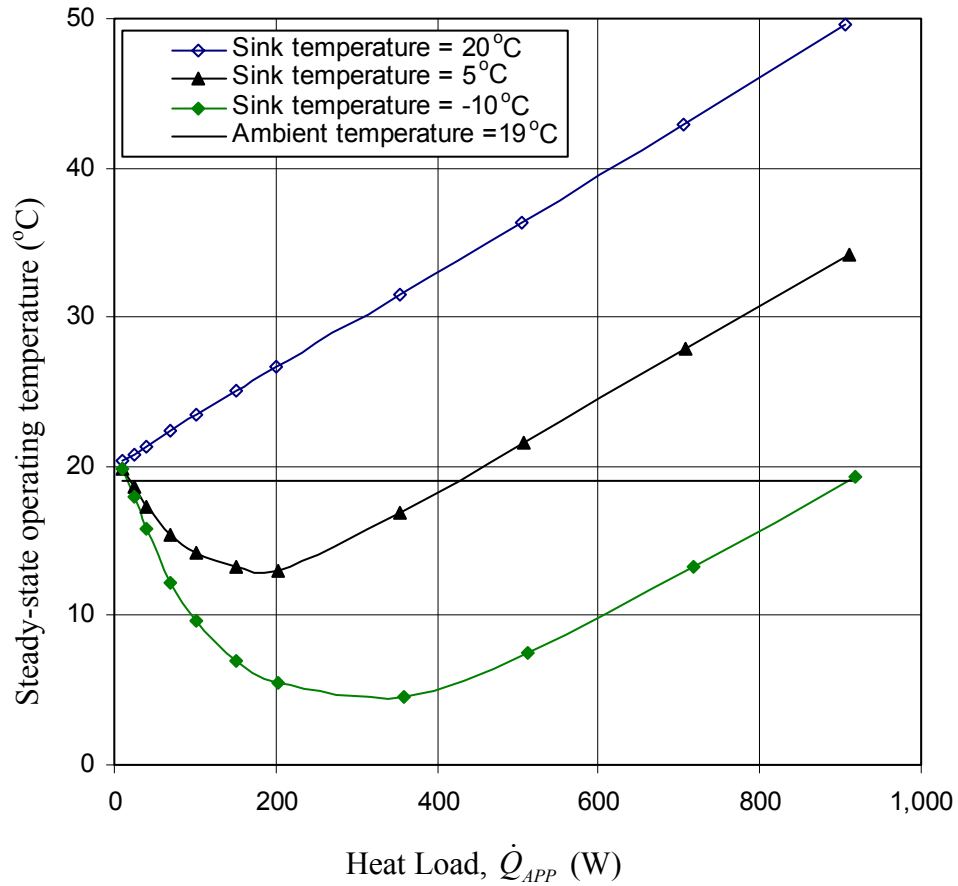
Fig. 6.16: Effect of sink temperature on the trend of steady-state operating temperature. ($T_{AMB} = 19$ $^{\circ}$C and zero elevation)

Positive Elevation:

The baseline configuration is studied at three sink temperatures: 19 $^{\circ}$C, 5 $^{\circ}$C, and -10 $^{\circ}$C, when the LHP is operated at 2-inch positive elevation. The trends of the steady-state operating temperature at different sink temperatures are shown in Fig. 6.17. The transition heat load, $\dot{Q}_2$, between the capillary-controlled and gravity-controlled modes, is between 100 and 150 W for the three different cases. When the heat load is higher

than $\dot{Q}_2$, the trend is similar to that at zero elevation. When the heat load is lower than

$\dot{Q}_2$, the trend follows the proposed trend for positive elevation in Section 4.2.3.
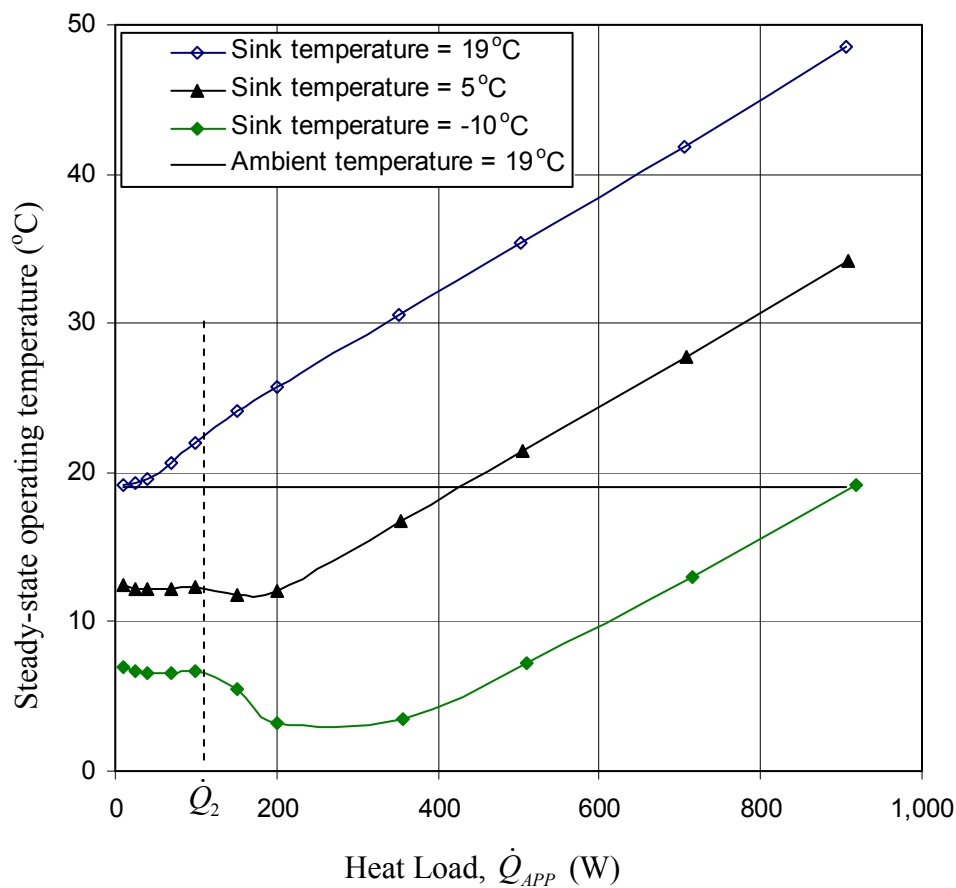
Fig. 6.17: Effect of sink temperature on the trend of steady-state operating temperature. ($T_{AMB} = 19$ °C and 2-inch positive elevation)

6.2.2   Effect of Ambient Temperature

The effect of ambient temperature on the performance of a LHP is studied at zero

elevation and positive elevation.   Again, the effect of ambient temperature on the

performance of a LHP when it is operated at adverse elevation is similar to that at zero elevation.

Zero Elevation:

The baseline configuration is studied at three ambient temperatures: 30 $^{\circ}$C, 19 $^{\circ}$C, and 0 $^{\circ}$C, when the LHP is operated at zero elevation. The trends of the steady-state operating temperature at three different ambient temperatures are shown in Fig. 6.18. When the ambient temperature is higher than the sink temperature (e.g. $T_{AMB} = 30$ $^{\circ}$C or 19 $^{\circ}$C), the typical U-shaped trend line is followed. The transition heat load between the variable-conductance and fixed-conductance modes is around 300 W when the ambient temperature is 30 $^{\circ}$C, and is around 200 W when the ambient temperature is 19 $^{\circ}$C; it increases as the ambient temperature increases. Higher ambient temperature leads to higher steady-state operating temperature, and thus, greater temperature difference between the steady-state operating temperature and the sink temperature. Therefore, to remove the same amount of heat, the higher ambient temperature condition requires less condenser length than the lower ambient temperature condition. When the ambient temperature is lower than the sink temperature, the LHP is always operating in the fixed-conductance mode as explained in the previous section.

A higher ambient temperature leads to a higher steady-state operating temperature, as can be explained from the energy balance equation in the reservoir (Eq. 4.2). Higher ambient temperature means more heat gain or less heat loss from the ambient to the reservoir. This has to be fulfilled by bringing back more subcooling from the liquid line through higher steady-state operating temperature, T_{SSOT}. In addition to that, the higher

ambient temperature also leads to a higher liquid temperature at the end of the liquid line,

TL_{OUT}. This makes the steady-state operating temperature even higher for a high ambient

temperature condition than for a low ambient temperature condition.
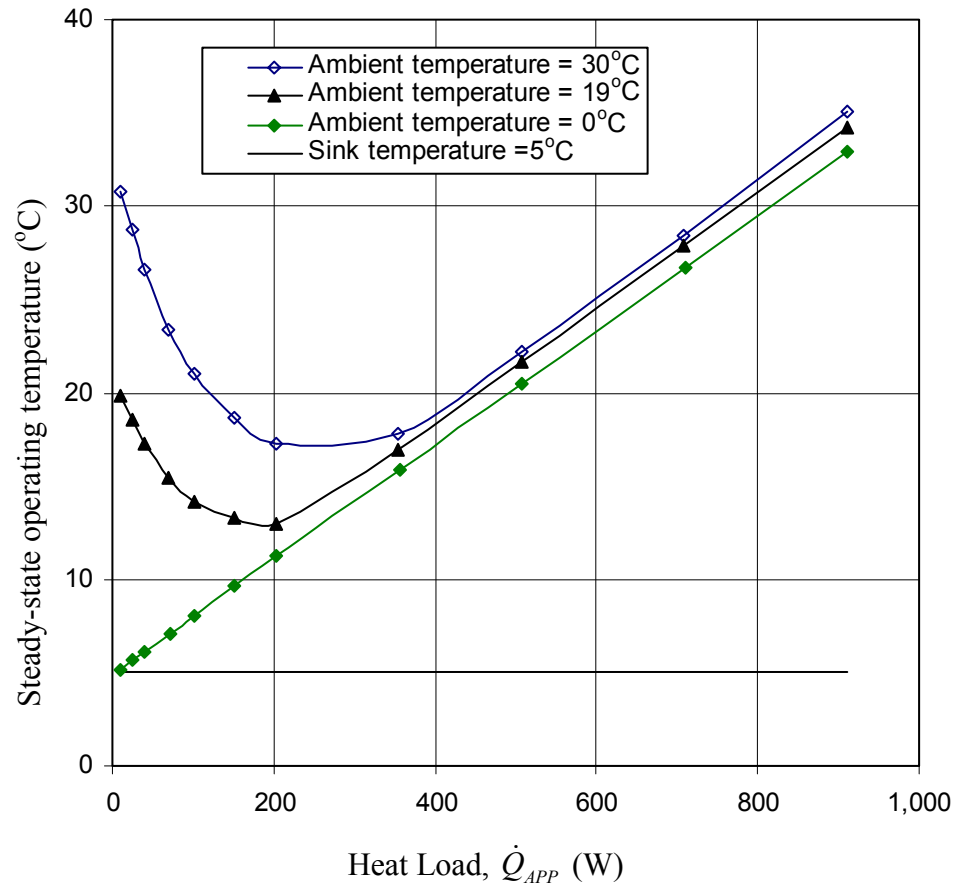
Fig. 6.18: Effect of ambient temperature on the trend of steady-state operating temperature. ($T_{SINK} = 5\ ^{o}C$ and zero elevation)

Positive Elevation:

The baseline configuration is studied at three ambient temperatures: 30 ^{o}C, 19 ^{o}C, and 0 ^{o}C, when the LHP is operated at 2-inch positive elevation. The trends of the steady-state operating temperature at three different ambient temperatures are shown in

Fig. 6.19. The transition heat loads, $\dot{Q}_2$, between the capillary-controlled and gravity-controlled modes are between 100 and 150 W for three different cases. When the heat load is higher than $\dot{Q}_2$, the trend is similar to that at zero elevation. When the heat load is lower than $\dot{Q}_2$, the trend follows the proposed trend at positive elevation in Section 4.2.3.
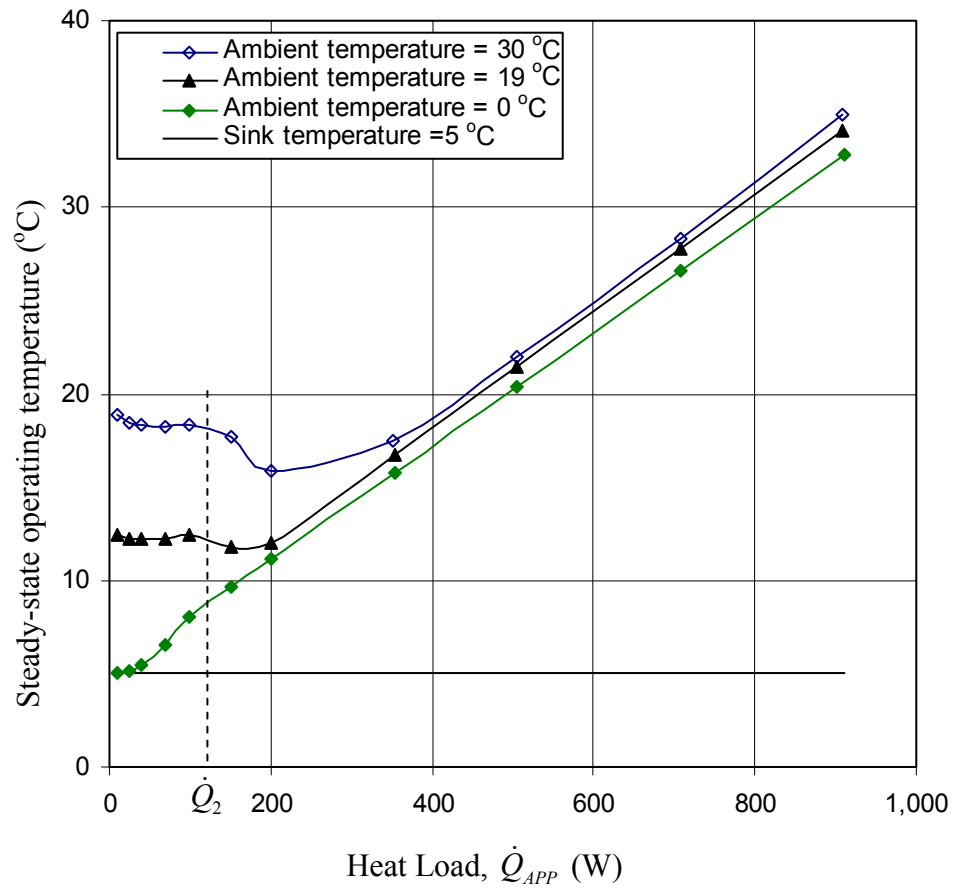
Fig. 6.19: Effect of ambient temperature on the trend of steady-state operating temperature. ($T_{SINK} = 5\ ^{\circ}C$ and 2-inch positive elevation)

6.2.3 Effect of Elevation

The effect of elevation on the performance of a LHP is studied. The baseline configuration is applied as the input parameters at five elevations: 4-inch and 2-inch adverse elevation, zero elevation, and 2-inch and 4-inch positive elevation. The trends of the steady-state operating temperature at these five elevations are shown in Fig. 6.20.
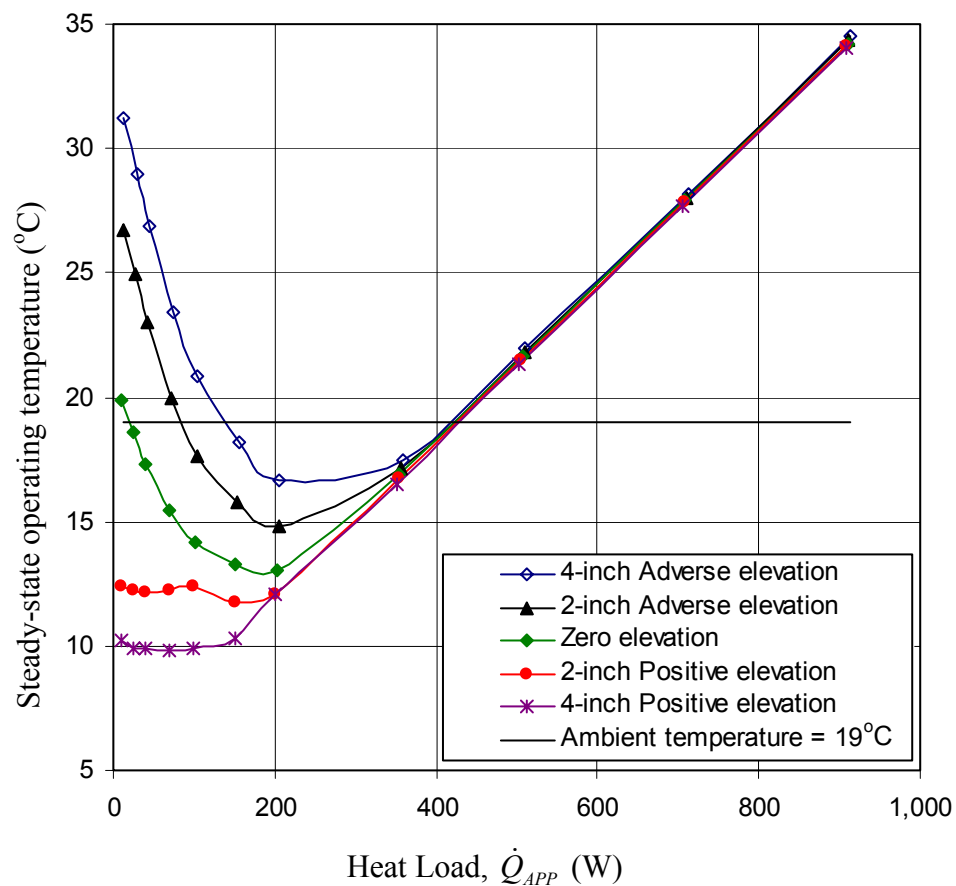
Fig. 6.20: Effect of elevation on the trend of steady-state operating temperature. ($T_{SINK} = 5$ °C and $T_{AMB} = 19$ °C)

Elevation has little effect on the LHP when the heat load is high ($\geq$ 400 W in Fig. 6.20), because when the heat load is high, the frictional pressure drop in the system

overwhelms the gravitational head gain or loss caused by different elevations. In contrast, elevation has a great impact on the LHP when the heat load is low ($\leq$ 350 W in Fig. 6.20), because when the heat load is low, the gravitational head plays an important role in the total system pressure drop. Thus, higher elevation results in higher system pressure drop, which in turn increases the amount of radial heat leak. Finally the steady-state operating temperature increases as the heat leak increases.

It can be observed from Fig. 6.18 and Fig. 6.20 that elevation has a similar effect on the trend of steady-state operating temperature as does ambient temperature. The more adverse elevation leads to a higher heat leak from the evaporator to the reservoir whereas the higher ambient temperature leads to less heat loss or more heat gain to the reservoir. From the energy balance equation from the reservoir's point of view, these two phenomena have the same impact on the system.

The transition heat load between the fixed-conductance and variable-conductance modes increases as the elevation decreases from positive (+) to adverse (-), because the more adverse elevation condition has a higher steady-state operating temperature, and thus, higher cooling capacity in the condenser as explained in the previous section. From the location of the liquid-vapor interface in the condenser in Fig. 6.21, the transition heat load can be identified. It is around 200 W for both positive elevation conditions and is a little lower than 400 W for 4-inch adverse elevation.
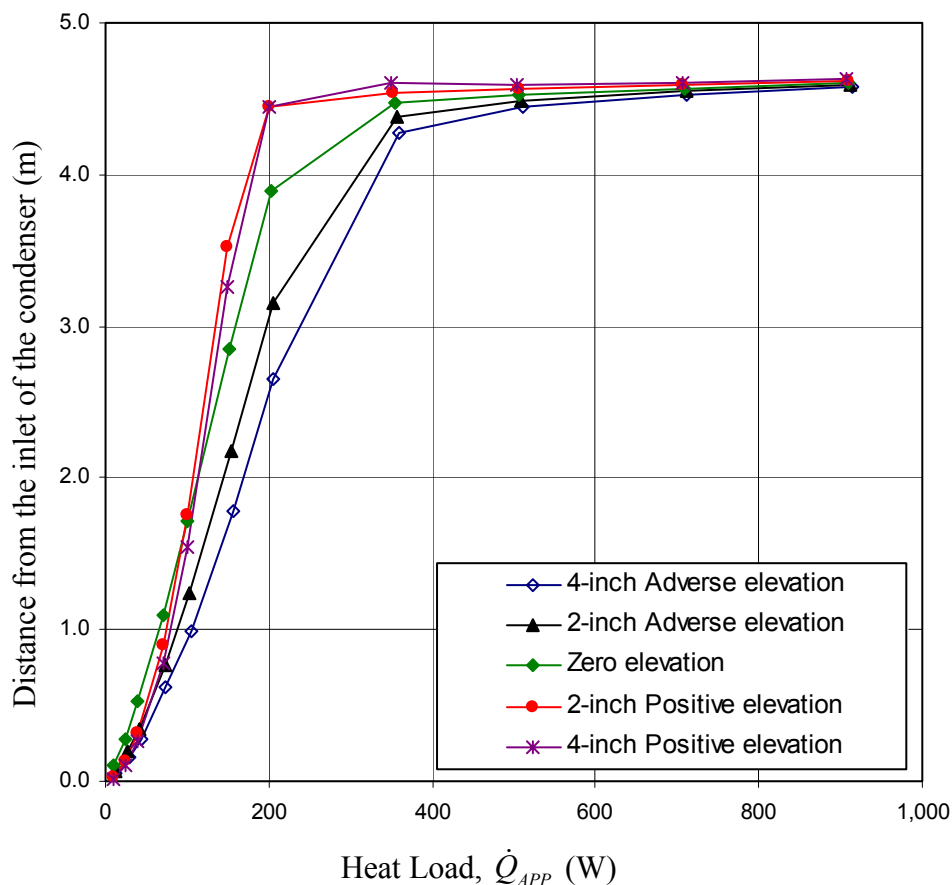
Fig. 6.21: Effect of elevation on the location of the liquid-vapor interface in the condenser. ($T_{SINK} = 5$ $^{\circ}$C and $T_{AMB} = 19$ $^{\circ}$C)

When the LHP is operated at positive elevation, the transition heat load between the capillary-controlled and gravity-controlled modes increases as the positive elevation increases. Fig. 6.22 shows the vapor quality in the vapor channel as a function of heat load at different elevations. For zero and adverse elevation conditions, the vapor channel is always filled with vapor. For a positive elevation condition, the LHP may operate in the gravity-controlled mode where the vapor channel is filled with two-phase flow. From the observation in Fig. 6.22, the transition heat load is between 100 W and 150 W, and

around 200 W when the LHP is operated at 2-inch positive elevation and 4-inch positive

elevation, respectively.
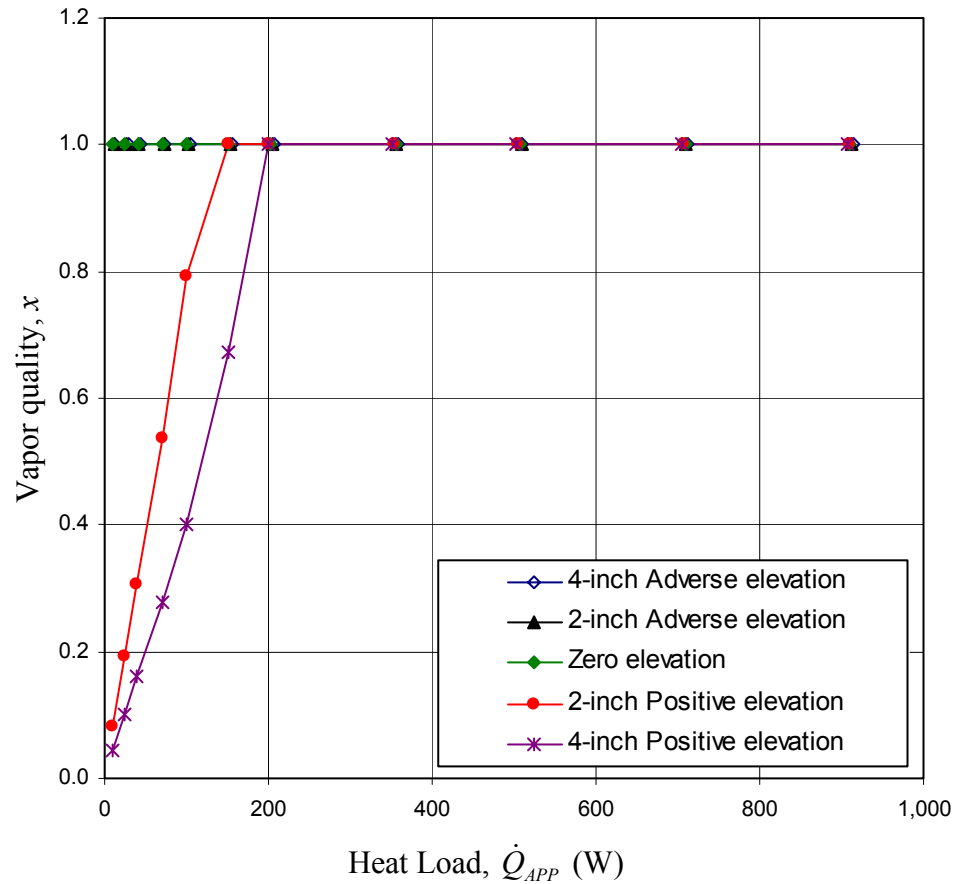
Fig. 6.22: Effect of elevation on the vapor quality exiting the vapor channel.
($T_{SINK} = 5\ ^{o}C$ and $T_{AMB} = 19\ ^{o}C$)

6.2.4   Effect of the External Thermal Conductance of the Condenser

The effect of the external thermal conductance of the condenser on the

performance of a LHP is studied. The baseline configuration is applied as the input

parameters with three values of external thermal conductance: 20 W/m-K, 10 W/m-K,

and 5 W/m-K. The trends of the steady-state operating temperature for these three values
of external thermal conductance are shown in Fig. 6.23.
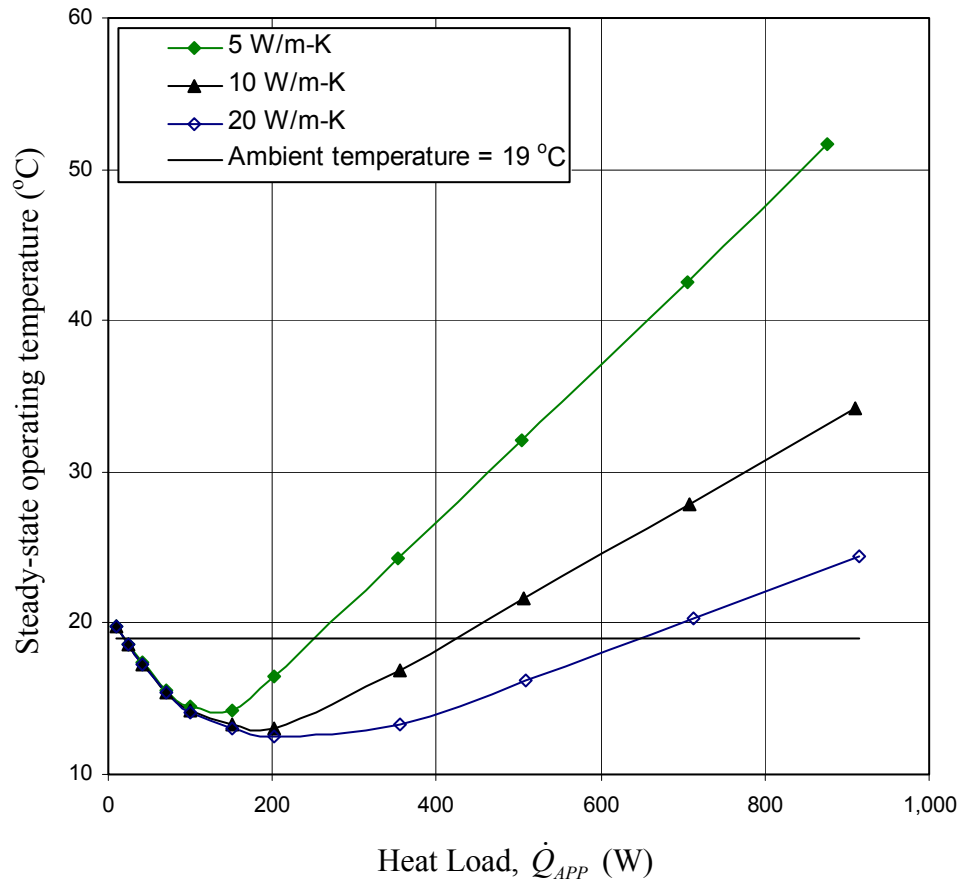
Fig. 6.23: Effect of external thermal conductance of the condenser on the steady-state
operating temperature. ($T_{SINK} = 5$ $^{\circ}$C, $T_{AMB} = 19$ $^{\circ}$C, and zero elevation)

When the heat load is low ($\leq$ 100 W), there is almost no effect on the
performance of the LHP, because the LHP is operating in the variable-conductance mode
and the liquid temperature exiting the condenser is close to the sink temperature for all
three cases. When the heat load is high, the LHP is operating in the fixed-conductance
mode and the steady-state operating temperature follows different slopes for different
value of external thermal conductance.

The cooling capacity of the condenser increases with increasing external thermal conductance. Thus, the transition heat load between the variable-conductance and fixed-conductance modes increases with increasing external thermal conductance. It is around 150, 200, and 300 W, when the external thermal conductance equals 5 W/m-K, 10 W/m-K, and 20 W/m-K, respectively.

6.2.5   Effect of Two-Phase Heat Transfer Correlations

The effect of two-phase heat transfer correlations on the performance of the LHP is studied. The baseline configuration is applied as the input parameters with four different two-phase heat transfer correlations. The trends of the steady-state operating temperature for the four correlations are shown in Fig. 6.24.

Basically, different two-phase heat transfer correlations result in different tube-side thermal conductance (inner thermal conductance), where the external thermal conductance of the condenser is fixed at 10 W/m-K. When the heat load is lower than 200 W, there is almost no effect on the performance of the LHP, because the length of the two-phase fluid flow in the condenser is very short. When the heat load is higher than 200 W, the LHP is operating in the fixed-conductance mode and the steady-state operating temperature follows different slopes for different correlations. After careful review, similarity can be found between the effects of external thermal conductance (Fig. 6.23) and two-phase heat transfer correlations (Fig. 6.24). This is because the overall thermal conductance is composed of external and inner thermal conductance. Thus, a fixed inner thermal conductance with increasing external thermal conductance

should behave similarly to a fixed external thermal conductance with increasing inner thermal conductance.
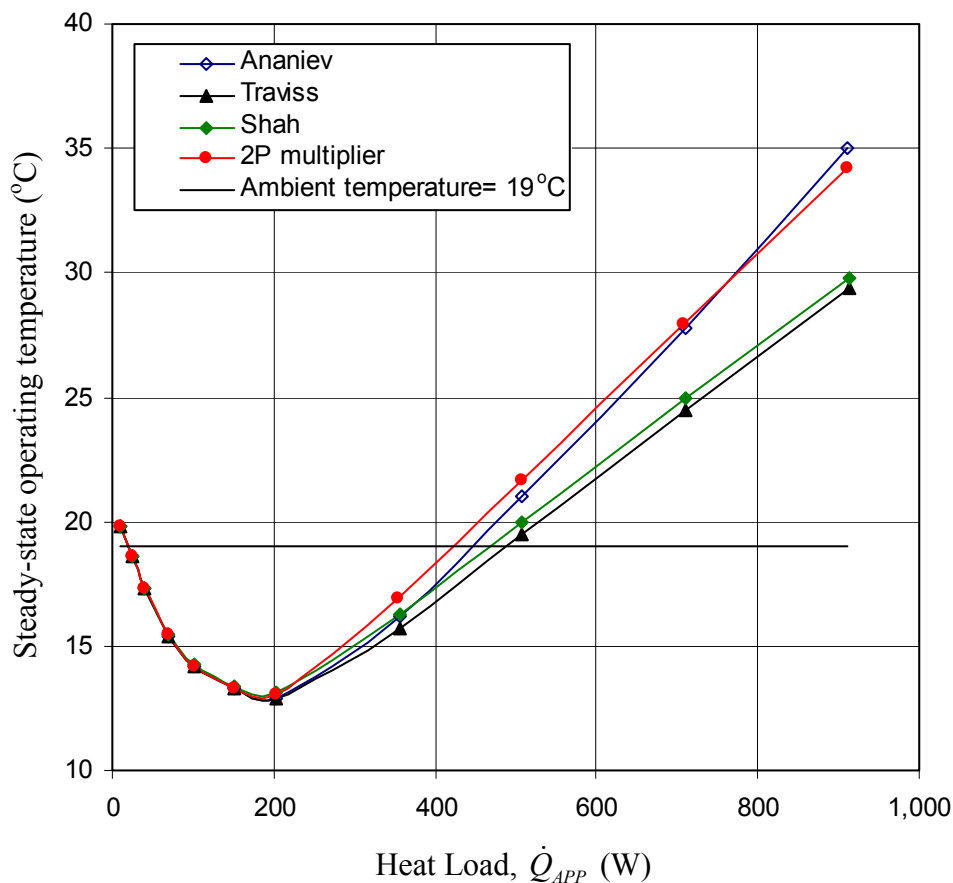
Fig. 6.24: Effect of two-phase heat transfer correlations on the steady-state operating temperature. ($T_{SINK} = 5$ °C , $T_{AMB} = 19$ °C , zero elevation, and smooth annular correlation)

It can be observed from Fig. 6.24 that the Ananiev and two-phase multiplier correlations have one similar trend and the Traviss and Shah correlations have a different, but similar trend. The difference between the steady-state operating temperatures increases with increasing heat load. Fig. 6.25 shows the inner two-phase thermal conductance as a function of vapor quality when the heat load is around 900 W. The

inner two-phase thermal conductance increases with increasing vapor quality. For the Traviss and two-phase multiplier correlations, the heat transfer coefficient increases rapidly when the vapor quality is close to 1.0. This is because the correlation depends on parameters which increase dramatically when x is close to 1.0, like $(1-\alpha)^{-1}$ in the two-phase multiplier or (ρ_L / ρ_m) in the Traviss. Generally, for the same heat load, the higher the inner two-phase thermal conductance, the lower the steady-state operating temperature.
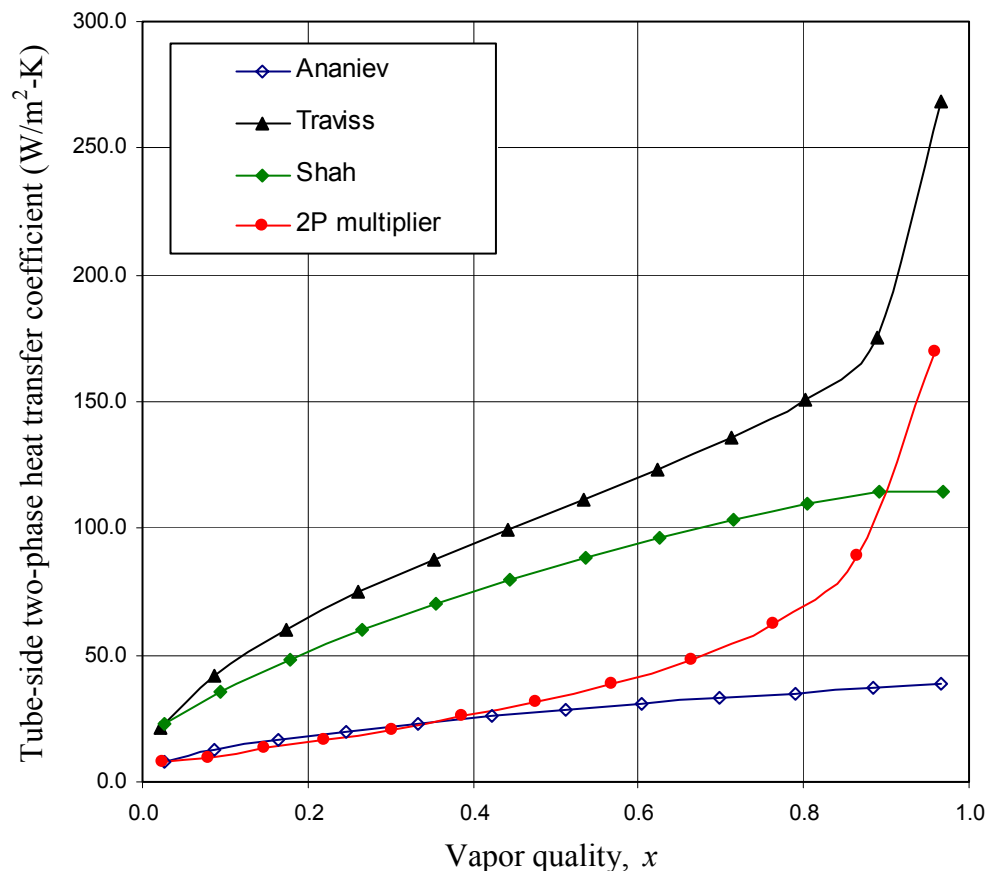
Fig. 6.25: Tube-side two-phase thermal conductance as functions of vapor quality. ($T_{SINK} = 5\ ^{\circ}C$, $T_{AMB} = 19\ ^{\circ}C$, zero elevation, smooth annular correlation, and $\dot{Q}_{APP} \approx 900$ W)

6.2.6   Effect of Heat Leak

The most challenging task in LHP modeling is how to accurately determine the amount of heat leak in LHP operation. The heat leak model proposed in Section 5.5.7 is the theoretical prediction used in the steady-state model. In a real application, depending on the design of the evaporator and primary wick, the proposed heat leak model may not be accurate. This section studies the effect of heat leak on the performance of a LHP. The amount of heat leak is composed of two parts: axial heat leak and radial heat leak. The effects of axial heat leak and radial heat leak are studied independently.

Axial Heat Leak

The effect of axial heat leak on the performance of the LHP is studied by changing the axial heat leak obtained from the baseline configuration manually. Four cases are studied: the baseline configuration, and three other cases assuming that the axial heat leak is one tenth, ten times, and twenty times that obtained from the baseline configuration. The trends of steady-state operating temperature for the four cases are shown in Fig. 6.26.

Axial heat leak refers to the heat conducted from the evaporator to the reservoir through the connection in between. The amount of axial heat leak obtained from the baseline configuration is extremely small due to small conduction area, low thermal conductivity of the material (stainless steel), and low temperature difference between the evaporator and the reservoir.

As discussed in Section 6.1.2 and 6.1.3, axial heat leak dominates the total heat leak when the heat load is small. Thus, when the heat load is higher than 400 W, the

steady-state operating temperature is not affected by the amount of axial heat leak. When the heat load is lower than 350 W, the effect of axial heat leak is important. The steady-state operating temperature increases with increasing axial heat leak. The transition heat load between the variable-conductance and the fixed-conductance modes increases with increasing axial heat leak.
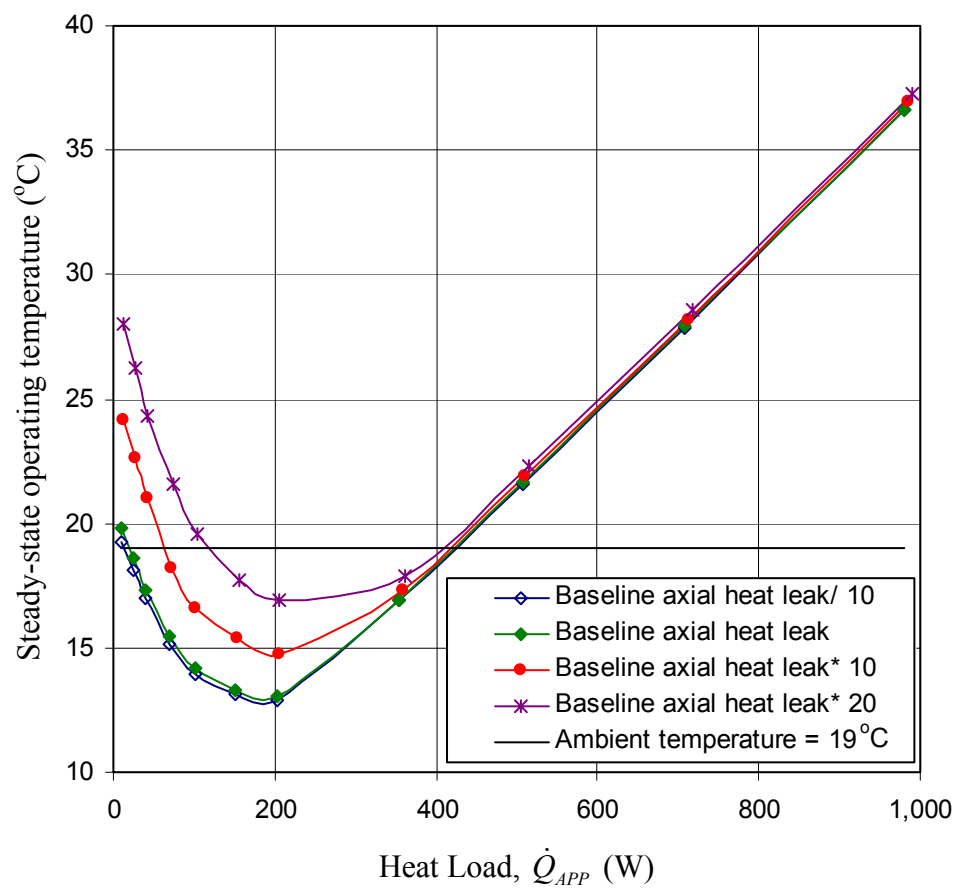
Fig. 6.26: Effect of axial heat leak on the steady-state operating temperature. ($T_{SINK} = 5\ ^{\circ}C$, $T_{AMB} = 19\ ^{\circ}C$, zero elevation, and smooth annular correlation)

Radial Heat Leak

Similarly, the effect of radial heat leak on the performance of a LHP is studied by changing the radial heat leak obtained from the baseline configuration manually. Four different cases are studied: the baseline configuration and three other cases assuming that the radial heat leak is one tenth, three times, and five times that obtained from the baseline configuration. The trends of steady-state operating temperature for the four different cases are shown in Fig. 6.27.
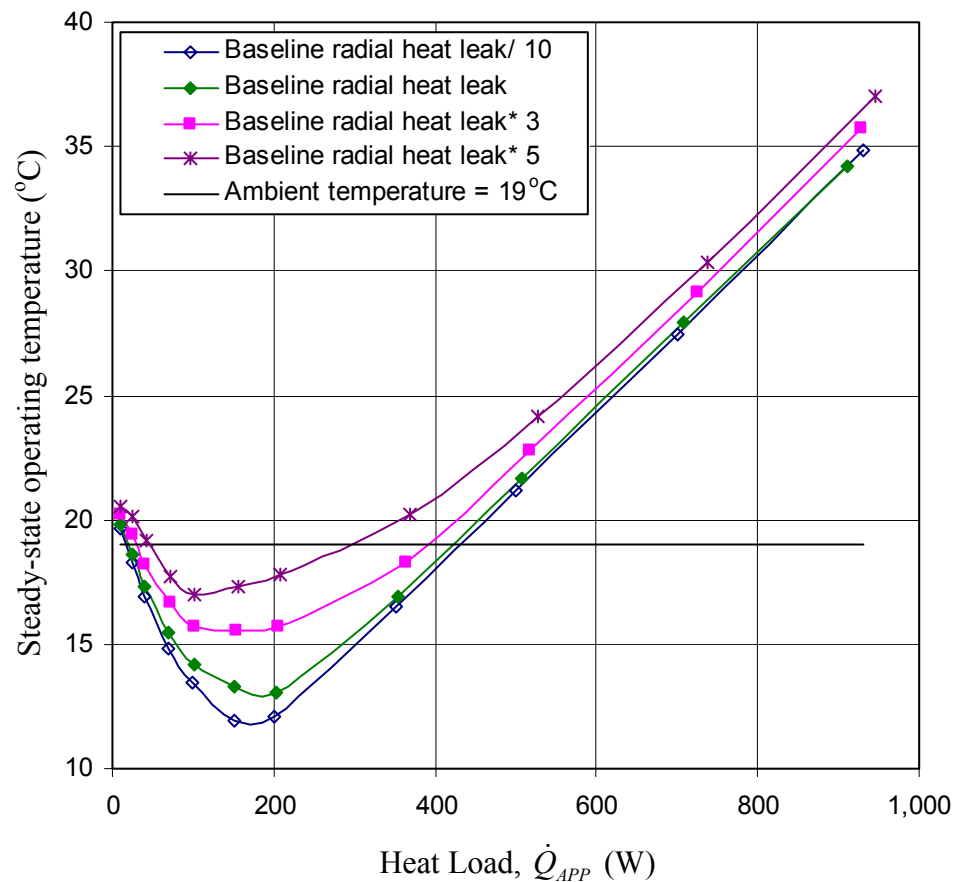
Fig. 6.27: Effect of radial heat leak on the steady-state operating temperature. ($T_{SINK} = 5\ ^{o}C$, $T_{AMB} = 19\ ^{o}C$, zero elevation, and smooth annular correlation)

Radial heat leak refers to the heat conducted across the primary wick, into the evaporator core, and then on to the reservoir. The amount of axial heat leak obtained from the baseline configuration depends on the pressure difference across the primary wick and the effective thermal conductivity of the primary wick. The primary wick in the baseline configuration is made of nickel and has a thermal conductivity of 93.0 W/m-K. The effect of radial heat leak is important throughout the whole range of the heat load. It can be observed from Fig. 6.27 that a higher heat leak leads to a higher steady-state operating temperature.

6.2.7   Effect of Two-Phase Pressure Drop Correlations

The effect of two-phase pressure drop correlations on the performance of a LHP is studied. The baseline configuration is applied as the input parameters with five two-phase pressure drop correlations. In the baseline configuration, instead of using the two-phase multiplier, the Traviss two-phase heat transfer correlation is used in this study. This makes the comparison more accurate, because the two-phase heat transfer calculation using Traviss correlation is independent of the two-phase pressure drop correlation. The trends of steady-state operating temperature for the five correlations are shown in Fig. 6.28.

When the heat load is at the lower end (≤ 75 W) or higher end (≥ 500 W), the differences of the steady-state operating temperature among the five different correlations are minimal. When the heat load is at moderate level, the effect of two-phase pressure drop correlations is noticeable. Basically, different two-phase pressure drop correlations

result in different frictional two-phase pressure drops (see Fig. 6.29). This in turn changes the radial heat leak across the primary wick: the higher the pressure drop, the greater the radial heat leak.
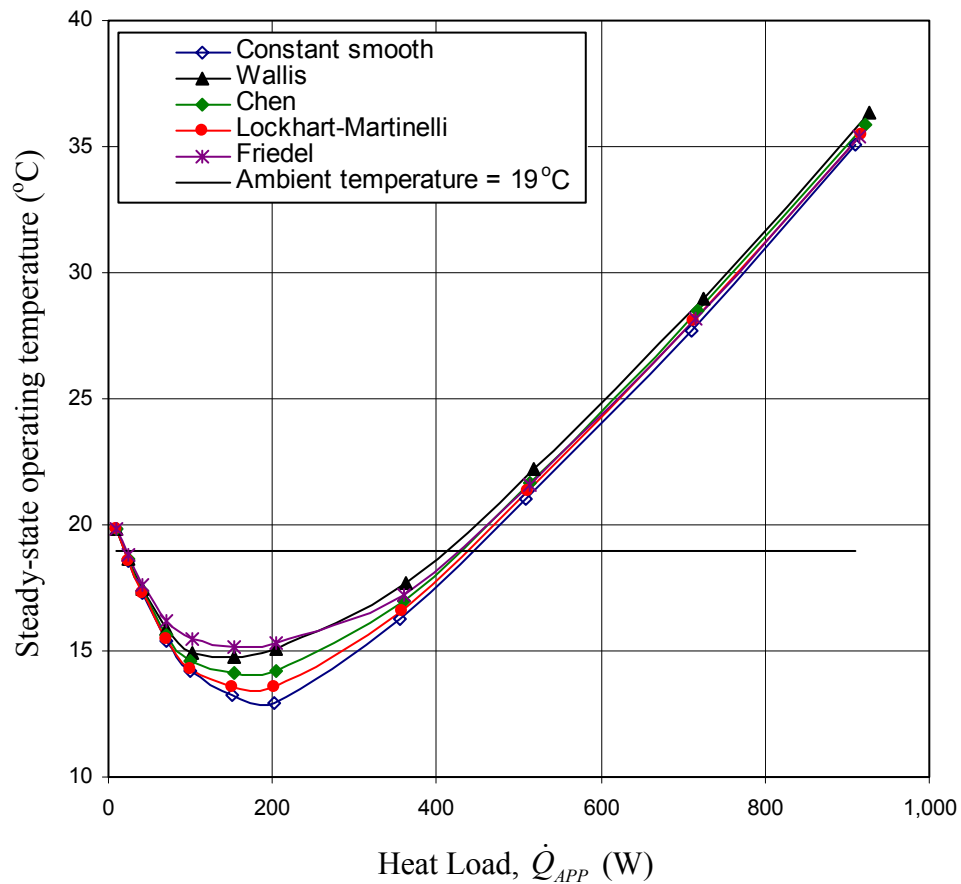
Fig. 6.28: Effect of two-phase pressure drop correlations on the steady-state operating temperature. ($T_{SINK} = 5$ °C, $T_{AMB} = 19$ °C, and Ananiev correlation)

When the heat load is small ($\leq$ 75 W), the two-phase length in the condenser is short and the frictional two-phase pressure drop is not important in the total pressure drop. Thus, there is almost no effect of two-phase pressure drop when the heat load is smaller than 75 W. On the other end when the heat load is high ($\geq$ 500 W), the mass flow rate in the system is high. A small temperature difference between the liquid temperature

exiting the liquid line, TL_{OUT} , and the steady-state operating temperature, T_{SSOT} , can bring enough liquid subcooling to balance the difference of the heat leak caused by the difference of the frictional two-phase pressure drop. Therefore, only a small steady-state operating temperature difference can be observed when the heat load is higher than 500 W. When the heat load is increasing between 75 W and 500 W, the frictional two-phase pressure drop is an important component in total pressure drop and the mass flow rate in the system is moderate. With the combination of these two characteristics, the effect of two-phase pressure drop correlations on the performance of the LHP becomes significant.

Fig. 6.29 shows the frictional two-phase pressure drop as a function of heat load for five different pressure drop correlations. The constant smooth correlation predicts the lowest frictional two-phase pressure drop while the Wallis correlation predicts the highest. When the heat load is around 900 W, the ratio of frictional two-phase pressure drop to total system pressure drop predicted by the Wallis correlation is around 70 % while that predicted by the constant smooth correlation is around 40 %.
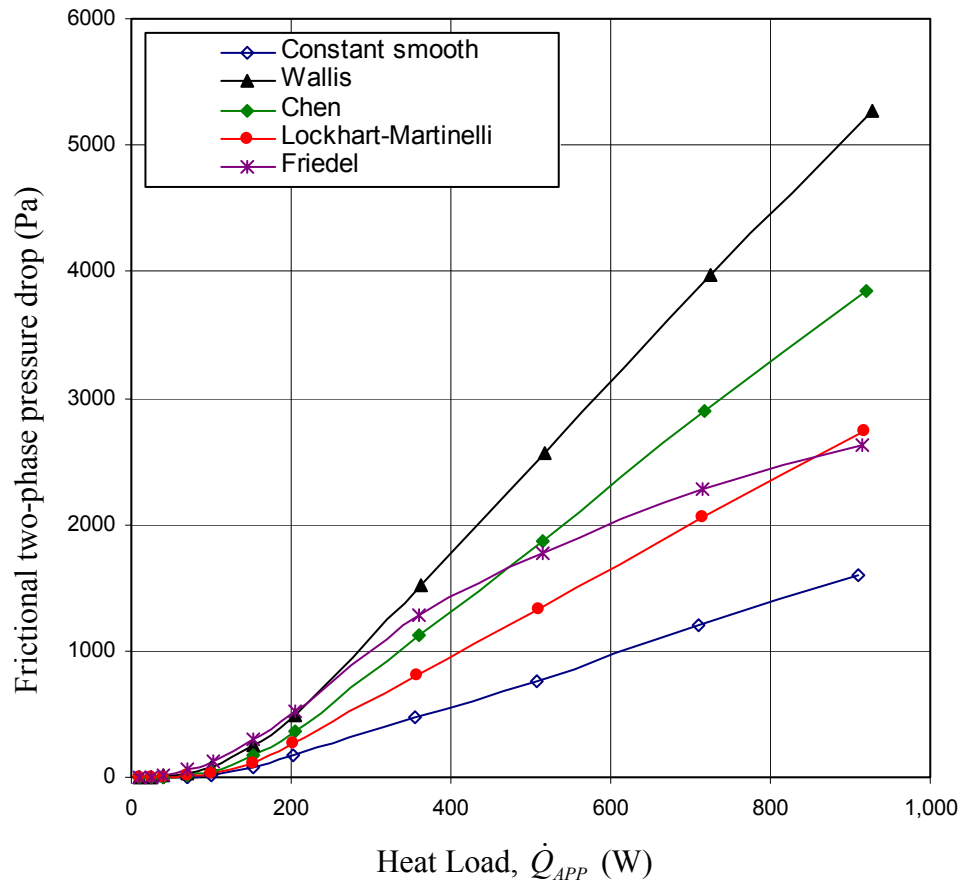
Fig. 6.29: Effect of two-phase pressure drop correlations on the frictional two-phase pressure drop. ($T_{SINK} = 5\ ^{\circ}\mathrm{C}$, $T_{AMB} = 19\ ^{\circ}\mathrm{C}$, and Ananiev correlation)

6.2.8   Effect of Insulation of the Reservoir

The effect of insulation of the reservoir on the performance of a LHP is studied. The baseline configuration is applied as the input parameters with or without insulation of the reservoir. The trends of steady-state operating temperature are shown in Fig. 6.30.

From the energy balance equation of the reservoir, the amount of heat leak must be balanced with the amount of subcooling and the amount of heat exchange with the

ambient. The heat exchange between the ambient and the reservoir is assumed to be through natural convection, and depends strongly on the temperature difference. When the heat load is higher than 350 W in Fig. 6.30, insulation of the reservoir has almost no effect on the steady-state operating temperature. At the highest heat load around 910 W, a small effect can be seen because the temperature difference between the steady-state operating temperature and the ambient temperature is significant.

If the reservoir is insulated, there is no heat exchange with the ambient and the amount of heat leak must be balanced with the amount of subcooling only. Depending on the steady-state operating temperature, T_{SSOT}, the ambient may act like a heat sink ($T_{SSOT} > T_{AMB}$) or like a heat source ($T_{SSOT} < T_{AMB}$) to the reservoir. Thus, when $T_{SSOT} > T_{AMB}$, insulation of the reservoir makes the steady-state operating temperature higher than the case with no insulation, and the situation is opposite when $T_{SSOT} < T_{AMB}$.
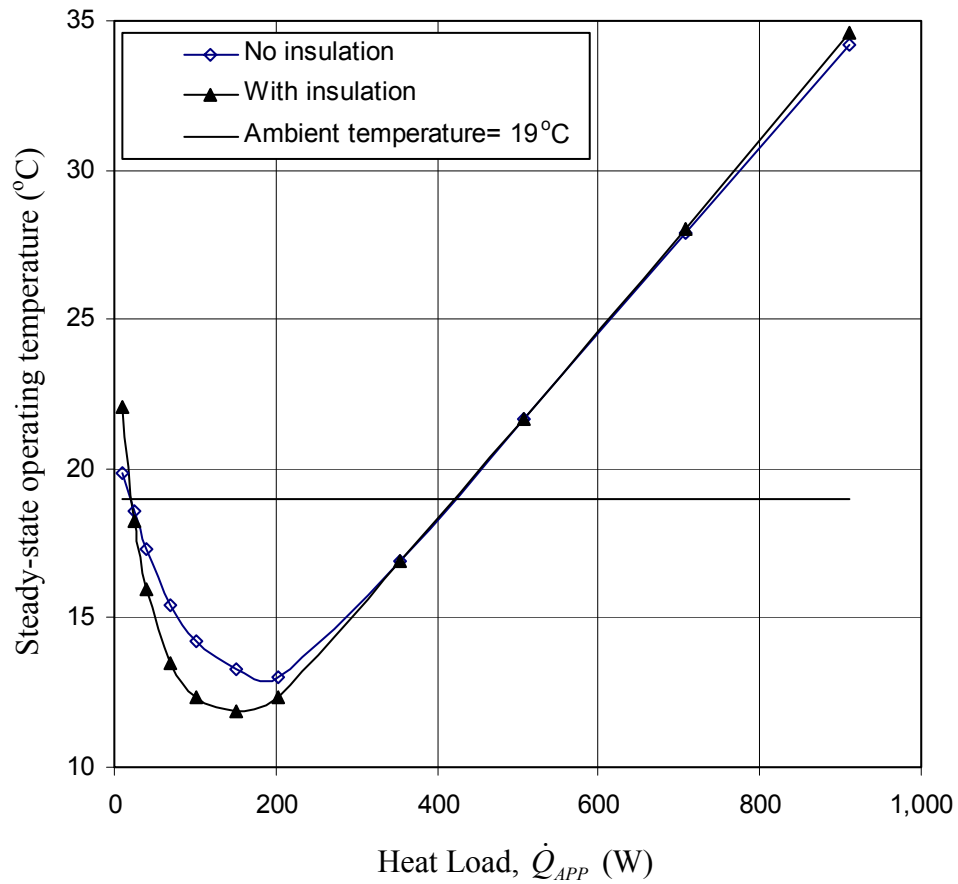
Fig. 6.30: Effect of insulation of the reservoir on the steady-state operating temperature. ($T_{SINK} = 5$ $^{\mathrm{o}}$C, $T_{AMB} = 19$ $^{\mathrm{o}}$C, and zero elevation)

6.3   CONCLUSION OF PARAMETRIC STUDY OF LOOP HEAT PIPES

A LHP is a complex two-phase heat transfer device that is very sensitive to many parameters. A slight change of one parameter may result in a considerable difference in the steady-state operating temperature. In addition, it may take a couple of hours to achieve a steady-state condition. The effect of a parameter on the performance of a LHP may be important only when the heat load is low or only when the heat load is high or it

may be important over the entire range of the heat load. Nevertheless, all the parameters have direct or indirect impact on the energy balance of the reservoir, $\dot{Q}_{HL} = \dot{Q}_{R-A} + \dot{Q}_{SC}$. Table 6.3 summarizes the effects of different parameters on the performance of a LHP qualitatively. The LHP performances listed in the table include the steady-state operating temperature, the transition heat load between the variable-conductance and fixed-conductance modes, $\dot{Q}_C$, the heat load corresponding to the minimum steady-state operating temperature, $\dot{Q}_M$, and the effect of the studied parameter at different ranges of the applied heat load.

The effects of different parameters on $\dot{Q}_C$ and $\dot{Q}_M$ are very complicated and determined by ambient temperature, the amount of heat leak, the amount of liquid subcooling brought back from the liquid line to the reservoir, the mass flow rate, the sink temperature, and physical setup of the LHP. It is very difficult to predict the change of $\dot{Q}_C$ and $\dot{Q}_M$ by intuition. Therefore, the present steady-state mode provides a unique tool to study the effects of various parameters in the design stage.

Table 6.3: Summary of the effect of various parameters on the performance of a LHP.

Parameter	Change of parameter	T_{SSOT}	Low $\dot{Q}_{APP}$	Medium $\dot{Q}_{APP}$	High $\dot{Q}_{APP}$	$\dot{Q}_C$	$\dot{Q}_M$
Sink temperature, T_{SINK}	↑	↑	◐	●	●	↓	↓
Ambient temperature, T_{AMB}	↑	↑	●	◐	○	↑	↑
Elevation (adverse: -, positive: +)	↑	↓	●	◐	○	↓	↓
External thermal conductance of the condenser, $\left(h_o A_o / L\right)_S$	↑	↓	○	◐	●	↑	↑
Axial heat leak, $\dot{Q}_{HL,A}$	↑	↑	●	◐	○	↑	↑
Radial heat leak, $\dot{Q}_{HL,R}$	↑	↑	◐	●	◐	↑	↓
Inner two-phase heat transfer coefficient	↑	↓	○	◐	●	↑	↑
Frictional two-phase pressure drop	↑	↑	○	●	◐	↑	↓
Insulation of the Reservoir	—	↑ ($T_{SSOT} > T_{AMB}$) ↓ ($T_{SSOT} > T_{AMB}$)	◐	◐	○	—	—

↑: Increase, ↓ : Decrease, ●: Strong influence, ◐: Moderate influence, ○: Little influence, —: Not applicable.

Low $\dot{Q}_{APP}$: 0 – 100 W, Medium $\dot{Q}_{APP}$: 100 – 400 W, High $\dot{Q}_{APP}$: 400 – 1000 W.

$\dot{Q}_C$: Transition heat load between variable-conductance and fixed-conductance modes

$\dot{Q}_M$: Heat load corresponding to the minimum steady-state operating temperature

Chapter 7

DISCUSSION OF RESULTS

The results discussed in this section are divided into three parts. The first part is the neutron radiography and neutron radioscopy results, which are used to demonstrate the ability of using neutron imaging as a tool to enhance both the design and the modeling of a LHP. The second part is the results of the loop heat pipe temperature tests, which are used to describe the characteristics of the test loop. The last part is the comparisons of the LHP temperature tests and the predicted results calculated by the proposed steady-state model. Due to physical restrictions on the flexible tubing, the test LHP could be operated only between 5-inch positive and 5-inch adverse elevations.

7.1   NEUTRON RADIOGRAPHY TESTS

Neutron radiography and radioscopy were employed in order to see through the aluminum casing of the LHP and to visualize the working ammonia flow within. The neutron beam facility at the Radiation Science and Engineering Center, The Pennsylvania State University, was utilized for these experiments. Most experiments were done with neutron radioscopy to observe the change of the flow condition in the LHP in real time. Some films were also taken using neutron radiography to observe the characteristics of steady-state conditions. Several key issues and findings were identified through the observations of neutron radiography.

7.1.1 Real Time Tests (Neutron Radioscopy)

Neutron radioscopy can be used to monitor the loop while it is operating. Dynamic and transient phenomena can be identified by neutron radioscopy. Radioscopic images were recorded on high-resolution videotape. Real-time difference images were used to qualitatively study the change in ammonia distribution.

One neutron radioscopic image of the reservoir is shown in Fig. 7.1. This image shows the details inside the reservoir, including the liquid level in the reservoir and the details of the bayonet. The aluminum and stainless steel portions of the LHP are essentially transparent to the neutrons. The ammonia and cooling water are sufficiently attenuating to produce good contrast, even in two-phase flow. This technique has great potential to help resolve issues of LHPs, including pressure oscillations, temperature hysteresis, start-up, and transient problems.
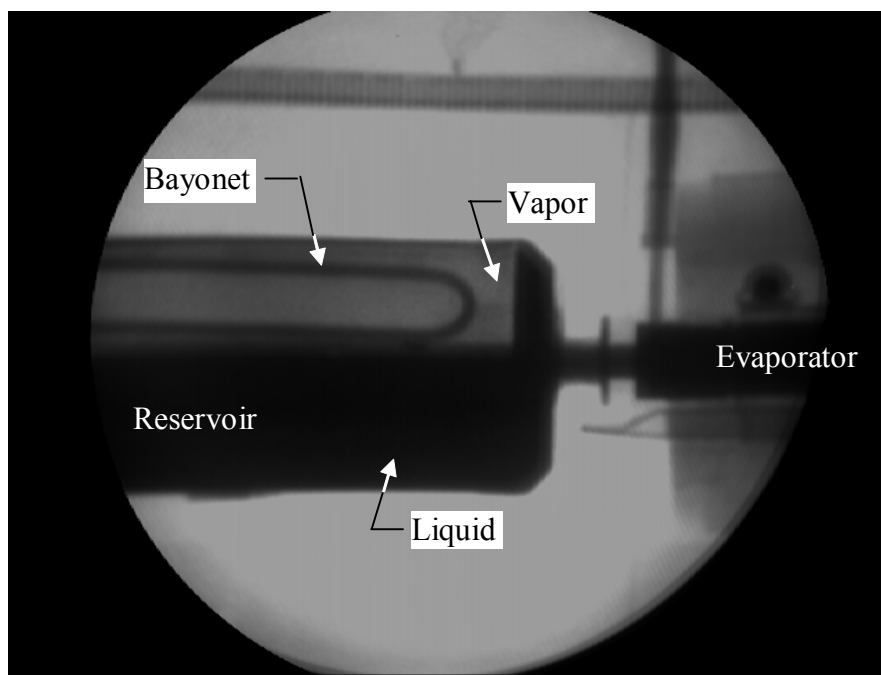
Fig. 7.1: Neutron radioscopic image of the reservoir and the evaporator.

7.1.2   Neutron Radiography Tests

Neutron radiography is the more traditional technique of exposing a film to the neutron beam. Due to the long exposure time (several minutes), neutron radiographs are useful only for steady-state operation or for long time averages.   The radiographic method gives higher spatial resolution than the radioscopic method, but provides no temporal information. These radiographs show more detail than the radioscopic pictures. A sample radiograph, which shows details of the reservoir and the evaporator, is provided in Fig. 7.2.
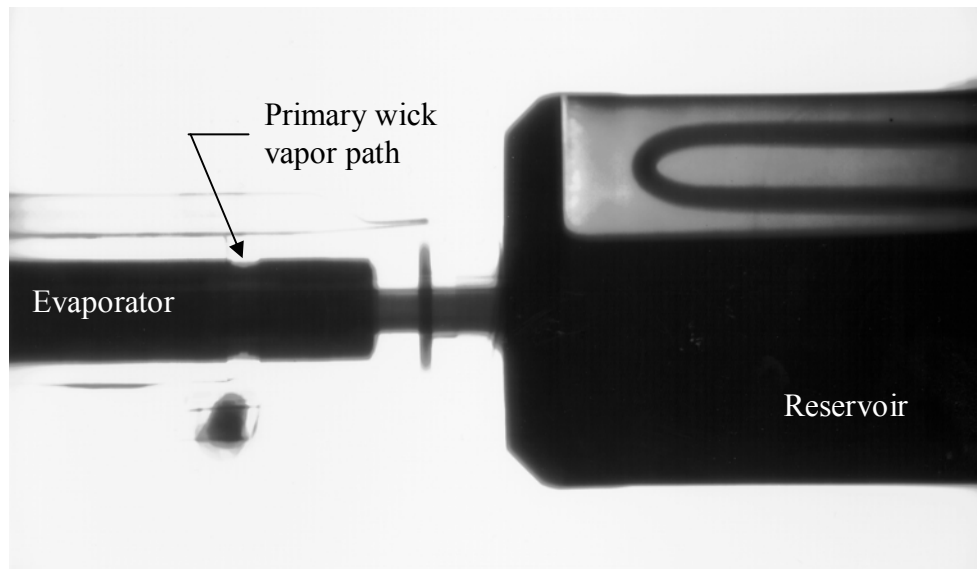
Fig. 7.2: Neutron radiograph of the reservoir and evaporate regions.

7.1.3   Observations Made by Neutron Radiography and Radioscopy

From the results obtained with neutron radiography and radioscopy, operating characteristics like reverse flow in the liquid line or two-phase flow in the vapor line were observed; these are discussed as follows.

Reverse Flow:

The flow of the working fluid in the liquid line is sometimes opposite to the normal flow direction, as observed with neutron radiography. This is a transient phenomenon, observed only when there's a sudden drop of applied heat load, e.g., when the heater is turned off. With less heat load, the liquid-vapor interface moves toward the inlet of the condenser, which draws back liquid downstream of the interface from the evaporator core. This interface self-adjusting phenomenon causes reverse flow in the loop.

Two-Phase Flow in the Liquid Line:

Under certain operating conditions, the liquid line may be filled with vapor or two-phase fluid rather than liquid. These conditions include when the sink temperature is higher than the ambient temperature, and at transient operating conditions (after adjustment of the heater power or the sink temperature). These phenomena were observed by neutron radioscopy as shown in Fig. 7.3. These observations agree with the predicted results of the steady-state model.
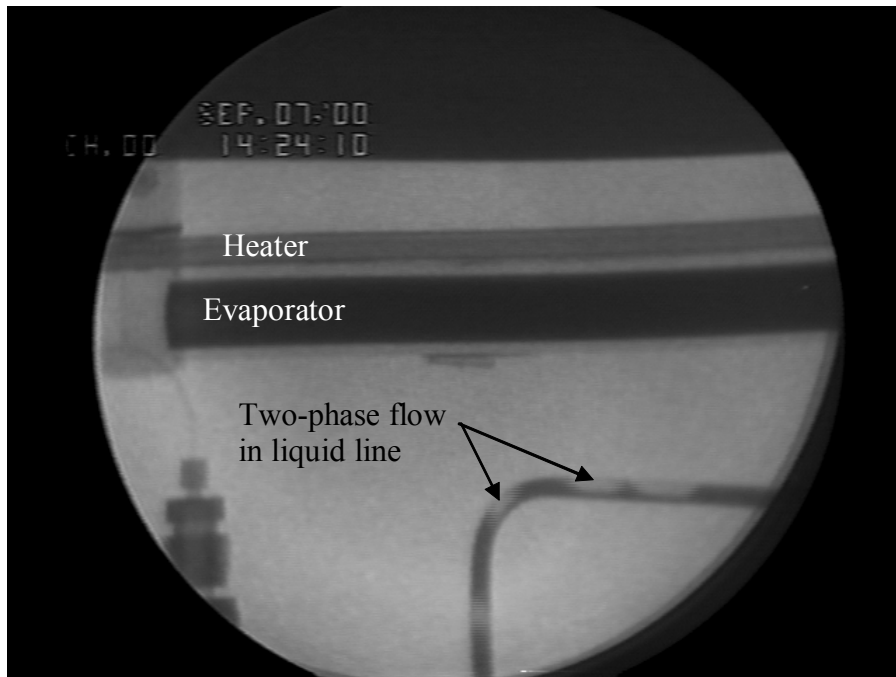
Fig. 7.3: A sample neutron radioscopic image of the liquid line demonstrating two-phase flow in the liquid line. (Transient condition with decreasing heat load.)

Location of the liquid-vapor interface:

Observations like the location of the liquid-vapor interface in the condenser and the liquid level in the reservoir at different heat loads were also identified by neutron radioscopy. When the LHP is operating in the fixed-conductance mode, the liquid-vapor interface in the condenser is observed to consistently occur near the condenser exit. This observation agrees with the analysis and predicted result of the steady-state model. Details of these discussions can be found in reference [Cimbala et al. 2001].

Two-phase flow in the vapor line (gravity-assisted operating theory):

To validate the proposed operating theory at positive elevation, neutron radiography was used to examine the LHP vapor line. Images were taken at different

heat loads with a positive elevation of 4 inches (102 mm). The images from neutron radioscopy are difficult to interpret without knowing the physical setup of the LHP in front of the neutron camera, therefore a picture of the setup is shown in Fig. 7.4.
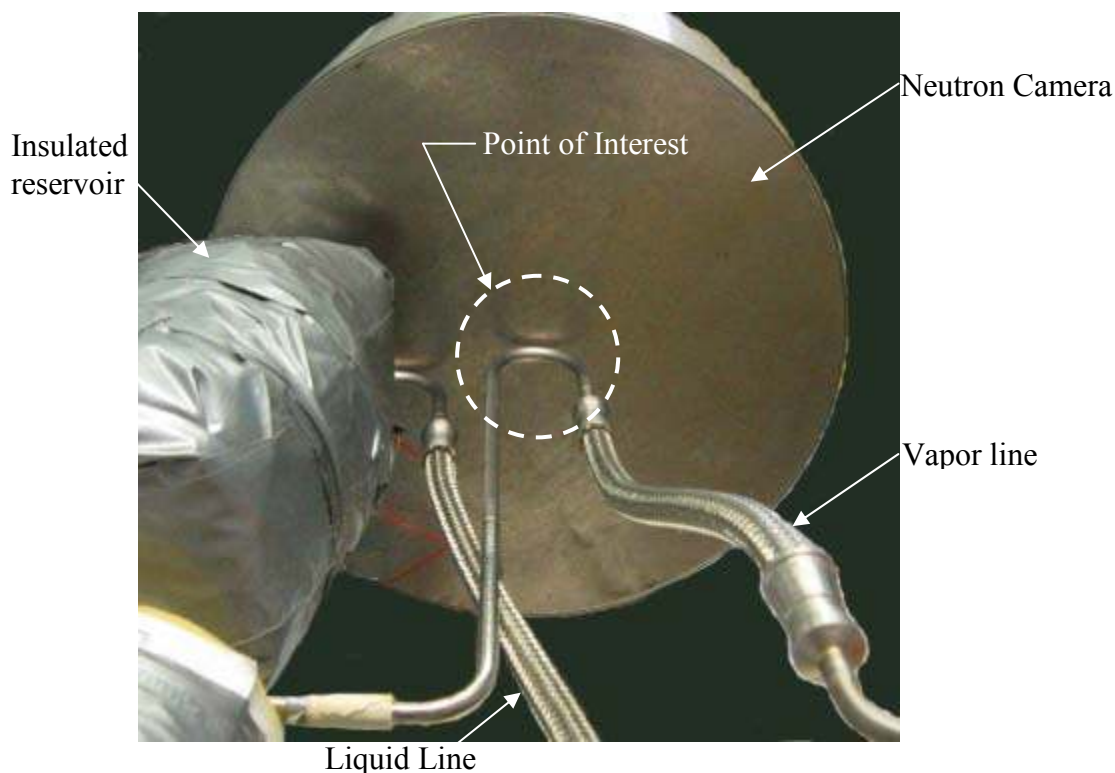
Fig. 7.4: A picture of the LHP setup in front of the neutron camera.

Fig. 7.5 shows images from neutron radioscopy taken at steady-state conditions when the heat load is equal to 5, 25, 70, 150, and 300 watts, respectively. These images give qualitative information of what happens in the vapor line. When the heat load is equal to 5 W, liquid chunks in the vapor line can be easily observed, and the flow pattern is slug flow (Fig. 7.5a). As the power is increased to 25 W, liquid slugs could still be observed in the vapor line (Fig. 7.5b). However, the slug at 25 W is lighter than that at 5

W, indicating less liquid. From the neutron radioscopy, it is observed that the slug travels at a higher speed with the heat load equal to 25 W than with the heat load equal to 5 W.
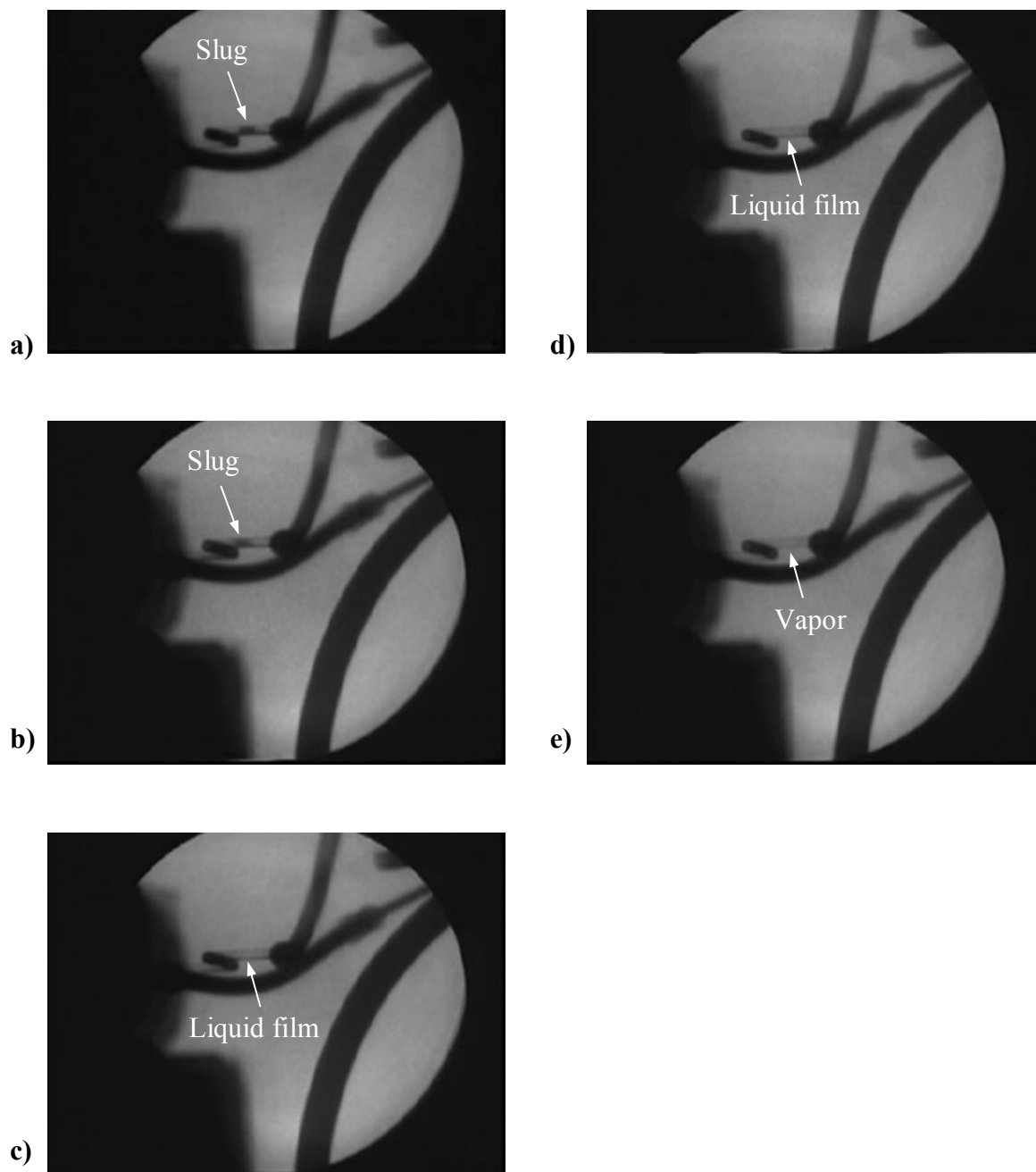
Fig. 7.5: Images from neutron radioscopy when the heat load is equal to a) 5 W, b) 25 W, c) 70 W, d) 150 W, and e) 300 W at 4-inch positive elevation.

As the heat load is further increased from 25 to 70 W (Fig. 7.5c), the flow pattern changes from slug flow to stratified flow. Instead of liquid slugs, a thin liquid film at the bottom of the tube is consistently observed. When the heat load is further increased to 150 W, this liquid film at the bottom can still be observed (Fig. 7.5d), although it is thinner than that in Fig. 7.5c). As the power is further increased to 300 W (Fig. 7.5e), the liquid disappears completely and the vapor line is filled with 100% vapor. In this test, the LHP operates in the gravity-controlled mode when the heat load is equal to or less than 150 W, and in the capillary-controlled mode when the heat load is equal to or greater than 300 W. The transition heat load fell somewhere between 150 and 300 W. The observations from the images of neutron radioscopy agree very well with the proposed gravity-assisted operating theory.

7.2   ANALYSIS OF THE EXPERIMENTAL DATA

To obtain reliable experimental test data, a substantial understanding of how a LHP works is necessary. For the past three years, by gaining more and more knowledge of LHPs, the author made changes to the procedures of taking experimental data. As discussed previously, the performance of a LHP is very sensitive to many parameters, like the setup of the LHP, the environment, applied heat load, etc. To ensure that the experimental data were reliable, the following guidelines were followed when performing the experiment.

Orientation of the test LHP:

The condenser was horizontally oriented at all times for a fixed elevation of the liquid-vapor interface in the condenser. The elevation refers to the vertical distance measured physically between the center of condenser tubes and the center of the evaporator. The evaporator/reservoir assembly was always placed horizontally. In other words, there was no tilt of the evaporator and the reservoir. The evaporator was connected to the reservoir with an offset rather than in the center (see Fig. 7.6b). This design is to ensure that the liquid level in the reservoir is higher than the evaporator. Therefore, the evaporator/reservoir assembly was placed as the position shown in Fig. 7.6b) throughout the entire study.

a) Top-view
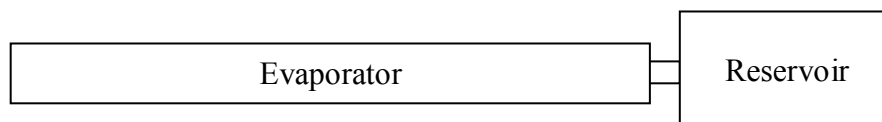
b) Side-view

Fig. 7.6: A schematic of the evaporator and the reservoir. (Not to scale)

Sink temperature and cooling water volume flow rate:

The sink temperature was fixed for a set of experimental data. This was controlled by the recirculating chiller. Also, the volume flow rate of the cooling water was controlled to be 1.1 ± 0.1 GPM by a valve.

Ambient temperature:

Without a fixed ambient temperature, a real steady-state condition could never be achieved. However, since a set of experimental data usually took more than 24 hours to complete, it was extremely difficult to control the ambient room temperature. An environmental chamber with an air-conditioner was therefore constructed and used to control the ambient temperature.

Applied heat load:

The applied heat load is the driving force of the LHP. For a reliable set of steady-state data, the heat load applied to the evaporator must be steady. A Variac and a watt meter were used to control and measure the heat load applied to the evaporator. The evaporator and strip heater assembly was insulated at all times to ensure minimum heat loss from the strip heater to the ambient.

Steady-state operating temperature:

The steady-state operating temperature (SSOT) of the LHP refers to the reservoir temperature when the LHP achieves a steady-state condition. In the experiments, the criterion for a steady-state condition to have been achieved is that the operating temperatures measured on the reservoir changed by no more than 0.5 $^{\circ}$C over 25 minutes.

Period of the experiment:

When the heat load is low, the LHP may take hours to achieve steady-state conditions. Thus, with a study of the whole range of the heat load, an experimental set of data usually took more than 24 hours to complete. The reliability of a steady-state experimental data set with a short experimental time period is questionable.

<u>Preconditioning:</u>

It was found that the performance of the LHP depends greatly on the preconditioning of the system, which determines the vapor quality in the evaporator core. This is the most ambiguous guideline to follow because there is no way to verify the vapor quality in the evaporator core. Different vapor quality in the evaporator core would result in different LHP performances. Thus, to ensure uniformity of the experimental sets, the rig sat idle for more than two nights between each experiment. In addition, the chiller and the environmental chamber were turned on more than 2 hours before applying any heat to the evaporator.

7.2.1 Experimental Study of Steady-State Operating Temperature at Different Elevations

After the flow visualization study (discussed in Section 7.1.3), detailed steady-state experiments for the LHP operating at different elevations were performed. To ensure similar vapor quality in the evaporator core, the following precondition was consistently used for all the experimental data sets: right at the beginning of each data set, high power (700 W) was applied for more than 30 minutes. The sequence of the heat load applied to the evaporator was 10, 25, 40, 70, 100, 150, 200, 300, 400, 500, and 700 W. The actual heat load was measured by a watt meter and might vary slightly from one data set to another because it was difficult to adjust the Variac to the same reading every time. Each experimental data set took more than 24 hours to complete, because it took more than 4 hours to achieve a steady-state condition when the heat load was extremely low.

To improve the accuracy of the data, some components of the LHP were insulated. As described previously, the evaporator and strip heater assembly was always insulated to control the heat load applied to the LHP. The reservoir was also insulated. Therefore, the amount of heat leak from the evaporator must be balanced by the amount of subcooling brought back from the liquid line, as seen in Eq. 4.2. To prevent any condensation or evaporation from occurring in the vapor line, the vapor line was insulated also.

The inlet temperature of the cooling water supplied by the chiller was set at 5 ^{o}C. Because the cooling water tube and condenser plate were open to the ambient air, there was heat gained from the ambient. Therefore, the actual sink temperature depended on the heat load and was slightly higher than 5 ^{o}C. The ambient temperature of the LHP was controlled by the environmental chamber and was set to 18.5 ± 0.5 ^{o}C.

Experiments at five elevations: 2-inch adverse, zero, 1-inch, 3-inch, and 5-inch positive elevations, were performed. The results of the measured heat load and temperatures at these five elevations are listed in Table 7.1, Table 7.2, Table 7.3, Table 7.4, and Table 7.5, respectively. Trends of steady-state operating temperature, temperature exiting the condenser and the liquid line, and ambient temperature at 2-inch adverse, zero, 1-inch, 3-inch, and 5-inch positive elevations, are plotted in Fig. 7.7, Fig. 7.8, Fig. 7.9, Fig. 7.10, and Fig. 7.11, respectively. These data sets agree with the trends presented in Section 4.1.2 for zero or adverse elevation and in Section 4.2.3 for positive elevation.

Table 7.1: Applied heat load, steady-state operating temperature, temperatures exiting the liquid line and the condenser, and ambient temperature when the LHP was operated at 2-inch adverse elevation.

Step	1	2	3	4	5	6	7	8	9	10	11
$\dot{Q}_{APP}$ (W)	9.0	24.0	41.0	71.0	100.0	153.0	197.0	302.0	396.0	507.0	698.0
T_{SSOT} (°C)	27.1	25.2	23.9	22.4	20.7	18.4	16.8	15.7	17.1	20.2	25.3
TL_{OUT} (°C)	20.7	18.8	18.1	16.7	15.6	13.8	13.0	12.7	14.4	17.1	21.9
TC_{OUT} (°C)	8.0	7.3	7.1	7.2	7.1	7.0	7.1	9.1	12.3	16.3	22.3
T_{AMB} (°C)	18.7	18.7	18.5	18.6	18.7	18.4	18.6	18.5	18.5	18.6	18.4
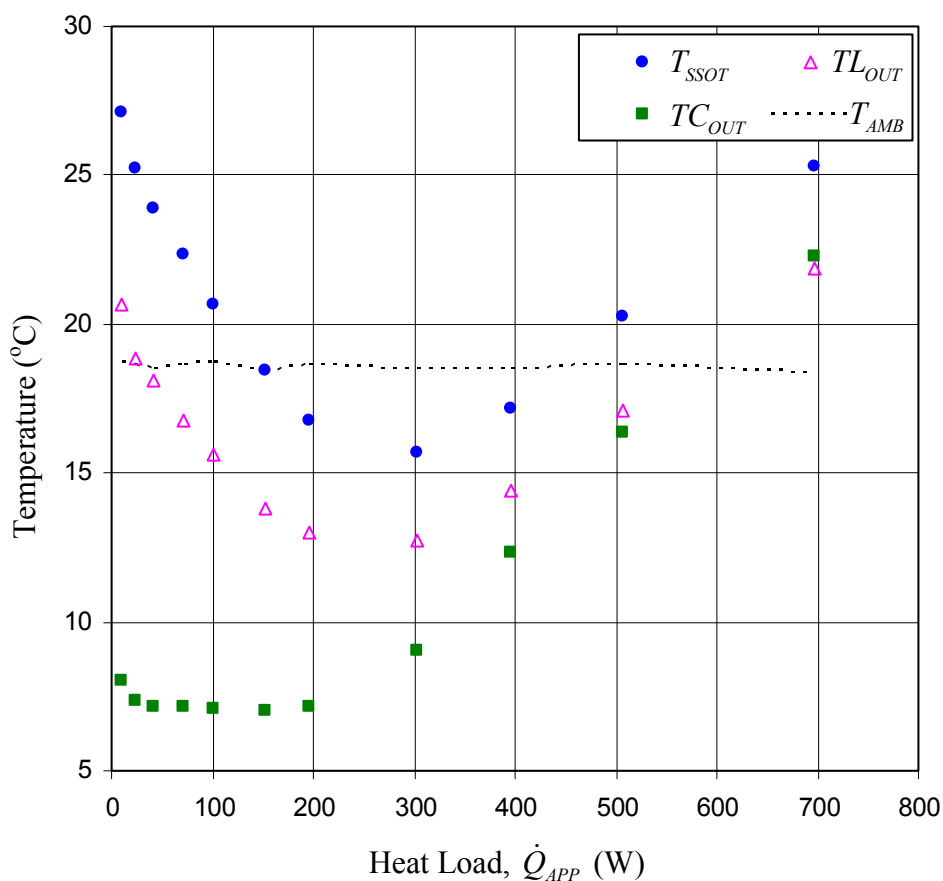
Fig. 7.7: Trends of steady-state operating temperature, temperatures exiting the liquid line and the condenser, and ambient temperature as functions of heat load. ($T_{SINK} = 5$ °C, 2-inch adverse elevation, insulation on evaporator, reservoir, and vapor line)

Table 7.2: Applied heat load, steady-state operating temperature, temperatures exiting the liquid line and the condenser, and ambient temperature when the LHP was operated at zero elevation.

Step	1	2	3	4	5	6	7	8	9	10	11
$\dot{Q}_{APP}$ (W)	9.0	26.0	37.0	69.0	100.0	150.0	203.0	299.0	400.0	498.0	703.0
T_{SSOT} (^{o}C)	23.3	22.1	21.7	20.6	19.3	17.7	16.0	15.5	17.4	19.9	25.4
TL_{OUT} (^{o}C)	19.1	18.7	18.4	17.1	15.6	14.1	13.1	12.9	14.7	17.3	21.7
TC_{OUT} (^{o}C)	7.9	7.5	7.4	7.2	7.1	7.3	7.4	9.3	13.1	16.6	22.1
T_{AMB} (^{o}C)	18.5	18.5	18.6	18.5	18.5	18.5	18.6	18.5	18.5	18.9	18.8
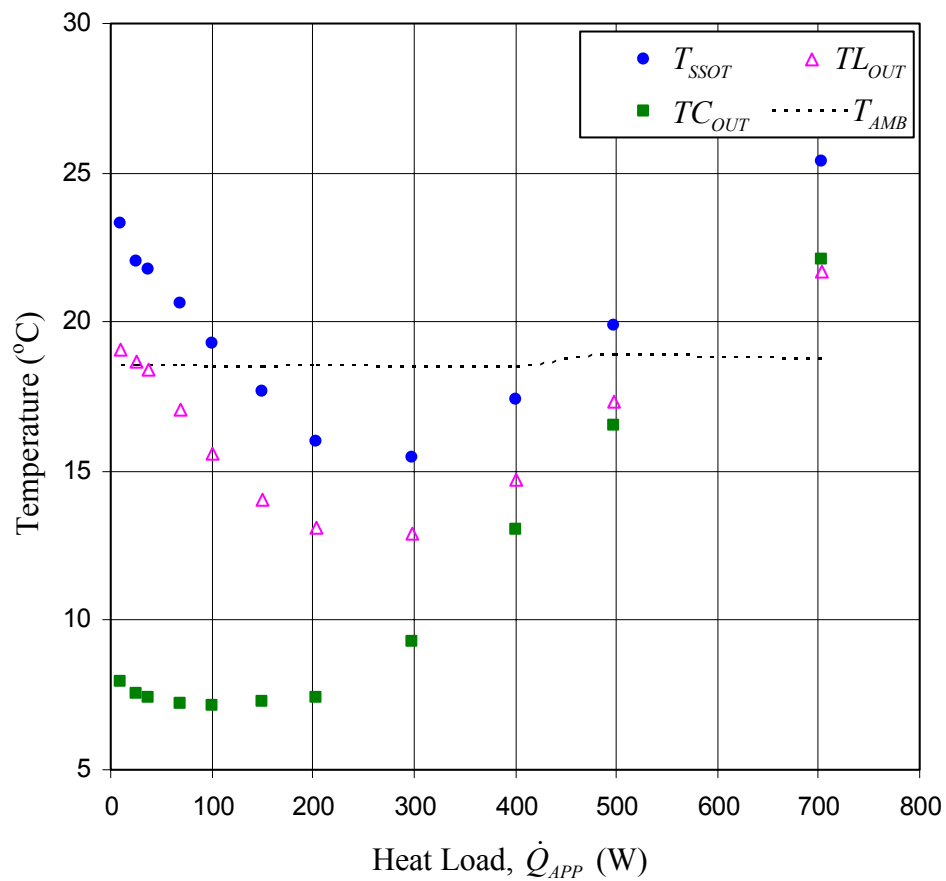
Fig. 7.8: Trends of steady-state operating temperature, temperatures exiting the liquid line and the condenser, and ambient temperature as functions of heat load. ($T_{SINK} = 5$ ^{o}C, zero elevation, and insulations on evaporator, reservoir, and vapor line)

Table 7.3: Applied heat load, steady-state operating temperature, temperatures exiting the liquid line and the condenser, and ambient temperature when the LHP was operated at 1-inch positive elevation.

Step	1	2	3	4	5	6	7	8	9	10	11
$\dot{Q}_{APP}$ (W)	11.0	23.0	40.0	70.0	101.0	153.0	199.0	300.0	397.0	498.0	683.0
T_{SSOT} (°C)	22.8	22.3	20.9	20.3	19.0	17.3	16.3	15.5	17.4	19.9	25.3
TL_{OUT} (°C)	18.9	18.7	18.3	17.1	15.7	14.1	13.4	13.3	14.9	17.5	21.8
TC_{OUT} (°C)	7.4	7.2	7.0	7.1	7.1	7.1	7.3	9.3	12.9	16.7	22.3
T_{AMB} (°C)	17.8	17.8	17.9	18.1	18.1	18.2	18.4	18.4	18.5	18.7	19.0
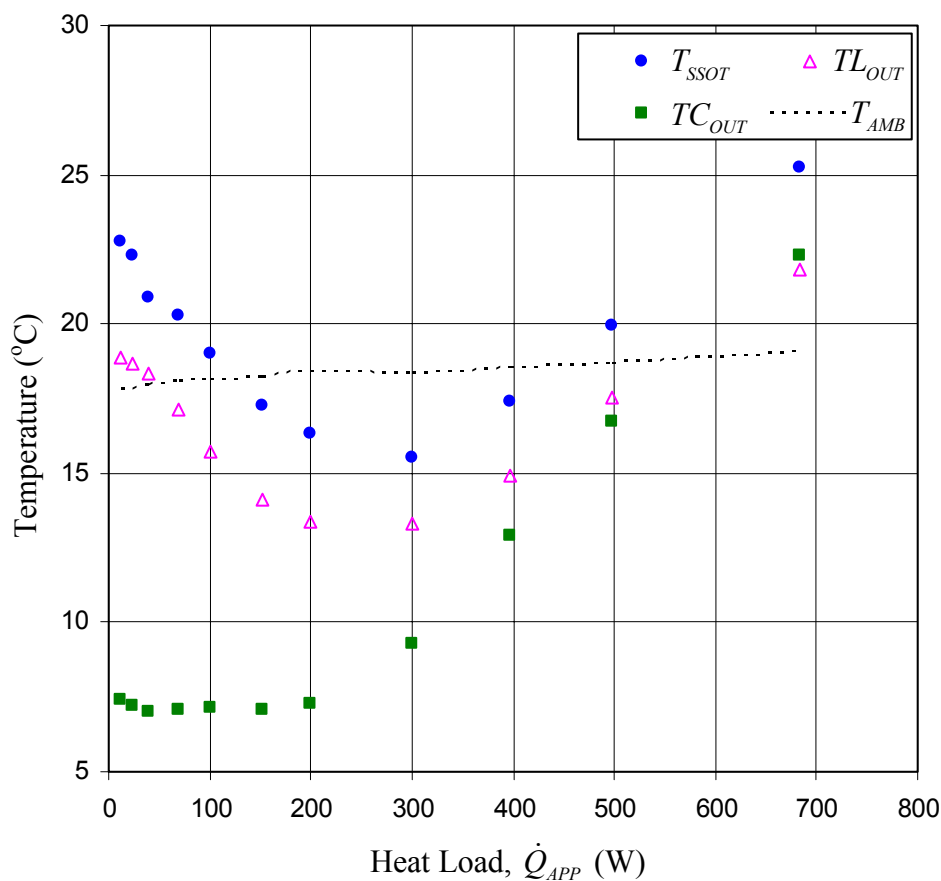
Fig. 7.9: Trends of steady-state operating temperature, temperatures exiting the liquid line and the condenser, and ambient temperature as functions of heat load. ($T_{SINK} = 5$ °C, 1-inch positive elevation, and insulations on evaporator, reservoir, and vapor line)

Table 7.4: Applied heat load, steady-state operating temperature, temperatures exiting the liquid line and the condenser, and ambient temperature when the LHP was operated at a 3-inch positive elevation.

Step	1	2	3	4	5	6	7	8	9	10	11
$\dot{Q}_{APP}$ (W)	11.0	25.0	41.0	69.0	103.0	148.0	199.0	301.0	401.0	502.0	685.0
T_{SSOT} (°C)	17.9	17.2	17.1	17.3	17.0	16.9	16.1	15.5	17.4	20.2	25.3
TL_{OUT} (°C)	17.0	15.9	15.7	15.8	15.4	14.3	13.3	13.4	15.4	17.7	21.9
TC_{OUT} (°C)	7.0	7.0	7.0	7.1	7.2	7.1	7.3	9.4	13.4	17.0	22.4
T_{AMB} (°C)	18.0	17.9	18.0	17.9	18.0	17.9	17.9	18.1	18.4	18.6	19.3
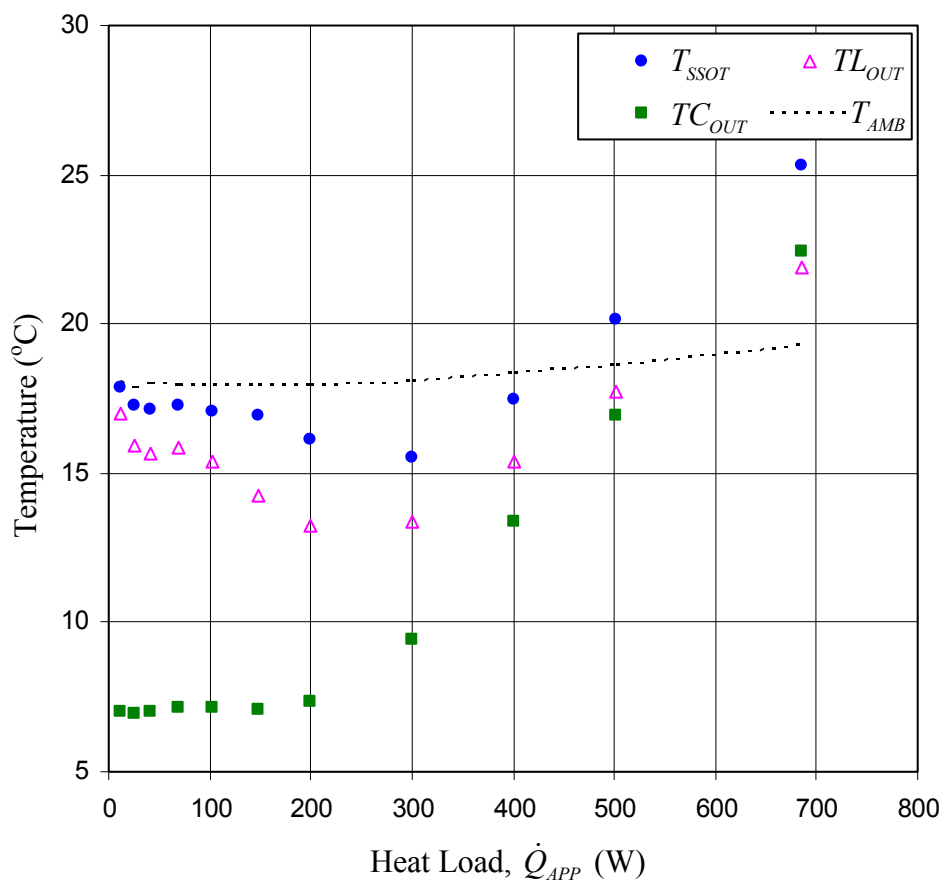
Fig. 7.10: Trends of steady-state operating temperature, temperatures exiting the liquid line and the condenser, and ambient temperature as functions of heat load. ($T_{SINK} = 5$ °C, 3-inch positive elevation, and insulations on evaporator, reservoir, and vapor line)

Table 7.5: Applied heat load, steady-state operating temperature, temperatures exiting the liquid line and the condenser, and ambient temperature when the LHP was operated at 5-inch positive elevation.

Step	1	2	3	4	5	6	7	8	9	10	11
$\dot{Q}_{APP}$ (W)	10.0	24.0	38.0	70.0	103.0	149.0	203.0	304.0	404.0	500.0	698.0
T_{SSOT} (°C)	12.8	12.4	11.5	12.3	13.1	14.3	15.0	15.9	17.4	20.1	25.6
TL_{OUT} (°C)	12.7	11.8	11.6	11.8	12.2	12.4	12.6	12.7	15.5	18.2	22.5
TC_{OUT} (°C)	6.9	6.9	6.9	7.0	6.9	7.0	7.3	9.1	14.1	17.3	22.3
T_{AMB} (°C)	18.5	18.5	18.3	18.6	18.3	18.4	18.3	18.3	18.3	18.6	18.6

Fig. 7.11: Trends of steady-state operating temperature, temperatures exiting the liquid line and the condenser, and ambient temperature as functions of heat load. ($T_{SINK} = 5$ °C, 5-inch positive elevation, and insulations on evaporator, reservoir, and vapor line)

Fig. 7.12 shows a comparison of the steady-state operating temperature as a function of heat load at different elevations. The steady-state operating temperature was obtained by averaging the temperatures measured by four thermocouples on the reservoir (see Fig. 3.1 for details) with an accuracy of ± 0.5 °C. It is clear that for all five elevations, the transition heat load between the fixed-conductance and the variable-conductance modes was between 300 and 350 W.
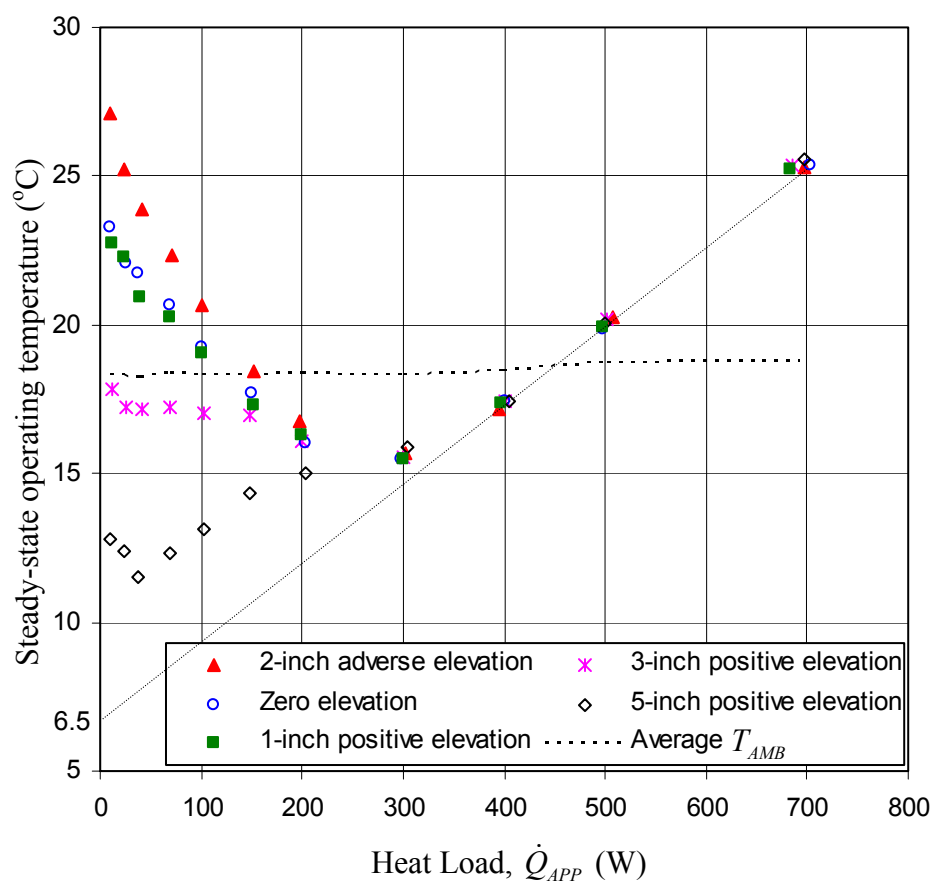
Fig. 7.12: Comparison of steady-state operating temperature as a function of heat load at different elevations. ($T_{SINK} = 5$ °C and insulations on evaporator, reservoir, and vapor line)

From the data analysis, the actual average sink temperature was around 6.5 $^{\circ}$C instead of 5 $^{\circ}$C because of the heat gain from the ambient and working fluid. The maximum heat transfer coefficient of the LHP, $(UA)_{LHP}$, was calculated to be 37.5 ± 1.0 W/K. The overall trends of the experimental data at different elevations agree with the results predicted by the steady-state model presented in Section 6.2.3. The steady-state operating temperature increases with increasing adverse elevation or decreasing positive elevation. Elevation has significant influence when the heat load is low, but little influence when the heat load is high. The transition heat load between the capillary-controlled mode and the gravity-controlled mode increases with increasing positive elevation. The transition heat load corresponding to 1, 3, and 5-inch positive elevation is between 40 and 70 W, 100 and 150 W, and 200 and 300 W, respectively.

The fluid temperature exiting the condenser, TC_{OUT}, as a function of heat load at different elevations is plotted in Fig. 7.13. This temperature was physically measured by a thermocouple with an accuracy of $\pm$ 0.5 $^{\circ}$C at a location 0.5 inches downstream of the exit of the condenser. In Fig. 7.13, it is seem that the fluid temperature exiting the condenser was not a function of elevation. Because the temperature was measured 0.5 inches downstream of the condenser, the temperature measured might be slightly different than the actual temperature exiting the condenser, especially when the mass flow rate in the system is extremely small. This explains why the fluid temperatures at 2-inch adverse and zero elevation were slightly higher than those at positive elevation when the heat load was lower than 50 W in Fig. 7.13.
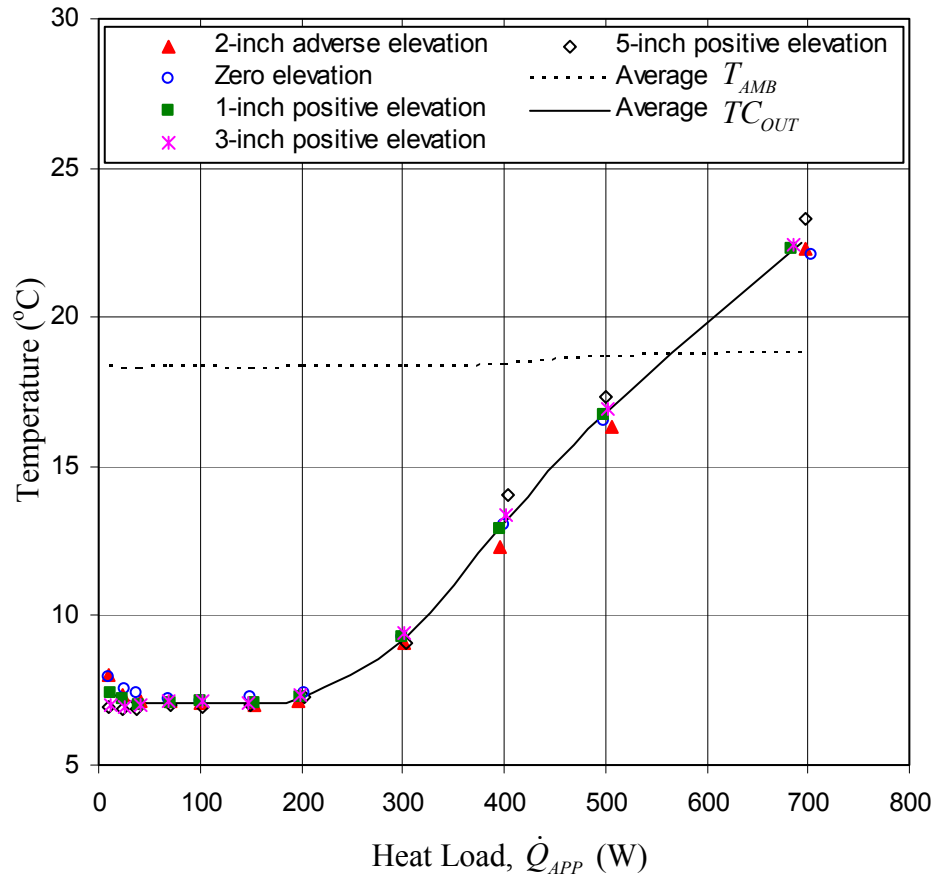
Fig. 7.13: Comparison of fluid temperature exiting the condenser, TC_{OUT}, as a function of heat load at different elevations. ($T_{SINK} = 5$ °C and insulations on evaporator, reservoir, and vapor line)

From theoretical analysis, the temperature exiting the condenser depends mainly on the saturation temperature and applied heat load for the same condenser operating conditions, like cooling water temperature and volume flow rate. When the heat load was lower than 200 W in Fig. 7.13, the vapor was quickly condensed back to liquid and then subcooled to a temperature close to the sink temperature. From a point of view concerned with the performance of the condenser, this operating condition is referred to as the variable-conductance mode. In contrast, when the heat load was higher than 300

W in Fig. 7.13, the vapor was fully condensed back to liquid almost at the end of the condenser and then slightly subcooled. The temperature exiting the condenser follows the trend of the steady-state operating temperature.

Fig. 7.14 shows the fluid temperature exiting the liquid line, TL_{OUT}, as a function of heat load at different elevations. This temperature was physically measured by a thermocouple with an accuracy of $\pm$ 0.5 $^{\circ}$C at a location 0.5 inches upstream of the exit of the liquid line, just before the entrance to the reservoir.
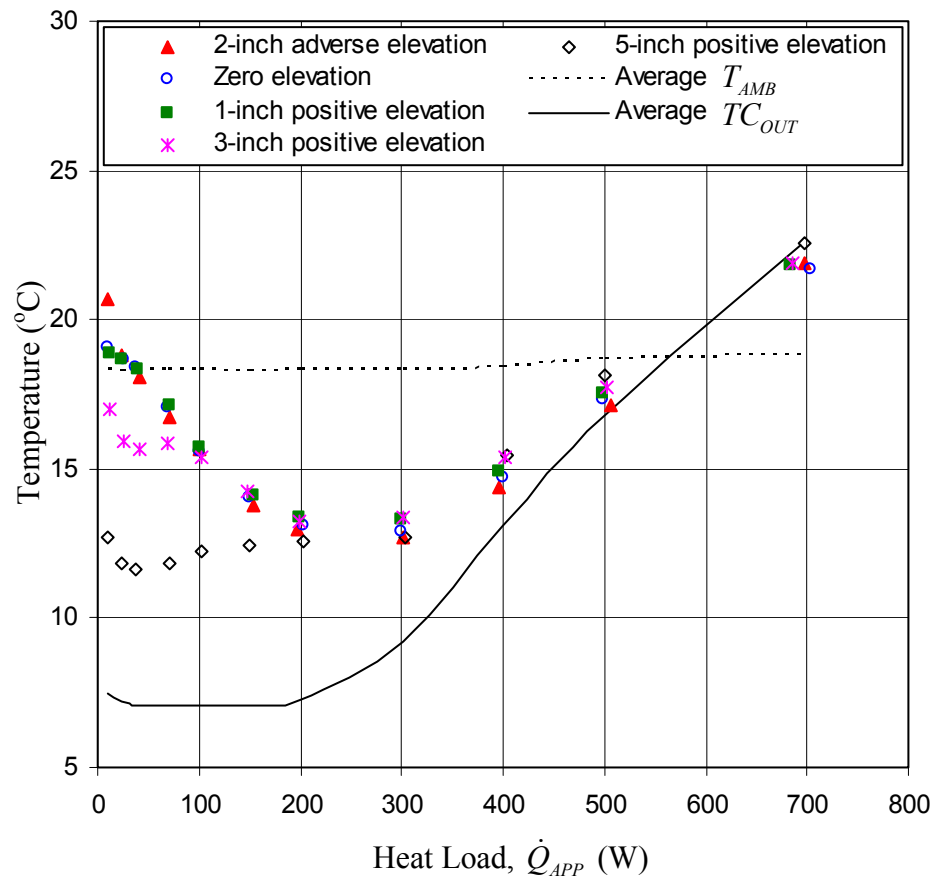
Fig. 7.14: Comparison of fluid temperature exiting the liquid line, TL_{OUT}, as a function of heat load at different elevations. ($T_{SINK} = 5$ $^{\circ}$C and insulations on evaporator, reservoir, and vapor line)

The fluid flowing in the liquid line exchanges heat with the ambient by natural convection. Thus, the temperature exiting the liquid line depends on inlet temperature, mass flow rate, heat transfer coefficient, and ambient temperature. Since inlet temperature, TC_{OUT}, was consistent for different elevations, and ambient temperature was controlled by the environmental chamber and varied within 0.5 ^{o}C, the temperature exiting the liquid line depended only on mass flow rate in the LHP. An operating condition with a lower mass flow rate resulted in a greater temperature difference between the inlet and exit temperatures.

In Fig. 7.14, the fluid temperature exiting the liquid line for 2-inch adverse, zero, and 1-inch positive elevation conditions was very consistent. For 2-inch adverse and zero elevation conditions, the LHP was always operating in the capillary-controlled mode. Thus, the mass flow rate depended only on applied heat load and heat of vaporization, and should be consistent. For 1-inch positive elevation, experimental data show that the test LHP is insensitive to small elevations, like 1 inch, and the operating conditions are similar to zero elevation.

When the LHP was operated at 3-inch or 5-inch positive elevations, the trends of the fluid temperature exiting the liquid line were obviously different from those of 2-inch adverse, zero, and 1-inch positive elevations. The transition heat load between the capillary-controlled mode and gravity-controlled mode was around 100 W and 200W for 3-inch and 5-inch positive elevation, respectively. The trends agree with the theoretical analysis presented in Section 4.2.3.

7.2.2   Study of Temperature Hysteresis

Temperature hysteresis is identified by the fact that the steady-state operating temperature depends not only on the imposed heat load but also on the previous history of the heat load variation and pre-conditioning.   The phenomenon of temperature hysteresis was observed in the test LHP at different elevations.   Fig. 7.15 show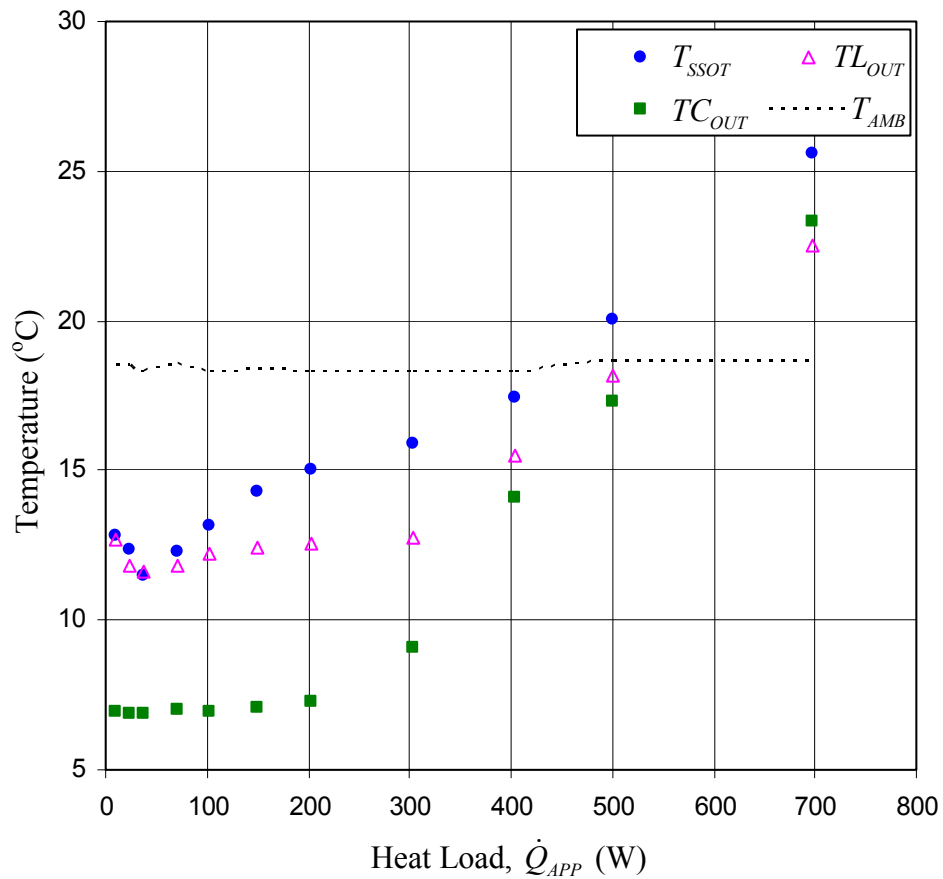s the steady-state operating temperature, the temperature exiting the liquid line and the condenser, and the ambient temperature as functions of heat load when the LHP was operated at 3 ½-inches adverse elevation.   The results of the measured heat load and temperature are listed in Table 7.6.   The test LHP was allowed to lay still overnight before the experiment.   There were 13 steps of heat load performed in this experimental data set, starting at 20 W (step 1), increasing gradually until 600 W (step 7), and then following the same path back to 20 W (step 13).

In Fig. 7.15, the steady-state operating temperature followed the lower trend with increasing heat load, and followed the upper trend with decreasing heat load.   A 4 ^{o}C magnitude of temperature hysteresis was observed in this data set.   The temperature exiting the condenser and the liquid line for the upper trend and lower trend did not show significant hysteresis, except at steps 5 and 9.   The higher steady-state operating temperature (step 9) resulted in lower fluid temperature exiting the condenser and the liquid line, because a greater temperature difference between the sink temperature and the steady-state operating temperature required less condenser length to remove the same heat load (300 W).   However, when the heat load was low and the location of the liquid-

vapor interface was well within the condenser (steps 1, 2, 3, 4, 10, 11, 12, and 13), the fluid temperature exiting the condenser was always subcooled to sink temperature.

When the heat load was around 20 W in Fig. 7.15, the fluid temperature exiting the liquid line was higher than the ambient temperature. A certain amount of heat was conducted from the reservoir to the liquid line. Because temperature TL_{OUT} was measured at 0.5 inches before the end of the liquid line just upstream of the reservoir, and the thermocouple was mounted on the outer surface of the tube. It is reasonable that the measured liquid temperature exiting the liquid line is higher than the ambient temperature when the mass flow rate in the LHP is small.

Table 7.6: Applied heat load, steady-state operating temperature, temperatures exiting the liquid line and the condenser, and ambient temperature when the LHP was operated at 3 ½-inch adverse elevation.

Step	1	2	3	4	5	6	7	8	9	10	11	12	13
$\dot{Q}_{APP}$ (W)	21	48	100	152	311	459	598	450	303	150	96	50	20
T_{SSOT} (°C)	22.0	22.1	20.6	19.3	17.7	21.3	24.6	21.3	19.9	22.3	24.4	26.1	26.3
TL_{OUT} (°C)	21.5	19.5	15.9	14.1	13.8	15.0	20.1	15.0	12.0	14.2	16.6	19.7	22.0
TC_{OUT} (°C)	7.6	7.8	7.7	7.8	11.2	13.6	19.1	13.5	8.4	7.6	7.7	7.9	8.0
T_{AMB} (°C)	19.1	19.7	19.3	20.7	21.8	21.3	22.5	21.5	20.9	20.8	20.8	20.4	20.4
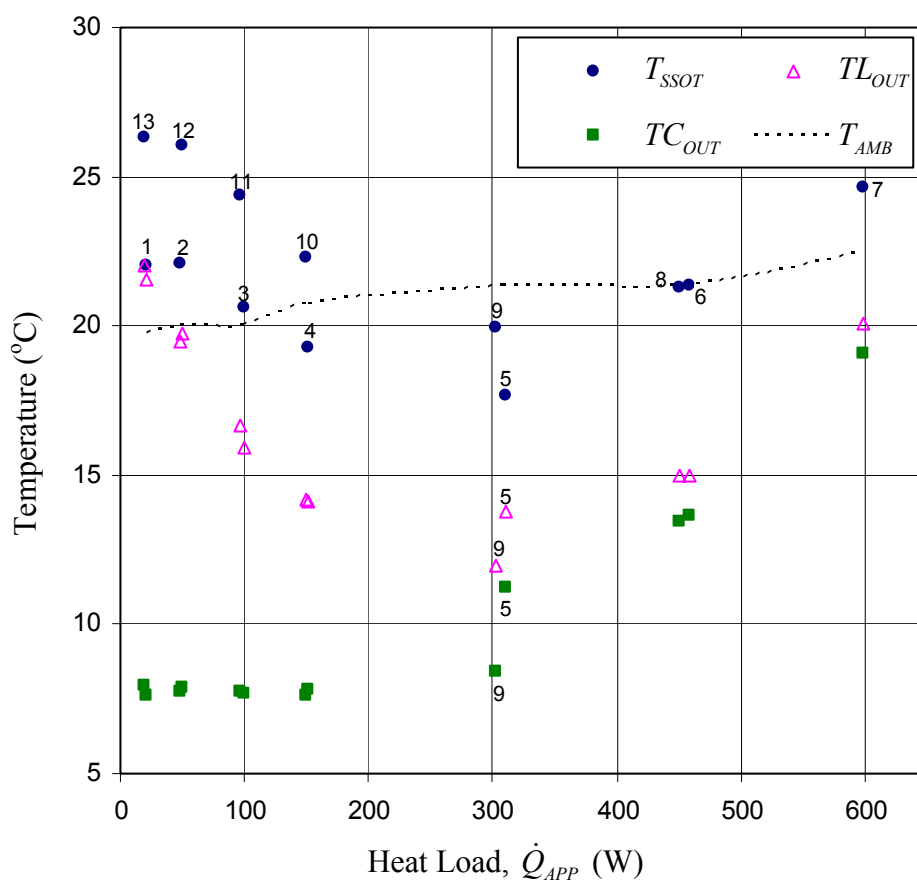
Fig. 7.15: Steady-state operating temperature, temperatures exiting the liquid line and condenser, and ambient temperature as functions of heat load. (T_{SINK}=5 °C, 3 ½-inch adverse elevation, and insulation on the evaporator). The numbers represent steps in the sequence of applying heat load.

Fig. 7.16 shows the difference between the steady-state operating temperature and the fluid temperature exiting the liquid line as a function of heat load. This temperature difference represents the amount of subcooling, $\dot{Q}_{SC}$, brought back by the liquid from the liquid line to the reservoir. It is assumed in the energy balance equation of the reservoir (Eq. 4.2) that the heat exchanged between the reservoir and the ambient, $\dot{Q}_{R-A}$, is through natural convection and is substantially small compared to heat leak, $\dot{Q}_{HL}$, and subcooling, $\dot{Q}_{SC}$. Thus, more subcooling brought back to the reservoir means more heat leak from the evaporator to the reservoir.

In Fig. 7.16, when operated at the same heat load, the upper trend had higher heat leak than the lower trend. This observation confirms that although the LHP is operated with the same operating conditions including heat load, the heat leak from the evaporator to the reservoir may be different and thus results in a different steady-state operating temperature.
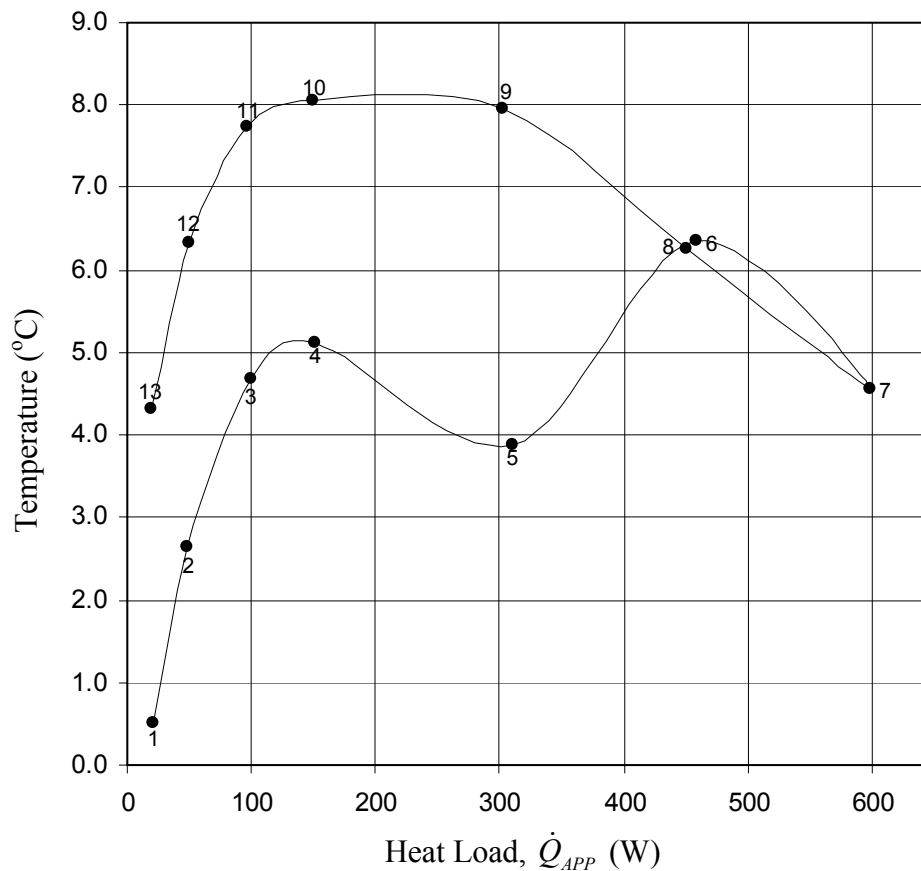
Fig. 7.16: Difference between the steady-state operating temperature and the fluid temperature exiting the liquid line as a function of heat load. (T_{SINK} =5 ^{o}C, 3 ½-inch adverse elevation, and insulation on the evaporator). The numbers represent steps in the sequence of applying heat load.

The phenomenon of temperature hysteresis was also investigated experimentally when the test LHP was operated at zero and 3 ½-inch positive elevation. The results of the measured heat load and temperature when the LHP was operated at zero elevation are listed in Table 7.7. Fig. 7.17 shows the steady-state operating temperature, temperature exiting the liquid line and the condenser, and the ambient temperature as functions of heat load when the LHP was operated at zero elevation.

Table 7.7: Applied heat load, steady-state operating temperature, temperatures exiting the liquid line and the condenser, and ambient temperature when the LHP was operated at zero elevation.

Step	1	2	3	4	5	6	7	8	9	10	11	12	13
$\dot{Q}_{APP}$ (W)	20	51	100	154	296	458	600	444	310	148	98	51.5	18.0
T_{SSOT} (°C)	23.6	23.0	21.3	19.7	17.7	20.5	24.6	21.0	19.7	22.9	24.2	25.1	25.3
TL_{OUT} (°C)	22.6	19.9	16.5	14.8	13.3	18.8	20.2	15.4	12.7	15.1	16.8	20.1	23.4
TC_{OUT} (°C)	8.3	7.9	7.8	7.8	10.0	17.4	19.1	13.9	8.9	7.8	7.8	7.9	8.1
T_{AMB} (°C)	22.4	22.6	22.3	22.8	22.7	23.1	23.5	22.9	22.5	22.5	22.3	22.4	23.4
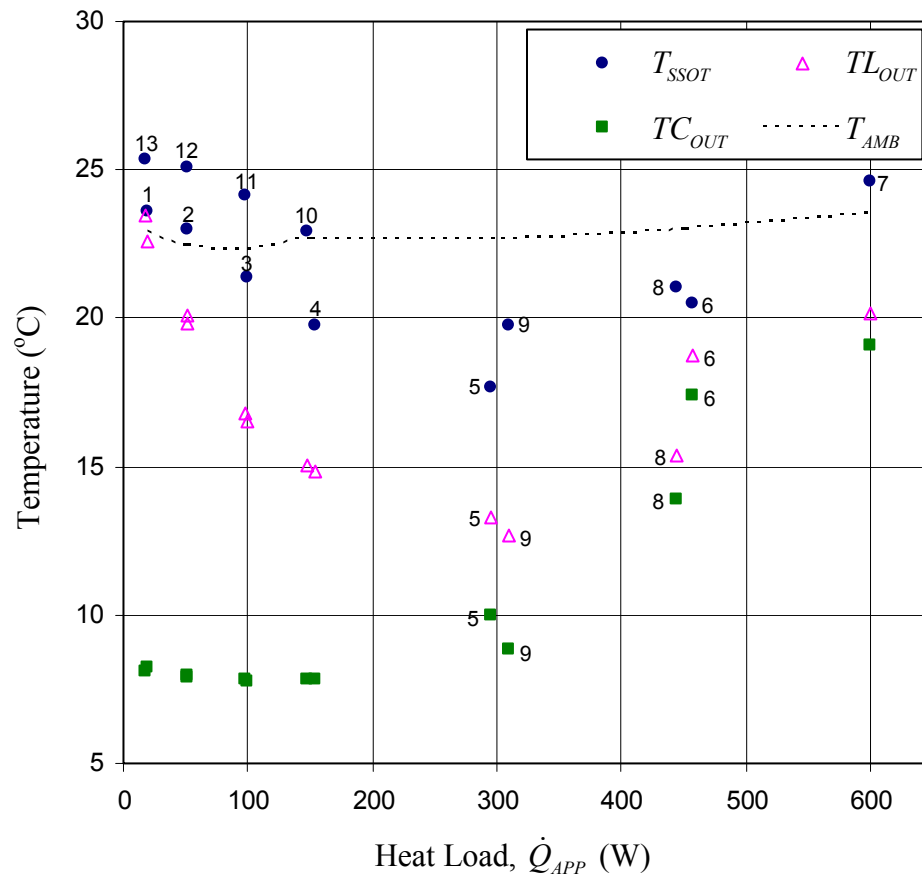
Fig. 7.17: Steady-state operating temperature, temperatures exiting the liquid line and condenser, and ambient temperature as functions of heat load. (T_{SINK} =5 °C, zero elevation, and insulation on the evaporator). The numbers represent steps in the sequence of applying heat load.

A maximum temperature hysteresis of 3.1 °C was observed in steady-state operating temperature. The difference between the steady-state operating temperature and the fluid temperature exiting the liquid line as a function of heat load is plotted in Fig. 7.18.
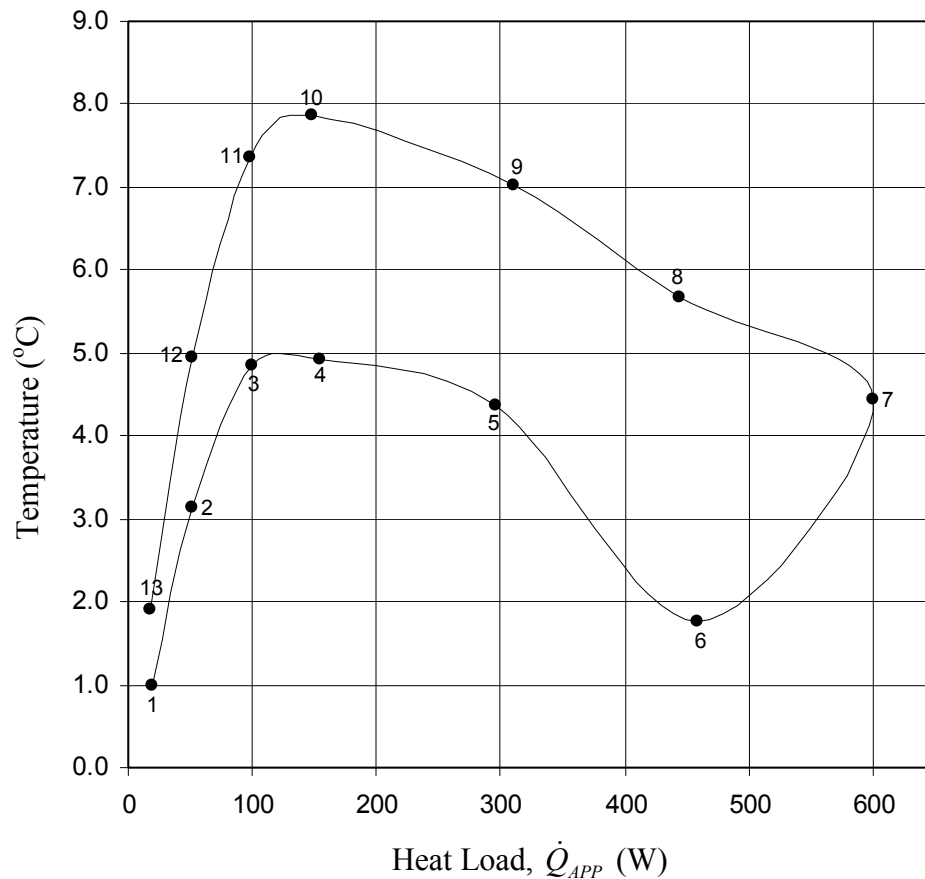
Fig. 7.18: Difference between the steady-state operating temperature and the fluid temperature exiting the liquid line as a function of heat load. (T_{SINK} =5 °C, zero elevation, and insulation on the evaporator). The numbers represent the steps in the sequence of the applying heat load.

The results of the measured heat load and temperature when the LHP was operated at 3 ½-inch positive elevation are listed in Table 7.8 and plotted in Fig. 7.19.

Table 7.8: Applied heat load, steady-state operating temperature, temperatures exiting the liquid line and the condenser, and ambient temperature when the LHP was operated at 3 ½-inch positive elevation.

| Step	1	2	3	4	5	6	7	8	9	10	11	12	13
$\dot{Q}_{APP}$ (W)	20	50	100	150	300	453	606	458	298	150	100	50	20
T_{SSOT} (°C)	20.3	19.5	20.2	19.7	18.1	20.9	25.0	21.5	20.3	22.9	22.5	21.7	22.2
TL_{OUT} (°C)	15.0	13.7	14.5	13.9	13.1	18.8	20.9	16.0	12.1	13.9	14.3	14.5	15.9
TC_{OUT} (°C)	7.5	7.4	7.4	7.5	9.6	17.1	19.7	14.1	8.1	7.3	7.3	7.5	7.5
T_{AMB} (°C)	22.8	23.0	23.3	23.1	23.1	23.4	23.6	23.2	23.0	22.8	22.4	23.7	24.1
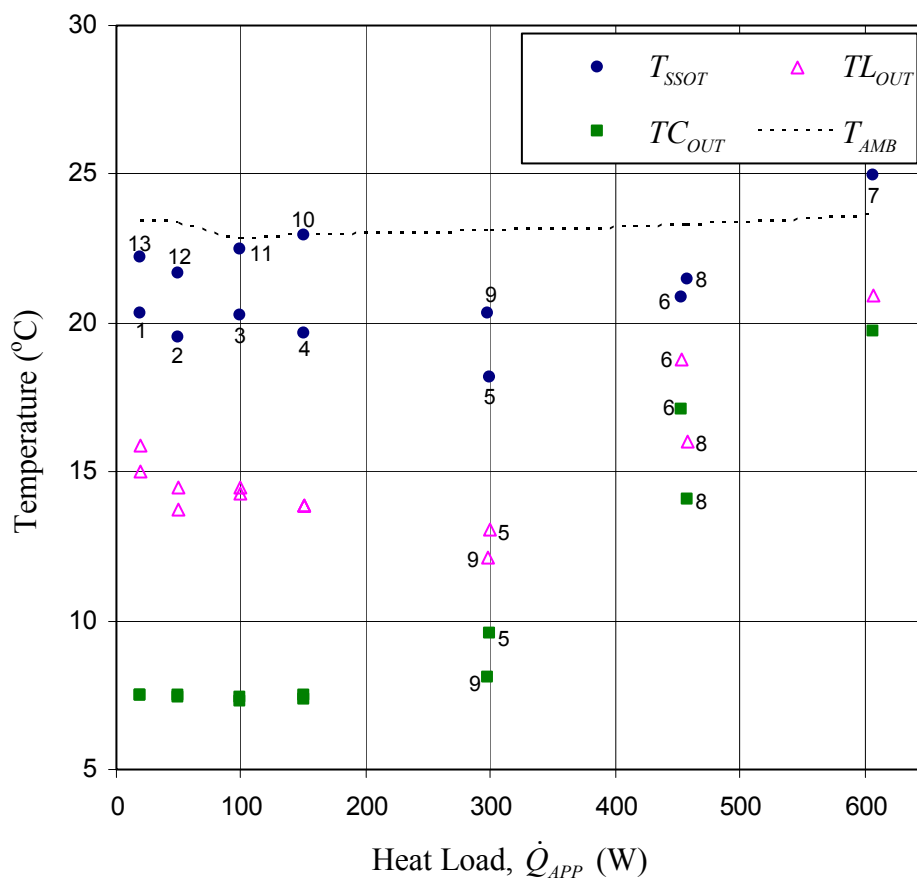
Fig. 7.19: Steady-state operating temperature, temperatures exiting the liquid line and condenser, and ambient temperature as functions of heat load. (T_{SINK} =5 °C, 3 ½-inch positive elevation, and insulation on the evaporator). The numbers represent the steps in the sequence of applying heat load.

A maximum temperature hysteresis of 3.2 ^{o}C was observed in steady-state operating temperature. The difference between the steady-state operating temperature and the fluid temperature exiting the liquid line as a function of heat load is plotted in Fig. 7.20.
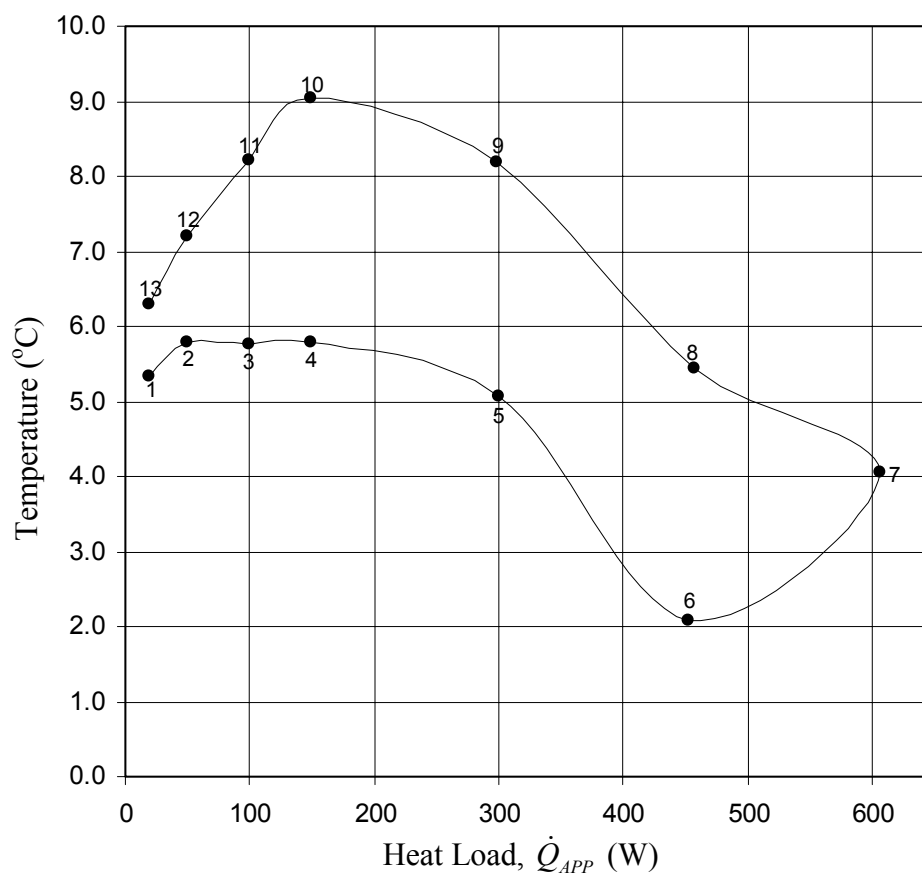
Fig. 7.20: Difference between the steady-state operating temperature and the fluid temperature exiting the liquid line as a function of heat load. (T_{SINK}=5 ^{o}C, 3 ½-inch positive elevation, and insulation on the evaporator). The numbers represent the steps in the sequence of applying heat load.

Comparing the experimental data of temperature hysteresis obtained from different elevations, it was very consistent that the upper trend of steady-state operating temperature had higher heat leak than that of the lower trend. To further understand the

phenomenon of temperature hysteresis, the heat leak from the evaporator to the reservoir has to be studied comprehensively. Total heat leak consists of axial heat leak, which is heat conducted axially from the evaporator to the reservoir, and radial heat leak, which is heat conducted radially from the primary wick to the evaporator core and then to the reservoir. Axial heat leak is relatively small compared to radial heat leak, except when the heat leak is extremely small, and is determined by the evaporator temperature and reservoir temperature. Radial heat leak is more complicated and depends on many parameters, like temperature at the outer and inner surfaces of the primary wick, primary wick effective thermal conductivity, and the vapor quality in the evaporator core. The vapor quality in the evaporator core cannot be controlled externally and it determines the amount of heat transferring into the reservoir. If the evaporator core is filled with liquid, the radial heat leak is essentially zero because the heat transferred to the liquid in turn flows back to the primary wick. However, if the evaporator core is filled with two-phase fluid, heat transferred from the primary wick into the evaporator core increases the vapor quality in it, and the vapor is then transported to the reservoir. Under this condition, the amount of heat transferred from the primary wick to the fluid in the evaporator core depends on the two-phase heat transfer coefficient in the evaporator core, which is a function of void fraction. Therefore, a change of vapor quality in the evaporator core results in a change in the amount of radial heat leak. This characteristic becomes a key parameter that determines the performance of a LHP.

After careful review of the experimental data, the initiation of temperature hysteresis happened at either step 9 (3 ½-inch adverse elevation) or step 8 (zero and 3 ½-inch positive elevation). More specifically, temperature hysteresis began with a

decreasing heat load because the location of the liquid–vapor interface receded into the condenser and drew liquid from the evaporator core to the condenser. This action in turn introduced more vapor from the reservoir to the evaporator core and resulted in higher radial heat leak.

The above discussion explains the cause of temperature hysteresis qualitatively. To further study the vapor quality in the evaporator core, the detailed design of the secondary wick, including the configuration, material, and properties, has to be taken into consideration. However, information regarding secondary wicks is considered proprietary to the vender. Thus, it was not possible to study temperature hysteresis quantitatively, and no model could be formulated to predict the performance of temperature hysteresis.

7.2.3 Study of Low-Power Start-Up Problem

A successful start-up of the LHP means that a forward flow of the fluid in the system has been established. In other words, the circulation of the working fluid in the outer loop, explained in Section 5.3, has to be functioning. In our experimental tests, both successful and unsuccessful start-ups were experienced.

Fig. 7.21 shows an example of a successful start-up temperature profile when the LHP was operated at zero elevation with both the evaporator and the reservoir insulated. The temperature profile shown in Fig. 7.21 includes the working fluid temperatures measured at the evaporator, reservoir, vapor line exit (0.5 inches before the condenser), and condenser exit (0.5 inch after the condenser), the cooling water temperature, and the

ambient temperature. Before heat was applied to the evaporator, the chiller was turned on and the condenser temperature changed from the ambient temperature to the sink temperature. The sink temperature, condenser exit temperature, and vapor line exit temperature reached steady condition before the LHP was started (12:30).
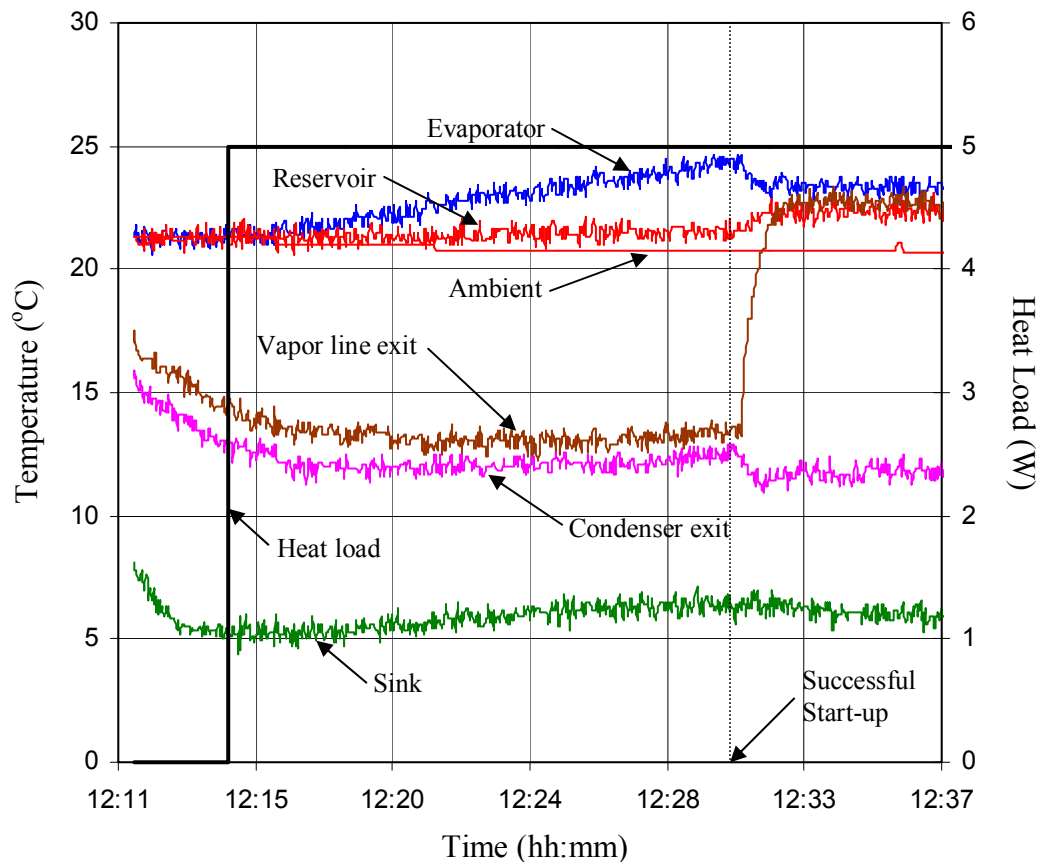
Fig. 7.21: Successful start-up temperature profile when heat load was equal to 5 W. ($T_{SINK} = 5\ {}^{o}C$, zero elevation, and insulations on the evaporator and the reservoir)

A 5 W heat load was applied to the evaporator at 12:14 (hh:mm), and the LHP was successfully started after 16 minutes (12:30). The successful start-up was identified by two signs: sudden decrease of the temperature difference between the evaporator and the reservoir, and sudden increase of the fluid temperature measured at the exit of the

vapor line. Similar to pool boiling, wall superheat is required to initiate nucleate boiling. Before the LHP was started, the heat was transferred via heat conduction and convection. In this data set, when the superheat reached about 3.0 K, nucleate boiling in the evaporator began and the temperature difference between the evaporator and the reservoir decreased suddenly. After boiling started, heat was transferred from the evaporator body to the working fluid much more efficiently than by conduction; thus, a smaller superheat was required. The sudden increase of the fluid temperature at the vapor line exit confirmed that the forward flow in the LHP was established. This is a typical start-up temperature profile.

An example of an unsuccessful start-up temperature profile is shown in Fig. 7.22 when the LHP was operated at exactly the same operating conditions (zero elevation with both the evaporator and the reservoir insulated). A 5 W heat load was applied to the evaporator at 13:05, and the LHP was unsuccessfully started (inner loop only) after around 28 minutes (13:33). In this data set, when the superheat reached about 4.5 K, nucleate boiling in the evaporator began and the temperature difference between the evaporator and the reservoir decreased suddenly. However, the fluid temperature at the vapor line exit remained the same, close to the sink temperature. There was no sign of forward flow in the LHP. The fluid temperature measured at the vapor line, condenser, and liquid line remained unchanged, which meant the fluid was stagnant. This confirmed that only the inner loop circulation of the working fluid, explained in Section 5.3, was functioning.

Because the evaporator and the reservoir were insulated, the heat had nowhere to
go and the temperature kept increasing after unsuccessful start-up. The heat load was
turned off after 2 hours and the evaporator and reservoir temperature was around 30 $^{\circ}$C.
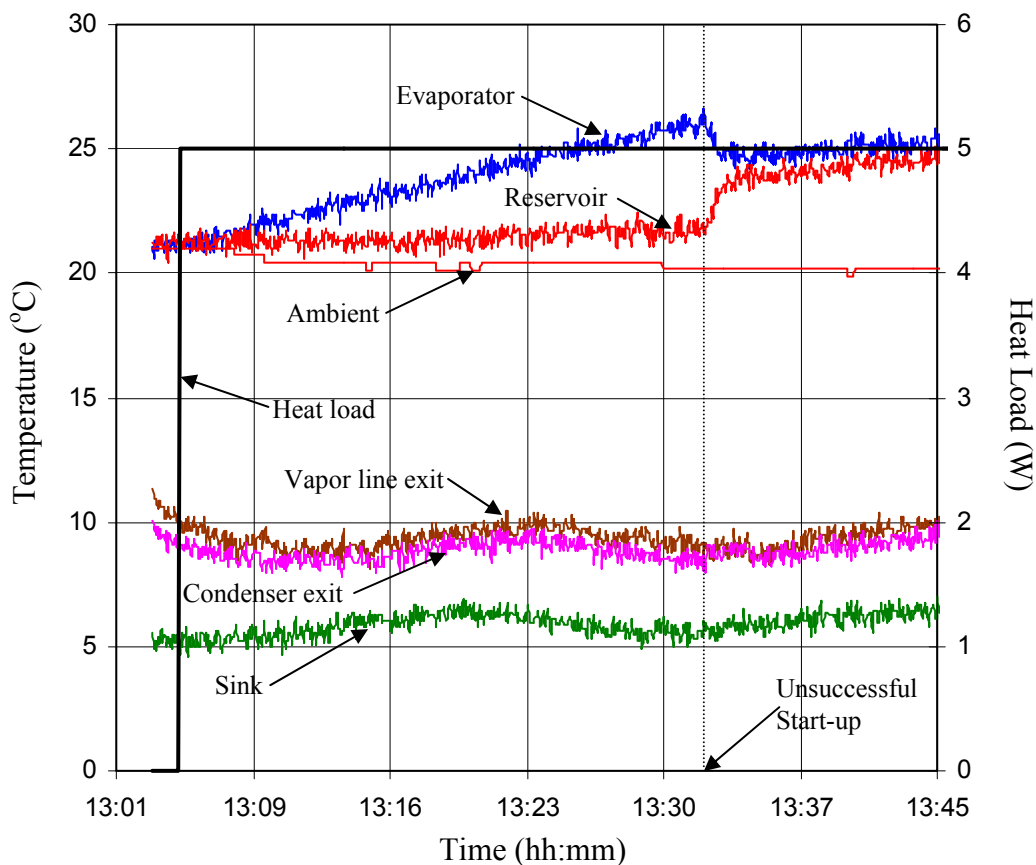
Fig. 7.22: Unsuccessful start-up temperature profile when heat load is equal to 5 W.
(T_{SINK} = 5 $^{\circ}$C, zero elevation, and insulations on the evaporator and reservoir)

To further study the unsuccessful start-up, a specific preconditioning was used
before applying heat load to the evaporator. Among four different start-up scenarios
proposed by Ku [1999], the worse case is that the vapor channel is flooded with liquid,
and the evaporator core is two-phase. Under this condition, the boiling process takes
place at the inner surface of the primary wick rather than the outer surface. Thus, a 10 W

flexible heater tape was installed on the reservoir, and the reservoir was heated right before the experiment. The purpose of heating the reservoir is to increase the local pressure in the reservoir to force the liquid to flood the vapor channel.

An example of an unsuccessful start-up temperature profile is shown in Fig. 7.23 when the LHP was operated at 3 ½-inch positive elevation with only the evaporator insulated. The small heater on the reservoir was turned on to heat up the reservoir before the experiment. It was then turned off after the reservoir temperature was 5 ^{o}C higher than the ambient temperature. Right after the small heater on the reservoir was turned off, a 10 W heat load was applied to the evaporator at 11:16. The LHP was unsuccessfully started (only inner loop) after around 16 minutes (11:32). In this data set, the superheat required to initiate nucleate boiling was around 3.5 K. Again, no forward flow was identified because the fluid temperature at the vapor line exit was much lower than the saturation temperature in the reservoir. A sign of reverse flow was observed from the temperatures measured at the condenser exit and vapor line exit when the LHP was unsuccessfully started. Because the boiling process took place in the evaporator core, the liquid in the evaporator core was pushed into the bayonet. This action developed a temporary reverse flow in the liquid line, condenser, and the vapor line. Thus, the fluid in the liquid line (at ambient temperature) went into the condenser (at sink temperature) and the condenser fluid (at sink temperature) went into the vapor line (at ambient temperature). This explains why the temperature at vapor line exit dropped while the temperature at condenser exit increased when boiling occurred. After the temporary reverse flow when incipient boiling occurred, the fluid in the vapor line, condenser, and liquid line returned to their stagnation conditions.
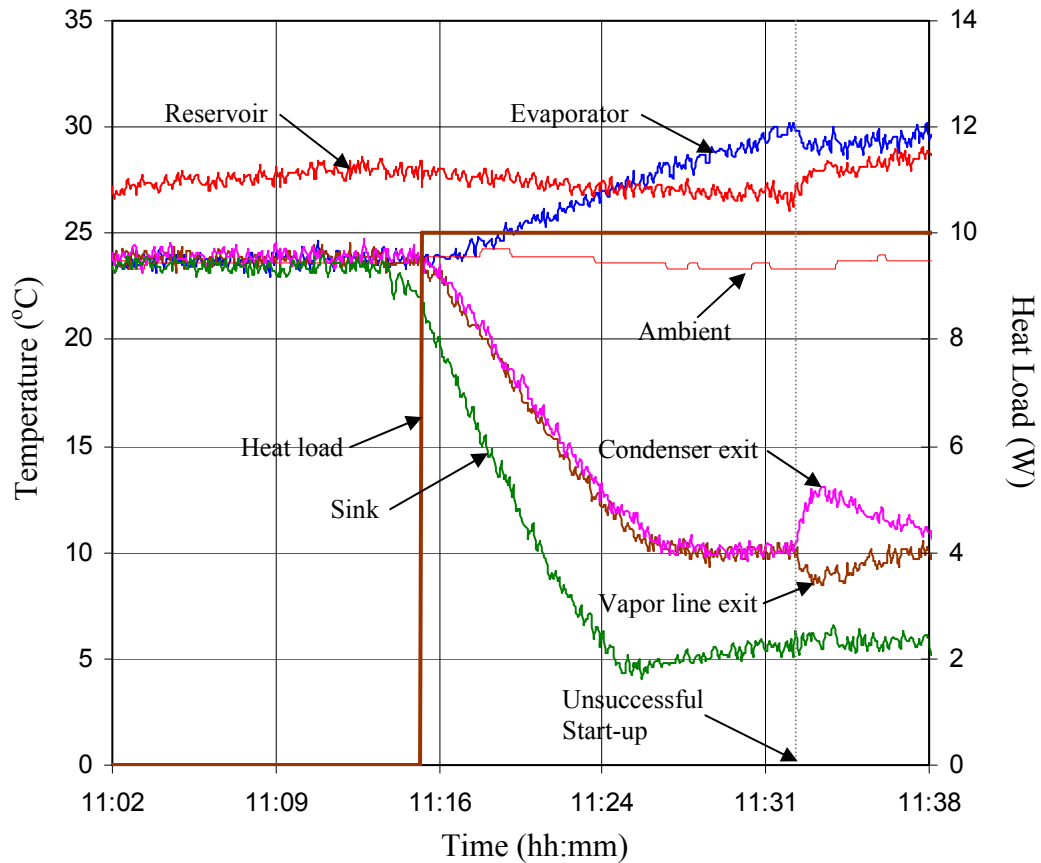
Fig. 7.23: Unsuccessful start-up temperature profile when heat load is equal to 10 W. ($T_{SINK} = 5\ ^oC$, 3 ½-inch positive elevation, and insulation on the evaporator)

Although the outer loop circulation was not successfully started, the experiment continued running and more heat load was applied to the evaporator for further study. Fig. 7.24 shows the temperature profiles over 26 hrs of the start-up experiment. Four different heat loads: 10, 20, 30, and 50 W, were applied to the evaporator successively. After the incipient boiling in the evaporator core (11:32), the LHP took about three hours to achieve steady state at temperature 36.1 ^oC and the evaporator superheat reached around 1.5 K. Under this condition, the vapor generated in the evaporator core traveled to the reservoir and then condensed back to liquid due to heat loss to the ambient. The

entire heat load became heat leak from the evaporator to the reservoir because there was no flow between the evaporator and the condenser (outer loop). The reservoir acted as a condenser for this operation and the ambient became the heat sink.
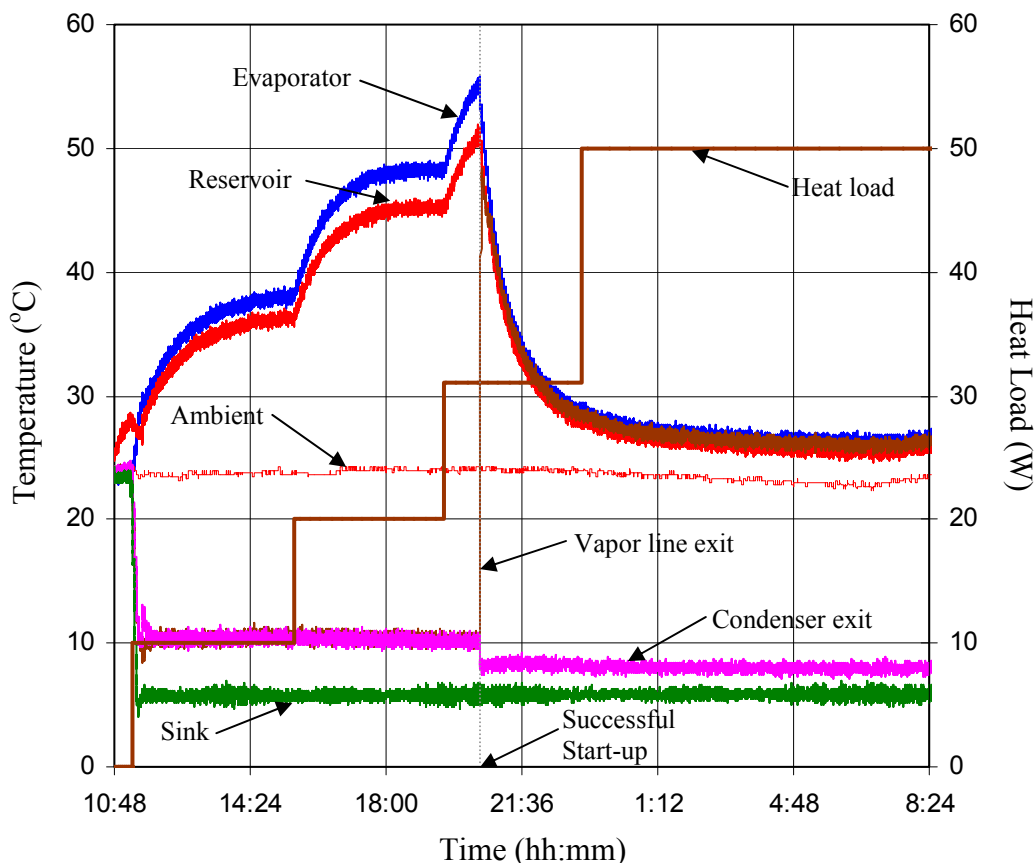
Fig. 7.24: Temperature and heat load profiles of whole period of start-up study. (T_{SINK} = 5 ^{o}C, 3 ½-inch positive elevation and insulation on the evaporator)

After the LHP reached a steady-state condition at 10 W, the heat load was then increased to 20 W. Similar operating conditions continued, and there was still no flow between the evaporator and the condenser. It took about four hours to achieve another steady-state condition at temperature 45.0 ^{o}C, and the evaporator superheat reached around 3.5 K. Then the heat load was further increased to 30 W. About one hour after

the heat load was increase to 30 W, the LHP was successfully started when the evaporator superheat reached around 4.5 K. A sudden increase of the temperature at the inlet of the condenser confirmed that forward flow in the LHP had been established. After the LHP successfully started, the temperatures of the evaporator and reservoir dropped more than 16.7 °C within an hour. When the heat load was further increased to 50 W, the loop achieved a steady- state operating temperature of 26.7 °C after around 5 hours.

7.3   COMPARISON OF EXPERIMENTAL AND MODELING RESULTS

The experimental data were compared with the predicted results by the steady-state model presented in Chapter 5 at three elevations: 3 ½-inch adverse, zero, and 3 ½-inch positive elevations. The following input parameters were selected in the steady-state model based on the experimental test conditions:

1. The external thermal conductance of the condenser, $\left(h_o A_o / L \right)_S$ in Eq. 5.21, was assumed to be 11 $W/(m \cdot K)$.

2. The condenser cooling water was running at a volume flow rate of 1.0 gallon-per-minute (GPM).

3. Only the evaporator was insulated to prevent any heat exchange with the ambient.

4. The cooling water inlet temperature, T_{SINK}, was measured to be around 6 °C due to heat loss to the ambient. The ambient temperature, T_{AMB}, was input depending on the measured ambient temperature.

5. The constant smooth and the Ananiev correlations were used for two-phase pressure drop and heat transfer calculations, respectively. The void fraction calculated by the constant smooth correlation was used to obtain the accelerational two-phase pressure drop.

6. Vapor superheat was considered in the vapor channel heat transfer calculation.

7. Both radial and axial heat leaks were considered in the heat leak calculation.

The results predicted by the steady-state model were compared with the experimental data presented in Section 7.2.2.

Comparisons between the experimental and modeling results of steady-state operating temperature and temperature exiting the liquid line and the condenser as functions of heat load at 3 ½-inch adverse, zero, and 3 ½-inch positive elevation elevations are plotted in Fig. 7.25, Fig. 7.26, and Fig. 7.27, respectively.

The modeling results of the temperature exiting the liquid line and the condenser agreed with the experimental data very well. Although the sink temperature was set at 5 ^{o}C, the lowest temperature of the working fluid exiting the condenser was around 7.5 ^{o}C due to heat loss to the ambient. Temperature hysteresis was observed in three sets of experimental data. The results predicted by the steady-state model followed the upper trend of steady-state operating temperature when the LHP was operated at 3 ½-inch adverse elevation. In contrast, the predicted results followed the lower trend of steady-state operating temperature when the LHP was operated at zero or 3 ½-inch positive elevations.
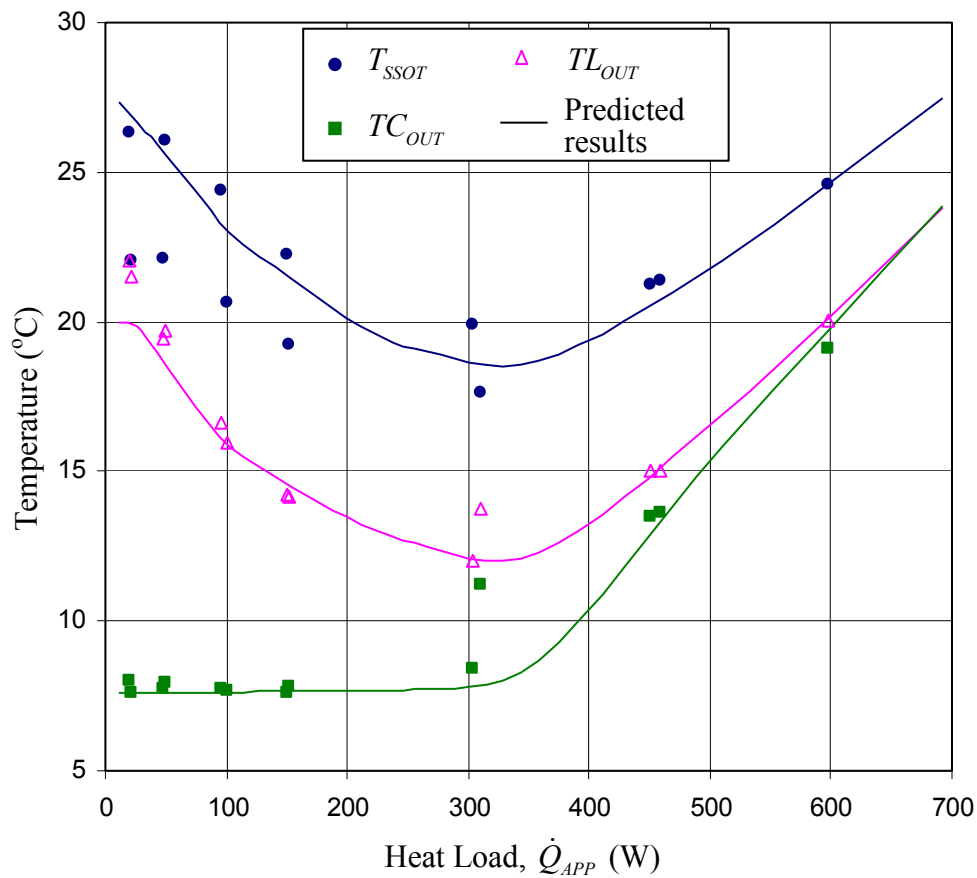
Fig. 7.25: Comparisons between the experimental and predicted results of steady-state operating temperature and temperature exiting the liquid line and condenser as functions of heat load. (T_{SINK} =5 ^{o}C, 3 ½-inch adverse elevation, and insulation on the evaporator)
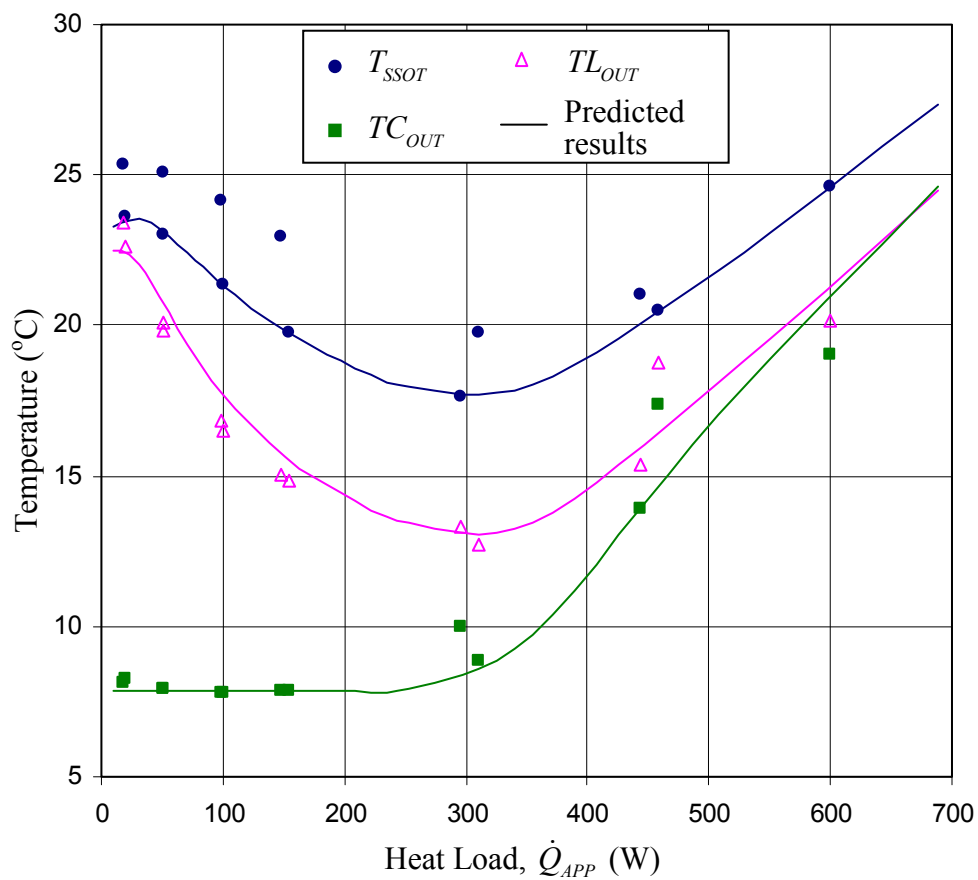
Fig. 7.26: Comparisons between the experimental and predicted results of steady-state operating temperature and temperature exiting the liquid line and condenser as functions of heat load. (T_{SINK} =5 ^{o}C, zero elevation and insulation on the evaporator)
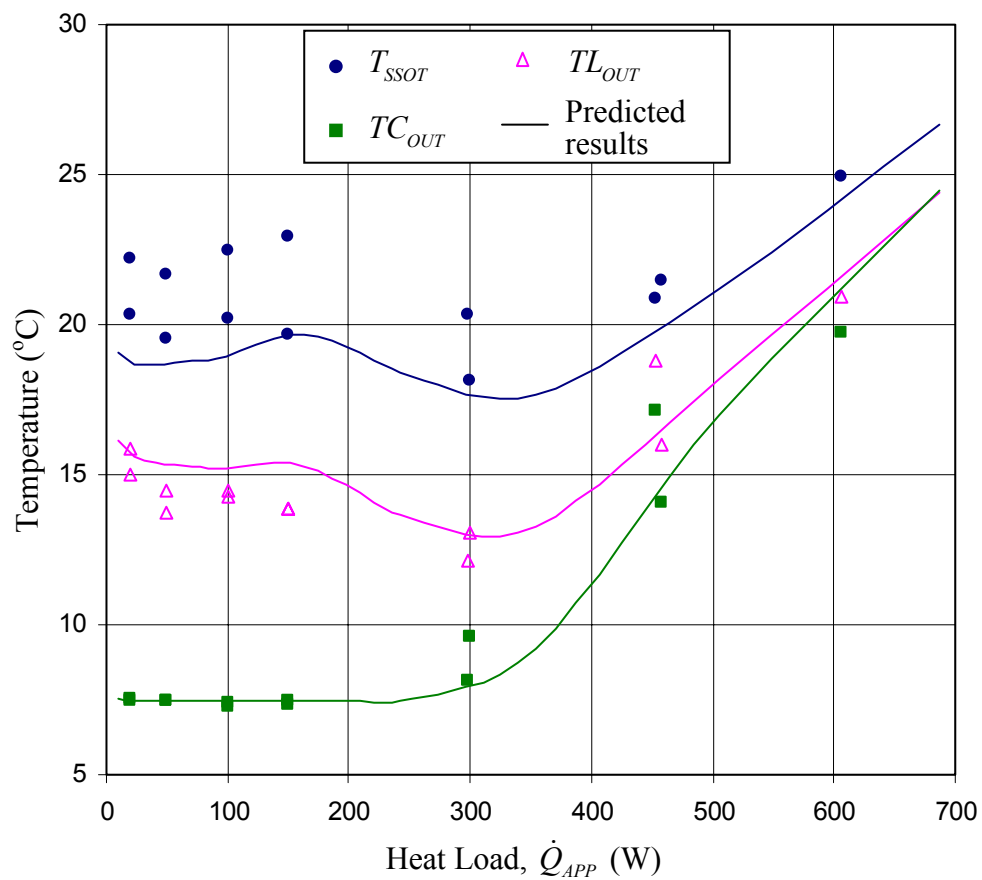
Fig. 7.27: Comparisons between the experimental and predicted results of steady-state operating temperature and temperature exiting the liquid line and condenser as functions of heat load. (T_{SINK} =5 ^{o}C, 3 ½-inch positive elevation, and insulation on the evaporator)

7.4   SUMMARY OF RESULTS

In the early stage of this study, neutron radiography was utilized to observe the operating characteristics inside the LHP. Successful observations were made through the transportation lines, the condenser, and the reservoir. Different two-phase regimes in the condenser, reverse flow in the liquid line, and condensation in the reservoir were successfully observed. With the aid of neutron radiography, the newly formulated gravity-assisted operating theory was confirmed.

Temperature tests of the LHP were performed throughout this study. The quality of the experimental data consistently improved with better understanding of the LHP operating characteristics. The parameters affecting the performance of the LHP, like sink temperature, ambient temperature, heat load, and elevation, were all controlled and monitored. Experiments were performed at different sink temperatures and elevations.

Temperature hysteresis was observed when the heat load was lower than 300 W at different elevations. There are two trends of the steady-state operating temperature: higher heat leak results in the upper trend, while lower heat leak results in the lower trend. For the same operating conditions, the steady-state operating temperature might be anywhere between the upper and lower trend depending on the vapor quality in the evaporator core.

Studies of low-power start-up problems were also performed. For normal operation, the minimum heat load and superheat required to start the LHP was around 5 W and 3.5 ^{o}C, respectively. With certain conditions, e.g., when the reservoir temperature is higher then that of the evaporator, the minimum heat load to start the LHP can be

higher than 10 W. When the LHP was not successfully started, only the inner loop was operating to remove the heat load. Under this condition, the steady-state operating temperature (50 $^{\circ}$C) could be much higher than normal operation (20 $^{\circ}$C). After the LHP was unsuccessfully started, the minimum required heat load to start the outer loop was around 30 W. After the outer loop was started, the LHP resumed normal operation, and the steady-state operating temperature decreased rapidly.

The experimental data were also compared with the results predicted by the steady-state model presented in Chapter 5 at different elevations. The predicted results agreed with the experimental data reasonably well. The newly developed steady-state model is the only available mathematical model that can predict the performance of a LHP when it is operated at positive elevation.

Accurate prediction of the performance of a LHP is extremely difficult because it involves empirical correlations of pressure drop and heat transfer calculations. In addition, the current heat leak model, presented in Section 5.5.7, might not be accurate. Radial heat leak is calculated from the difference of the saturation temperature across the primary wick, which in turn depends on the local saturation pressure. This might be true for the liquid flowing in the primary wick, but is not valid for the temperature distribution in the wick material. A new heat leak model must be developed based on both liquid and metal temperature distribution in the primary wick.

Chapter 8

CONCLUSIONS AND RECOMMENDED FUTURE WORK

8.1   CONCLUSIONS

This study presents a theoretical and experimental study of loop heat pipes (LHPs). The most significant result of this study is the discovery, development, and modeling of the operating theory at gravity-assisted conditions. The operating characteristics when the LHP is operating in the gravity-controlled mode are unique and have never been studied before, neither experimentally nor analytically. In this study, the gravity-assisted operating theory is explained thoroughly and the performance of a LHP can be predicted analytically.

In addition, a non-invasive visualization tool (neutron radiography) was utilized to see-through the test LHP. Numerous temperature tests were performed to study the operating characteristics of steady-state and transient operation of a LHP. A steady-state model with the capability to predict the performance of a LHP at different elevations was also developed and studied.

The newly formulated gravity-assisted operating theory is presented and incorporated in the steady-state model. The observations from neutron radiography confirmed the operating characteristics when the LHP was operated in the gravity-controlled mode. The predicted results agreed with the experimental data very well.

In this study, neutron radiography was proven to be a useful visualization tool to study the operating characteristics of a LHP. It would be an ideal tool to study specific problems like temperature oscillation, which can be identified in the transportation line or in the condenser. However, due to the construction of the evaporator, neutron radiography was unable to see-through the evaporator. The operating conditions in the evaporator core were unable to be identified, which is the key factor for several important issues, like temperature hysteresis and low-power start-up. To see through the evaporator core using neutron radiography, special design of the evaporator is required, including the geometry, thickness, length, and material. With proper design, neutron radiography has great potential for visualizing what is happening in the evaporator core.

Obtaining an accurate and reliable experimental data set of LHP temperatures is very difficult because the performance of a LHP is sensitive to many parameters. Most of the parameters can be easily controlled like heat load, elevation, and tilt. However, ambient temperature is difficult to control, and vapor quality in the evaporator core cannot be controlled at all. An environmental chamber with fine temperature control is necessary to control the ambient temperature. Both cooling and heating abilities are required to study the effect of ambient temperature on the performance of a LHP. It was often found to be very frustrating that the same operating conditions resulted in different steady-state operating temperatures. This was because the vapor quality in the evaporator core was different and resulted in inconsistent heat leak from the evaporator to the reservoir.

Modeling of LHP operation is very complicated because it involves two-phase pressure drop and heat transfer, fluid flow through porous material, and boiling on a

porous surface. Without experimental measurement of pressure drop, mass flow rate, and temperature in the LHP, it is impossible to verify the accuracy of the modeling results. The steady-state model can be an ideal tool to study the performance of a LHP under normal operating conditions. However, each LHP has its own features and designs, which determine its own performance.

Currently, the main challenge and biggest unknown in the LHP community is how to determine the radial heat leak from the evaporator to the reservoir, which is a function of the temperature distribution in the primary wick, effective thermal conductivity of the primary wick, vapor quality in the evaporator core, and design and properties of the secondary wick. The design of the evaporator is the key factor determining the performance of a LHP. The designs vary from company to company and are not fully developed yet. Furthermore, they are proprietary, and therefore, no specific information can be found in the open literature.

Despite the complexities and uncertainties, LHPs offer a potential solution to the next generation's thermal management problems. LHPs are the most reliable two-phase heat transfer devices, and have very high thermal conductivity. Within 10 years, LHPs may become the most popular device in the thermal management industry, both in space and ground applications.

8.2   FUTURE WORK

This study initiated the research of LHPs at The Pennsylvania State University. Both experimental and analytical work has been investigated thoroughly on an ammonia

test LHP provided by Bechtel Bettis, Inc. A steady-state code was written based on the general operating characteristics of a LHP. Solid understanding of the fundamental operating characteristics of LHPs has been established. In the author's opinion, the following research directions can be investigated in the future:

1. Design and build a LHP with sufficient devices to measure pressure drops along the system, mass flow rate, and temperature distribution in the evaporator.

2. Design and build an environmental chamber with the capability to control the ambient temperature from 0 ^{o}C to 100 ^{o}C with an accuracy of ± 0.5 ^{o}C. It is highly recommended that the environmental chamber can simulate both natural convection and forced convection inside the chamber.

3. Study the vapor quality in the evaporator core. Neutron radiography can be utilized to study a specially designed LHP, or the evaporator can be constructed of transparent material.

4. Establish a better radial heat leak model based on heat load, temperature distribution in the primary wick, orientation, properties of the primary wick, and vapor quality in the evaporator core.

5. Develop a transient model of LHP operation using commercial software like Sinda/Fluint or computational fluid dynamics (CFD) codes.

REFERENCES

Annaiev, E. P., Boyko, L. D., and Kruzhilin, G. N., 1961, "Heat Transfer in the presence of Steam Condensation in a Horizontal Tube," *Proc. 1st Int. Heat Transfer Conf.*, part 2, p290

Baroczy, C. J., 1965, "Correlation of Liquid Fraction in Two-Phase Flow with Applications to Liquid Metals," *Chem. Eng. Prog. Symp. Ser.*, Vol. 61, No. 57, pp. 179-191

Carey, V. P., 1992, *Liquid-Vapor Phase-Change Phenomena: An Introduction to the Thermophysics of Vaporization and Condensation Processes in Heat Transfer Equipment*, Taylor & Francis, Washington, DC, p. 127-138

Chen, I., et al., 1989, "An Experimental Study and Prediction of a Two-Phase Pressure Drop in Microgravity," *26th Aerospace Sciences Meeting*, Reno, Nevada, AIAA 89-0074

Churchill, S. W. and Bernstein, M., 1977, "A Correlating Equation for Forced Convection from Gases and Liquids to a Circular Cylinder in Crossflow," *J. Heat Transfer*, vol. 99, pp. 300-306

Cimbala, J. M., Brenizer, J. S., Chuang, P. A., et al., 2001, "Study of a Loop Heat Pipe Using Neutron Radiography," *4th International Topical Meeting On Neutron Radiography*, State College, PA

Crowley, C. J., Izenson, M. G., Barry, J. J., Valenzuela, J. A., Martin, J. L. and Ent, R. S., 1992, "Design Manual for Two-phase Components of Spacecraft Thermal Management Systems," PL-TR-92-3002, Prepared by Creare Inc.

Cheung, M. K., Hoang, T. T., Ku, J., and Kaya, T., 1998, "Thermal Performance and Operational Characteristics of Loop Heat Pipe," *Proceedings of the 28th International Conference on Environmental Systems*, Society of Automotive Engineers, (SAE Paper No. 981813)

Cotter, T. P., 1967, "Heat Pipe Startup Dynamics," *Proc. SAE Thermionic Conversion Specialist Conference*, Palo Alto, CA.

Faires, J. D. and Burden, R. L., 1993, *Numerical Methods,* PWS-Kent, Boston, Massachusetts

Faghri, A., 1995, *Heat Pipe Science and Technology*, Taylor & Francis, Washington, DC

Friedel, L, 1979, "Improved Friction Pressure Drop Correlations for Horizontal and Vertical Two Phase Pipe Flow," Paper E2, *European Two Phase Flow Group Meeting*, Ispra, Italy

Gaugler, R. S., 1944, "Heat Transfer Means," U.S. Patent 2350348

Gorring, R. L. and Churchill, S. W., 1961, "Thermal Conductivity of Heterogeneous Materials," *Chem. Eng. Progr.*, Vol. 57, pp53-59

Grover, G. M., Cotter, T. P., and Erikson, G. F., 1964, "Structures of Very High Thermal Conductivity," *Journal of Applied Physics*, Vol. 35, pp. 1190-1191

Grover, G. M., 1966, "Evaporation-Condensation Heat Transfer Device," U.S. Patent 3229759

Haaland, S. E. 1983, "Simple and Explicit Formulas for the Friction Factor in Turbulent Pipe Flow," *J. Fluids Eng.*, pp. 89-90

Hoang, T. T., Cheung, M. K., Kim, J. H., and Ku, J., *Loop Heat Pipe Handbook*, 1999

Hoang, T. T. and Kaya, T, 1999, "Mathematical Modeling of Loop Heat Pipes with Two-phase Pressure Drop," *33rd Thermophysics Conference*, Norfolk, VA (AIAA Paper No. 99-3448)

Holman, J. P., 1990, *Heat Transfer*, 7th Edition, McGraw-Hill, p356

Incropera, R. P. and DeWitt, D. P., 1996, *Fundamentals of Heat and Mass Transfer*, 4th Edition, John Wiley & Sons, p439-441[1], p444-447[2]

Judge, J. F., 1966 "RCA Test Thermal Energy Pipe," *Missiles and Rockets*, Vol. 18, pp. 36-38

Kaya, T. and Ku, J., 1999[1], "A Parametric Study of Performance Characteristics of Loop Heat Pipe," *Proceedings of the 29th International Conference on Environmental Systems*, Society of Automotive Engineers, Denver, CO (SAE Paper No. 1999-01-2006) [1]

Kaya, T. and Ku, J., 1999[2], "Investigation of the Temperature Hysteresis Phenomenon of a Loop Heat Pipe," *33rd National Heat Transfer Conference*, Paper No. 108, Albuquerque, New Mexico [2]

Kaya, T., Ku, J., Hoang, T. T., and Cheung, M. K, 1999[3], "Investigation of Low Power Start-Up Characteristics of a Loop Heat Pipe," *Space Technology and Applications International Forum-1999,* CP458, pp. 799-804

Ku, J., et al., 1986, "Capillary Pumped Loop GAS and Hitch-hiker Flight Experiments," *AIAA/ASME 4th Joint Thermophysics and Heat Transfer Conference* (AIAA Paper No. 86-1249)

Ku, J., et al., 1993, "Overview of Capillary Pumped Loop Technology," *ASME 29th National Heat Transfer Conference*, Atlanta, GA, v236, pp. 1-17

Ku, J., 1999, "Operating Characteristics of Loop Heat Pipes," *Proceedings of the 29th International Conference on Environmental Systems*, Society of Automotive Engineers, Denver, CO (SAE Paper No. 1999-01-2007)

Ku, J, Ottenstein, L, Kobel, M, Rogers, P., and Kaya, T, 2001," Temperature Oscillations in Loop Heat Pipe Operation," *Space Technology and Applications International Forum-2001,* American Institute of Physics, Albuquerque, New Mexico

Ku, J, Ottenstein L, Roger, P., and Cheung, M. K., 2002," Capillary Limit in a Loop Heat Pipe with a Single Evaporator," SAE Paper No. 2002-01-2502

Liao, Q. and Zhao, T. S., 1999, "Evaporative Heat Transfer in a Capillary Structure Heated by a Grooved Block," *Journal of Thermophysics and Heat Transfer*, Vol. 13, No. 1, pp126-133

Lockhart, R. W. and Martinelli, R. C., 1949, "Proposed Correlation of Data for Isothermal Two-Phase, Two-Component Flow in Pipes, *Chem. Eng. Prog.*, Vol. 45, no. 1, pp39-48

Maidanik, J. F., Vershinin, S. V., Kholodov, V. F., and Dolgirev, J. E., 1985, "Heat Transfer Apparatus," U.S. Patent No. 4515209

Maxwell, J., 1891, "A Treatise on Electricity and Magnetism," Vol. 1, 3rd Edition, OUP, reprinted by Dover, New York, 1954

Moran, M. J. and Shapiro, H. N., 1993, *Fundamentals of Engineering Thermodynamics*, 2nd edition, John Wiley &Sons, p457

Nikitkin, M. N. and Bienert, W. B., 1998," Non-Condensable Gases and Loop Heat Pipe Operation," SAE Paper No. 981584

Perkins, J, 1836, UK Patent No. 7059

Perkins, L. P., and Buck, W. E., 1892, "Improvements in Devices for the Diffusion or Transference of Heat," UK Patent 22272, London, England

Shah, M. M., 1979, "A General Correlation for Heat Transfer during Film Condensation inside Pipes," *Int. J. Heat Mass Transfer*, Vol. 22, pp. 547-556

Stenger, F. J., 1966, "Experimental Feasibility Study of Water-Filled Capillary-Pumped Heat Transfer Loops," NASA TM-X-1310

Stroud, A. H. and Secrest, D., 1966, *Gaussian Quadrature Formulas,* Englewood Cliffs, N.J.: Prentice-Hall, pp. 100-151

Thom, J. R. S., "Prediction of Pressure Drop during Forced Circulation Boiling of Water," *Int. J. Heat Mass Transfer*, Vol. 7, pp. 709-724

Traviss, D. P., Rohsenow, W. M., and Baron, A. B., 1973, "Forced Convection Condensation in Tubes: A Heat Transfer Correlation for Condenser Design," *ASHRAE Trans.*, Vol. 79, part 1, pp157-165

Trefethen, L., 1962, "On the Surface Tension Pumping of Liquids or a Possible Role of the Candlewick in Space Exploration," *G.E. Tech. Info.*, Serial No. 615 D114

Von Der Hardt, P. and R ö ttger, H., 1981, *Neutron Radiography Handbook*, D. Reidel, Boston, Massachusetts,

Wallis, G. B., 1969, *One-Dimensional Two-Phase Flow*, McGraw-Hill

Webb, R. L., 1998, "Convective Condensation of Superheated vapor," *Journal of Heat Transfer*, Vol. 120, pp. 418-421

White, F. M., 1999, *Fluid Mechanics*, 4th edition, McGraw-Hill, p133-137[1], p338-340[2]

Wolf, D. and Bienert, W, 1994," Investigation of Temperature Control Characteristics of Loop Heat Pipe," *24th International Conference on Environmental Systems*, Society of Automotive Engineers, Friedrichshafen, Germany (SAE Paper No. 941576)

Zivi, S. M., 1964, "Estimation of Steady-State Steam Void-Fraction by means of the Principle of minimum entropy production," *Journal of Heat Transfer*, Vol. 86, pp. 247-252

Appendix A

STUDY OF LIQUID SUPERHEAT IN THE PRIMARY WICK

The necessary requirement for a bubble to exist in a liquid is that the liquid must be superheated. The amount of superheat depends on the size of the bubble and the properties of the working fluid. A drawing of a bubble in a liquid is illustrated in Fig. A.1.
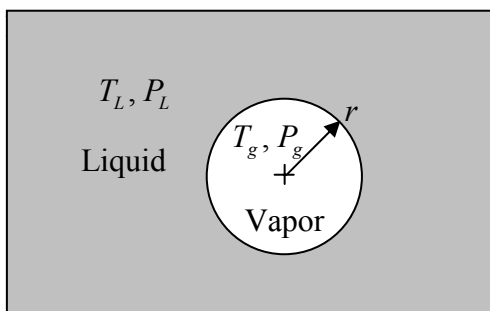
Fig. A.1: Drawing of a bubble in a liquid.

The temperature and pressure in the vapor and liquid can be written as:

$$\begin{cases} T_L = T_g = T_f \\ P_g - P_L = \dfrac{2\sigma}{r} \end{cases} \tag{A.1}$$

From the thermodynamic analysis using a pressure-temperature diagram, the amount of superheat can be derived. Fig. A.2 illustrates the liquid and vapor thermodynamic states on the pressure-temperature diagram.
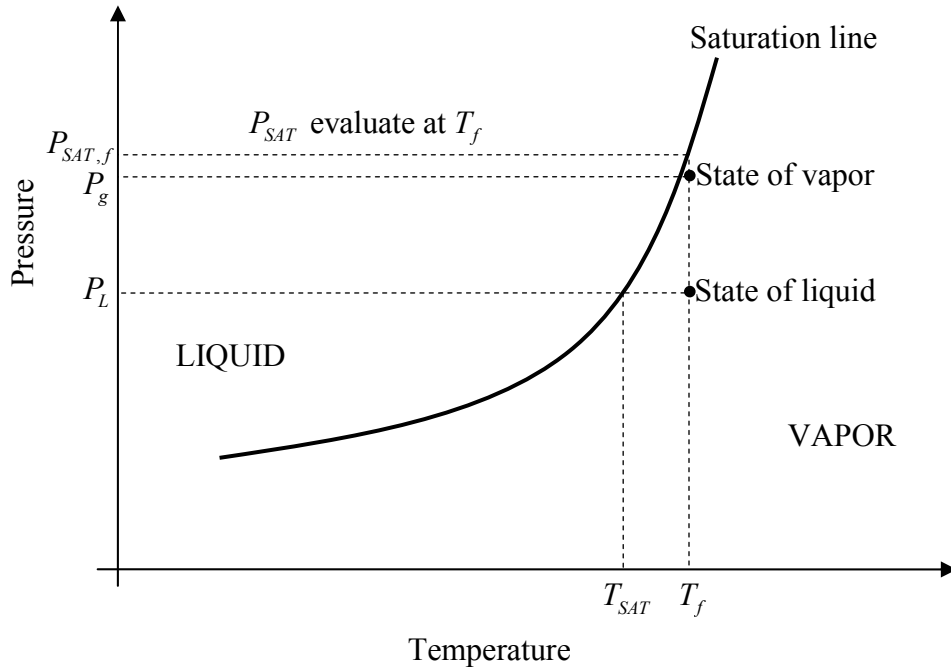
Fig. A.2: A sample pressure versus temperature diagram.

The pressure difference between the vapor and $P_{SAT,f}$ can be calculated by:

$$P_{SAT,f} - P_g = \frac{\rho_g}{\left(\rho_L - \rho_g\right)}\left(\frac{2\sigma}{r}\right) \tag{A.2}$$

Thus, the amount of superheat required for the existence of a vapor with a radius r can be obtained from the Clausius-Clapeyron Equation (Eq. 4.7):

$$\Delta T_{SH} = T_f - T_L = \frac{\left(P_{SAT,f} - P_L\right)}{\left(dP/dT\right)_{SAT}} = \frac{2\sigma}{r}\left(\frac{\rho_L}{\rho_L - \rho_g}\right)\left(\frac{T\left(v_g - v_L\right)}{\lambda}\right) \tag{A.3}$$

Since the liquid density is usually much higher than the vapor density, the superheat can then be written as:

$$\Delta T_{SH} = \frac{2\sigma}{r}\left(\frac{T\left(v_g - v_L\right)}{\lambda}\right) \tag{A.4}$$

From the analysis above, a sample calculation of the superheat required for a bubble to exist in the primary wick is performed. It is assumed that the radius of the vapor bubble is equal to the pore radius of the primary wick (1.6 μ m), and the properties are those at 25 °C. The amount of superheat is calculated to be:

$$\Delta T_{SH} = \frac{2\sigma}{r} \left(\frac{T(v_g - v_L)}{\lambda} \right) = \frac{2 \times 0.0249 \text{N/m}}{1.6 \times 10^{-6} \text{m}} \times \left(\frac{298 \text{K} \times 0.127 \text{m}^3/\text{kg}}{1.1664 \times 10^6 \text{J/kg}} \right) \approx 1.01 \text{ K} \quad \text{(A.5)}$$

Therefore, the minimum liquid superheat required for boiling to occur in the primary wick is around 1 K. If the liquid temperature is less than 1 K superheated, it exists inside the primary wick as superheated liquid.

Appendix B

PROPERTIES OF AMMONIA

All of the working fluid properties utilized in the steady-state code are functions of fluid temperature, and are curve-fitted from National Institute of Standards and Technology (NIST) data. These properties include saturation pressure, liquid density, liquid viscosity, vapor density, vapor viscosity, surface tension, latent heat, liquid thermal conductivity, vapor conductivity, liquid specific heat, and vapor specific heat. They are expressed as a function of saturation temperature in the form of 5th–order polynomial equations, and are plotted in Figs. B.1 to B.12. The polynomials in the equations shown in the figures have only three significant digits while the properties utilized in the steady-state model have more than 8 significant digits.
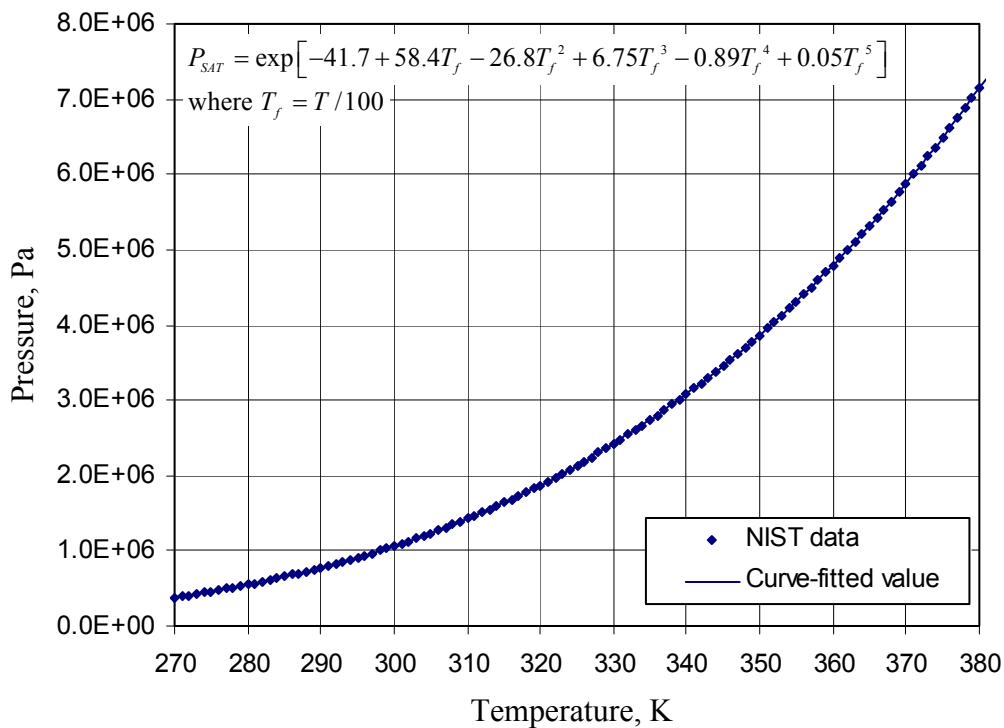
Fig. B.1: Pressure of saturated ammonia.

$$P_{SAT} = \exp\left[-41.7 + 58.4T_f - 26.8T_f^2 + 6.75T_f^3 - 0.89T_f^4 + 0.05T_f^5\right]$$

where $T_f = T/100$
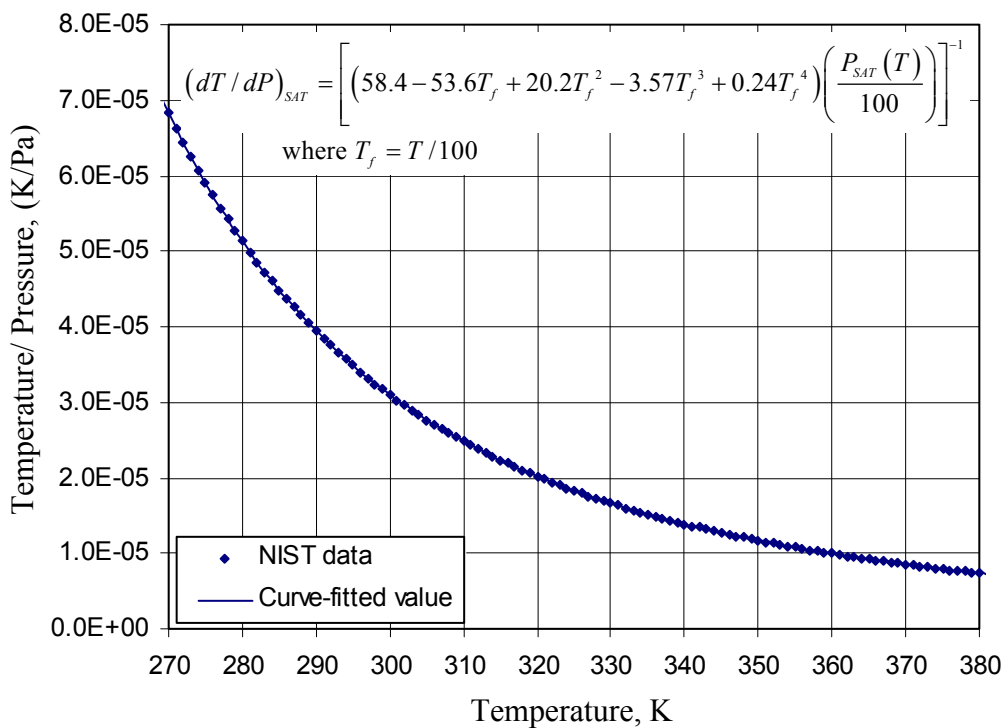
Fig. B.2: Temperature change/ Pressure change of saturated ammonia.

$$(dT/dP)_{SAT} = \left[\left(58.4 - 53.6T_f + 20.2T_f^2 - 3.57T_f^3 + 0.24T_f^4\right)\left(\frac{P_{SAT}(T)}{100}\right)\right]^{-1}$$

where $T_f = T/100$
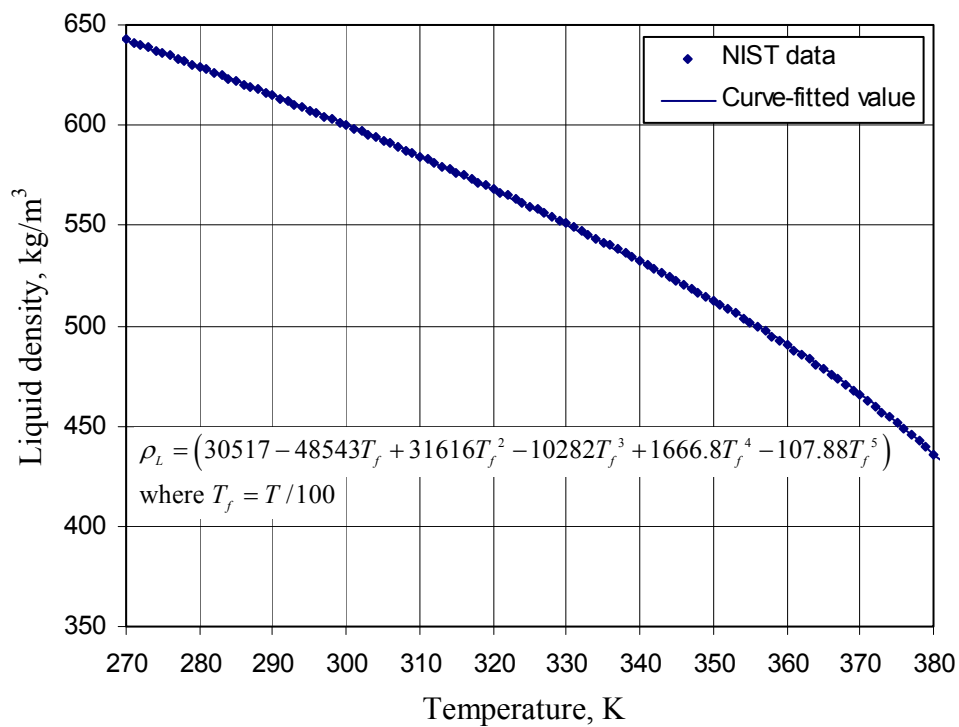
Fig. B.3: Liquid density of saturated ammonia.

$$\rho_L = \left(30517 - 48543T_f + 31616T_f^2 - 10282T_f^3 + 1666.8T_f^4 - 107.88T_f^5\right)$$

where $T_f = T/100$
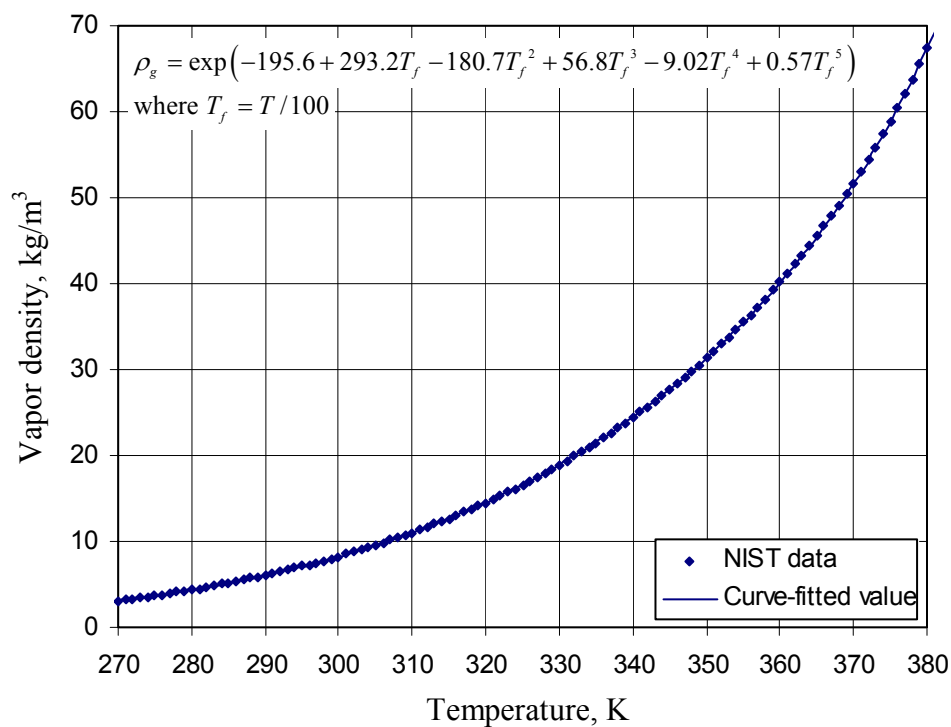
Fig. B.4: Vapor density of saturated ammonia.

$$\rho_g = \exp\left(-195.6 + 293.2T_f - 180.7T_f^2 + 56.8T_f^3 - 9.02T_f^4 + 0.57T_f^5\right)$$

where $T_f = T/100$

$$\mu_L = 1.41e^{-2} - 1.95e^{-2}T_f + 1.12e^{-2}T_f^{\ 2} - 3.28e^{-3}T_f^{\ 3} + 4.84e^{-4}T_f^{\ 4} - 2.88e^{-5}T_f^{\ 5}$$

where $T_f = T/100$
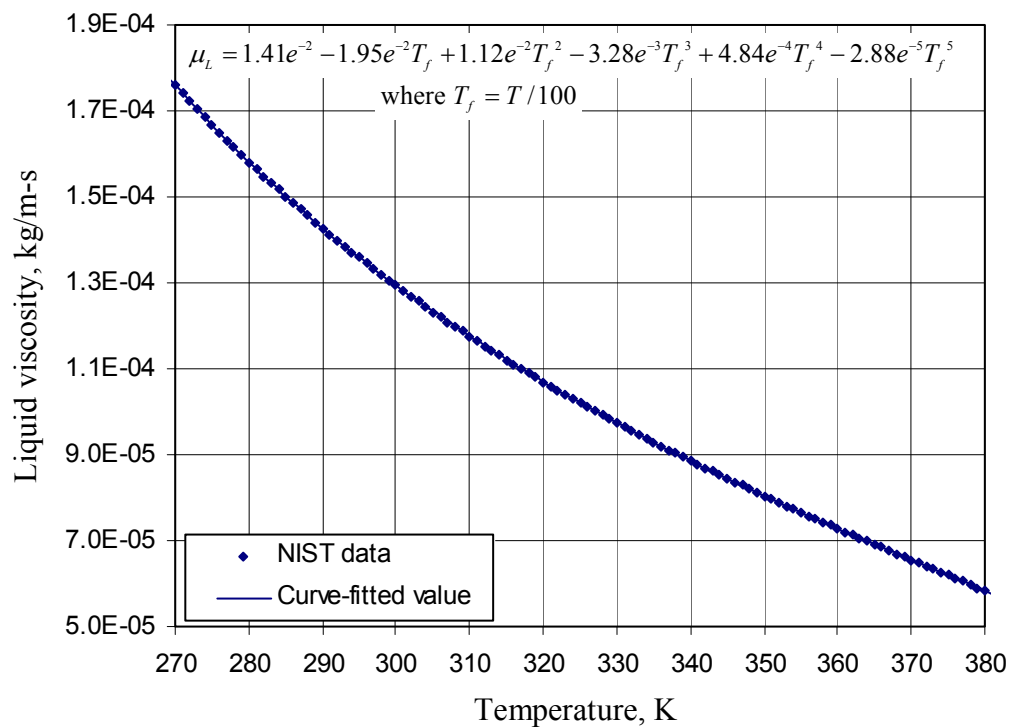
Fig. B.5: Liquid viscosity of saturated ammonia.

$$\mu_g = -1.07e^{-3} + 1.75e^{-3}T_f - 1.14e^{-3}T_f^{\ 2} + 3.72e^{-4}T_f^{\ 3} - 6.07e^{-5}T_f^{\ 4} + 3.96e^{-6}T_f^{\ 5}$$

where $T_f = T/100$
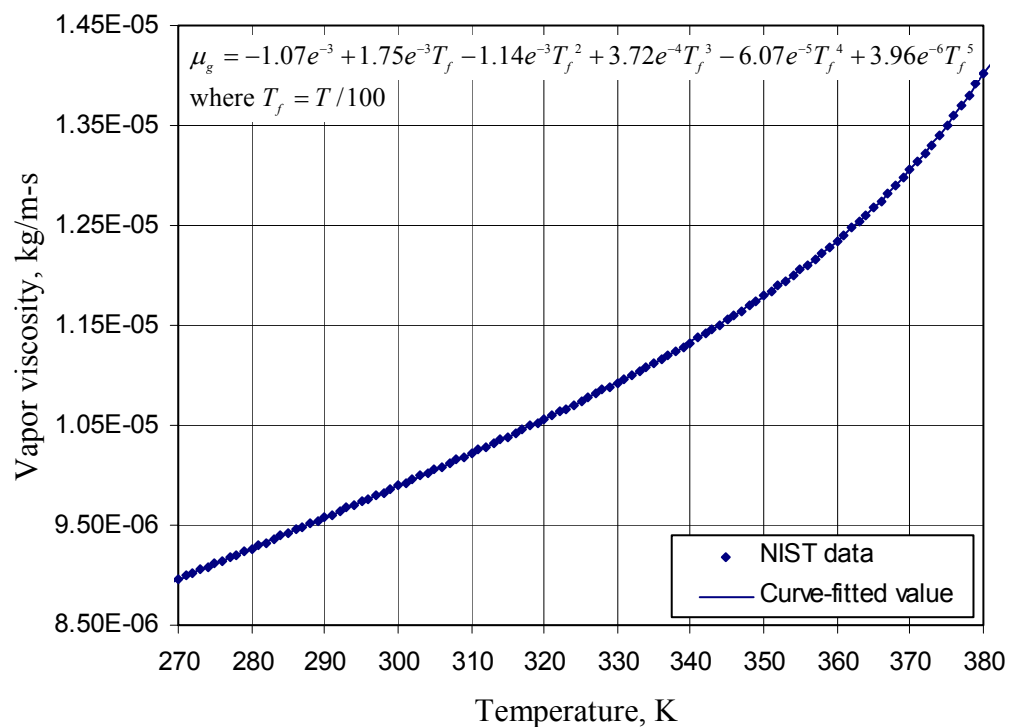
Fig. B.6: Vapor viscosity of saturated ammonia.
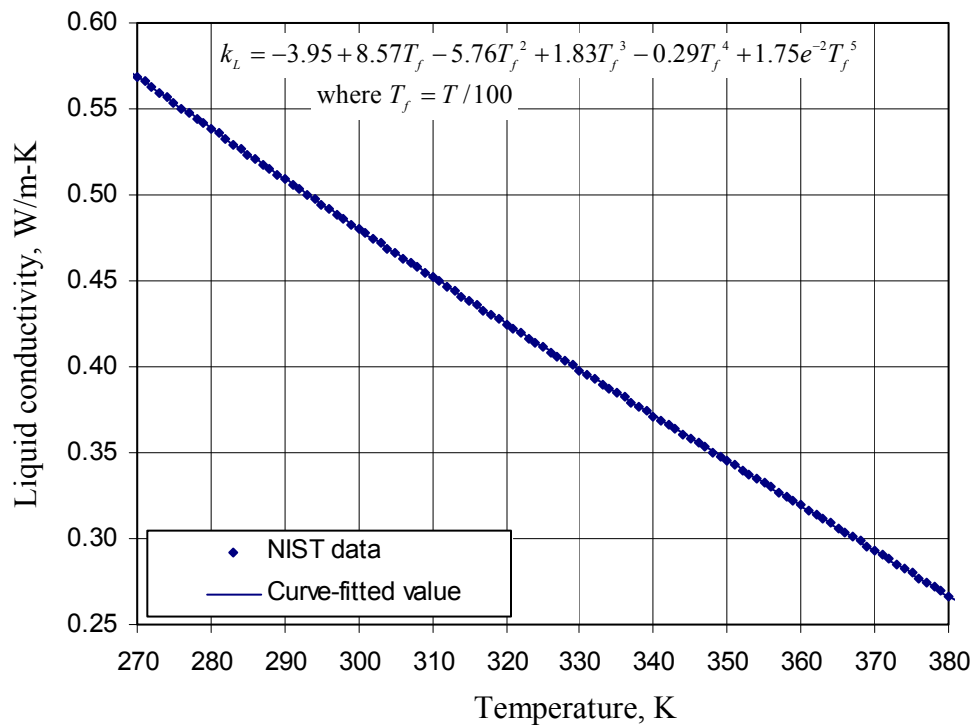
Fig. B.7: Liquid conductivity of saturated ammonia.

$$k_L = -3.95 + 8.57T_f - 5.76T_f^2 + 1.83T_f^3 - 0.29T_f^4 + 1.75e^{-2}T_f^5$$
where $T_f = T/100$
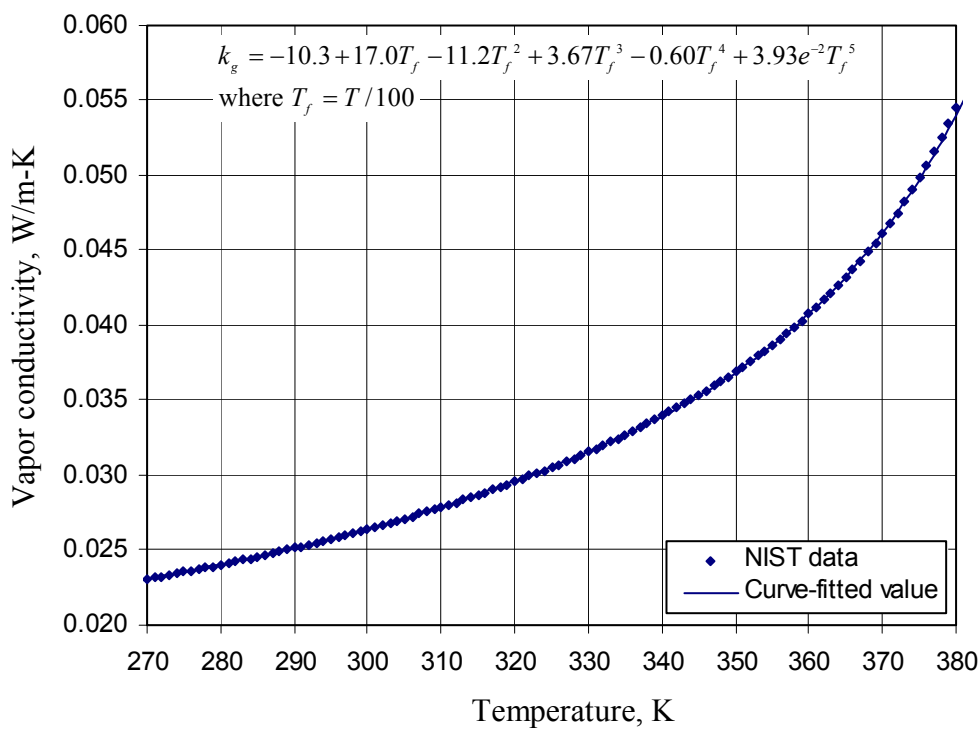
Fig. B.8: Vapor conductivity of saturated ammonia.

$$k_g = -10.3 + 17.0T_f - 11.2T_f^2 + 3.67T_f^3 - 0.60T_f^4 + 3.93e^{-2}T_f^5$$
where $T_f = T/100$

$$C_{P,L} = -1.22e^6 + 2.05e^6 T_f - 1.38e^6 T_f^2 + 4.60e^5 T_f^3 - 7.69e^4 T_f^4 + 5.13e^3 T_f^5$$

where $T_f = T/100$

- ◆ NIST data
- — Curve-fitted value
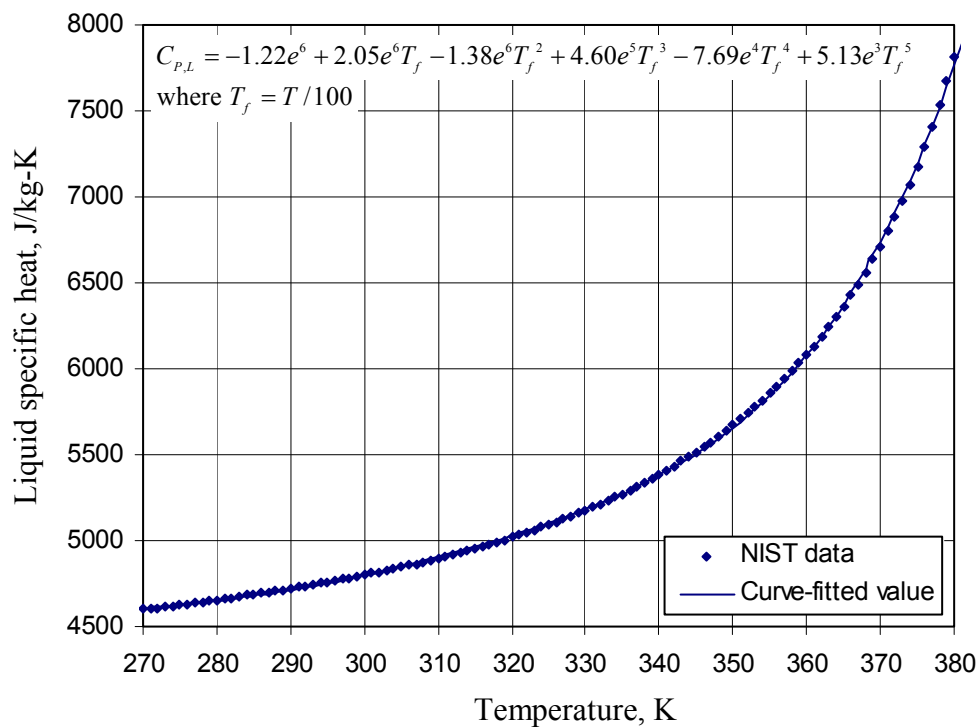
Fig. B.9: Liquid specific heat of saturated ammonia.

$$C_{P,g} = -3.27e^6 + 5.36e^6 T_f - 3.51e^6 T_f^2 + 1.15e^6 T_f^3 - 1.88e^5 T_f^4 + 1.23e^4 T_f^5$$

where $T_f = T/100$

- ◆ NIST data
- — Curve-fitted value
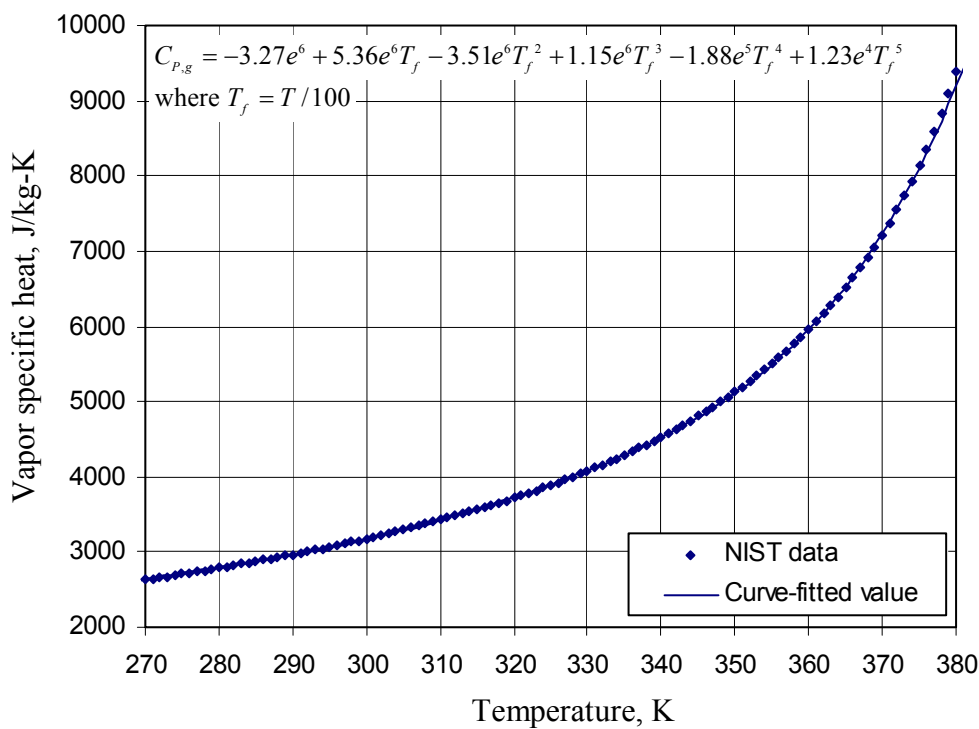
Fig. B.10: Vapor specific heat of saturated ammonia.
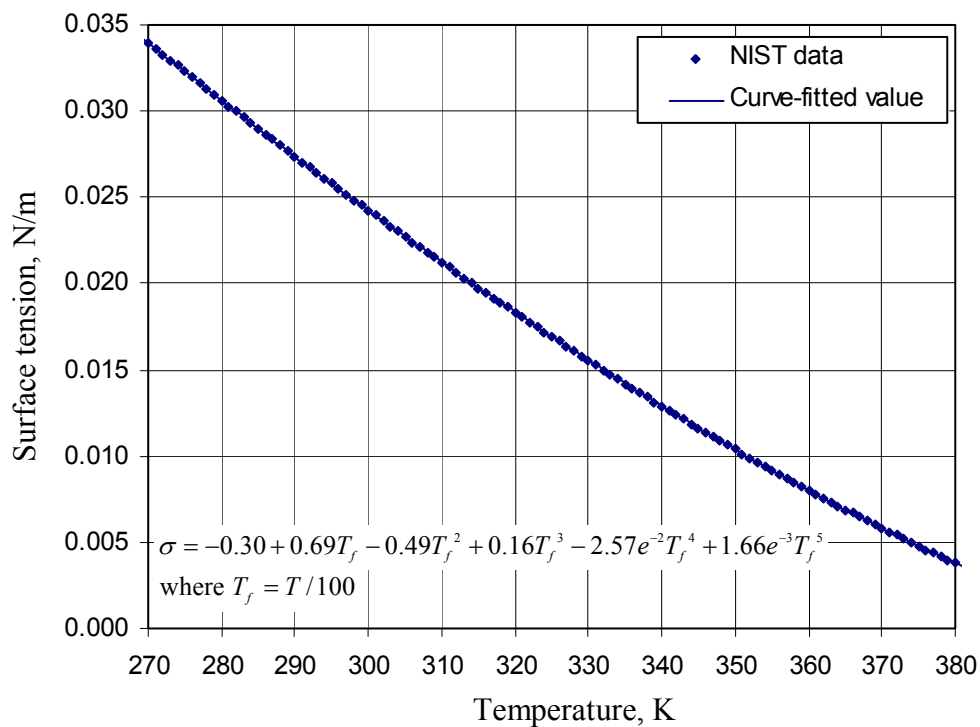
Fig. B.11: Surface tension of saturated ammonia.

$$\sigma = -0.30 + 0.69T_f - 0.49T_f^{\,2} + 0.16T_f^{\,3} - 2.57e^{-2}T_f^{\,4} + 1.66e^{-3}T_f^{\,5}$$

where $T_f = T/100$

$$\lambda = 4.14e^7 - 6.49e^7 T_f + 4.23e^7 T_f^{\,2} - 1.39e^7 T_f^{\,3} + 2.27e^6 T_f^{\,4} - 1.49e^5 T_f^{\,5}$$

where $T_f = T/100$
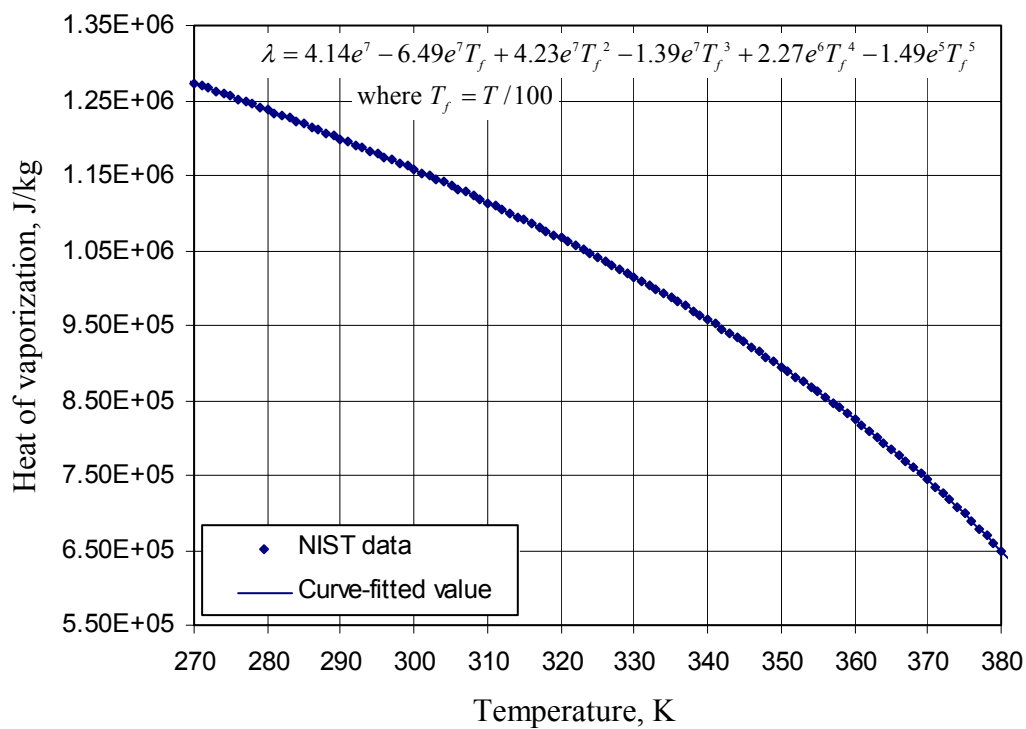
Fig. B.12: Heat of vaporization of saturated ammonia.

Appendix C

CALCULATIONS OF VISCOUS DISSIPATION

Viscous dissipation represents an increase in internal energy due to friction. It causes deformation of the fluid elements, and transforms kinetic energy into internal energy. In the present steady-state model, the viscous dissipation was neglected. This section performs a sample analysis to calculate the viscous dissipation in our test LHP operation.

From Eq. 5.10, the energy equation of 1-D steady flow with one inlet and one outlet can be written as:

$$\dot{Q} = \dot{m}_{out}\left(u + \frac{p}{\rho} + \frac{1}{2}V^2 + gz\right)_{out} - \dot{m}_{in}\left(u + \frac{p}{\rho} + \frac{1}{2}V^2 + gz\right)_{in} \qquad (C.1)$$

Assuming that there is no elevation change, that the inlet velocity is equal to the outlet velocity, and that there is no heat exchange between the LHP and the surroundings, the viscous dissipation can be written as:

$$\Phi = \dot{m}\left(u_{out} - u_{in}\right) = \dot{m}\left[\left(\frac{p}{\rho}\right)_{in} - \left(\frac{p}{\rho}\right)_{out}\right] \qquad (C.2)$$

In pipe flow analysis, viscous dissipation, Φ, can be calculated from the mass flow rate and the pressure drop along the loop.

Table C.1 shows the predicted results of the sample calculation when a LHP is operated at zero elevation. In predicted results, the Wallis correlation was selected to calculate the two-phase pressure drop in the LHP because it predicts the highest pressure

drop among the correlations. The predicted viscous dissipation was small numbers in all

cases, as expected. For example, when the heat load was 1000 W, the viscous dissipation

was only 0.0923 W. Therefore, it is valid to neglect the effect of viscous dissipation in

the steady-state model.

Table C.1: Predicted results of the sample calculation of viscous dissipation when a LHP
is operated at zero elevation.

Case No.		1	2	3	4	5	6
$\dot{Q}_{APP}$	(W)	10.0	50.0	100.0	300.0	600.0	1000.0
ΔP_{TOTAL}	(Pa)	22.0	116.0	258.0	1550.0	4585.0	8403.0
$\dot{m}$	(kg/s)	8.56E-6	4.27E-5	8.49E-5	2.53E-4	5.16E-4	9.04E-4
Φ	(W)	2.27E-5	6.02E-4	2.66E-3	4.75E-2	2.87E-1	9.23E-1
$\left(\Phi / \dot{Q}_{APP}\right)$	(%)	0.0002	0.0012	0.0027	0.0158	0.0479	0.0923

Appendix D

NUMERICAL METHODS IN THE STEADY-STATE MODEL

D.1   GAUSSIAN QUADRATURE

The basic procedure for approximating the definite integral of a function f on the interval [a, b] is to determine an interpolating polynomial that approximates f, and then integrate this polynomial. The Midpoint rule approximation [Faires and Burden, 1993] can be easily determined geometrically, as shown in Fig. D.1.
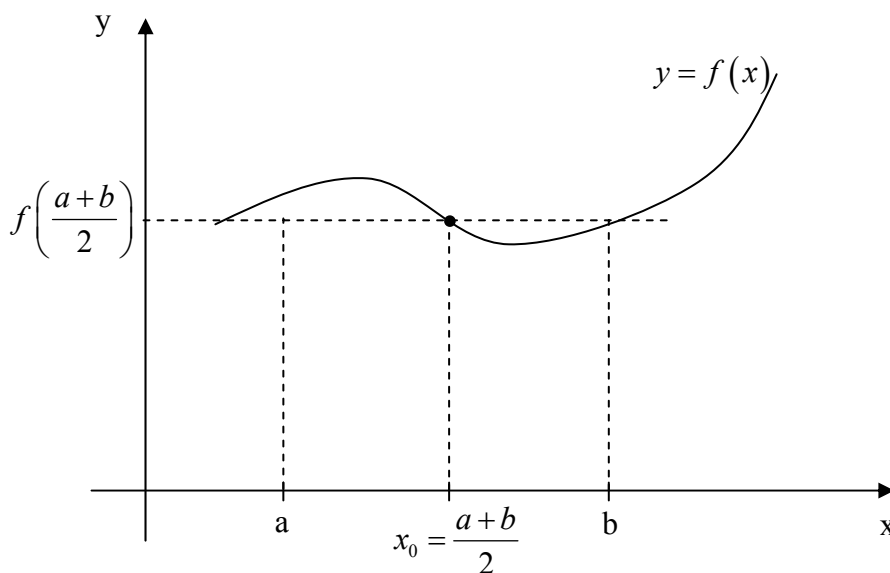
Fig. D.1: Midpoint rule approximation.

Gaussian quadrature chooses the points for evaluation in an optimal, rather than equally spaced, manner. The nodes x_1, x_2,..., x_n in the internal [a, b], and coefficients

c_1, c_2, ..., c_n are chosen to minimize the expected error obtained in performing the approximation

$$\int_a^b f(x)dx \approx \sum_{i=1}^{n} c_i f(x_i)$$ (D.1)

for an arbitrary function f. To measure the accuracy, we assume that the best choice of these values is that producing the exact result for the largest class of polynomials.

Legendre polynomials can be used to approximate

$$\int_a^b f(x)dx = \int_{-1}^{1} f\left(\frac{(b-a)t+b+a}{2}\right)\frac{(b-a)}{2}dt$$ (D.2)

Using the roots $r_{n,1}$, $r_{n,2}$,..., $r_{n,n}$ and the coefficients $c_{n,1}$, $c_{n,2}$, ..., $c_{n,n}$ given in Table D.1 transforms the approximation to the following: (Gaussian Quadrature)

$$\int_a^b f(x)dx = \frac{(b-a)}{2}\sum_{j=1}^{n} c_{n,j} f\left(\frac{(b-a)r_{n,j}+b+a}{2}\right)$$ (C.3)

Table D.1 is an excerpt from Gaussian Quadrature formulas [Stroud and Secrest, 1966], rounded to 16 places after the decimal point to make the values suitable for double-precision computer use. In the steady-state model, Legendre polynomials of degree 10 were applied to solve the finite integral.

Table D.1: Roots and coefficients of Gaussian Quadrature. (All roots are ± except for the zero values)

n	Roots, $r_{n,i}$	Coefficients, $c_{n,i}$
2	0.577 350 269 189 625 8	1.000 000 000 000 000 0
3	0.000 000 000 000 000 0	0.888 888 888 888 888 9
	0.774 596 669 241 483 4	0.555 555 555 555 555 6
4	0.339 981 043 584 856 3	0.652 145 154 862 546 1
	0.861 136 311 594 052 6	0.347 854 845 137 453 9
5	0.000 000 000 000 000 0	0.568 888 888 888 888 9
	0.538 469 310 105 683 1	0.478 628 670 499 366 5
	0.906 179 845 938 664 0	0.236 926 885 056 189 1
10	0.148 874 338 981 631 2	0.295 524 224 714 752 9
	0.433 395 394 129 247 2	0.269 266 719 309 996 4
	0.679 409 568 299 024 4	0.219 086 362 515 982 0
	0.865 063 366 688 984 5	0.149 451 349 150 580 6
	0.973 906 528 517 171 7	0.066 671 344 308 688 1

D.2   SECANT METHOD

In the steady-state model, the Secant method was used to solve for the void fraction, α. The void fraction can be expressed as:

$$\alpha = \frac{Af_1(\alpha)}{1+Af_1(\alpha)} \tag{D.4}$$

where A is a constant. The Secant method was used to solve:

$$f(\alpha) = \alpha - \frac{Af_1(\alpha)}{1+Af_1(\alpha)} = 0 \tag{D.5}$$

The Secant method is the approximation p_{i+1} to a root of $f(x) = 0$ computed from the approximations p_i and p_{i-1} using the equation:

$$p_{i+1} = p_i - \frac{f(p_i)(p_i - p_{i-1})}{f(p_i) - f(p_{i-1})} \tag{D.6}$$

In the steady-state model, the following calculation was performed, starting with an initial guess, α_0:

$$\alpha_0 = \frac{A}{1+A} \quad \text{and} f(\alpha_0) = \alpha_0 - \frac{Af_1(\alpha_0)}{1+Af_1(\alpha_0)} \tag{D.7}$$

$$\alpha_1 = \frac{Af_1(\alpha_0)}{1+Af_1(\alpha_0)} \quad \text{and} f(\alpha_1) = \alpha_1 - \frac{Af_1(\alpha_1)}{1+Af_1(\alpha_1)} \tag{D.8}$$

$$\alpha_2 = \frac{Af_1(\alpha_1)}{1+Af_1(\alpha_1)} \quad \text{and} f(\alpha_2) = \alpha_2 - \frac{Af_1(\alpha_2)}{1+Af_1(\alpha_2)} \tag{D.9}$$

Then an approximation of void fraction can be obtained from the Secant method:

$$\alpha = \alpha_2 - \frac{(\alpha_2 - \alpha_1)f(\alpha_2)}{f(\alpha_2) - f(\alpha_1)} \tag{D.10}$$

Appendix E

STUDY OF FLUID FLOW IN THE PRIMARY WICK

The radial heat leak of a LHP due to heat and mass transfer in the primary wick is discussed in Section 5.5.7 and can be written as:

$$\dot{Q}_{HL,R} = \frac{2\pi k_{EFF} L_{WICK} \varsigma}{\left(D_W^O / D_W^I\right)^\varsigma - 1} \Delta T_{AC.WICK}$$ (E.1)

where $\varsigma = \dfrac{\dot{m} C_P}{2\pi k_{EFF} L_{WICK}}$. When the mass flow rate in the primary wick is very small, the coefficient ς approaches zero. Therefore, the radial heat leak becomes pure conduction, and the equation can be written as:

$$\dot{Q}_{HL,R} = \frac{2\pi k_{EFF} L_{WICK}}{\ln\left(D_W^O / D_W^I\right)} \Delta T_{AC.WICK}$$ (E.2)

Comparing Eq. E.1 and Eq. E.2, the difference between considering and neglecting fluid flow in the primary wick is studied in Table E.1.

Table E.1: Study of the effect of fluid flow in the primary wick on radial heat leak.

ς	$\dfrac{\varsigma}{\left(D_W^O / D_W^I\right)^\varsigma - 1}$	$\dfrac{1}{\ln\left(D_W^O / D_W^I\right)}$	Error (%)
0.001	1.4422	1.4427	0.035
0.01	1.4377	1.4427	0.347
0.0331	1.4262	1.4427	1.157
0.1	1.3933	1.4427	3.547

In the test LHP, the design maximum heat load is equal to 1000 W. The parameter ς can be calculated from the properties of the primary wick and operating conditions of the test LHP as followed:

$$\varsigma = \frac{\dot{m}C_P}{2\pi k_{EFF} L_{WICK}} \approx \frac{0.000876 \frac{\text{kg}}{\text{sec}} \times 4800 \frac{\text{J}}{\text{kg-K}}}{2\pi \times 33.1 \frac{\text{W}}{\text{m-K}} \times 0.6096\text{m}} = 0.0331 \qquad (\text{E.3})$$

The corresponding maximum error of radial heat leak by neglecting the fluid flow in the primary wick is 1.157 % (shown in Table E.1).

Although the fluid flow in the primary wick was considered in the calculation of the radial heat leak in the steady-state model, it is valid to assume pure conduction in the primary wick in our test LHP modeling.

Appendix F

DETAILED FLOW CHART OF THE STADY-STATE MODEL

The steady-state model is used to predict the LHP performance with given operating conditions. Known parameters are read in from the input datasheet, which acts as the user interface for the calculation code. A detailed and sophisticated calculation program is included in a macro within the spreadsheet, and is illustrated as a flow chart shown below:

Read in all the input parameters from the input datasheet.

Set constants used in the calculations: $T_{ABS} = -273.16$ °C, Stefan-Boltzmann constant = 5.669E-8 W/m^{2}K^4, $\pi = 3.14159$, and gravitational acceleration = 9.81m/s^2.

Initialize the variables: $T_{SAT,h}$, $T_{SAT,l}$, and $D\dot{Q}$.

Set the iteration criteria: $D\dot{Q} = \dot{Q}_{HL} - \dot{Q}_{R-A} + \dot{Q}_{SC} \leq 0.0001$ or reached the maximum number of iterations (1000).

Guess steady-state operating temperature, T_{SSOT}.

Calculate evaporator body temperature.

Calculate mass flow rate.

Calculate pressure drop and temperature superheat in the vapor channel.

Guess a new steady-state operating temperature.

Vapor line is insulated.

Vapor line is not insulated.

$T_{SSOT} < T_{AMB}$

$T_{SSOT} > T_{AMB}$

Perform pressure drop and heat transfer calculation and obtain the length of the two-phase flow, $L_{2\phi}$.

Calculate pressure drop in the vapor line.

Perform pressure drop and heat transfer calculation and obtain the vapor quality at the vapor line exit.

$L_{2\phi} > L_{V.L.}$

$L_{2\phi} < L_{V.L.}$

Perform pressure drop and heat transfer calculation and obtain the vapor quality at the vapor line exit.

Calculate the pressure drop in the vapor line, condenser, and the liquid line and the liquid temperatures at vapor line exit, condenser exit, and liquid line exit.

Perform pressure drop and heat transfer calculation and obtain the length of the two-phase flow in the condenser, $L_{2\phi}$.

$L_{2\phi} > L_C$

$L_{2\phi} < L_C$

Perform pressure drop and heat transfer calculation and obtain the vapor quality at the vapor line exit.

Calculate the pressure drop in the condenser and the liquid line and the liquid temperatures at condenser exit, and liquid line exit.

$T_{SSOT} < T_{AMB}$

$T_{SSOT} > T_{AMB}$

Perform pressure drop and heat transfer calculation and obtain the vapor quality at the liquid line exit.

Perform pressure drop and heat transfer calculation and obtain the length of the two-phase flow, $L_{2\phi}$.

$L_{2\phi} > L_{L.L.}$

$L_{2\phi} < L_{L.L.}$

```
┌─────────────────────┐          ┌─────────────────────┐
│ Perform pressure    │          │ Calculate the       │
│ drop and heat       │          │ pressure drop in the│
│ transfer calculation│          │ liquid line and the │
│ and obtain the vapor│          │ liquid temperatures │
│ quality at the liquid│         │ at liquid line exit.│
│ line exit.          │          │                     │
└─────────────────────┘          └─────────────────────┘
```

Calculate pressure drop in the bayonet and temperature at the exit of the bayonet.

Calculate total pressure drop of the system and the pressure difference across the primary wick.

Calculate heat exchange between the ambient and the reservoir, $\dot{Q}_{R-A}$.

Calculate the amount of subcooling brought back by the fluid from the liquid line, $\dot{Q}_{SC}$.

Calculate axial heat leak, $\dot{Q}_{HL,A}$.

Calculate radial heat leak, $\dot{Q}_{HL,R}$.

Check if the convergent criteria have been achieved:
$$D\dot{Q} = \dot{Q}_{HL} - \dot{Q}_{R-A} + \dot{Q}_{SC} \leq 0.0001.$$

No

Guess a liquid mass flow rate in the vapor line, $\dot{m}_L$. The total mass flow rate becomes $\dot{m}_{TOTAL} = \dot{m}_L + \dot{m}_g$.

Yes

No

Check if total pressure drop, $\left|\Delta P_{TOTAL}\right| \leq 1$.

Gravity-controlled mode

Capillary-controlled mode

Yes

Achieve State-state condition and obtained final answer.

Output the calculating results to the output sheets.

VITA

Po-Ya Abel Chuang

Place and Date of Birth   Hsinying, Tainan, TAIWAN   August, 1973

Education

December, 2003   Doctor of Philosophy in Mechanical Engineering
                 Pennsylvania State University, PA, USA
June, 1997   Master of Science in Aerospace Engineering
                 National Cheng-Kung University (NCKU), Tainan, TAIWAN
June, 1995   Bachelor of Science in Aerospace Engineering
                 National Cheng-Kung University (NCKU), Tainan, TAIWAN

Employment History

06/2003 ~ 08/2003   The Pennsylvania State University, PA USA
                         Instructor of Fluids Laboratory, ME83
08/2000 ~ 12/2003   The Pennsylvania State University, PA USA
                         Research Assistant
05/2001 ~ 12/2003   TTH Research, Inc., MD USA
                         Research Assistant
01/2000 ~ 05/2000   The Pennsylvania State University, PA USA
                         Teaching Assistant of Fluid Mechanics, ME33
08/1997 ~ 06/1999   R.O.C. Air Force, Chiayi Taiwan
                         F-16 Maintenance Technician - Avionics

Publication

1. Chuang, P. A., Cimbala, J. M., Brenizer, J. S., et al, Comparison of experiments and 1-D steady-state model of a loop heat pipe, International Mechanical Engineering Congress and Exposition, November 17-22, 2002, New Orleans, LA USA
2. Cimbala, J. M., Brenizer, J. S., Chuang, P. A., et al, Study of a loop heat pipe using neutron radiography, 4th International Topical Meeting on Neutron Radiography, June 3-6, 2001, State College, PA USA

Honors

10/1998   R.O.C. Air Force Excellence Award
07/1998   F-16 Maintenance Technician
01/1997   Honorary Member of The Phi-Tau-Phi Scholastic Honor Society
07/1996 ~ 06/1997 Outstanding Fellowship of IAA, NCKU